Plasma Physics Reports, Vol. 26, No. 3, 2000, pp. 177–190. Translated from Fizika Plazmy, Vol. 26, No. 3, 2000, pp. 195–208.

Reversed-Shear Experiments in the T-10 Tokamak

V. V. Alikaev, A. A. Borshchegovskiĭ, M. M. Dremin, Yu. V. Esipchuk, D. V. Kalupin, N. A. Kirneva, A. Ya. Kislov, D. A. Kislov, A. A. Martynov, T. B. Myalton, G. E. Notkin, V. I. Poznyak, Yu. D. Pavlov, I. N. Roĭ, M. M. Stepanenko, A. V. Sushkov, V. M. Trukhin, and V. V. Chistyakov

Russian Research Centre Kurchatov Institute, pl. Kurchatova 1, Moscow, 123182 Russia

Received January 10, 1999; in final form, September 2, 1999

Abstract—Results from T-10 experiments in regimes with nonmonotonic plasma current profiles are presented. The possibility of controlling the current profile $j(r)$ by electron-cyclotron current drive is demonstrated experimentally. Nonmonotonic q profiles with the reversed shear are obtained in which the $q_{\min}$ value varies in a wide range, $q_{\min} = 1$–2.3. It is shown that the current profiles with $q_{\min} \sim 2$ (in this case, there are two resonant magnetic surfaces $q = 2$ in the plasma) can cause the onset of MHD instabilities. The possibility of the formation of an internal transport barrier in reversed-shear discharges in the T-10 tokamak is analyzed. In T-10, electron transport is governed by short-wavelength electron turbulence. As a result, there is no clear evidence of the formation of an inner transport barrier in these experiments. *© 2000 MAIK "Nauka/Interperiodica".*

1. INTRODUCTION

The possibility of the formation of an internal transport barrier (ITB) was studied in the T-10 tokamak in regimes with nonmonotonic $q(r)$ profiles. In this case, the reversed-shear region $r/q(dq/dr) < 0$ occurs in the plasma core ($r/a < 0.35$) (Fig. 1). Such a q profile was produced by on-axis electron-cyclotron current drive (ECCD) in the direction opposite to the ohmic current (counter-CD).

An extraordinary polarized microwave beam was launched into the tokamak at an angle of $\varphi = 21°$ with respect to the major radius R. The microwave power absorbed in the plasma attained $P_{ab} = 1$ MW. The microwave frequency corresponded to the second harmonic of the electron cyclotron resonance (ECR). The duration of the microwave pulse $\Delta t_{HF} = 0.4$ s exceeded the skin time needed for the profile of the total current $j(r)$ to rearrange; this allowed us to obtain a steady-state q profile by the end of the microwave pulse.

The ITB formation in reversed-shear discharges was observed experimentally in different tokamaks, e.g., in TFTR [1], DIII-D [2], and JT-60 [3]. Inside the ITB, the ion heat conductivity decreased to the neoclassical level. The electron transport also decreased, but remained anomalous. In the above tokamaks, the ITB formation was observed in hot-ion discharges, when the power of auxiliary heating was mainly absorbed by the ion component. At high ion temperatures, the transport was apparently determined by the ion-gradient-mode (ITG) turbulence.

The feature of the T-10 experiments was that the microwave power was absorbed by the electrons ($T_e \gg T_i$), which allowed us to assume that the plasma behavior was governed by the electron turbulence.

2. PRELIMINARY CALCULATIONS

In order to choose the appropriate experimental conditions, we carried out preliminary calculations of the $q(r)$ profiles with the use of the ASTRA transport code [4] and the canonical profile model [5], which adequately describes the profiles of the plasma temperature and density from the T-10 database. The ECCD current $j_{CD}(r)$ was calculated with the TORAY code [6].

The results of calculations (see Fig. 1) showed that

(i) for the available microwave power (up to 1 MW in the plasma) it is possible to produce nonmonotonic q profiles with the reversed shear in the plasma core ($r \le 0.35a_L$, where $a_L = 0.3$ m is the limiter radius) and

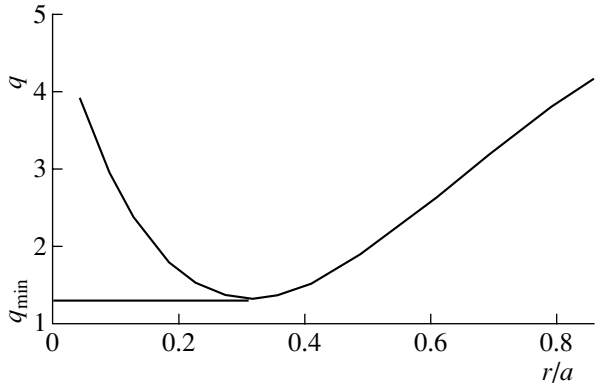

Fig. 1. The q profiles calculated with allowance for the EC current j_{CD}. The curve shows the possibility of obtaining the reversed-shear profiles. The microwave power absorbed in the plasma is $P_{ab} = 0.75$ MW, $I_p = 150$ kA, $B_T = 2.4$ T, and $\bar{n}_e = 10^{19}$ m^{-3}.

1063-780X/00/2603-0177$20.00 © 2000 MAIK "Nauka/Interperiodica"

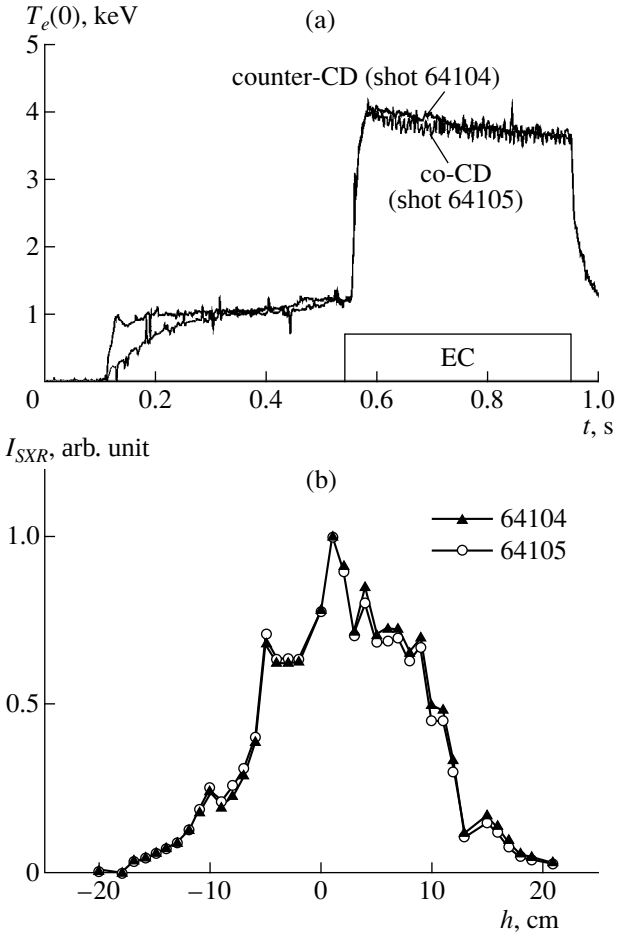

Fig. 2. (a) Time behavior of the central temperature $T_e(0)$ for I_p = 150 kA ($q_{\min}$ = 1.2–1.3), B_T = 2.4 T, and P_{ab} = 0.75 MW. For comparison, the $T_e(0)$ trace in the co-CD mode is shown (as in Figs. 3 and 5). (b) A comparison of the I_{SXR} profiles in the co- and counter-CD modes.

(ii) the value of $q_{\min}$ can be varied over a wide range ($q_{\min}$ = 1–3) by varying the plasma current I_p from 75 to 150 kA.

3. EXPERIMENTAL CONDITIONS

According to the results of calculations, we carried out the experiments with plasma currents of I_p = 75, 100, and 150 kA. The line-averaged plasma density was varied over the range $\bar{n}_e = (1–1.5) \times 10^{19}$ m^{-3}. The toroidal magnetic field B_T = 2.4–2.46 T corresponded to the on-axis ECCD.

In all cases, the experiments were carried out for both the co- and counter-CD in order to compare the energy confinement and transport for monotonic q profiles (co-CD) and q profiles with reversed shear (counter-CD).

The data presented below were obtained with the use of the following diagnostics:

(i) The electron temperature $T_e(r, t)$ was measured by the emission at the second EC harmonic (eight diagnostic channels were equally spaced over r from 0 to a_L, the time resolution being ~0.1 ms).

(ii) Fast MHD processes were studied with the use of a pinhole camera recording soft X radiation (SXR) in the photon energy range E = 1–6 keV with a spatial resolution of ~1 cm and time resolution of 16–100 μs.

These methods were supplemented by other standard diagnostics.

4. EXPERIMENTAL RESULTS

4.1. According to calculations, for I_p = 150 kA (Fig. 2a), the minimum value of the safety factor is $q_{\min}$ = 1.2–1.3, which is substantially less than the resonant value q = 2. As is seen in Fig. 2a, the central temperature was the same for both the counter- and co-CD regimes, $T_e(0)^{\text{counter}} \simeq T_e(0)^{\text{co}}$; i.e., there was no clear evidence of ITB formation, although the reversed-shear region was formed in the counter-CD regime. This is also seen from comparing the profiles of the SXR intensity I_{SXR} (Fig. 2b).

4.2. The calculations show that, as I_p decreases to 100 kA, $q_{\min}$ approaches the resonant value q = 2 and the distance between two resonant magnetic surfaces with q = 2 decreases substantially (Fig. 1). It is seen in Fig. 3 that, in the reversed-shear mode (in contrast to the co-CD mode), about 100 ms after the microwave pulse is switched on, the central temperature drops abruptly ($T_e(0)$ decreases by ~30%), which indicates a substantial deterioration of the core energy confinement.

Figure 3 shows the time behavior of the SXR intensity $I_{SXR}(0)$ along the central chord. It is seen that the observed decrease in $T_e(0)$ occurs as a sequence of internal disruptions similar to internal disruptions that take place in case of sawtooth oscillations. The profiles of I_{SXR} in Fig. 4a show that the radius at which these disruptions occur (r_d = 9–10 cm) is close to the outer of two resonant surfaces q = 2 (not 1).

The observed internal disruptions are accompanied by the onset of the m = 2 MHD activity. This is seen from Figs. 4b and 4c. Figure 4b presents the traces of the SXR intensity for the central chord and two chords shifted symmetrically with respect to the axis (the perturbation amplitude along these chords is close to the maximum amplitude). The phase diagram for these perturbations is presented in Fig. 4c. This diagram differs from the diagram that could be expected in the presence of an m = 2 island and only one q = 2 resonant surface, because, in that case, there would be only two points of the phase reversal rather than four (as in Fig. 4c). It seems that, here, we can refer to the presence of two q = 2 resonant surfaces in the plasma. The I_{SXR} signals

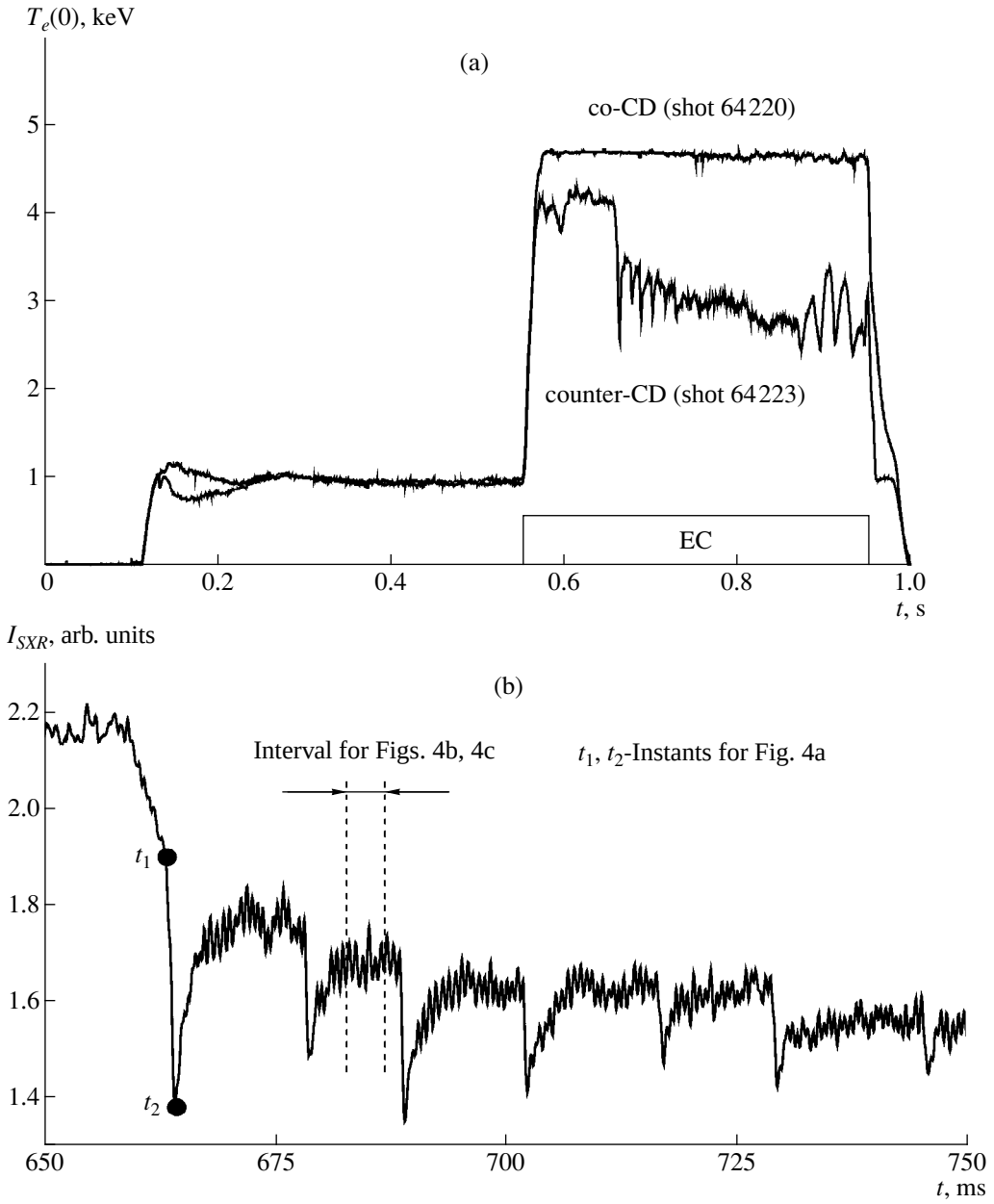

Fig. 3. (a) The trace of the central temperature $T_e(0)$ in the counter-CD mode with I_p = 100 kA ($q_{\min}$ approaches 2) for $\bar{n}_e = 10^{19}$ m^{-3}, P_{ab} = 0.85 MW, and B_T = 2.46 T. (b) $I_{SXR}(0)$ trace.

from the chords lying at h = –(13–19) cm and h = 17–21 cm do not show the phase reversal. However, the I_{SXR} signals from these chords are already strongly suppressed and distorted due to noise. For this reason, the phases on these chords in Fig. 4c are marked by a different symbol (vertical bar).

Thus, as $q_{\min}$ increases and, consequently, the tearing modes occurring in the vicinity of the two resonant surfaces approach each other, these modes begin to interact and form a single magnetic structure (double-tearing mode) that rotates at the very low frequency of f = 300–500 Hz (Fig. 4b).

4.3. Calculations show that, for the plasma current I_p = 75 kA, the value of $q_{\min}$ at the end of the microwave pulse substantially exceeds the resonant value q = 2. In this regime, a new phenomenon was observed after the same MHD phase as in the previous case (I_p = 100 kA). There is a sharp increase in the central temperature $T_e(0)$ (Fig. 5a), which is evidence of the decrease in the additional electron transport in the plasma core caused by the onset of the MHD activity. As a result, the central

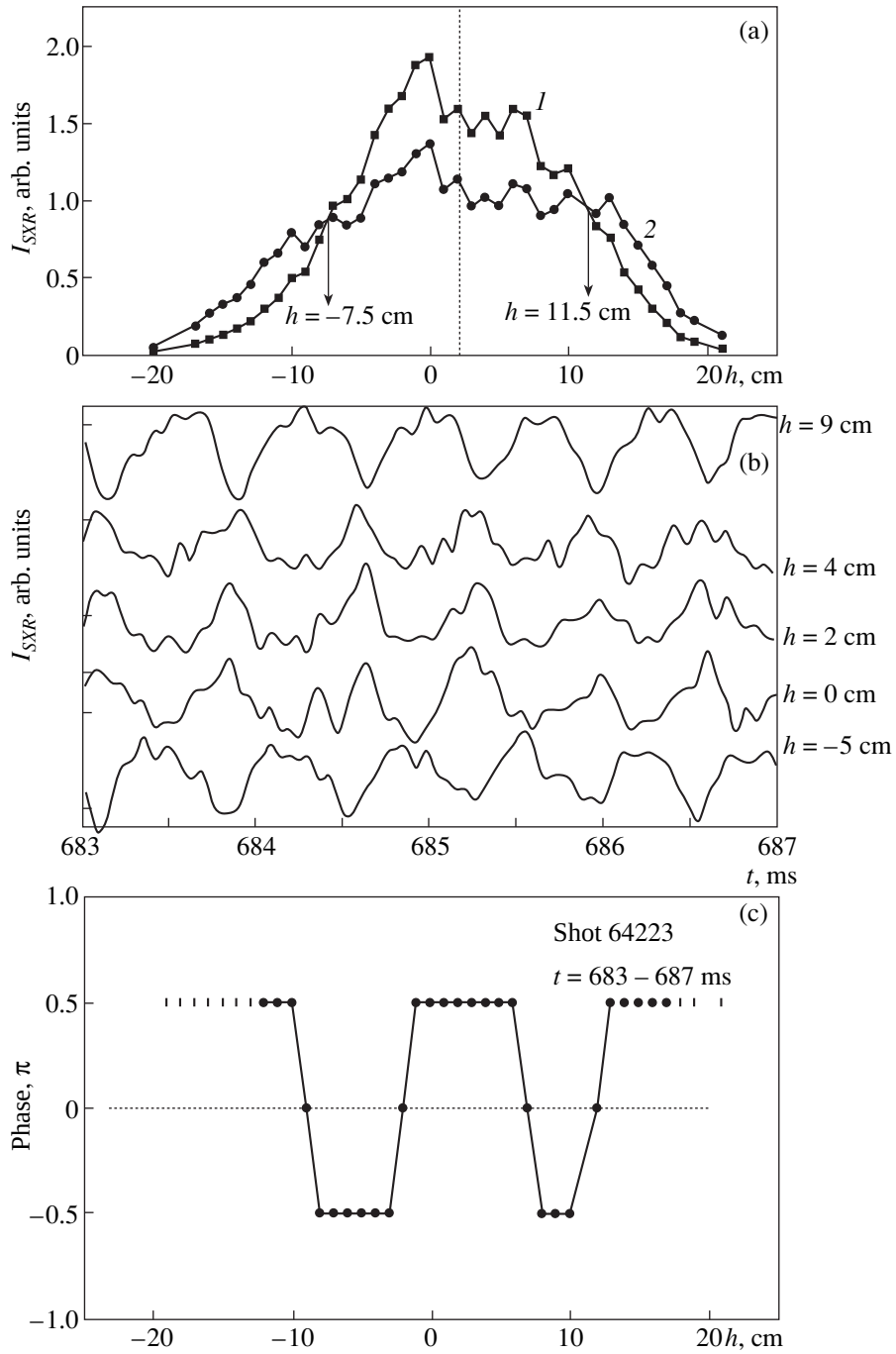

Fig. 4. (a) I_{SXR} profiles before and after an internal disruption at the instants shown in Fig. 3b: (*1*) t_1 = 663.04 ms and (*2*) t_2 = 664.09 ms. (b) I_{SXR} traces for different chords, demonstrating the structure of the $m = 2$ MHD mode. (c) Phase diagram of the $m = 2$ oscillations, showing the presence of two $q = 2$ resonant surfaces.

temperature is restored completely (i.e., it reaches the level it had been at before the onset of the MHD activity) but is about 10% lower than the temperature in the identical co-CD mode with a monotonic q profile.

Thus, in the regime in question, $q_{\min}$ reaches the resonant value $q = 2$ at the instant the temperature starts to be restored. Thereafter, $q_{\min}$ exceeds this value in spite of a decrease the central temperature during the MHD phase. After the temperature is restored, the SXR signals do not show the $m = 2$ MHD activity (Figs. 5b, 5c), which seems to disappear as the temperature is restored.

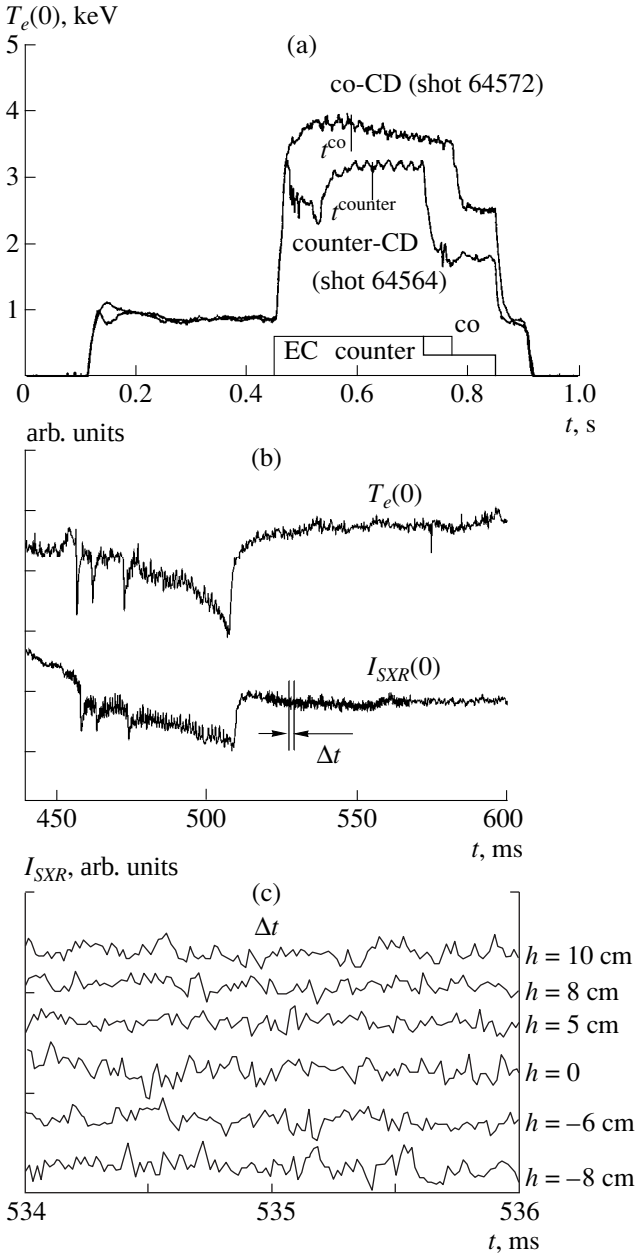

Fig. 5. (a) $T_e(0)$ trace in the counter-CD mode with I_p = 75 kA (the calculated value of $q_{\min}$ exceeds 2) for B_T = 2.46 T, P_{ab} = 0.85 MW, and $\bar{n}_e = 10^{19}$ m^{-3}. (b, c) $I_{SXR}(0)$ traces, demonstrating the vanishing of the m = 2 oscillations after the temperature is restored. Figure 5b also presents the $T_e(0)$ trace.

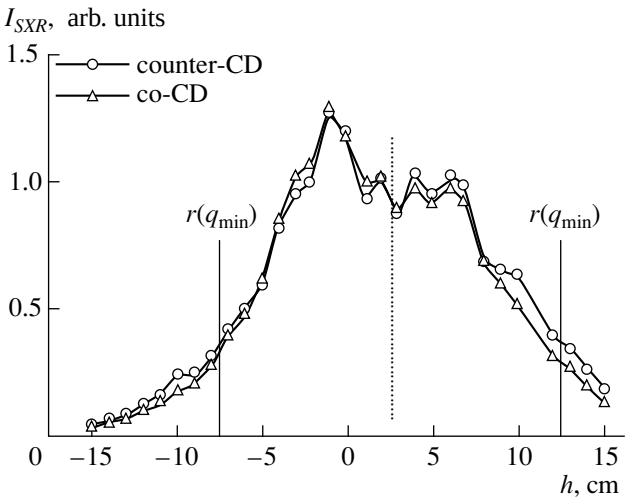

Fig. 6. A comparison of the I_{SXR} profiles in the co- and counter-CD modes at the instants shown in Fig. 5a.

4.4. The question remains open of whether a sharp increase in the central temperature is evidence of ITB formation? There are three arguments against such a conclusion:

(i) In all cases, a sharp increase in temperature was observed only after the onset of the MHD activity.

(ii) Even when the central temperature is completely restored, it always remains lower than in the identical co-CD mode with a monotonic q profile, which is a typical L-mode.

(iii) Figure 6 presents the I_{SXR} profiles at the end of the temperature restoration phase in the reversed-shear mode and in the steady-state stage of the co-CD mode (instants t^{Counter} and t^{Co} in Fig. 5a). A comparison of these profiles shows the absence of an appreciable increase in the temperature gradient in the vicinity of $q_{\min}$ in the reversed-shear discharge.

Thus, the experimental results allow us to draw the following conclusions (see Fig. 7):

When $T_e(0)$ reaches the steady-state level after the microwave pulse is switched on, the electron transport is close to that typical of L-mode confinement.

The onset of the internal m = 2 MHD mode is accompanied by an additional electron transport and a decrease in the temperature in the plasma core.

For a sufficiently intense ECCD, $q_{\min}$ increases and, at certain instant, becomes higher than the resonant value q = 2. Thus, the cause of the additional transport vanishes, the transports returns to the level typical of the L-mode, and the temperature $T_e(0)$ is restored.

5. TEST FOR THE VALIDITY OF THE CALCULATED $q(r)$ PROFILES

5.1. A preliminary analysis of the experimental results was based on the q profiles calculated with allowance for the EC current j_{CD}. Therefore, in order to confirm the above conclusions, it was necessary to check the correctness of the calculated q profiles (including their temporal behavior). For this purpose, experiments were carried out in which the microwave pulse was switched on simultaneously with the beginning of the growth of the plasma current, as is seen in

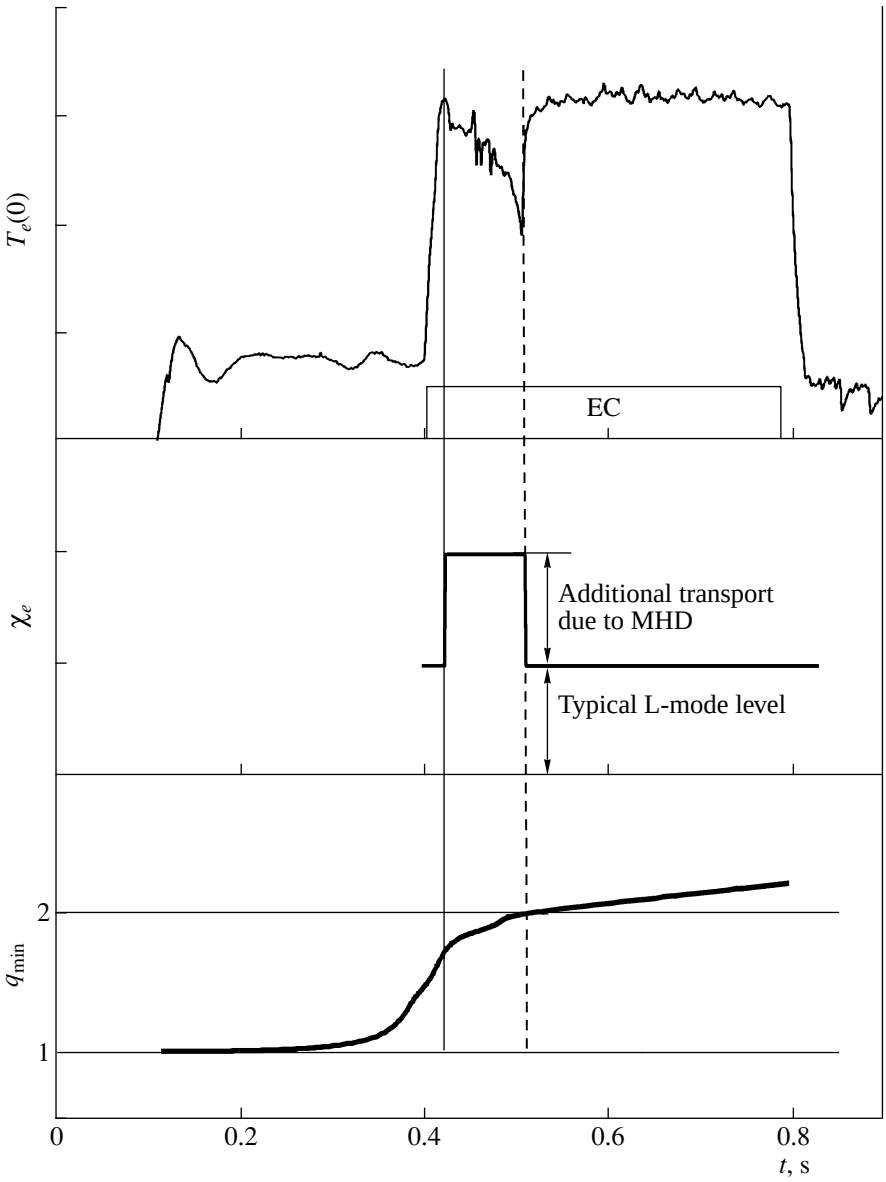

Fig. 7. Processes in the counter-CD mode with I_p = 75 kA.

Fig. 8. The experiments were carried out in the ohmic, co-CD, and counter-CD modes.

5.2. One of the methods used to check the correctness of the calculated q profiles was a comparison of the calculated and experimental instants t_{st} of the onset of sawtooth oscillations, i.e., the instants when the value $q = 1$ is reached on the experimentally determined phase reversal radius r_s of sawtooth oscillations is reversed. Figure 9 presents the traces of the SXR intensity, in which t_{st} is different in all three (ohmic, co-CD, and counter-CD) modes. We note that the difference in t_{st} in the co-CD and counter-CD modes is related only to the ECCD effect. The calculated values of $(t_{st})^{\text{calc}}$ presented in the same figure are in good agreement with the experiment.

5.3. The features of the plasma behavior observed in these experiments (mainly in the counter-CD mode) allowed us to check the validity of the calculated q profiles in more detail.

The traces of the electron temperature $T_e(0)$ and SXR intensity $I_{SXR}(0)$ along the central chord are presented in Fig. 10. In the counter-CD mode, during the Δt_1 and Δt_2 time intervals (Fig. 10c), the above features were observed as a sharp decrease and subsequent restoration of the central temperature.

In the interval Δt_2 (Fig. 11), the plasma behavior is similar to that observed in the basic experiments and described in Section 4.2: the decrease in the temperature $T_e(0)$ is a sequence of internal disruptions related to the onset of the $m = 2$ MHD activity. Thus, it can be

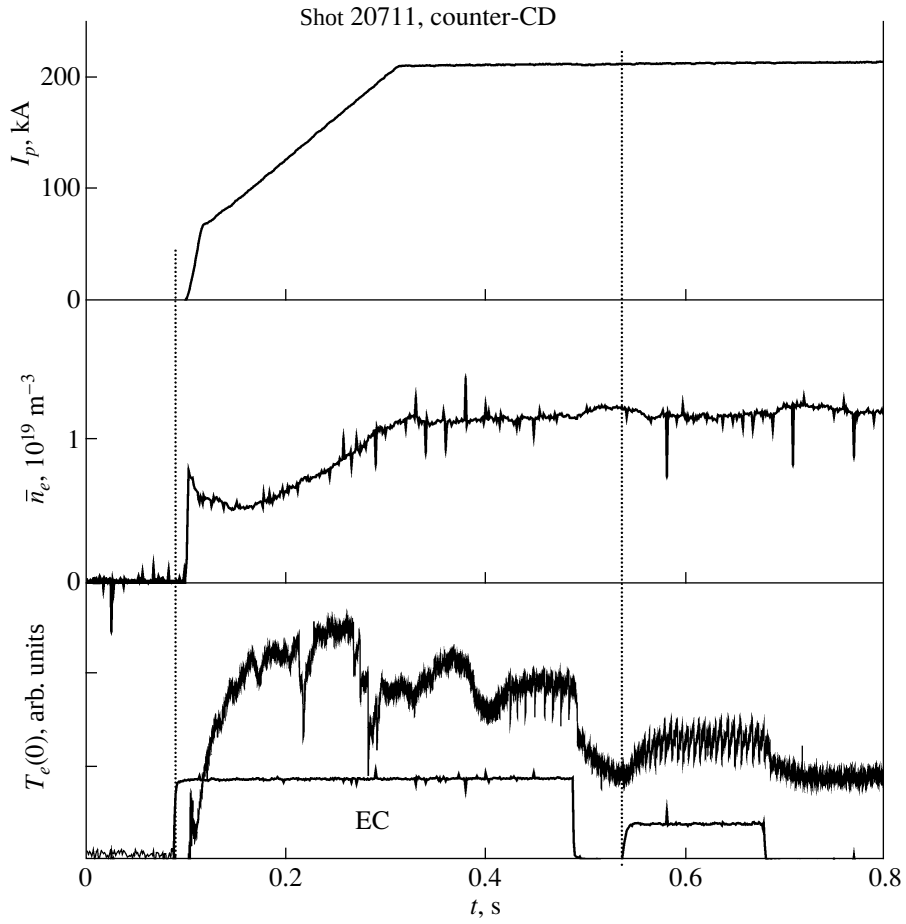

Fig. 8. Scenario of experiments in which the microwave pulse was switched on in the initial stage of the discharge.

expected that, in the interval Δt_2, the safety factor q in the plasma core goes through the resonant value $q = 2$.

It is seen in Fig. 12 that, in the interval Δt_1, the structure of the MHD activity is different. The phase diagram of perturbations (Fig. 12c) is similar to that expected in the presence of an $m = 3$ island (Fig. 12c, dashed line). Thus, we can expect that, in the interval Δt_1, the value of q in the plasma core passes through the resonant value $q = 3$.

5.4. The calculated $q(r, t_k)$ profiles for the counter-CD mode are presented in Fig. 13b for the instants t_k marked on the $T_e(0)$ trace in Fig. 13a. A comparison of the dynamics of the calculated q profiles in the counter-CD mode showed the following features of the plasma behavior:

(i) When the $m = 3$ MHD activity was observed, the calculated values of q in the time interval Δt_1 (Fig. 10) were close to the resonant value $q = 3$ (t_1 and t_2 instants in Fig. 13).

(ii) When the $m = 2$ MHD activity was observed, the calculated q profile in the time interval Δt_2 (Fig. 10) was nonmonotonic and $q_{\min}$ was close to the resonant value $q = 2$ (t_3 and t_4 instants in Fig. 13).

Taking into account these facts and the agreement between the calculated and experimental instants of the onset of sawtooth oscillations ($q = 1$ at r_s), we can conclude that the dynamics of the calculated q profiles does not contradict the experimentally observed plasma behavior.

5.5. The above conclusion is also confirmed by the results of modeling the basic experiments (see Section 4.3), which are presented in Fig. 14 for the most interesting regime with $I_p = 75$ kA (counter-CD mode). During the MHD phase, the q profile is nonmonotonic and has two $q = 2$ resonant surfaces and the value of $q_{\min}$ is close to $q = 2$. In spite of the temperature drop in the plasma core (which was taken into account in calculations), the value of I_{CD} appears to be sufficient for $q_{\min}$ to increase. As is seen in Fig. 14, the instant at which $q_{\min}$ passes through the resonant value $q = 2$ coincides with the experimentally observed instant at which the temperature $T_e(0)$ starts to be restored.

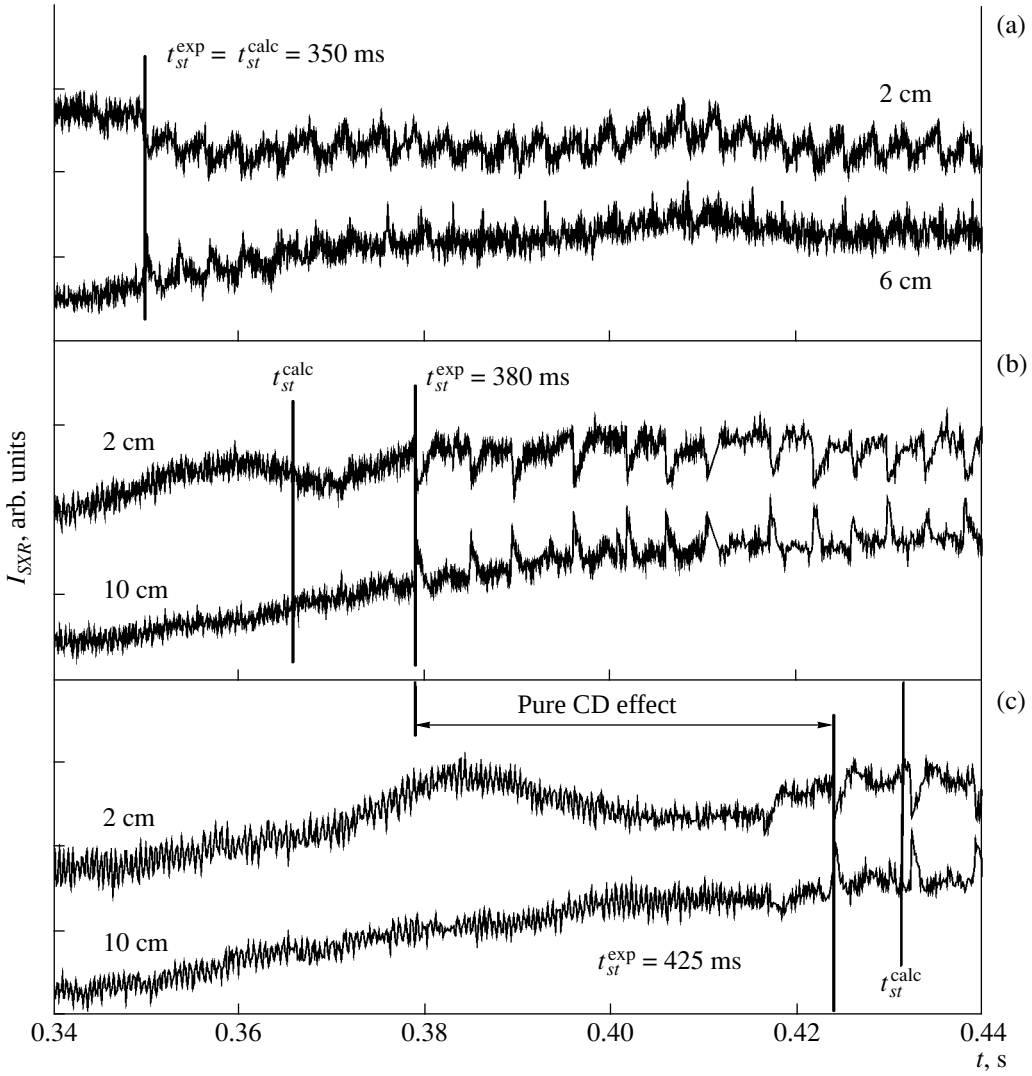

Fig. 9. Experimental I_{SXR} traces in the (a) ohmic, (b) co-CD, and (c) counter-CD modes. The traces demonstrate the instants $(t_{st})^{exp}$ of the onset of sawtooth oscillations. The calculated instants t_{st}^{calc} for the co-CD and counter-CD modes (365 and 430 ms, respectively) are also shown.

6. NONMONOTONIC q PROFILES CAN BE DANGEROUS WHEN q_{min} IS CLOSE TO $q = 2$

The experimental results presented in Fig. 10 show that the plasma behavior is very different in the ohmic, co-CD, and counter-CD modes.

The features of the plasma behavior in the counter-CD mode that are associated with the onset of the $m = 3$ and $m = 2$ MHD activity are also observed in the co-CD mode (shown by arrows in Fig. 10b); however, these features are much less pronounced. In the ohmic mode, the $T_e(0)$ traces show no peculiarities until the temperature reaches the steady-state level.

We note that, in all three modes, the safety factor q in the plasma core decreases from $q > 3$ to $q = 1$ (sawtooth oscillations were observed in all three modes) and, consequently, passes through the $q = 3$ and $q = 2$ resonant values. Therefore, the question arises of what is the reason for such different plasma behavior in these modes?

The results of calculations presented in Figs. 13 and 15 show the difference in the q profile in the three modes in question. As was noted above, in the counter-CD mode, when q_{min} is close to $q = 2$, the q profile is nonmonotonic and has two $q = 2$ surfaces located close to each other. This leads to the onset of the $m = 2$ MHD activity and internal disruptions. As is seen in Fig. 13, the experimentally found radius r_d at which internal disruptions occur is close to the radius corresponding to q_{min}. As a result of the onset of MHD activity, a fraction of the electron energy (shaded area in Fig. 13) in the

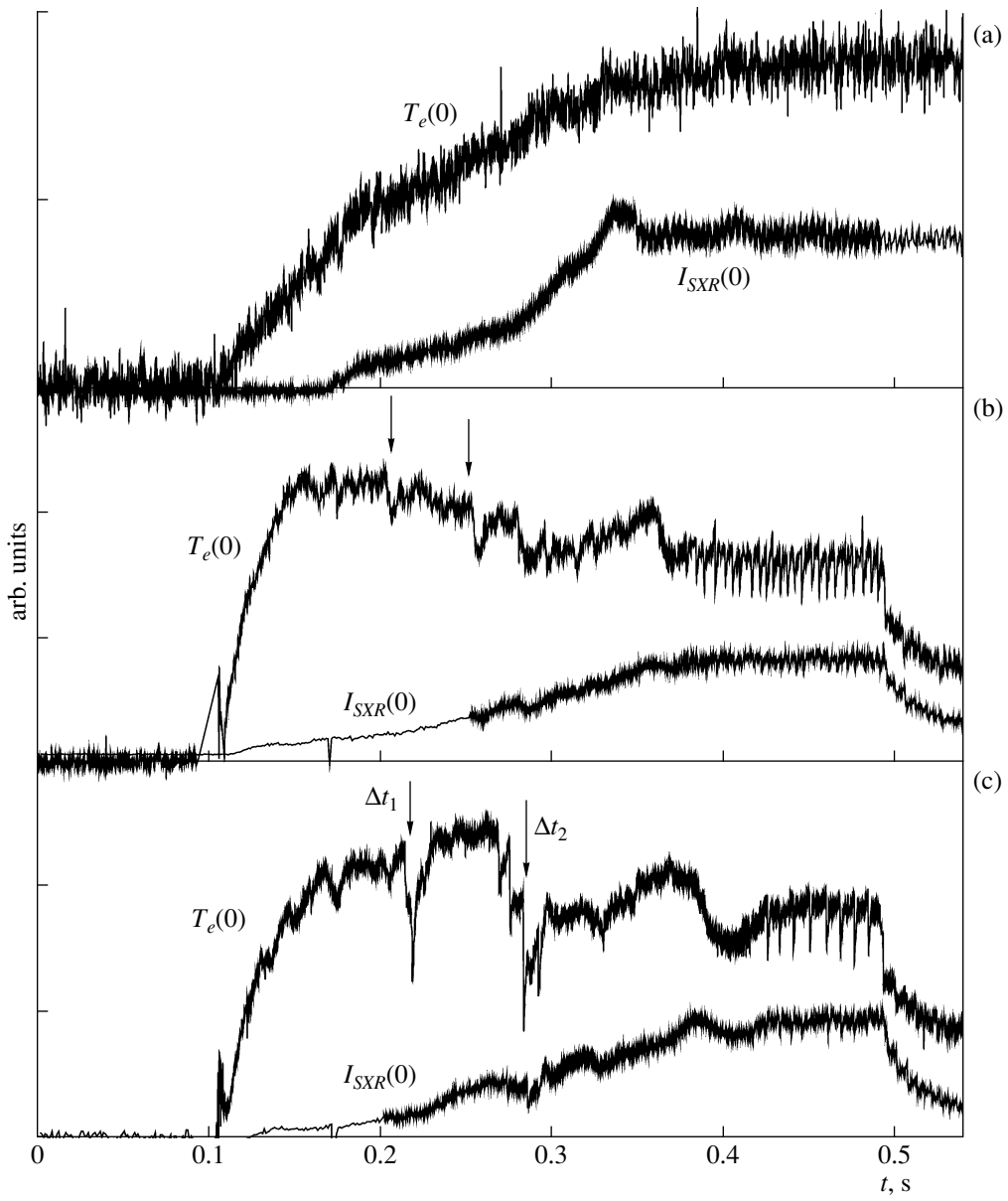

Fig. 10. $T_e(0)$ and $I_{SXR}(0)$ traces in the (a) ohmic, (b) co-CD, and (c) counter-CD modes.

plasma core is lost; this leads to the ~30% decrease in $T_e(0)$. In the co-CD mode (Fig. 15a), the q profile is also nonmonotonic when $q_{\min}$ is close to $q = 2$. However, the radius corresponding to $q_{\min}$ appears to be smaller than in the counter-CD mode ($r_d \le 0.18a$ compared to $r_d \sim 0.35a$ in the counter-CD mode). As a result, a smaller fraction of the electron energy in the plasma core is lost; consequently, the peculiarity in the $T_e(0)$ trace is less pronounced. In the ohmic mode (Fig. 15b), the q profile becomes monotonic even in the early stage. Therefore, there exists only one magnetic surface with $q = 2$, and the $T_e(0)$ trace has no peculiarities.

From the above said, it follows that the nonmonotonic q profile with two $q = 2$ resonant surfaces becomes dangerous when $q_{\min}$ is close to the resonant value $q = 2$. In this case, the internal $m = 2$ MHD mode develops, which leads to the additional electron transport and the ~30% decrease in the electron energy in the plasma core ($r \le r(q_{\min})$).

Similar features of the plasma behavior were also observed in other tokamaks. In the FTU device [7], for a hollow current profile and in the presence of two $q = 2$ (as well as $q = 3$) resonant surfaces, the onset of the double-tearing modes was observed. In [8], it was shown that MHD activity increases as $q_{\min}$ approaches 2, which can even lead to the destruction of the reversed-shear region.

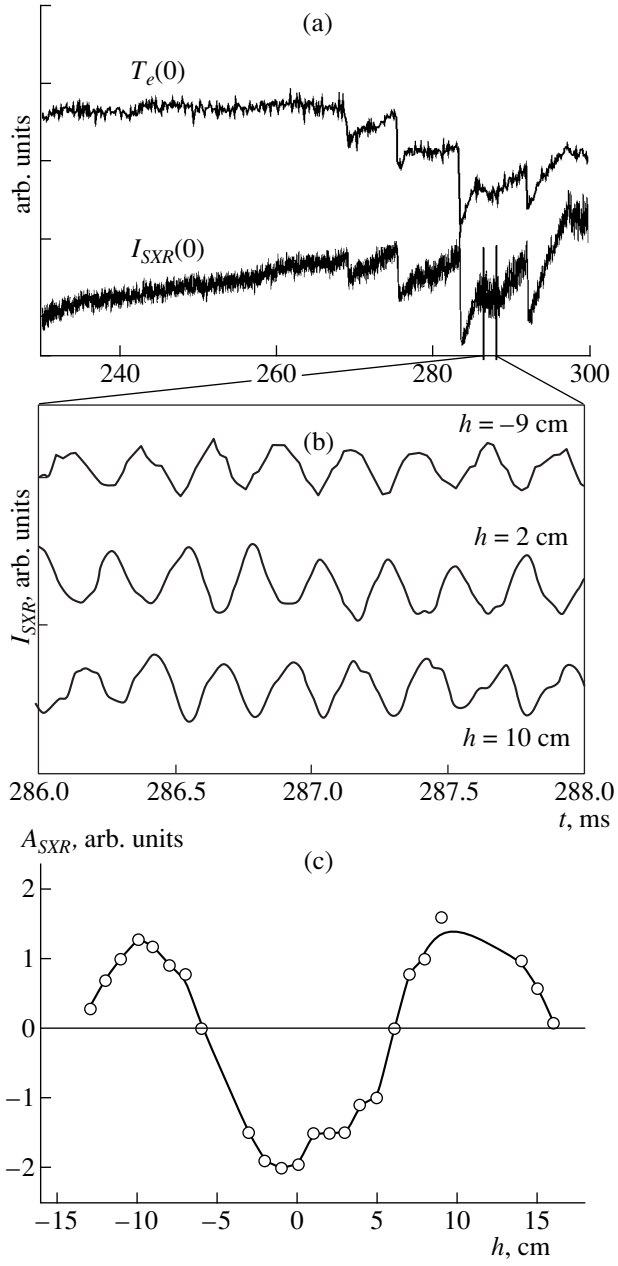

Fig. 11. (a) $I_{SXR}(0)$ and $T_e(0)$ traces in the Δt_2 interval shown in Fig. 10; (b) I_{SXR} signals from different chords, showing the structure of the $m = 2$ MHD mode; and (c) amplitude–phase diagram of the $m = 2$ MHD activity shown in Fig. 11b (A_{SXR} is the amplitude of the I_{SXR} oscillations).

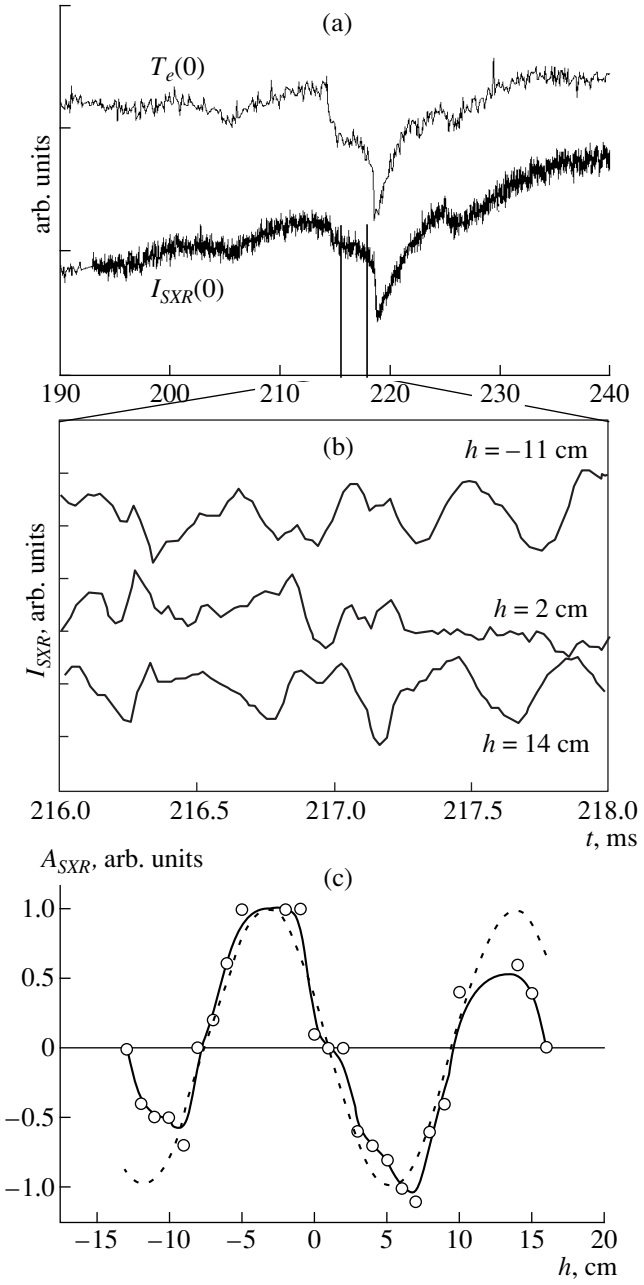

Fig. 12. (a) $I_{SXR}(0)$ and $T_e(0)$ traces in the Δt_1 interval shown in Fig. 10, (b) I_{SXR} signals for different chords, and (c) amplitude–phase diagram of the MHD oscillations (dashed curve shows the expected amplitude–phase diagram in the presence of an $m = 3$ island). The traces demonstrate the onset of the $m = 3$ MHD oscillations in the Δt_1 interval.

7. DISCUSSION OF THE RESULTS. THE POSSIBLE REASON FOR THE ABSENCE OF CLEAR EVIDENCE OF THE ITB FORMATION IN THE T-10 EXPERIMENTS

7.1. According to the present notions, the condition for the ITB formation is

$$\omega_{\mathbf{E}\times\mathbf{B}} > \gamma,$$

where

$$\omega_{\mathbf{E}\times\mathbf{B}} = \frac{B_p R}{B}\frac{d}{dr}\left(\frac{E_r}{RB_p}\right)$$

is the shear of the $\mathbf{E}\times\mathbf{B}$ flux and γ is the growth rate of the drift mode that governs the transport.

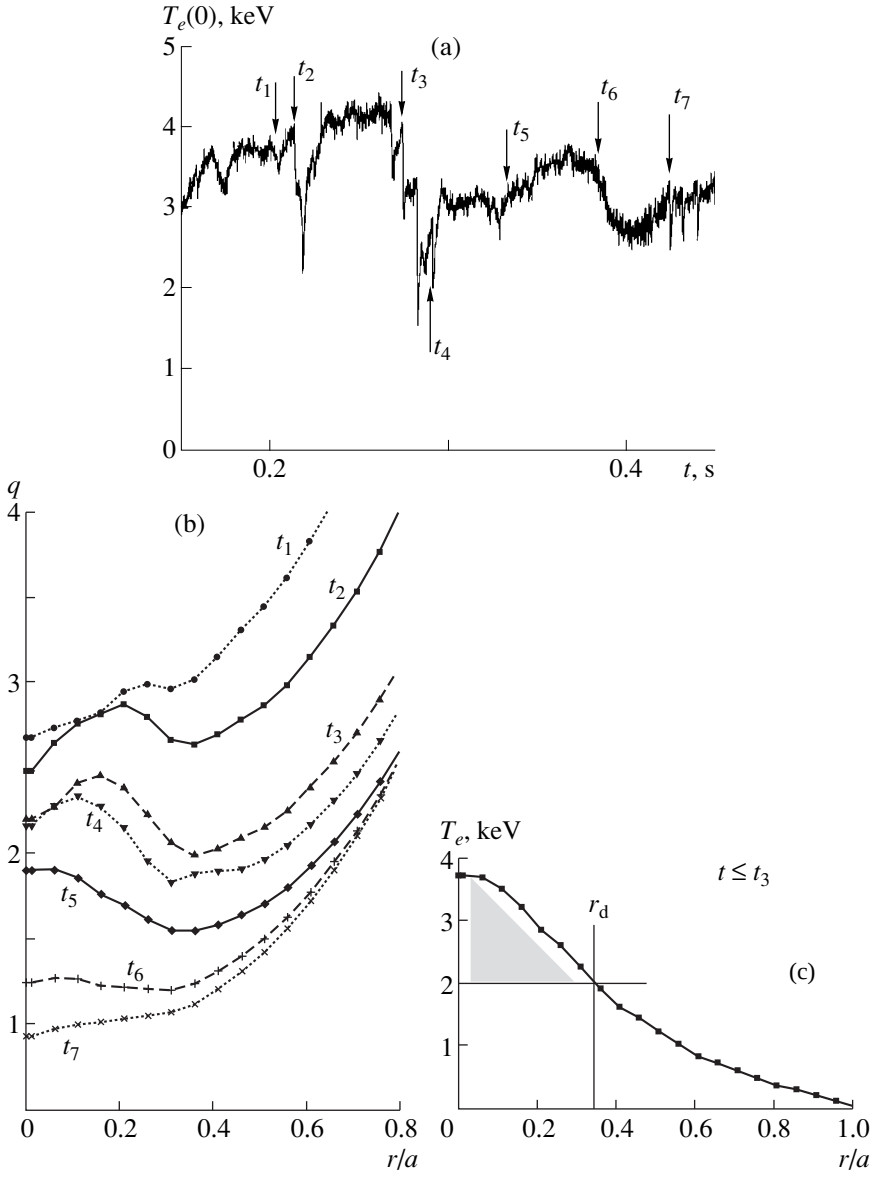

Fig. 13. (a) $T_e(0)$ trace in the counter-CD mode, (b) calculated q profiles for the instants shown in Fig. 13a, and (c) the fraction of the electron energy in the plasma core (shaded area) lost due to the onset of the $m = 2$ MHD activity (r_d is the radius at which the internal disruption with $q = 2$ is observed in the experiment).

The common feature of the most successful experiments with the ITB formation in the TFTR, DIII-D, and JT-60U devices is a high ion temperature. Under these conditions, the ion transport is assumed to be governed by the long-wavelength (small k) ITG mode. The growth rate for this mode [9] is

$$\gamma_{\mathrm{ITG}} = f_s k_\theta \rho_s \frac{c_s}{a}\sqrt{\frac{a}{R}\left(\frac{a}{L_n}+\frac{a}{L_T}\right)\frac{T_i}{T_e}},$$

where $\rho_s = c_s/\omega_{Bi}$, $c_s = \sqrt{T_e/m_i}$, $L_n = (d\ln n/dr)^{-1}$, $L_T = (d\ln T/dr)^{-1}$, k_θ is the poloidal component of the wave vector of the ITG mode, and $f(s)$ is the form factor dependent on the magnetic shear s. An example of such an analysis based on the results of DIII-D experiments is presented in [10].

7.2. A similar analysis based on the results of the T-10 experiments showed that, under the conditions in question in the region where the safety factor is close to $q_{\min}$ ($r/a \le 0.3$), we have

$$\omega_{\mathbf{E}\times\mathbf{B}} = 0.2\times 10^5\ \mathrm{s}^{-1},$$

$$\gamma_{\mathrm{ITG}} = (0.6\text{–}0.8)\times 10^5\ \mathrm{s}^{-1};$$

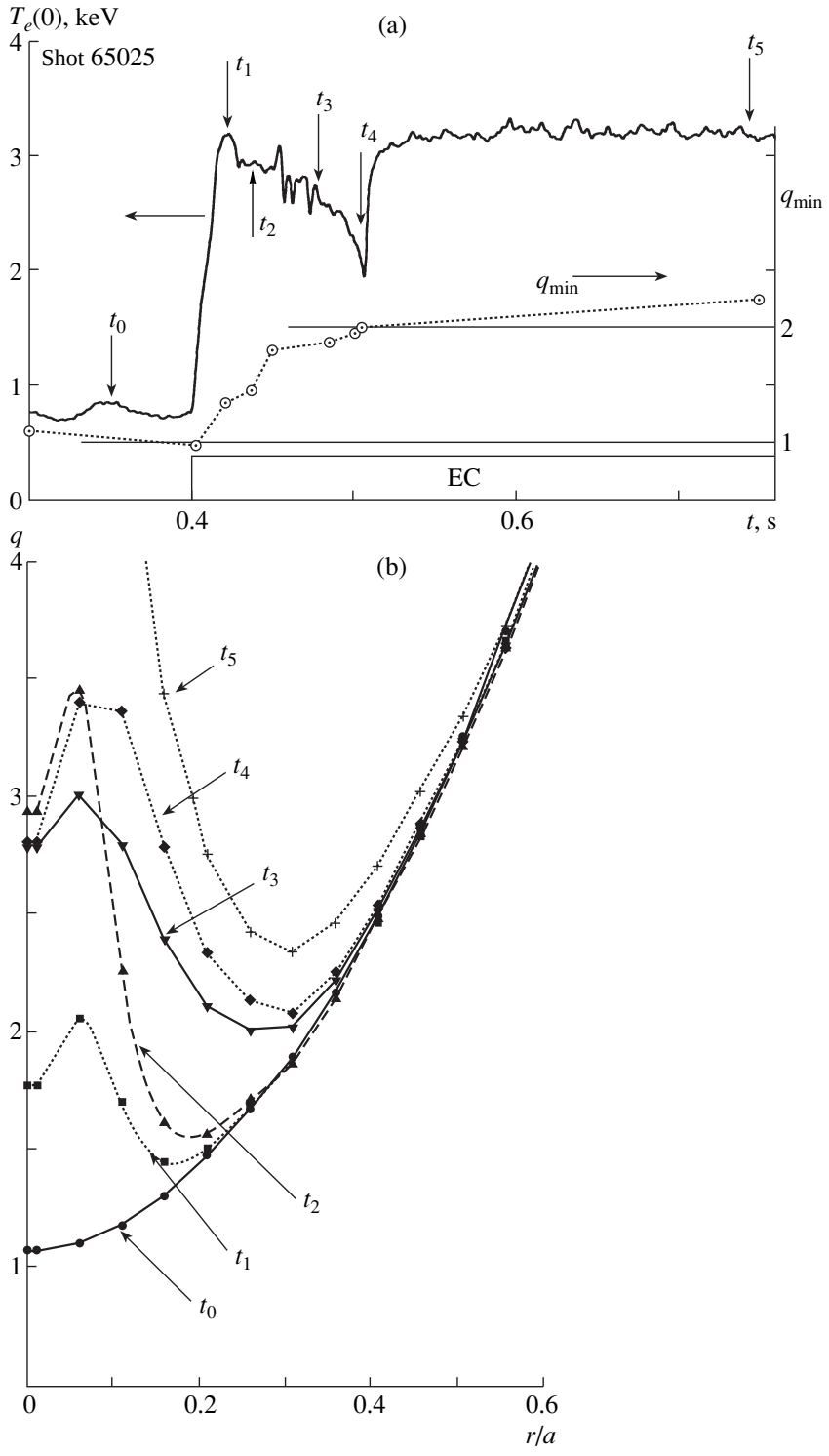

Fig. 14. Simulation of the counter-CD mode with I_p = 75 kA.

i.e., the value of the shear of the $\mathbf{E} \times \mathbf{B}$ flux is about three times less than the growth rate of the ITG mode. However, under the ECR heating conditions in T-10, the inequality $\omega_{\mathbf{E}\times\mathbf{B}} < \gamma$ may be even stronger because the ion transport is close to neoclassical; consequently, the ion ITG mode does not substantially affect the ion and, moreover, electron transport. This seems natural because it is hard to assume that, at $T_i(0)$ = 0.3–0.4 keV, the ITG mode can ensure the transport of the 1-MW microwave power through the electron component.

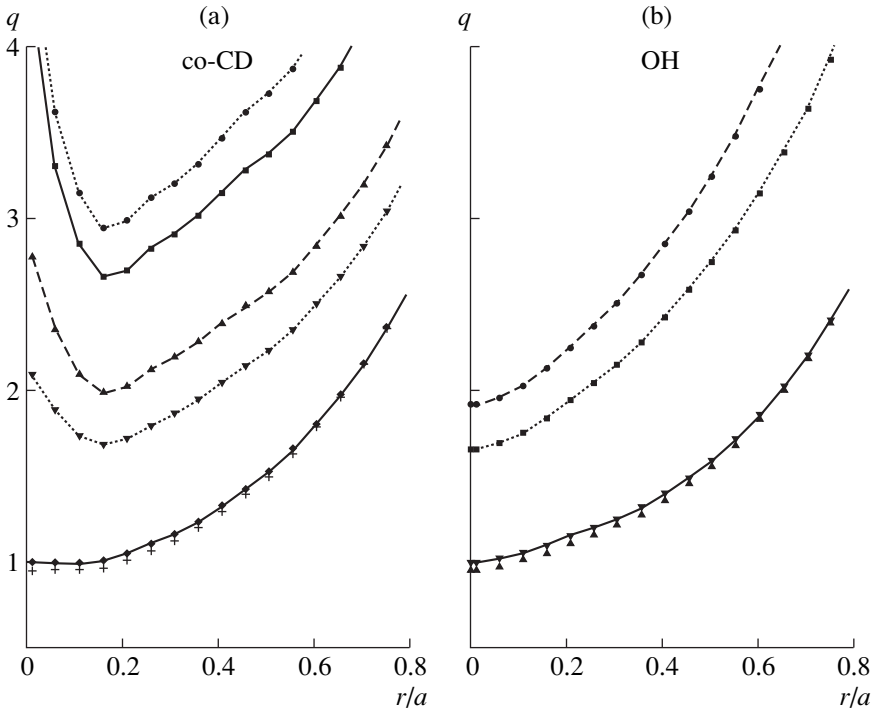

Fig. 15. Calculated q profiles for (a) co-CD and (b) ohmic modes.

Thus, the electron transport in the T-10 tokamak during ECR heating is governed by short-wavelength electron turbulence, which evidently have a higher growth rate γ [11].

Thus, the possible reason for the absence of clear evidence of the ITB formation in the T-10 experiments is that the growth rate of the electron drift mode substantially exceeds the shear of the $\mathbf{E} \times \mathbf{B}$ flow.

7.3. We note that, in the TFTR, DIII-D, and JT-60U tokamaks [12], after the ITB was formed, the electron transport decreased but still remained anomalous.

As was noted above, in the hot-ion discharges, the ion transport was governed by the long-wavelength ITG mode, which also contributes to the electron transport. Presumably, the electron transport in these discharges is also affected by the short-wavelength electron turbulence. After the ITB formation, the low-k turbulence is suppressed and the ion transport becomes neoclassical. The electron transport due to long-wavelength turbulence also decreases. However, it seems that short-wavelength (electron) turbulence is not suppressed and, therefore, the electron transport remains anomalous.

Under the conditions of ECR heating in the T-10 tokamak, long-wavelength turbulence does not contribute to the electron transport; therefore, there is no clear evidence of the ITB formation.

8. CONCLUSIONS

The results of this study can be summarized as follows:

(i) The possibility of controlling the current profile $j(r)$ by ECCD is demonstrated experimentally. Nonmonotonic q profiles with a reversed shear are obtained. The value of $q_{\min}$ could be varied over a wide range, $q = 1$–2.3.

(ii) The calculated $q(r)$ profiles agree with the peculiarities of the plasma behavior observed in different (ohmic, co-CD, and counter-CD) modes (the instants of the startup of sawtooth oscillations and the appearance of MHD activity with $m = 2$ and 3).

(iii) T-10 experiments provided no clear evidence of ITB formation. A specific feature of the T-10 conditions is that, for $T_e \gg T_i$, the electron transport is governed by the electron turbulence.

(iv) A nonmonotonic q profile with two $q = 2$ resonant surfaces becomes dangerous when $q_{\min}$ is close to the $q = 2$ resonant value. In this case, the internal $m = 2$ MHD mode develops, which leads to the loss of about 30% of the electron energy contained in the plasma core.

ACKNOWLEDGMENTS

This work was supported in part by the Russian Foundation for Basic Research (project no. 96-02-19631) and the Ministry of Science and Technology of the Russian Federation (project no. 363).

REFERENCES

1. R. E. Bell, F. M. Levinton, S. H. Batha, *et al.*, Plasma Phys. Controlled Fusion **40**, 609 (1998).
2. K. H. Burrell, M. E. Austin, C. M. Greenfield, *et al.*, Plasma Phys. Controlled Fusion **40**, 1585 (1998).
3. Y. Koide, M. Mori, T. Fujita, *et al.*, Plasma Phys. Controlled Fusion **40**, 641 (1998).
4. G. V. Pereverzev, P. N. Yushmanov, A. Yu. Dnestrovskiĭ, *et al.*, Report No. IAE-5358/6 (Kurchatov Institute of Atomic Energy, Moscow, 1992).
5. Yu. N. Dnestrovskiĭ, Yu. V. Esipchuk, N. A. Kirneva, *et al.*, Fiz. Plazmy **23**, 614 (1997) [Plasma Phys. Rep. **23**, 566 (1997)].
6. R. H. Cohen, Phys. Fluids **31**, 421 (1988).
7. P. Buratti, F. Alladio, P. Micozzi, *et al.*, Plasma Phys. Controlled Fusion **39**, B383 (1997).
8. E. Joffrin, X. Litaudon, T. Aniel, *et al.*, in *Proceedings of 25th EPS Conference on Controlled Fusion and Plasma Physics, Prague, 1998* [ECA **22C**, 1398 (1998)].
9. D. E. Newman, B. A. Carreras, D. López-Bruna, *et al.*, Preprint No. ORNL/P-97/91373 (Oak Ridge National Laboratory, Oak Ridge, TN, 1997).
10. V. S. Chan, in *Proceedings of 16th International Conference on Fusion Energy, Montreal, 1996* (IAEA, Vienna, 1997), Vol. 1, p. 95.
11. G. M. Staebler, Plasma Phys. Controlled Fusion **40**, 569 (1998).
12. T. Fujita, S. Ide, H. Shirai, *et al.*, Phys. Rev. Lett. **78**, 2377 (1997).

Translated by A. D. Smirnova

Plasma Physics Reports, Vol. 26, No. 3, 2000, pp. 191–198. Translated from Fizika Plazmy, Vol. 26, No. 3, 2000, pp. 209–216.

TOKAMAKS

Formation of an Internal Transport Barrier in the Ohmic H-Mode in the TUMAN-3M Tokamak

M. V. Andrejko, L. G. Askinazi, V. E. Golant, N. A. Zhubr, V. A. Kornev, S. V. Krikunov, S. V. Lebedev, L. S. Levin, G. T. Razdobarin, V. V. Rozhdestvensky, A. I. Smirnov, A. S. Tukachinsky, and S. P. Yaroshevich

Ioffe Physico-Technical Institute, Russian Academy of Sciences, Politekhnicheskaya ul. 26, St. Petersburg, 194021 Russia

Received April 14, 1999; in final form, July 8, 1999

Abstract—In experiments on studying the ohmic H-mode in the TUMAN-3M tokamak, it is found that, in high-current (I_p ~ 120–170 kA) discharges, a region with high electron-temperature and density gradients is formed in the plasma core. In this case, the energy confinement time τ_E attains 9–18 ms, which is nearly twice as large as that predicted by the ELM-free ITER-93H scaling. This is evidence that the internal transport barrier in a plasma can exist without auxiliary heating. Calculations of the effective thermal diffusivity by the ASTRA transport code demonstrate a strong suppression of heat transport in the region where the temperature and density gradients are high. © *2000 MAIK "Nauka/Interperiodica".*

1. INTRODUCTION

The formation of an internal transport barrier (ITB) in tokamaks was observed for the first time in experiments with auxiliary plasma heating and a specially shaped nonmonotonic profile of the safety factor $q(r)$ [1, 2]. According to the current concepts, several effects can be responsible for the suppression of turbulence and, thus, transport processes in the plasma core. One effect may be attributed to the high rotation-velocity shear, which causes the suppression of fluctuations through the decorrelation mechanism [3]. Another effect may be the suppression of η_i and η_e modes generated by the ion and electron temperature gradients in the presence of a high density gradient. Finally, ITB formation can be caused by the generation of a negative magnetic shear suppressing resistive MHD perturbations and the TE mode [4]. As a rule, the ITB formation is bifurcational in character and starts in the region with a negative magnetic shear. To obtain nonmonotonic profiles $q(r)$, rather complicated discharge scenarios are used in order to provide a hollow current profile, e.g., heating during the current-rise phase [negative central shear (NCS) and enhanced reversed shear (ERS) modes].

The experiments on studying the ohmic H-mode in the TUMAN-3M tokamak demonstrated that, in high-current (I_p ~ 120–170 kA) discharges, a region with high electron-temperature and density gradients can form in the plasma core. In this paper, we present the experimental data and the results of calculations of the evolution of the electron thermal diffusivity by the ASTRA transport code [5], which provide evidence of the generation of an ITB in the discharges under study. Numerical calculations were also used to analyze the influence of the evolution of the radial current-density profile on ITB formation. The important result is that an ITB was observed in the ohmic mode and the ITB began to form when the safety-factor profile was monotonic.

2. DESCRIPTION OF THE EXPERIMENT

The experiments were conducted in a boronized vessel for the following plasma parameters: $R_0 = 0.53$ m, $a_1 = 0.22$ m, $B_t \sim 0.8$ T, $I_p \sim 150$–170 kA, $\bar{n}_e \leq 6.2 \times 10^{19}$ m^{-3}, and $q^{cyl}(a) \sim 2.8$–2.9. The working gas was deuterium. The TUMAN-3M tokamak was equipped with a data-acquisition system operating at a sampling frequency of 50 kHz and recording information about the basic plasma parameters, such as the loop voltage, plasma current, intensities of the D_α line emission and soft X radiation, and signals from magnetic probes. The density profile was reconstructed using the Abel inversion of the data from chord measurements of the phase shifts by a ten-channel microwave interferometer (λ = 2.2 mm). The electron temperature was measured by Thomson scattering. This diagnostics provides information about the electron temperature in four 5-cm-spaced points along the minor radius in one shot. The line of sight of the spectrometer could be displaced between the tokamak shots by 8 cm, which provided shot-to-shot measurements of T_e both in the plasma core and at the edge (up to a minor radius of 21 cm). A feedback system for maintaining the density in the TUMAN-3M tokamak was not used.

Figure 1 shows the evolution of the basic plasma parameters in the experiment described. The plasma current rise ends at nearly 40 ms. Then, the plasma cur-

1063-780X/00/2603-0191$20.00

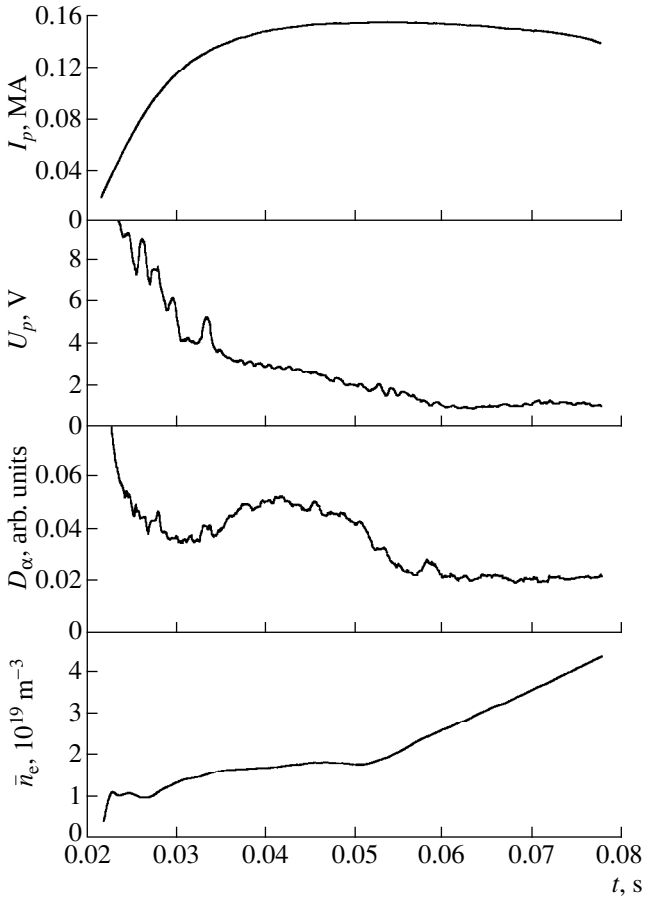

Fig. 1. Time behavior of the plasma current, loop voltage, D_α emission intensity, and average density in the ohmic H-mode with an ITB.

rent remains almost constant for 35 ms, while the loop voltage U_p continues to drop until nearly 57–59 ms, evidence that the rearrangement of the current profile continues. A transition to the ohmic H-mode occurs at 51.5 ms. This is evidenced by the fact that, at this instant, the line-averaged density $\bar{n}_e$ begins to grow, which is accompanied by a decrease in the intensity of D_α radiation. At the same time, the stored plasma energy measured by a diamagnetic loop starts to grow. During the subsequent ~5–6 ms, the voltage continues to fall, while the plasma current remains constant, which means that the energy input decreases. The above-mentioned facts allow us to draw the conclusion that the particle and energy confinement in the plasma is improved and can be interpreted as a transition to the ohmic H-mode [6].

The formation of an external transport barrier was confirmed by probe measurements, reflectometry, and high-resolution interferometry in the previous experiments carried out with lower (below ~120 kA) plasma currents [7]. Note that, in experiments with $I_p \le 120$ kA, the transition to the H-mode occurs rapidly, in a time of about 100 μs [6]. At high plasma currents, the intensity of D_α radiation begins to fall 4–5 ms before the density growth and occurs more slowly (in a time of 5–7 ms). These results allow us to suggest that, at high currents, the transport suppression also occurs in deeper plasma regions, so that the change in the particle fluxes at the plasma edge are delayed in this case.

Figure 2a shows the evolution of the electron-temperature profiles $T_e(r)$ measured by Thomson scattering in the regime described above. Here, the $T_e(r)$ profiles for 47.5, 68, and 77 ms were obtained experimentally, whereas the profile for 56 ms was chosen using numerical simulations described in the next section. The $T_e(r)$ profile measured in the steady-state phase of the discharge before the transition to the H-mode (47.5 ms) has no distinguishing features as compared to the profiles usually observed in the ohmic regime in the TUMAN-3M tokamak. A characteristic feature of the electron temperature profiles measured in the last stage (68 and 77 ms) of the H-mode is the presence of two regions with high temperature gradients. These regions are located between 10 cm (0.5a) and 16 cm (0.75a) and between 21 cm (0.95a) and the limiter and are separated by a plateau ($T_e \sim 120$ eV), which spans from 16 to 21 cm. The flattening of the $T_e(r)$ profiles at 68 and 77 ms can be caused by sawtooth oscillations with a period of about one millisecond that are usually observed after the transition to the H-mode. The formation of a plateau between 16 and 21 cm and the high temperature gradient at the edge are the consequence of the transition to the H-mode. The presence of high temperature gradients indicates the suppression of local heat transport, whereas the plateau at the edge of the $T_e(r)$ profile may indicate the local enhancement of heat transport. We note that the described features of the $T_e(r)$ profiles are observed in discharges without pronounced MHD activity (discharges with intense MHD oscillations observed at the same plasma parameters were excluded from consideration). Hence, the flattening of the $T_e(r)$ profile cannot be attributed to the existence of a magnetic island with a low m/n ratio.

In contrast to the $T_e(r)$ profiles, there are no strong variations in the shape of the density profiles shown in Fig. 2b. However, we can see a certain increase in the n_e gradient between 10 and 16 cm (0.5a–0.75a).

Figure 3 presents a comparison between the energy confinement time τ_E obtained from diamagnetic measurements of the plasma energy $W_{\rm dia}$ and that predicted by the ELM-free ITER-93H scaling. The confinement time τ_E was calculated by the formula

$$\tau_E = \frac{W_{\rm dia}}{U_p I_p - dW_{\rm dia}/dt}.$$

The maximum values of the energy confinement time in the ohmic H-mode are plotted. It is seen in the figure that most of the experimental points lie above the scal-

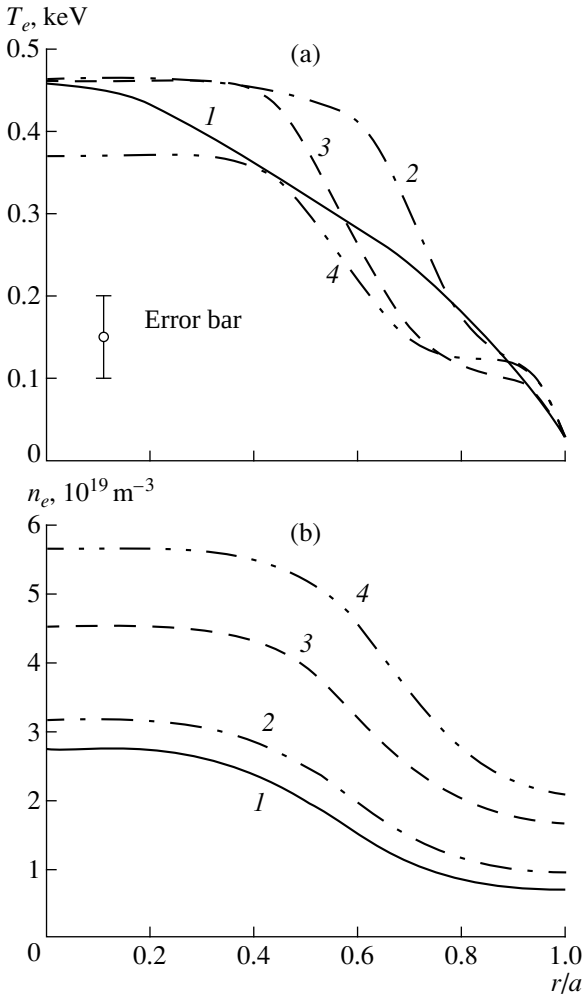

Fig. 2. (a) The electron temperature profiles and (b) density profiles at (*1*) 47.5 ms (before the transition to the H-mode), (*2*) 56 ms (simulation), (*3*) 68 ms, and (*4*) 77 ms (after the transition to the H-mode with an ITB).

ing prediction and the excess factor H_H attains 2. The excess factor increases as the current increases. This indicates an additional improvement of confinement in comparison with the H-mode confinement with the transport barrier at the edge. The confinement time τ_E estimated by the ITER89-P scaling for the L-mode with account of the derivative of the plasma energy is about 10–12 ms. Hence, the value of the H-factor in the experiment described is significantly lower than the H_H-factor. This is explained by the relatively small (ε = 2.3) aspect ratio of the TUMAN-3M tokamak.

Thus, an analysis of the evolution of the basic plasma parameters in high-current discharges allows us to draw a preliminary conclusion that, in the ohmic H-mode in the TUMAN-3M tokamak, two regions with very different transport features are formed inside the plasma column. The region with a high electron-temperature gradient between 10 and 16 cm can be interpreted as an ITB.

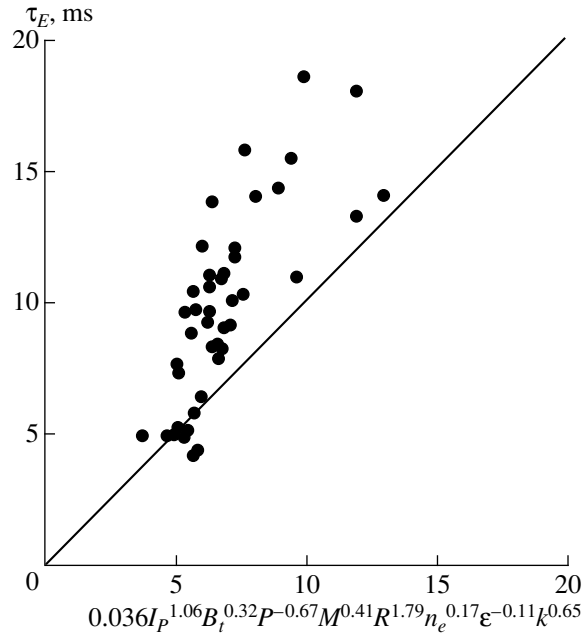

Fig. 3. Energy confinement time in the H-mode as a function of the ELM-free ITER93-H scaling.

3. NUMERICAL MODELING OF THE DISCHARGES WITH AN ITB

The evolution of the radial profile of the electron thermal conductivity was studied numerically using the ASTRA transport code. Simultaneously, the influence of transient processes occurring in a plasma of the TUMAN-3M tokamak on ITB formation was analyzed. We can assume that the rapid (with a characteristic time of about 10 μs) rise of the current in the initial phase of the discharge results in the formation of a hollow $j(r)$ profile and a region with a negative magnetic shear favorable for the formation of an ITB. Another reason for the ITB formation in our case may be the generation of the radial current j_r and, consequently, the radial field E_r due to the presence of a nonsteady or an inhomogeneous longitudinal electric field E_ϕ. The mechanism for the j_r generation was suggested in [8] and consists in that the radial-drift velocities of trapped electrons and ions differ from each other because E_ϕ is different at the outer and inner segments of the banana orbits. The resulting radial electric field causes a nonuniform plasma rotation that can suppress turbulent transport through the decorrelation mechanism [3]. For example, in the initial stage of the discharge, the longitudinal electric field E_ϕ in a tokamak is strongly inhomogeneous. If the current diffusion is sufficiently slow, then such an inhomogeneity can exist for a relatively long

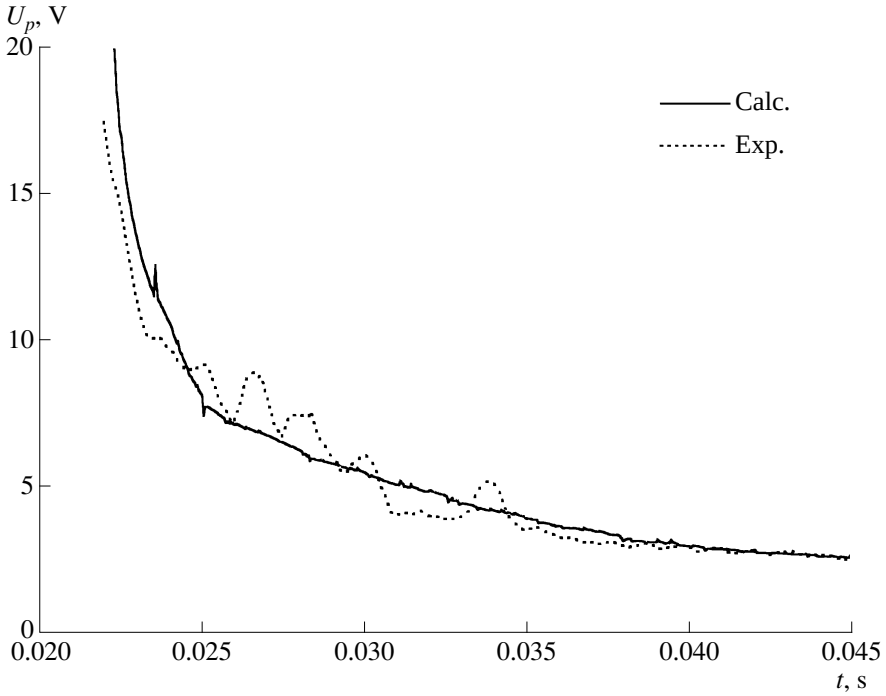

Fig. 4. Results of simulations of the loop voltage in the initial phase of the ITB discharge.

period. As shown in [9], this leads to the generation of a radial electric field, which, in turn, can give rise to an ITB.

The problem was divided into three steps:

(i) simulation of the initial phase of the discharge and studying the possibility of the formation of regions with a negative magnetic shear or with a strongly nonuniform $E_\phi(r)$ profile,

(ii) reconstruction of the evolution of the electron-temperature profile during the transition to the improved confinement phase, and

(iii) calculation of the electron thermal diffusivity and the estimation of the suppression of transport in the region with high gradients of $T_e(r)$.

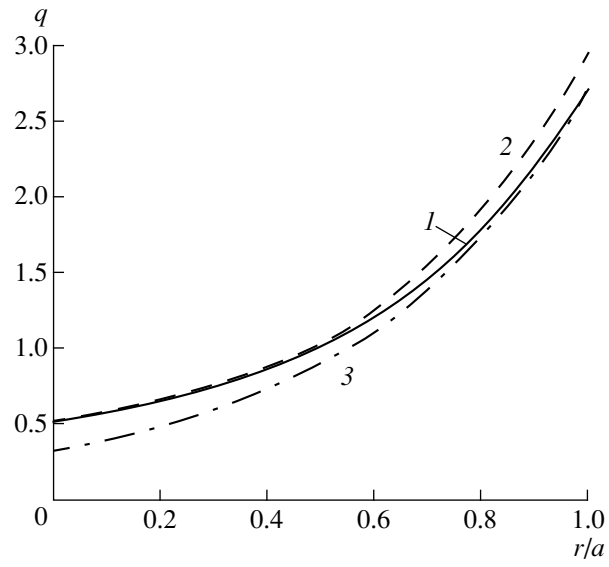

Fig. 5. Radial profile of the safety factor $q(r)$ in the ITB discharge calculated with allowance for the evolution of the plasma current at (*1*) 47.5 and (*2*) 77 ms and (*3*) in the steady state.

To find the current-density profile $j(r)$, which determines the heating source in the electron heat transport equation, the model incorporates the current diffusion equation, which was solved assuming that the Hinton–Hazeltine formula for neoclassical conductivity [10] is valid in our case. In calculations, we used the experimentally measured profiles of the electron temperature $T_e(r)$ and density $n_e(r)$. For the instants at which the laser measurements of the electron temperature were not performed, the $T_e(r)$ profile was chosen such that the calculated loop voltage best fitted the experimental value. The effective charge was assumed to be uniformly distributed over the minor radius and equal to unity. When solving the current diffusion equation, the experimentally measured total plasma current was employed as a boundary condition and the shape of the initial $j(r)$ profile coincided with the profile of neoclassical conductivity.

In the current-rise phase, the evolution of the electron-temperature profile was described as a linear rise to the values measured at 47.5 ms; i.e., for $t < 47.5$ ms,

the profiles in the calculations were defined by the following formulas:

$$T_e(r, t) = T_e(r, 47.5)(0.1 + 0.9at) \text{ for } t < 1/a,$$

$$T_e(r, t) = T_e(r, 47.5) \text{ for } t \geq 1/a,$$

where the factor a was chosen such that the calculated loop voltage coincided best with the experimental value. The evolution of the electron density profile in the initial phase of the discharge was modeled in a similar way, but its growth rate was chosen such that the calculated value of the line-averaged density coincided with the experiment.

Figure 4 shows the calculated and experimental behavior of the loop voltage in the current-rise phase for the optimum rate of the formation of the $T_e(r)$ profile. Satisfactory agreement with the experiment allows us to conclude that the profiles of the current and the toroidal electric field are adequately described by our model.

Figure 5 shows the results of calculations of the radial profile of the safety factor $q(r)$ for certain characteristic instants. It is seen that, throughout the discharge, the $q(r)$ profiles are monotonic and close to the steady-state profile. Hence, there is no reason to suggest that, in the plasma of the TUMAN-3M tokamak, there are regions with a reversed magnetic shear whose appearance might explain the ITB formation.

As was noted above, one cause of ITB generation can be the presence of a radially nonuniform or nonsteady longitudinal electric field E_ϕ. Figure 6 shows the evolution of the radial profile of the longitudinal electric field $E_\phi(r)$ obtained by modeling the current-rise phase as described above. It is seen from the figure that, as early as 56 ms, the $E_\phi(r)$ profile is almost uniform and close to the steady-state profile. Moreover, the calculations show that, even at 47.5 ms, the nonuniformity of the $E_\phi(r)$ profile is insufficient to generate a high electric field that might give rise to an ITB.

We note that the high values of $\partial E_\phi/\partial r$ and, correspondingly, high gradients of the electric field E_r can be caused by strong perturbations of the current density $j_\phi(r)$. Such perturbations can arise during internal disruptions according to the Kadomtsev model [11] for sawtooth oscillations. According to this model, internal disruptions give rise to strong perturbations of the $E_\phi(r)$ profile that are sufficient for the formation of high $\partial E_r/\partial r$ gradients. Figure 6 shows the longitudinal electric field ~100 μs after an internal disruption calculated by the model [11]. A significant longitudinal-electric-field inhomogeneity arising after the internal disruption decays with a characteristic time of about 500–700 μs, which is comparable with the period of the observed sawtooth oscillations (~1 ms). As is shown below, the position of the region with high $\partial E_\phi/\partial r$ gradients coincides with the region in which heat transport is suppressed ($0.5a$–$0.75a$). This fact suggests that sawtooth oscillations can play a decisive role in ITB formation.

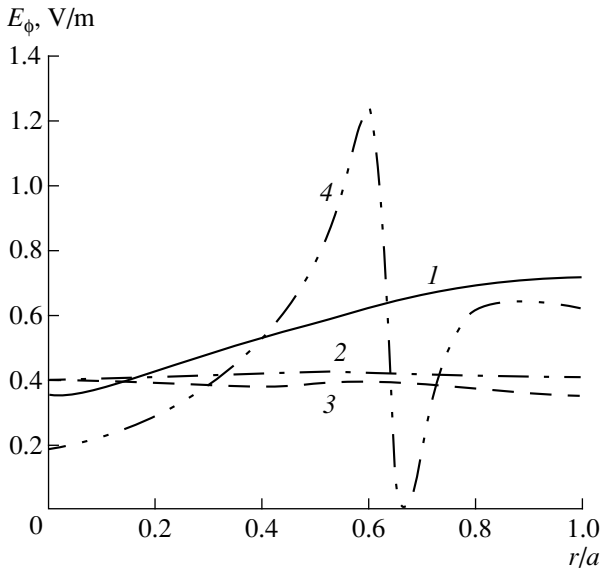

Fig. 6. Radial profiles of the longitudinal electric field E_ϕ at (*1*) 47.5 (at the end of the current-rise phase before the transition to the H-mode), (*2*) 56, and (*3*) 68 ms (after the transition to the ohmic H-mode with an ITB) and (*4*) 100 μs after the internal disruption. Profile *4* is calculated by the Kadomtsev model for an ohmic H-mode with an ITB.

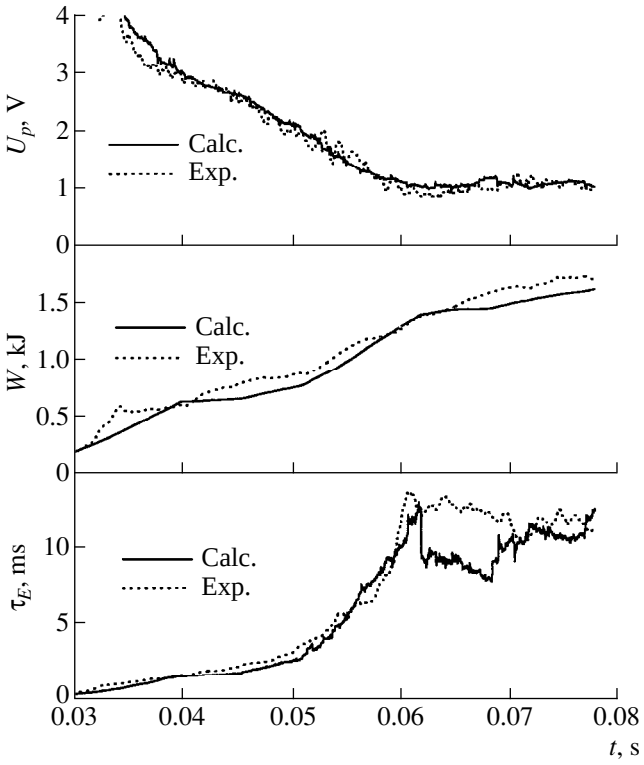

Fig. 7. Time evolution of the calculated and experimental values of the loop voltage U_p, stored plasma energy W, and energy confinement time τ_E in the ohmic H-mode with an ITB.

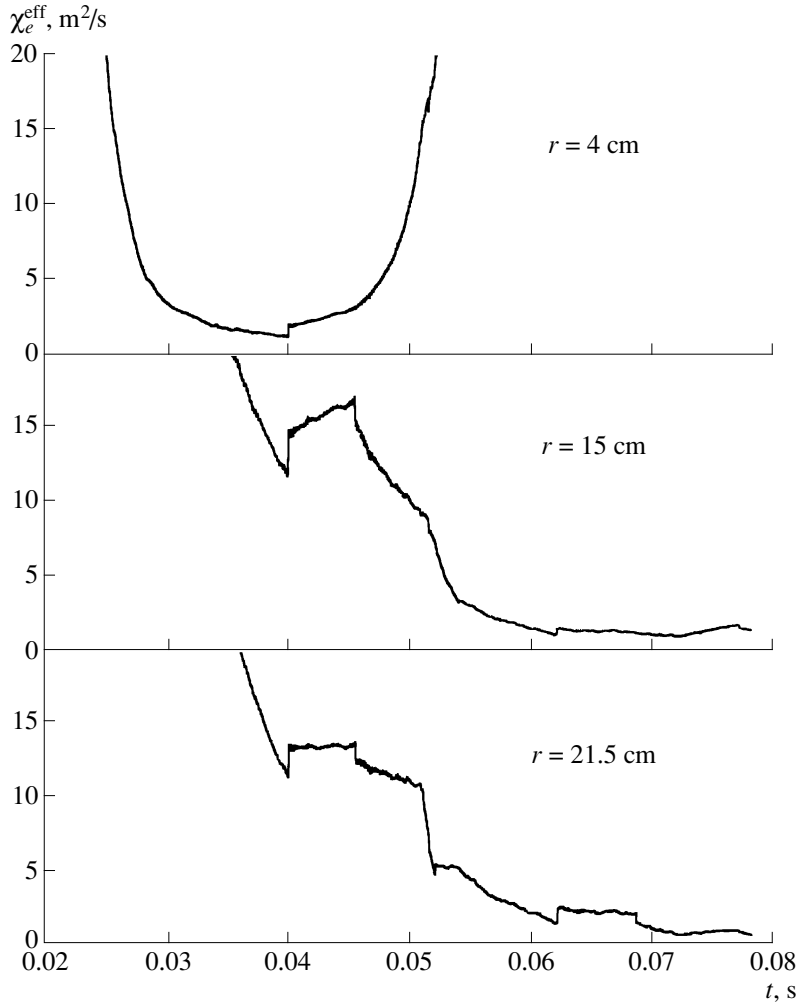

Fig. 8. Time evolution of the effective thermal diffusivity χ_e^{eff} in the plasma core, r = 4 cm (0.2a); in the region where the ITB is formed, r = 15 cm (0.65a); and at the plasma edge, r = 21.5 cm (0.95a).

When reconstructing the evolution of the electron-temperature profile during the transition to the H-mode (51–60 ms), we tested several possible scenarios. We failed to reconstruct T_e in each spatial point by linear extrapolation between the instants of laser measurements, because the calculated voltage U_p significantly exceeded the experimental values. Since Z_{eff} used in the calculations was assumed to be equal to unity, it was impossible to further decrease this quantity. Hence, the experimental evolution of the loop voltage could be described adequately only under the assumption that the $T_e(r)$ profile rearranges rapidly during the transition to the H-mode plasma confinement or, possibly, several milliseconds before the transition.

The cause of the reduction of U_p can be intense heating of the plasma edge during the transition to the H-mode. Indeed, under certain assumptions about the evolution of the electron temperature, it is possible to attain a satisfactory agreement between the calculated and experimental values of the loop voltage. However, in this case, we must assume that the plasma edge is heated to nearly 300 eV, which is hardly possible under the conditions of operating the TUMAN-3M tokamak.

In our opinion, the processes occurring in the plasma during the formation of an ITB are reflected in the scenario of $T_e(r)$ evolution illustrated in Fig. 2a. This scenario suggests that a high temperature gradient rapidly forms in the region 10–16 cm (0.5a–0.75a), while the temperature profile in the plasma core flattens significantly. The electron temperature profile begins to change before the transition to the H-mode plasma confinement, just at the instant the D_α line radiation drops. The rearrangement of the $T_e(r)$ profile continues for ~10 ms and ends by 56 ms. Then, the temperature profile varies slightly, gradually transforming to the profile measured at 68 ms by Thomson scattering. The corresponding evolution of the calculated values of the loop voltage U_p, stored plasma energy W_{tot}, and energy con-

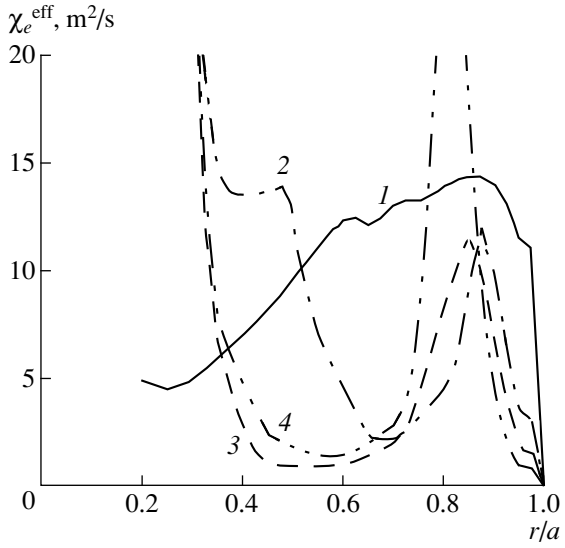

Fig. 9. The $\chi_e^{\text{eff}}(r)$ profiles (*1*) before and (*2–4*) after the ITB formation: t = (*1*) 47.5, (*2*) 56, (*3*) 68, and (*4*) 77 ms.

finement time τ_E is illustrated in Fig. 7. For comparison, the corresponding experimental curves are also shown. It is seen that this scenario provides good agreement between the calculated and experimental behavior of U_p and satisfactory agreement between W_{tot} and W_{dia} and between the calculated and experimental values of τ_E.

The $T_e(r)$ profiles shown in Fig. 2 were used to determine the radial profiles of the effective electron thermal diffusivity χ_e^{eff}. When calculating the local thermal diffusivity, the electron heating power density was defined as $P_e = P_{OH} - P_{ei} - P_{\text{rad}}$, where $P_{OH} = E(r)j(r)$ is the ohmic heating power, P_{ei} describes the heat exchange between electrons and ions, and P_{rad} is the radiative loss power. The radiative loss power in the boronized chamber was assumed to be ~5% of the total ohmic heating power, and its radial profile was assumed to be uniform. The ion temperature at each point was defined as $T_i = 0.3T_e$.

Figure 8 shows the calculated evolution of the effective electron thermal diffusivity χ_e^{eff} at several characteristic points of the plasma column: in the central region ($0.2a$), in the region of the ITB formation ($0.65a$), and at the plasma edge ($0.95a$). It is seen that, several milliseconds before the transition to the H-mode (~51 ms), an ITB begins to form, which is accompanied by an increase in heat transport in the central part of the plasma core. The transition to the H-mode is accompanied by a decrease in the thermal diffusivity at the edge.

The corresponding $\chi_e^{\text{eff}}(r)$ profiles at different characteristic instants are shown in Fig. 9. In the later, experimentally studied phase of the discharge, we distinguish two regions with enhanced transport which are separated by the region of suppressed transport—an ITB located between 10 and 16 cm ($0.4–0.7a$). After the ITB is formed, the thermal diffusivity in this region falls by almost one order of magnitude. The formed ITB exists almost to the end of the discharge. Unfortunately, because of the lack of information about the profile of the neutral density, we cannot separate the convective and diffusive heat fluxes. Nevertheless, the previous estimates [12] allow us to suggest that suppression of the convective flux can play a decisive role in suppression of heat transport in the region where an ITB is formed.

4. CONCLUSION

We have shown that, in the TUMAN-3M tokamak, an electron-component ITB can be formed in the ohmic regime at high discharge currents ($I_p > 120$ kA). The formation of an ITB is evidenced by the following circumstances: a substantial (approximately double) improvement of plasma confinement in comparison with the ELM-free ITER-93H scaling, a slow reduction of the particle flux from a plasma, and the formation of a region with high electron-temperature and density gradients in the plasma column.

Numerical simulations confirm the presence of two regions with suppressed heat transport in the plasma, which can be interpreted as internal and peripheral transport barriers.

Presumably, the ITB formation can be explained by the suppression of plasma turbulence due to the shear of the $\mathbf{E}_r \times \mathbf{B}$ rotation velocity. A strongly nonuniform radial electric field can arise in an ohmically heated plasma because of the different radial drift velocities of the trapped electrons and ions in a strongly inhomogeneous and nonsteady field E_ϕ caused by internal sawtooth oscillations.

ACKNOWLEDGMENTS

This work was supported in part by the Russian Foundation for Basic Research (project nos. 97-02-18107 and 97-02-18051) and the US Civilian Research and Development Foundation for the Independent States of the Former Soviet Union (CRDF) in cooperation with the Ministry of Science and Technology of the Russian Federation (grant no. RP1-197).

REFERENCES

1. M. Levinton, M. C. Zarnstorff, S. H. Batha, *et al.*, Phys. Rev. Lett. **75**, 4417 (1995).
2. E. J. Strait, L. L. Lao, M. E. Mauel, *et al.*, Phys. Rev. Lett. **75**, 4421 (1995).

3. H. Biglari, P. Diamond, and P. Terry, Phys. Fluids B **2**, 1 (1990).
4. G. M. Staebler, Plasma Phys. Controlled Fusion **40**, 569 (1998).
5. A. Yu. Dnestrovskiĭ, L. E. Zakharov, G. V. Pereverzev, *et al.*, Preprint No. 5358/6 (Kurchatov Institute of Atomic Energy, Moscow, 1991).
6. A. N. Arbuzov, L. G. Askinazi, V. I. Afanas'ev, *et al*., in *Proceedings of 17th EPS Conference on Controlled Fusion and Plasma Heating, Amsterdam, 1990* [ECA **14B**, 299 (1990)].
7. S. V. Lebedev, M. V. Andrejko, L. G. Askinazi, *et al.*, Plasma Phys. Controlled Fusion **38**, 1103 (1996).
8. M. G. Haines and P. Martín, Phys. Plasmas **3**, 4536 (1996).
9. S. I. Lashkul, V. N. Budnikov, V. V. Bulanin, *et al.*, in *Proceedings of 2nd EPS Topical Conference on RF Heating and CD in Fusion Devices, Brussels, 1998* [ECA **22A**, 161 (1998)].
10. F. L. Hinton and R. G. Hazeltine, Rev. Mod. Phys. **48**, 239 (1976).
11. B. B. Kadomtsev, Fiz. Plazmy **1**, 710 (1975) [Sov. J. Plasma Phys. **1**, 389 (1975)].
12. M. V. Andrejko, L. G. Askinazi, V. E. Golant, *et al.*, in *Proceedings of Workshop on Local Transport Studies in Fusion Plasmas (International School on Plasma Physics), Varenna, 1993*, p. 57.

Translated by N. F. Larionova

Plasma Physics Reports, Vol. 26, No. 3, 2000, pp. 199–202. Translated from Fizika Plazmy, Vol. 26, No. 3, 2000, pp. 217–220.

Parameters of a Tokamak Reactor Operating at a Fixed Fusion Power as Functions of the Aspect Ratio

N. N. Brevnov and Yu. V. Gott

Russian Research Centre Kurchatov Institute, pl. Kurchatova 1, Moscow, 123182 Russia

Received April 20, 1999

Abstract—Such parameters of a tokamak reactor as the major radius, plasma current, reactor volume, neutron load to the first wall, heat load to the divertor plates, and bootstrap current are studied as functions of the aspect ratio, assuming that the reactor operates at a fixed power. The conclusion is drawn that a demonstrative prototype reactor should be based on a large aspect ratio tokamak. © *2000 MAIK "Nauka/Interperiodica".*

1. INTRODUCTION

The programmatic goal of present-day tokamak studies is to gain information required for creating a tokamak reactor. Further efforts directed at designing a fusion reactor involve the following three steps:

1. Creating an experimental fusion reactor—ITER. The ITER device is aimed at demonstrating the feasibility of controlled fusion for achieving practical fusion power from both scientific and technological standpoints.

2. Creating a demonstrative prototype reactor—DEMO. The DEMO device should demonstrate the possibility of achieving steady-state self-sustaining fusion reactions.

3. Creating a commercial fusion reactor.

The ITER device, even with optimized geometrical dimensions and plasma parameters, appears to be fairly expensive to construct. The next step, the design of DEMO, involves solving a number of problems associated with its cost, convenience, and reliability. Consequently, it is necessary to further optimize the parameters that govern the cost of building DEMO, i.e., the geometrical dimensions, plasma current, and so on.

Here, the method that we developed in [1] is applied to study the main DEMO parameters, i.e., the geometrical dimensions, plasma current, heat load to the divertor plates, bootstrap current, etc. (which, in our opinion, mainly govern the cost of the device), as functions of the aspect ratio and the vertical elongation of the plasma column. We will consider a reactor operating at a fixed fusion power.

2. CALCULATION TECHNIQUE AND THE RESULTS OBTAINED

The status of the device (a device with plasma ignition, plasma burn, etc.) is governed by the so-called fusion parameter F_p:

$$F_p = n\tau T, \tag{1}$$

where n is the plasma density, T is the plasma temperature, and τ is the energy lifetime.

The ratio β of the thermal energy stored in the plasma to the magnetic-field energy is limited by the possible onset of ballooning instabilities:

$$\beta = 10^{-2}\beta_N\frac{I}{aB}, \tag{2}$$

where I is the plasma current, a is the tokamak minor radius, and B is the toroidal magnetic field.

At present, opinion is divided regarding the dependence of β_N on the aspect ratio. For example, Stambaugh *et al.* [2] suggested that $\beta_N = 12/A$. In paper [3], published in the same year, Miller *et al.* asserted that the dependence of β_N on the aspect ratio is weaker than $1/A$. Interestingly, some researchers participated in writing both of these papers. In optimizing ITER, the quantity β_N was taken to be independent of the aspect ratio [4].

We describe the energy lifetime using the ITER scaling [5] for the H-mode:

$$\tau = 0.028 I^{0.9} B^{0.2} P_\alpha^{-0.66} n_{19}^{0.4} M^{0.2} R^{2.03} \varepsilon^{0.19} k^{0.91}, \tag{3}$$

where M is the mass number of the plasma ions, P_α is the heating power fed to the plasma (for self-sustaining fusion reactions, this is the power carried by α-particles), $\varepsilon = A^{-1} = a/R$ is the inverse aspect ratio A, R is the

1063-780X/00/2603-0199$20.00

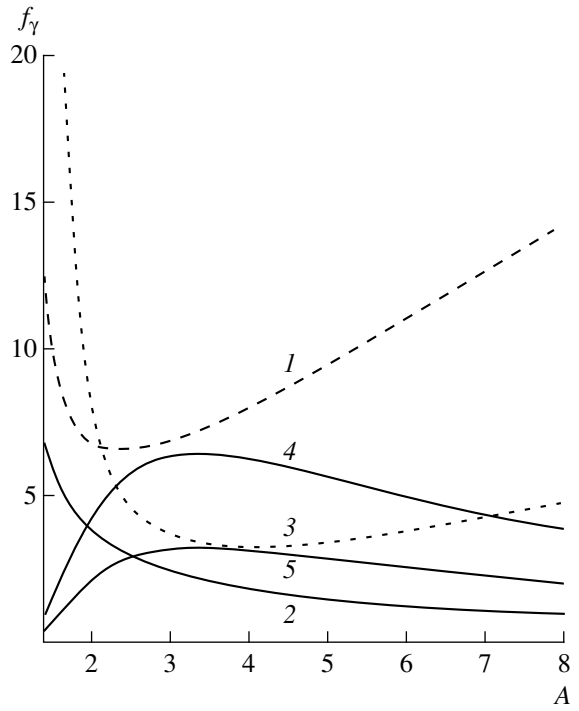

Fig. 1. Functions f_γ vs. the aspect ratio A: (*1*) tokamak minor radius, (*2*) plasma current, (*3*) plasma volume, (*4*) neutron load to the first wall, and (*5*) heat load to the divertor plates.

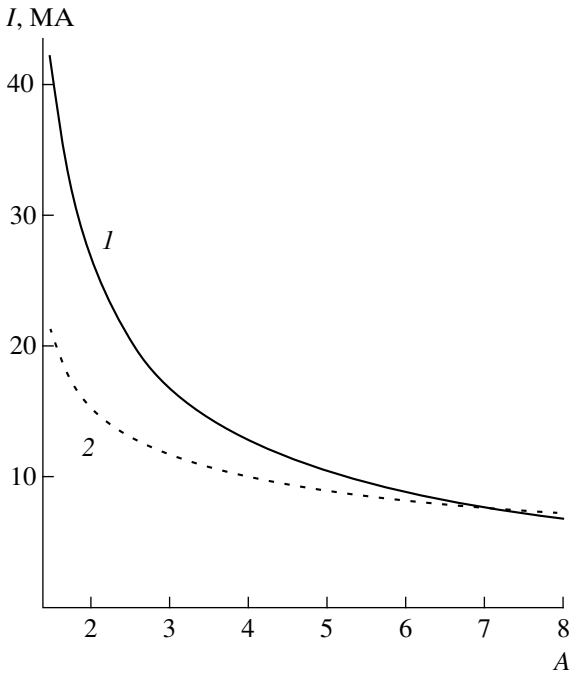

Fig. 2. (*1*) Total plasma current and (*2*) bootstrap current vs. the aspect ratio A.

major radius of the plasma column, and k is the ellipticity of its cross section. For further analysis, we set $\tau = 0.5\tau_{ITER}$.

We use Greenwald's formula for the maximum plasma density [6],

$$n_{20} = \frac{IA^2}{\pi R^2}, \tag{4}$$

and specify the plasma current as

$$I = \frac{5BR}{2qA^2}(1 + k^2), \tag{5}$$

where $q = q_\psi(A - 1)/A$ [7] with q_ψ the safety factor at the magnetic surface ψ near the plasma boundary.

The magnetic field at the center of the chamber is

$$B = \frac{B_c[A - (1 + \Delta)]}{A}, \tag{6}$$

where B_c is the maximum permissible magnetic field and $a\Delta$ is the distance between the inner circumference of the plasma column and the point at which the magnetic field is maximum.

From (1)–(6), we can find the main plasma parameters as functions of the aspect ratio and the vertical elongation of the plasma column for a reactor operating at a fixed fusion power. For example, we obtain the following formulas:

(a) the major radius (expressed in m) of the torus is

$$R = 2.9\frac{q^{0.9}}{\beta_N^{0.4}}\frac{P^{0.26}F_p^{0.4}}{M^{0.08}B_c^{1.38}}\frac{1}{k^{0.36}(1 + k^2)^{0.9}} \times \frac{A^{2.56}}{[A - (1 + \Delta)]^{1.38}}; \tag{7}$$

(b) the plasma current (in MA) is

$$I = 7.3\frac{1}{\beta_N^{0.4}q^{0.1}}\frac{P^{0.26}F_p^{0.4}}{M^{0.08}B_c^{0.4}}\frac{(1 + k^2)^{0.1}}{k^{0.36}} \times \frac{1}{A^{0.44}(A - (1 + \Delta))^{0.38}}; \tag{8}$$

(c) the plasma volume (in m^3) is

$$V = 488\frac{q^{2.71}}{\beta_N^{1.19}}\frac{P^{0.79}F_p^{1.19}}{M^{0.25}B_c^{4.13}}\frac{1}{k^{0.08}(1 + k^2)^{2.71}} \times \frac{A^{5.69}}{(A - (1 + \Delta))^{4.13}}; \tag{9}$$

(d) the neutron load (in MW/m^2) to the first wall is

$$P_N = 4.76\times10^{-3}\frac{\beta_N^{0.79}}{q^{1.81}}\frac{P^{0.48}M^{0.16}B_c^{2.75}}{F_p^{0.79}} \times\frac{k^{0.79}(1+k^2)^{1.81}}{L}\frac{(A-(1+\Delta))^{2.75}}{A^{4.12}}; \quad (10)$$

(e) the heat load to the divertor plates can be estimated under the assumption that the width of the divertor layer is proportional to the tokamak minor radius,

$$P_{\rm div}\sim\frac{A}{R^2}. \quad (11)$$

Relationships (7)–(10) imply that each plasma parameter can be represented as a product of a constant coefficient, which depends on the magnitudes of the physical quantities chosen for the analysis, with a function of the vertical elongation of the plasma column and a function of the aspect ratio $f_\gamma(A)$, where $\gamma = R, I$, etc.

Figure 1 shows A-profiles of the functions f_γ for R (profile *1*), I (profile *2*), V (profile *3*), P_N (profile *4*), and $P_{\rm div}$ (profile *5*) calculated at $\Delta = 0.1$. We can see that, near a certain optimum value $A_{\rm opt}$, the functions f_R and f_V have a minimum and the functions f_{P_N} and $f_{P_{\rm div}}$ have a maximum. In [1], we showed that $A_{\rm opt}\sim 1+\Delta$. As can be seen in Fig. 1, the tokamak major radius and plasma volume are both minimum at an aspect ratio approximately equal to $A\sim 2.5$–3.5. This circumstance indicates in particular that it is impossible to construct a compact reactor on the basis of a low aspect ratio tokamak. According to Fig. 1, the loads to the first wall and divertor plates fall off at both large and small aspect ratios, while the plasma current monotonically *decreases* as the aspect ratio grows. Formulas (7) and (9) imply that the geometrical dimensions of the reactor can be reduced exclusively by increasing the vertical elongation of the plasma column and/or the critical magnetic field.

For a tokamak with a circular cross section of magnetic surfaces, the ratio of the bootstrap current to the total plasma current can be found from the relationship [8]

$$\frac{I_{\rm boot}}{I} = 1.17\bar{\beta}_p A^{-0.61}\left[1-0.62\left(1-\frac{q_0}{q_{\rm a}}\right)\right], \quad (12)$$

where $\bar{\beta}_p$ is the ratio of the thermal energy to the energy of the poloidal magnetic field, q_0 is the central safety factor, and $q_{\rm a}$ is the edge safety factor. Note that, strictly speaking, formula (12) cannot be used to describe small aspect ratio reactors, because it was derived under the assumption that the tokamak magnetic field has a single toroidal component. However, in low aspect ratio tokamaks, the poloidal magnetic field is comparable with or even stronger than the toroidal field. Hence, the formulas describing the bootstrap current in small aspect ratio toroidal devices can only be used for rough estimates.

Figure 2 shows A-profiles of the total plasma current (profile *1*) and bootstrap current (profile *2*) computed for $\beta_N = 4$, $q = 3$, $P = 1500$ MW, $F_p = 26$, $M = 2.5$, $B_c = 10.5$ T, and $k = 1$. One can see that, as the aspect ratio increases, the plasma current falls off and the fraction of the bootstrap current grows. This indicates that noninductive current drive schemes for a large aspect ratio reactor are much simpler than those for a low aspect ratio device.

The estimates obtained in [4, 9] lead to the conclusion that reactors with an aspect ratio of $A\sim 4.5$ will be the least expensive. In devices with smaller aspect ratios, the systems for maintaining the plasma current appear to be more costly. Note that the estimates of [4, 9] were obtained without allowance for the fact that the plasma volume increases as the aspect ratio decreases (Fig. 1). Consequently, another factor that raises the cost of reactors with smaller aspect ratios is that their geometrical dimensions will be larger.

For the same reason, the magnetic systems used in larger aspect ratio reactors will be more expensive.

The cost of the remaining equipment used in the reactor is essentially independent of the aspect ratio.

Note also that fusion energy production in reactors with stronger critical magnetic fields is less expensive.

Hence, further analysis is needed to find an aspect ratio at which the cost of constructing a tokamak reactor and producing fusion energy would be the lowest.

3. CONCLUSION

Our analysis leads to the conclusion that DEMO should be constructed based on a large aspect ratio tokamak. The arguments in favor of this decision are as follows. The plasma current required for reactor operation falls off as the aspect ratio increases, thereby simplifying the scheme for maintaining a steady current. The fraction of the bootstrap current in the total plasma current increases with the aspect ratio, thereby facilitating the fabrication of a steady-state reactor. The larger the aspect ratio of the reactor, the lower the neutron load to the first wall and the heat load to the divertor plates (for $A > 3.5$–4). In reactors with larger aspect ratios, the central magnetic fields are stronger than in low aspect ratio devices with the same critical magnetic field on the inner surface of the solenoidal coils; consequently, significant plasma parameters are easier to attain in reactors with stronger toroidal magnetic fields. And finally, larger aspect ratios lead to better performance of the reactor.

REFERENCES

1. N. N. Brevnov and Yu. V. Gott, Fiz. Plazmy **24**, 293 (1998) [Plasma Phys. Rep. **24**, 263 (1998)].

2. R. D. Stambaugh, V. S. Chan, R. L. Miller, *et al.*, in *Proceedings of 16th IAEA Fusion Energy Conference, Montreal, 1996*, paper F1-CN-64/GI-2.
3. R. L. Miller, Y. R. Lin-Liu, A. D. Tumbull, *et al.*, in *Proceedings of 17th "Piero Caldirola" International School on Plasma Physics: Theory of Fusion Plasmas, Varenna, 1996*, Ed. by J. W. Connor, E. Sindoni, and J. Vaclavic (SIF, Bologna, 1996), p. 17.
4. *Summary of Point Design Meeting on Reduced Technical Objectives/Reduced Cost ITER, Naka, Japan, 1998.*
5. ITER Joint Central Team *et al.*, in *Diagnostics for Experimental Thermonuclear Fusion Reactors 2*, Ed. by P. E. Stott, G. Gorini, and E. Sindoni (Plenum, New York, 1998), p. 1.
6. M. Greenwald, J. L. Terry, S. M. Wolfe, *et al.*, Nucl. Fusion **28**, 2199 (1988).
7. Robinson, D. C., in *Proceedings of International Workshop "Tokamak Concept Improvement," Varenna, 1994*, Ed. by S. Barnabei, N. Sauthoff, and E. Sindoni (SIF, Bologna, 1994), p. 127.
8. V. D. Pustovitov, Fiz. Plazmy **18**, 819 (1992) [Sov. J. Plasma Phys. **18**, 425 (1992)].
9. The ARIES-I Tokamak Reactor Study, Report No. UCLA-PPG-1323 (UCLA, Los Angeles, 1991).

Translated by O. E. Khadin

Plasma Physics Reports, Vol. 26, No. 3, 2000, pp. 203–218. From Fizika Plazmy, Vol. 26, No. 3, 2000, pp. 221–237.

PLASMA DYNAMICS

Detonation Energy Amplification in Conical Channels[1]

J. G. Linhart*, L. Bilbao, R. Miklaszewski***, and W. Stepniewski*****

**Department of Physics, University of Ferrara*

***INFIP University of Buenos Aires, Buenos Aires*

****Institute of Plasma Physics and Laser Microfusion, Warsaw, Poland*

Received April 22, 1999; in final form, July 27, 1999

Abstract—A micro-Z-pinch has been recognized as a possible spark for the ignition of a dense D–T plasma [1–3]. The use of such a spark to ignite advanced fuels has been explored only superficially [4, 5]. In this paper, we address the problem of the transition between an ignited D–T plasma and a section of an advanced fuel such as D or D + He^3. Some general rules are derived for the parameters of a conical channel of D–T that amplifies the spark energy to a level suitable for the ignition of a detonation wave in an inertially confined cylinder of highly compressed advanced fuel plasma. *© 2000 MAIK "Nauka/Interperiodica".*

1. INTRODUCTION

The technological and economic problems associated with burning an equimolar D–T fuel are of such magnitude that the use of advanced fuels (AF) in fusion reactors should be seriously reconsidered. However, considering the high value of $nT\tau$ necessary for the ignition of an AF, it seems that the use of D or even of D + He^3 in magnetic confinement systems should be excluded. ICF may be a more suitable candidate, but not the spherical pellet version, in which spark ignition of AFs will not work [6]. An attempt to consider a spherical pellet with a D–T core and a D or D + He^3 mantel was made in the AFLINT concept [7, 8].

The driver energies in such a case appear realistic[2] only if compression ratios higher than 10^4 are considered, which brings one into the region of spherical symmetry requirements near the limits of practical feasibility.

It was suggested many years ago to consider only a conical slice of a spherical target [9], offering the advantages of (a) the ability to energize the spark region by means other than hydrodynamic processes and (b) the total compressional and spark energy to be much smaller than that required for a spherical pellet.

Two different realizations of such a mechanism have been proposed so far: one using a micro-Z-pinch igniting a cylindrical or conical D–T channel and finally a D or D + He^3 plasma [1–3], and the other in which a spark is created by a mechanism different from the one used for the precompression of the D–T target (fast ignitor [10, 11]).

Both of these concepts present a series of problems. The concept of the fast ignitor, when considered as part of a fusion reactor, is associated with severe problems of ballistics and timing (one proposes to focus a pulsed laser or particle beam on a compressed target whose diameter is of the order of 100 μm from a distance of typically 10 meters at the moment of maximum compression, requiring a precise timing within an interval of 1 ns). Numerical simulations [12] suggest that a nuclear burn can propagate into a tritium poor fuel from a spark initiated on the surface of the precompressed fuel; however, it is unlikely that the fast ignitor will work as a fusion reactor.

The micro-Z-pinch is a mechanism that is self-focusing and can be programmed (by initial conditions) to produce a spark at the moment of maximum axial current (I_z), i.e., at the maximum compression of the target, which is a great advantage over the fast ignitor; however, it requires a transport of I_z to the target, which, apart from technical difficulties, will almost certainly require a sort of umbilical cord between the device to be exploded and the outside of the explosion cavity. This, in turn, will be reflected in the higher cost of the target and will tend to shift the energy yield per shot into the range of more than 1 ton TNT (compare with ion beam guides and HYF mentioned in [13]).

The spread of the fusion detonation from a D–T plasma into an AF is possible only if the energy and the temperature in the D–T detonation is high enough. That this is possible in principle can be demonstrated by the example of a plane detonation in D–T striking a D plasma. It can be shown that the minimum energy capable of sustaining a detonation in D is

$$U_D \cong 5.7\alpha\phi' b \text{ GJ/cm}^2, \quad (1)$$

where $b = 2$ if neutrons are not contributing to the detonation wave, $\alpha = 10^{-8}T$, and $\phi' = \dfrac{\alpha^{3/2}}{10^{18}\langle\sigma v\rangle_{DD}}$ (see Appendix 1). The effective depth of the wave is

[1] This article was submitted by the authors in English.

[2] By realistic we mean that an A-bomb primer is not considered here as a driver in the category of "controlled" ICF.

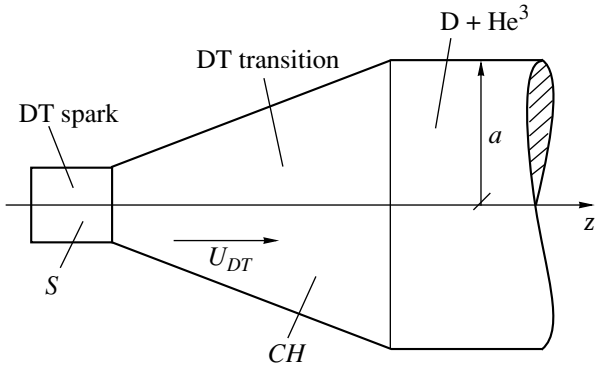

Fig. 1. Concept of axial detonation.

$l_D \cong 21\dfrac{n_s}{n}\phi' b$, ($n_s = 0.5 \times 10^{23}$), and the optimum temperature is approximately 4×10^8 K. This must be provided by the impact of the D–T detonation. A fully developed D–T detonation with no neutron absorption and a local α-deposition [14] has a mean temperature $\langle T\rangle = \dfrac{1}{2}(T_i + T_e) \sim 2 \times 10^9$ K and an effective depth $l_{DT} \cong 20\dfrac{n_s}{n}$. The U_{DT} is, therefore, approximately 160 GJ/cm^2 and consequently high enough to provide the U_D required for the D ignition.

A similar argument can be made for a D–T detonation in a cylindrical or conical channel intended as a trigger for the detonation in D in an adjacent cylindrical channel (Fig. 1). It is clear that the energy provided by the D–T spark is insufficient to ignite the D-plasma; it must be multiplied in the D–T transition.

This has been recognized in the AFLINT design. In a conical version of AFLINT, we cannot adopt the parameters of the spherical pellet, because the boundaries of the conical channel are not rigid; at most, they are inertially confined.

In this paper, we shall limit ourselves to estimating if and how the U_{DT} generated by a spark can be amplified to a level of the required U_D. We shall present first an approximate analytical description of the energy amplification along the lines presented in a previous publication [15]. This will be followed by numerical simulation of the propagation of the detonation wave in cylindrical and conical channels. The results provide the criteria for the value of ignition energy, the correct radius, the conical divergence, and the length of the channel resulting in final $U_{DT} > U_D$. We shall assume the spark energy W_s and T_s are given (a separate paper on spark generation by a micro-Z-pinch will be published shortly, [16]) and will show that below a certain W_s and T_s the ignition of a detonation wave is not possible.

2. D–T DETONATION IN A CYLINDRICAL CHANNEL

Simple two-dimensional simulations of a D–T nuclear detonation inside a cylindrical liner (radius R) were performed by Avrorin *et al.* [17]. When a steady propagation is encountered, it appears that the detonation zone can be represented by a slug having a certain effective length l and radius a, within which the plasma has a mean temperature T and density n. Of course, the slug does not continue to be composed of the same particles; it is the high T and n zone that propagates in the axial direction with a speed $v_s = \beta v_t$, where $v_t = \sqrt{\dfrac{kT}{M}}$ and $M = 4.18 \times 10^{-24}$ g (Fig. 2).

In our case, we shall assume that the heat conductivity in the radial direction is substantially reduced by an imbedded magnetic field (e.g., B_ϕ of a Z-pinch; see [2]). The length l of the slug will be given by inertial confinement only; we shall put $l = 0.41\dfrac{v_s}{v_t}\kappa a$, where κ is the coefficient of inertial confinement. When the radius of the liner $R \gg a$ and the burn-up in the slug is high, the only inertia comes from the material of the slug itself and $\kappa \simeq 1$. Neglecting heat conduction and radiation losses and assuming local α-deposition, we can write the energy equation for the propagation of the slug [4]:

$$\frac{s}{4}n^2\langle\sigma v\rangle Q_\alpha \Omega_0 \tau \geq q \times 3nkT\Omega_0 + 3nkT\Omega_0\left[1 - \left(\frac{\Omega_0}{\Omega}\right)^{2/3}\right] + 3n''kT''\Omega, \tag{2}$$

where $\Omega_0 = l\pi a^2$; $\tau = \dfrac{a\kappa(\sqrt{2}-1)}{v_t}$; Ω is the expanded volume (which is approximately equal to $\sqrt{2}\,\Omega_0$); and n'' and T'' are the mean density and temperature of the rarefacted zone, respectively. We shall assume that $n''T'' \ll Tn$ and the initial temperature T' of the plasma is much smaller than T. The coefficient q expresses the contribution of the kinetic energy to the total energy of the slug. The factor $s < 1$ models the decrease in reactivity due to the expansion of Ω_0.

We obtain

$$s\langle\sigma v\rangle n\frac{Q_\alpha}{12} = 2.4\frac{(kT)^{3/2}}{\sqrt{M}}(\kappa a)^{-1}(q + 0.2). \tag{2a}$$

In many cases, we can approximate $q = 1.3$ and $s = 3/4$ (although they are all functions of T) and get [4]

$$a \geq a_{\min} \cong 1.67\kappa^{-1}\frac{n_s}{n}\phi, \tag{3}$$

where $\phi = 10^{-28}\dfrac{T^{3/2}}{\langle\sigma v\rangle}$ and $\phi \sim 1$ for $T = 10^8$ K.

This expresses the limit of the possible propagation of a detonation wave in D–T in a cylindrical channel. If $a > a_{\min}$, the fusion output is able to raise the temperature T and (2) must contain a term representing this heating, i.e., $3nk\Delta T\Omega_0 q$.

The modified (2) then gives

$$q\dot{T} = \frac{s}{12}n\langle\sigma v\rangle\frac{Q_\alpha}{k} - 2.4(q+0.2)(\kappa a)^{-1}\sqrt{\frac{k}{M}}T^{3/2} \quad (4)$$

or

$$\dot{T} = 0.33\times 10^{10} n\langle\sigma v\rangle\frac{s}{q}\left(1-\frac{a_{\min}}{a}\frac{\phi}{\phi_0}\right). \quad (4a)$$

The temperature will rise until

$$\phi = \phi_0\frac{a}{a_{\min}}, \quad (4b)$$

where $\langle\sigma v\rangle_0$ is the initial $\langle\sigma v\rangle$. For example, if $\phi_0 = 1$ and $a = 2a_{\min}$, then $T_{eq} = 6.7\times 10^8$ K.

The maximum useful a follows from taking into account the depletion of D–T due to a large burn-up.

At temperatures $T > 20$ keV, the axial heat conductivity χ generates a heat precursor whose skin depth δ [9] is

$$\delta \cong \frac{\frac{2}{3}\chi}{\gamma n\sqrt{T}}\sqrt{\frac{M}{k^3}}. \quad (5)$$

The quantity δ may be comparable with $l = 0.41\frac{v_s}{v_t}\kappa a$ and must, therefore, be included in the energy equation (4a).

We get

$$\dot{T} = 0.11\times 10^{10} n\langle\sigma v\rangle\left[1-\frac{a_{\min}}{a}\frac{\phi}{\phi_0}\right]\left(1+l^{-1}\frac{\partial W}{\partial T}\right)^{-1}, \quad (6)$$

where $W = \delta q' 3kT$ and $q' < 1$ is taking into account that the mean T within δ is smaller than that of the slug. The final temperature will be the same as from (4b), but it will be attained later than if $\chi = 0$.[3]

Our analysis ceases to be valid when $\delta \geq l$ and the detonation propagates as a heat wave, the detonation speed is supersonic, and the α-energy deposition is nonlocal (see Appendix 2).

3. D–T DETONATION IN A CONICAL CHANNEL

In the preceding section, we saw that the energy in a detonation wave can be amplified in a cylindrical channel provided the radius $a > a_{\min}$. In this case, we shall require a $\left(\frac{a}{a_{\min}}\right)^3$ times larger spark energy than the minimum one. It would be more convenient to start with $a = a_{\min}$, requiring the minimum ignition energy and providing the energy multiplication by having a diverging conical channel. However, in this case, the energy equation for the slug (4) must contain a term representing the heat expenditure on the extra material to be energized. The new extra mass incorporated into the slug after a time $\tau = \frac{l}{v_s}$ is

$$\Delta m = nM\Delta\Omega,$$

where $\Delta\Omega \cong 2\pi\kappa a^2\times 2\Delta a + \pi a^2\Delta l$. Taking $\Delta l = (l/a)\Delta a$ and $l = 0.41\kappa a\beta$, where $\beta = \frac{v_s}{v_t}$, we get (Fig. 3, valid for small α)

$$\Delta m \cong 6nM\kappa\Omega_0\tan\alpha, \text{ where } \Omega_0 = 2\pi\kappa a^3,$$

and

$$\frac{\Delta\Omega}{\Omega_0} = 1.23\beta\kappa\tan\alpha. \quad (7)$$

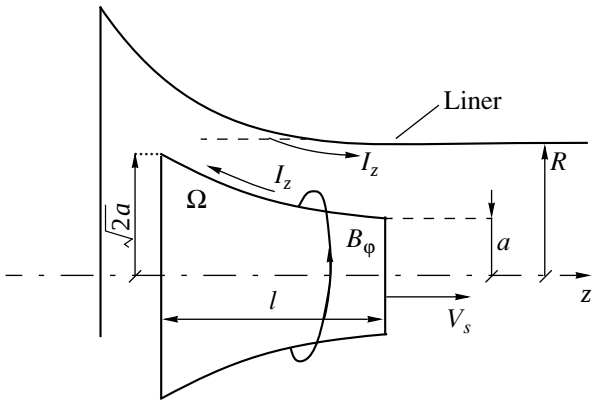

Fig. 2. Sketch of the slug model.

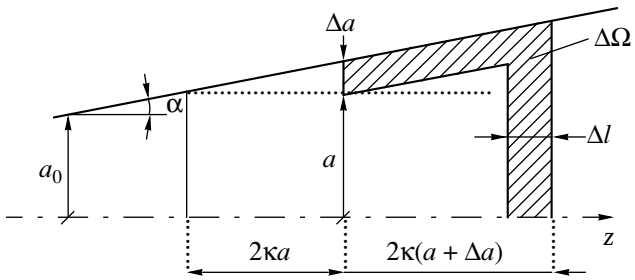

Fig. 3. Geometry of a conical channel.

[3] At $T > 5\times 10^8$, one should use a two fluid model, since $T_e < T_i$. It should be understood that, in our case, $T = \frac{1}{2}(T_i + T_e)$.

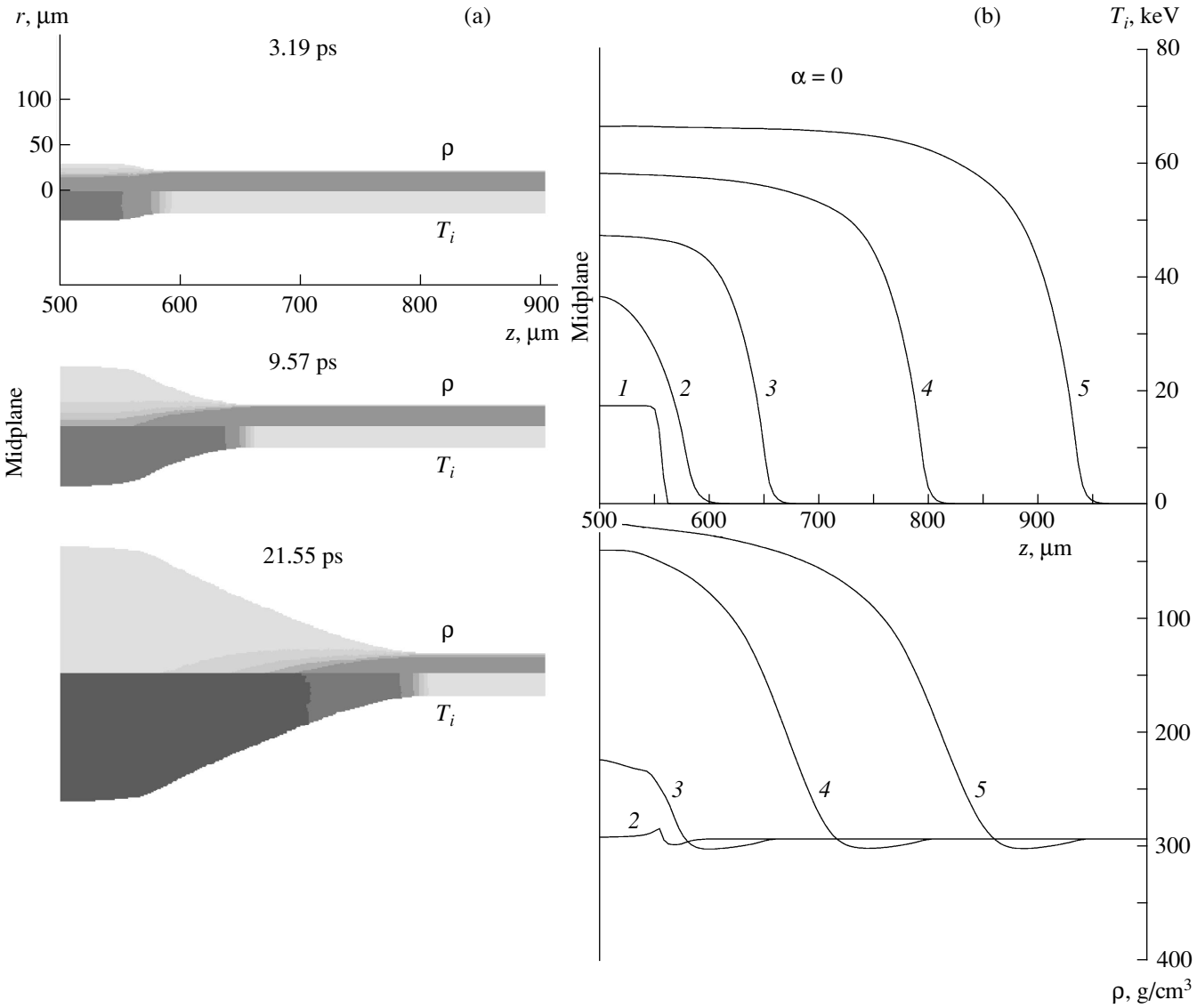

Fig. 4. (a) Detonation propagating in a cylindrical plasma for $a = 20$ μm, $N = N' = 8.8 \times 10^{20}$ ion/cm, $T = 2 \times 10^8$ K, and $T' = 2 \times 10^6$ K; (b) $\rho(z)$ and $T_i(z)$ profiles at $r = 0$ at five consecutive moments: (*1*) 0, (*2*) 3.2, (*3*) 9.6, (*4*) 21.5, and (*5*) 33 ps.

We must also take into account that, in transiting from Ω_0 to $\Omega_0 + \Delta\Omega$, the α-output is increased by

$$F = \left(1 + c_1\frac{\Delta\Omega}{\Omega_0}\right)\left(1 + c_2\frac{\Delta\tau}{\tau}\right) \cong 1 + c\kappa\tan\alpha. \quad (8)$$

The energy equation can now be written as

$$(1 + c0.2\beta\kappa\tan\alpha)\frac{s}{4}n\langle\sigma v\rangle Q_\alpha = 3\frac{2.4}{\kappa a}kT(q + 0.2 + 1.23\beta\kappa q\tan\alpha) + 3k\dot{T}q. \quad (9)$$

Again putting $q = 1.3$, $s = 3/4$, and $c \simeq 4$, we have initially

$$\dot{T} \cong 1.9 \times 10^9 n\langle\sigma v\rangle\left[1 - f\frac{a_{\min}}{a}\frac{\phi}{\phi_0}\right](1 + 0.8\beta x), \quad (10)$$

where $f(\alpha) = \dfrac{1 + 1.07x\tan\alpha}{1 + 0.82x\tan\alpha}$ and $x = a/a_{\min}$.

Thus, provided $\dfrac{a_{\min}}{a}\dfrac{\phi}{\phi_0} < 1/f$, the T will grow until the length l of the slug is equal to l_b, where l_b corresponds to a 50% burn. As $\phi = \phi_0$ initially, we get a rela-

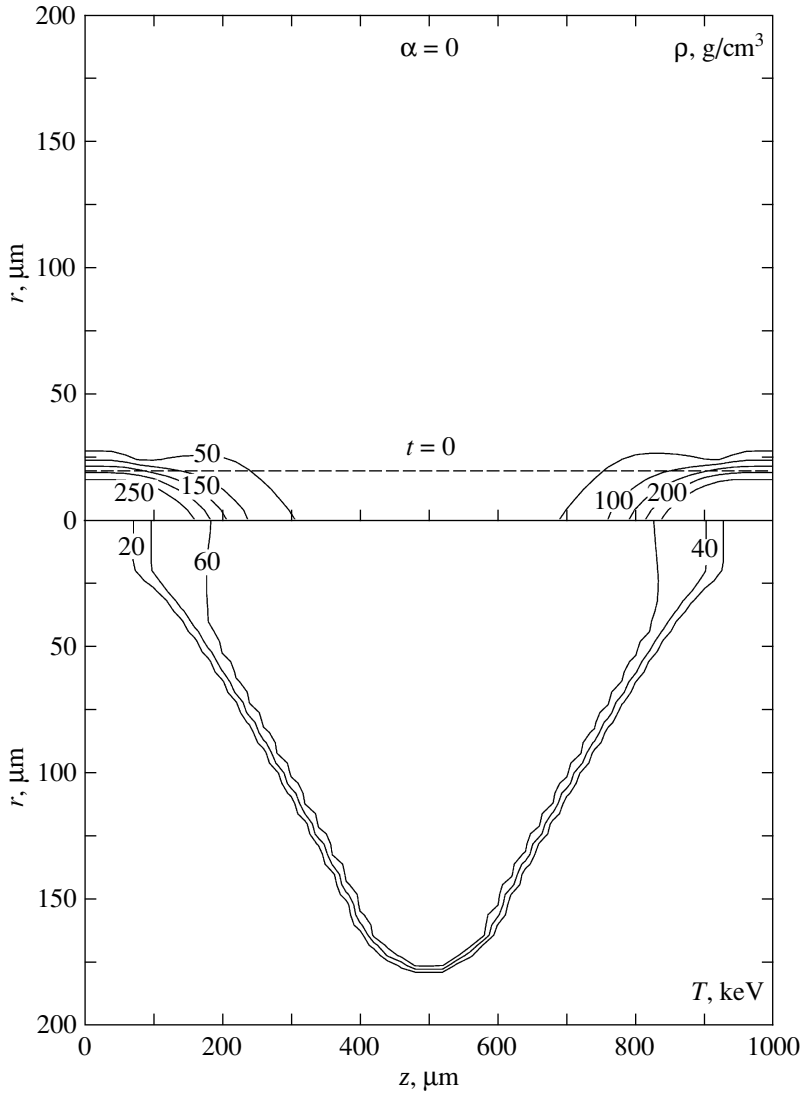

Fig. 5. The $\rho(r, z)$ and $T_i(r, z)$ contours at $t = 33$ ps for the case of Fig. 4.

tionship for α insuring the initial growth of T:

$$x > f. \tag{11}$$

Because $a_{\min}/a$ will decrease with z, one may anticipate that α can increase as z increases and, therefore, the initial α is the minimum α along the conical channel. It is clear that a detonation can always be obtained, even for $\alpha = \pi/2$, provided that the trigger energy is high enough.[4]

In this simple analysis, we have assumed that the conical plasma has a constant density n and that it is, before the transition of the detonation front, confined by a B_φ field of a current I_z and, therefore, $I_z^2 = 400N'kT'$. Since $N = \pi a^2 n$, we have $T' \propto 1/a^2$. As we have assumed that $T' \ll T$, equations (10) and (11) are not affected by the $T'(z)$ dependence. Our assumption will, however, provide the experimenter with practical problems.

4. NUMERICAL RESULTS

In our numerical simulation, we used a Lagrangian code with free mesh points. The system of equations is based on a two-fluid model of a D–T plasma with transport and viscosity coefficients used in [3]. The most important feature of this model is the nonlocal deposition of α-particles simulated by means of an α heat conductivity χ_α (see Appendix 3). The plasma is assumed to be transparent to the neutron flux; the depletion of D and T due to the D–T fusion is taken into account. The role of D–D and T–T reactions is neglected.

[4] From (11), we get for $\tan\alpha > 1$ and $\kappa = 1$ that $x > 1.4$, giving for the initial trigger energy W [J] $\geq 6\pi a^3 knT = 6 \times 10^8 \phi^3 (n_s/n)^2 T$ [keV].

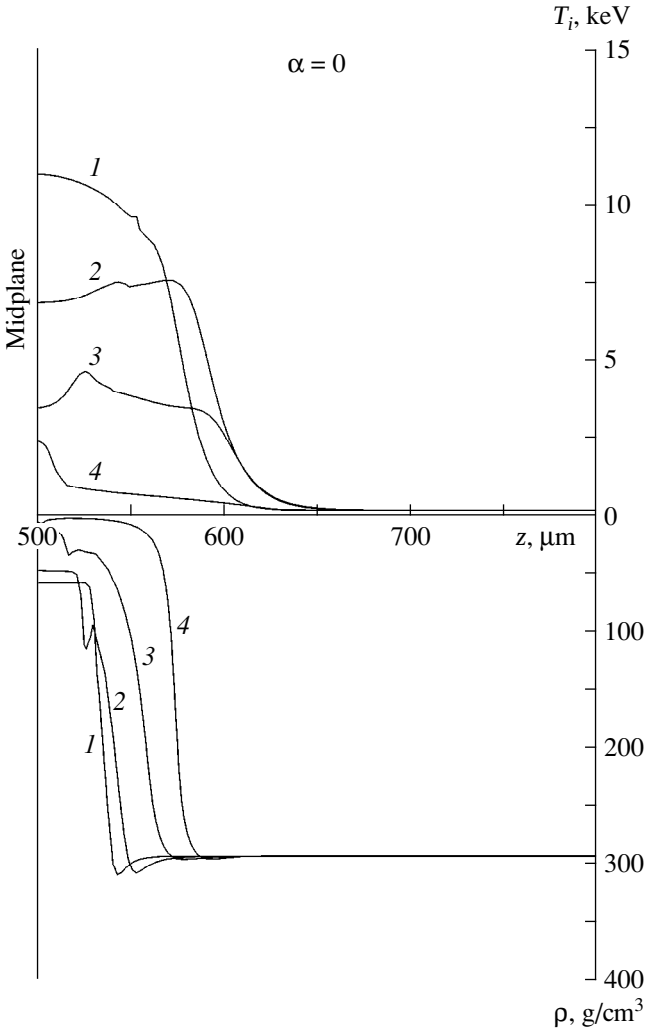

Fig. 6. Detonation fizzle in a cylindrical plasma for $N = 1.76 \times 10^{20}$ ion/cm (all else as in Fig. 4) at times (*1*) 7, (*2*) 15.75, (*3*) 30.17, and (*4*) 79.13 ps.

We have assumed that initially there is a hot cylindrical section (*S*) in which $T \gg T'$, T' being the temperature of the (as yet unaffected) cylindrical or conical channel (CH). This hot section is created by a certain, here unspecified, spark ignition process (see [16]), and we shall assume that $T > T_{\text{ignition}}$; we shall use in all our computations $T = 2 \times 10^8$ K. The plasma density n in CH is uniform (except in the current skin), and the axial current I is initially confined to a skin whose thickness $\delta \ll a$. The plasma in the cylindrical CH is in Bennett equilibrium. In a conical CH, this equilibrium exists initially only in the section adjacent to S; however, considering the short time required for the propagation of the detonation along CH, this lack of equilibrium does not result in an appreciable expansion of CH.[5]

[5] We can also assume $T \propto 1/a^2$ (see Conclusion).

In Fig. 4a, we show a case of detonation propagation in a cylindrical channel. The development of $\rho(z)$ and $T(z)$ on the axis is shown in Fig. 4b. The radius a = 20 μm, the length of S is 60 μm, and the length of CH is 440 μm. The line density $N = 8.8 \times 10^{20}$ (ion/cm), and $T' = 2 \times 10^6$ K. The corresponding axial current is $I_z \simeq 10$ MA. The structure (ρ, T_i) of the established detonation wave is depicted in Fig. 5. When the N becomes less than 3×10^{20} for the same geometry, the detonation fizzles out (Fig. 6). In Fig. 7a, we have a sequence of snapshots of the detonation propagating in a conical channel with $\alpha = 10°$. Figure 7b shows the T and ρ on the axis as a function of z and t. The contours of ρ and T at $t = 33.7$ ps are found in Fig. 8. The same parameters are used for $\alpha = 20°$; the time sequence is shown in Figs. 9a, 9b, and 10. In all of these cases, we have used the α-heat conductivity $\chi_\alpha = 10^{15}\alpha^{y+2-3u}$ (see Appendix 3). The form of the ρ and T distribution is quite different for local α energy deposition. The case with the parameters of Fig. 4, where $\chi_\alpha = 0$, is shown in Figs. 11a, 11b, and 12.

The degree of burn b on the axis as a function of z at the time detonation reaches the extremity of CH is depicted in Fig. 13 (which corresponds to curves *e* in Figs. 4b, 7b, and 9b). We have also integrated the thermal energy density in the cases of Figs. 5, 8, and 10 to obtain the total thermal energy W of the detonation as a function of time as well as $\dfrac{W}{\pi a^2} = U_{DT}$. This is shown in Fig. 15, showing the amplification of U_{DT} in the three channels (with divergences 0, 10°, and 20°).

5. DISCUSSION OF THE SIMULATION RESULTS

Let us first examine the case of the detonation in which we have assumed a local α-deposition (Figs. 11a, 11b). The plasma density is $n = \dfrac{N}{\pi a^2} = 7 \times 10^{25}$, and the compression factor is $n/n_s = 1400$. From (3), we get $a_{\min} \cong 12$ μm (for $\alpha = 2$, we have $\phi/\kappa \sim 0.8$). As in our case $a = 20$ μm, the detonation should propagate well and, according to (4a), the temperature should reach $T_{\max} \sim 70$ (keV) in a time $t_{eq} \approx 30$ ps [see (4)].

Although Fig. 11b shows a maximum temperature of approximately 100 keV on the axis, we must refer to Fig. 12, where it is seen that the temperature drops off away from the axis and, therefore, the mean temperature within $r = a$ beyond the shock front does not exceed 70 keV. This temperature is reached before $t = 20$ ps. The $\rho(z)$ distribution shows clearly a shock structure: $\Delta\rho/\rho \sim 0.5$. In a strong shock, this ratio should be much higher, showing that the various diffusion processes, particularly the electron heat conductivity, are smoothing the shock front. The shock speed v_s is (see Fig. 11b) almost constant and is approximately

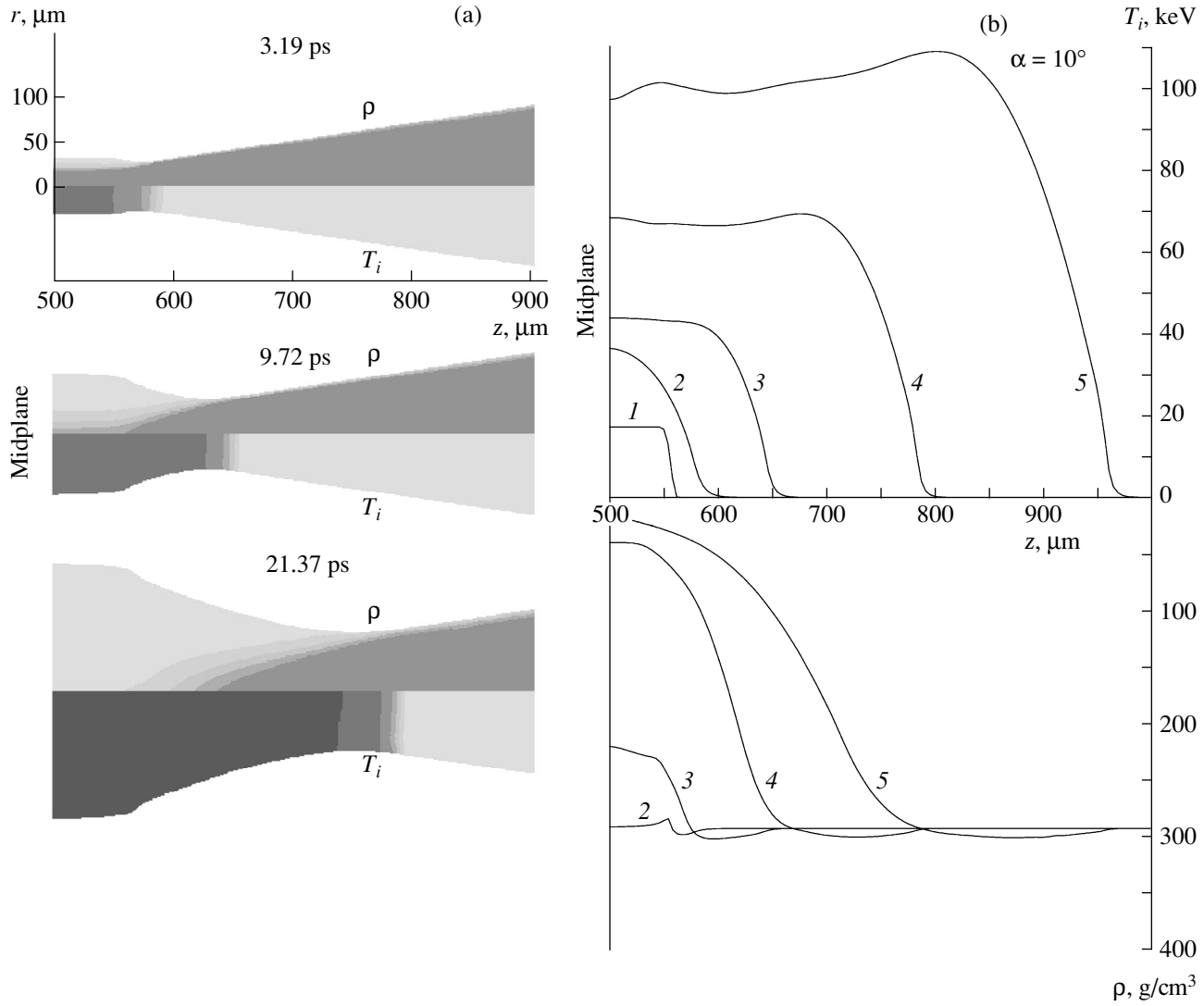

Fig. 7. (a) Detonation propagation in an isochoric conical CH ($\alpha = 10°$) for $N = 8.8 \times 10^{20}$ ion/cm and $N' = N\left(\frac{a'}{a}\right)^2$; (b) $\rho(z)$ and $T_i(z)$ profiles at $r = 0$ and times (*1*) 0, (*2*) 3.2, (*3*) 9.7, (*4*) 21.4, and (*5*) 33.7 ps.

3.8×10^8 cm/s, which corresponds well to a weak shock at a mean temperature of 70 keV.

Let us now compare this with the case in which the nonlocal α-deposition is taken into account through an α-heat conductivity χ_α (see Appendix 3). From Figs. 4b and 5, we see immediately that the character of the detonation is quite different as compared with the case in which $\chi_\alpha = 0$. We are dealing with a heat wave; the $\Delta\rho/\rho$ is negligible; and the speed v_h of the wave (see Fig. 4b) grows from 10^9 to 1.3×10^9 cm/s, which agrees well with equation (A2.6a) and is much higher than the shock-speed v_s in the previous case. The thickness of the heat front is of the order of 100 μm (Fig. 5) instead of 50 μm (Fig. 12) and the radial distribution of temperature is relatively uniform. The time to reach the equilibrium temperature T_{max} is more than 33 ps; in fact, the last *T*-curve in Fig. 4b (curve *5*) is still somewhat below the maximum. This is in agreement with (6), although, as already mentioned, it also implies that our slug-model is not too well adapted to the regime of a heat wave.

Figure 6 represents a situation in which the initial trigger energy W_{DT} is only one-fifth of Fig. 4. It is clear that, in this case, the trigger is not strong enough to ignite a detonation in $n' = 5n$. Only a weak shock initially propagates axially with $v_s \sim 2.5 \times 10^8$ cm/s, diminishing to $v_s \sim 0.5 \times 10^8$ cm/s at $t > 70$ ps. The heat conductivities are able to thicken the shock front, but there is not enough energy to launch a detonation wave.

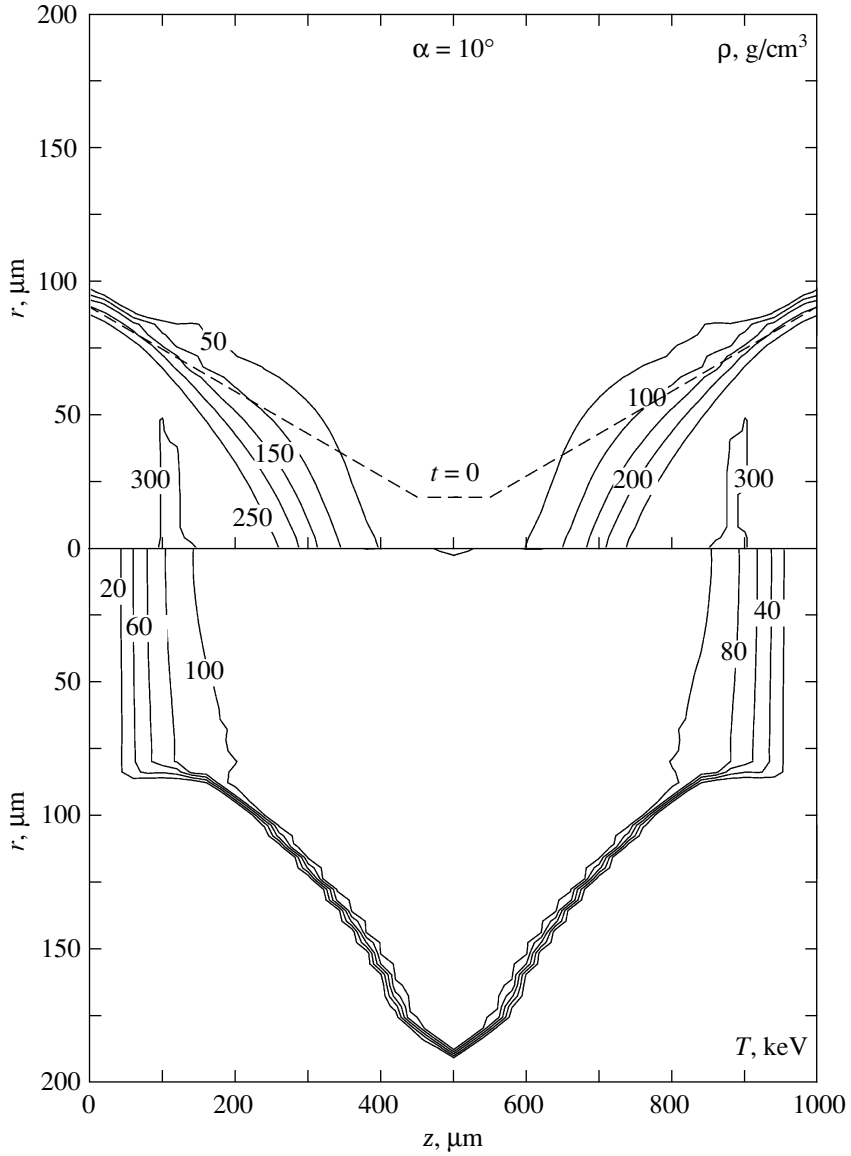

Fig. 8. ρ and T_i contours at t = 33.7 ps for the case of Fig. 7. The initial form of CH is hatched.

We have performed two-dimensional simulations considering conical CH with $\alpha = 10°$ and 20° for both $\chi_\alpha = 0$ and χ_α given by (A2.4) (see Appendix 2). The results for the cases with local α-deposition do not give the impression of a physically realistic event; we shall, therefore, analyze only the results of nonlocal α-deposition (Figs. 7a, 7b, 8, 9a, 9b, 10). Comparing the T growth in Figs. 7b and 9b with that of Fig. 4b, we see that, in conical channels, the T_{max} on the axis does not show any sign of saturation over a distance of 500 μm, whereas the T_{max} in the cylindrical channel shows a convergence towards a value indicated by (4b) (Fig. 14). Of course, given time, the T_{max} must, even for $\alpha = 90°$, converge to a T_{max} of a plane detonation wave in DT. This T_{max} follows from (2), setting for t the characteristic time $t_b \simeq 4 \times 10^{-7} \frac{n_s}{n} \alpha^{-s}$ necessary to achieve a burn of b = 50% and assuming that $\Omega = \Omega_0$ (as in Appendix 1). It also follows approximately from

$$v_h t_b \sim l_{DT} = 20 \frac{n_s}{n};$$

both methods giving [see (A2.6a)] $\alpha \simeq 22$, which corresponds to $T_{max} \approx 191$ keV, indicated in Fig. 14 as an upper limit.[6] In order to find out how the T in conical

[6] Another limit on T_{max} is given by burn-up b. It can be written as $T_{max} = 590 \frac{b}{1 - 0.2b}$ keV, having assumed a local α-deposition and no energy loss. For b = 0.25, we get T_{max} = 155 keV.

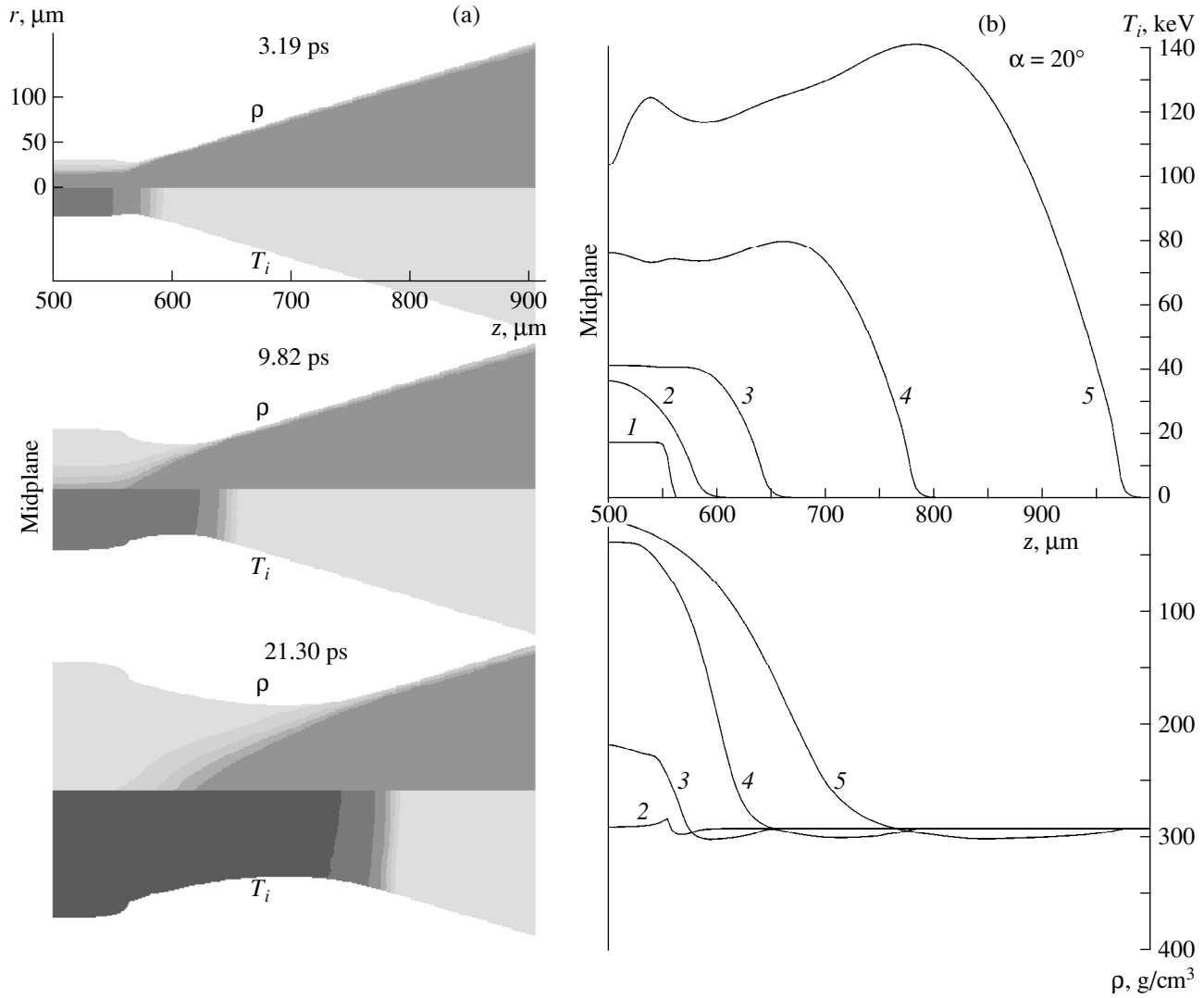

Fig. 9. (a) Detonation propagation in a cone $\alpha = 20°$ (all else as in Fig. 7); (b) $\rho(z)$ and $T_i(z)$ profiles at $r = 0$ and times (*1*) 0, (*2*) 3.2, (*3*) 9.8, (*4*) 21.3, and (*5*) 34.6 ps.

channels approaches this limit, we would have to follow the detonation for at least 50 ps.

Using the $T(z)$ and $\rho(z)$ values corresponding to curves *5* in Figs. 4b, 7b, and 9b, it is possible to work out the U_{DT} [GJ/cm^2] on the axis for the cases of $\alpha = 0°$, 10°, and 20°. We have approximated the U_{DT} by

$$U_{DT}\ [\mathrm{GJ/cm^2}] = \int_0^L \frac{3}{2} nk(T_i + T_e)dz \simeq 0.1\int_0^L \rho T_i dz, \quad (12)$$

where ρ is in g/cm^3; T is in keV; and $L = \langle L_\alpha \rangle \simeq 10\frac{n_s}{n}\frac{\alpha_e^{3/2}}{\Lambda}$ is the mean range of α-particles, Λ being the Coulomb logarithm. The results are plotted in Fig. 15.

Of course, this is the U_{DT} on the axis; it is clear from Figs. 5, 8, and 10 that off the axis both the ρ and T_i drop below the axial values. Taking the ρ and T_i at the initial boundary of the cylinder or the cones, we get U_{DT} values between 40 and 50% of the axial ones. The amplification factor $\gamma = \dfrac{U_{DT}}{(U_{DT})_0}$, where $(U_{DT})_0$ refers to the real energy density at $t = 0$, is clearly very high even off the axis. It should not be confused with the concept of gain, since the original $(U_{DT})_0$ is already energy amplified by a previous spread of the detonation from the spark [16].

The development of the detonation is somewhat asymmetric with respect to the initial situation. This is due to those terms in our equations that contain $\nabla T \times \mathbf{B}$

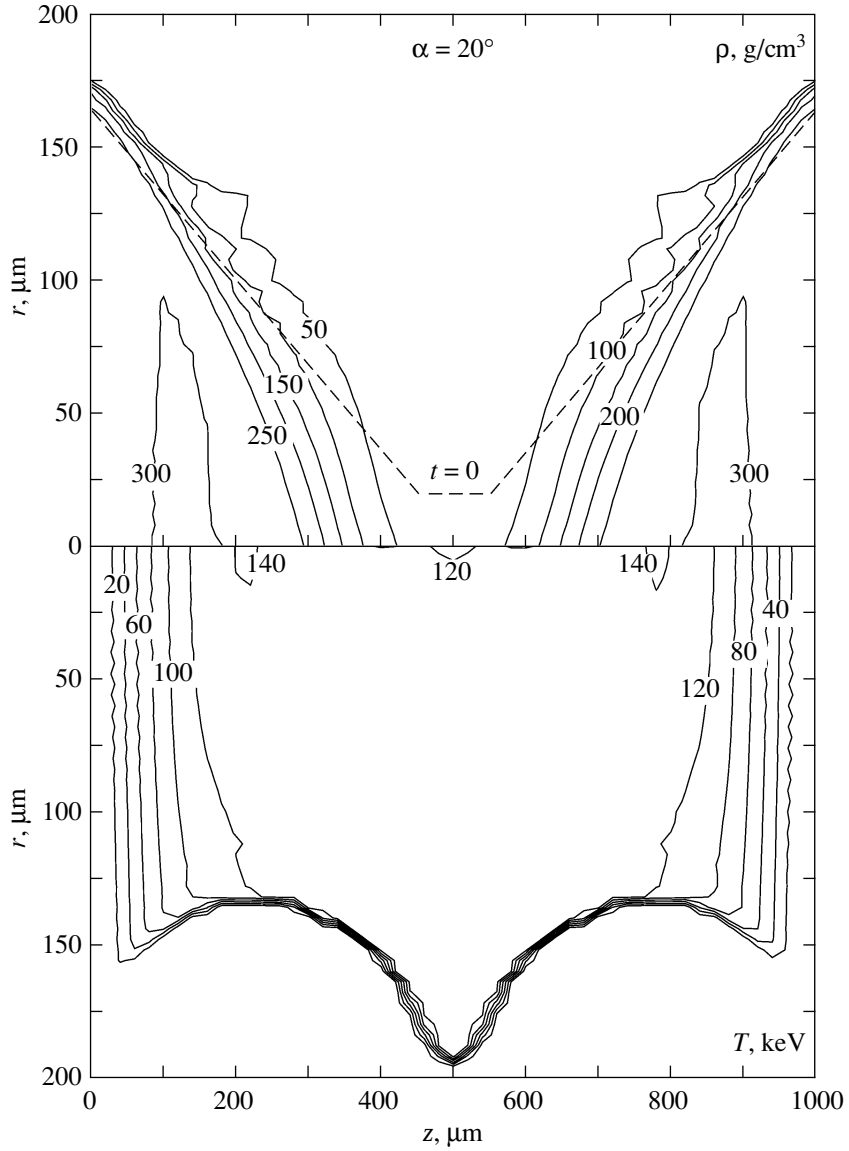

Fig. 10. ρ and T_i contours at t = 34.6 ps for the case of Fig. 9. The initial shape of CH is hatched.

(e.g., the Thomson effect, Hall effect, and Nernst effect). However, the fluid dynamics and nuclear phenomena predominate and the asymmetries amount to only a few percent.

6. CONCLUSION

The difference in detonation propagation between $\chi_\alpha = 0$ cases and those of $\chi_\alpha > \chi_e$ is considerable. In cases where the pinch current I_z is flowing mainly in a skin $\delta \ll a$, we would argue that the detonation is better represented by Figs. 4a, 4b, and 5 than by Figs. 11a, 11b, and 12. However, when the current I_z is almost uniformly distributed over the section of the pinch and, therefore, χ_α is diminished [see (A3.3)], the character of the detonation will be somewhere between these two extremes.

When the nonlocal α-deposition prevails, our simple analysis based on the slug model is inadequate; nonetheless, some results such as equations (3), (4a), and (6) are still approximately applicable. Also, as seen from Fig. 16, the concept of a slug still applies even in the case of a heat wave, only the length of the slug is $l \sim 3.2a$ instead of $l \simeq a$ (for $\kappa = 1$), which is a consequence of $v_h > v_s$ (in this case, $v_h \simeq 11 \times 10^8$ cm/s and $v_s \simeq v_t = 3 \times 10^8$ cm/s). The shape and dimensions of the slug remain almost constant between 10 and 33 ps in spite of the mean temperature rise from 40 to about 60 keV.

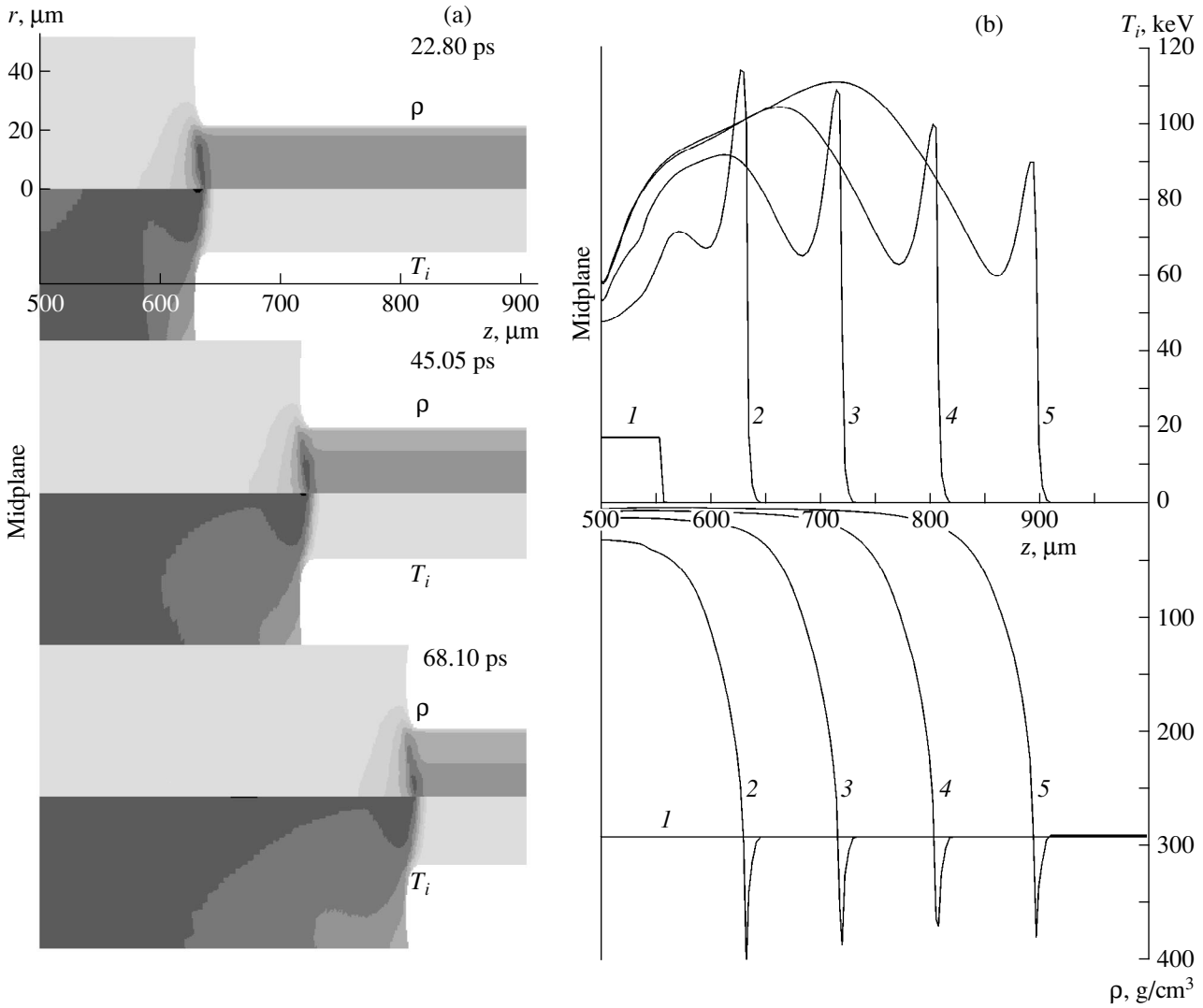

Fig. 11. (a) Detonation propagation for $\chi_\alpha = 0$ (all else as in Fig. 4); (b) $\rho(z)$ and $T_i(z)$ at $r = 0$ and times (*1*) 0, (*2*) 22.8, (*3*) 45, (*4*) 68, and (*5*) 92.5 ps.

A further confirmation that our (10) and (11) are significant comes from Fig. 14. One sees that, for the $\alpha = 0$ case, the temperature on the axis increases steadily; it stagnates initially for the $\alpha = 10°$ case; and it shows even a temporary decrease in the $\alpha = 20°$ case. This is in agreement with the prediction (11) that an excessive conical divergence may cause the spark to fizzle out.

From Fig. 15, it follows that U_{DT} is amplified to levels compatible with (1) and, therefore, the ignition of even pure D-plasma is possible. Of course, the D channel must correspond to a sufficiently large ρa in order for the detonation to propagate in it. From [4], we have for the minimum ρa in D

$$(\rho a)_{\min} = 2.72 \times 10^{-18} \frac{\alpha^{3/2}}{\langle \sigma v \rangle_{DD}} = 2.72\phi' \ [\text{g/cm}^2].$$

For $\alpha = 9$, we get $(\rho a)_{\min} \cong 2$ g/cm^2. For ρ corresponding to a typical compression of 10^3, we obtain that $a_{\min} \cong 120$ μm. The a of our CH conical transition ($\alpha = 20°$) at $z = 500$ μm is $a = 175$ μm. We conclude that the detonation in D–T depicted in Figs. 9a, 9b, and 10 has the strength (U_{DT}) and dimensions corresponding to the ignition of a detonation in a deuterium plasma compressed by a factor of 1000.

Of course, the transition from D–T to pure D and the propagation of a detonation in a D-channel would have to be studied by two-dimensional simulation—a task we hope to solve in the near future.

The practical realization of the conical pinch discussed here will be based, most probably, on the concept of a cylindrical or conical liner imploding on a Z-pinch in which the line density $N(z)$ is shaped in a

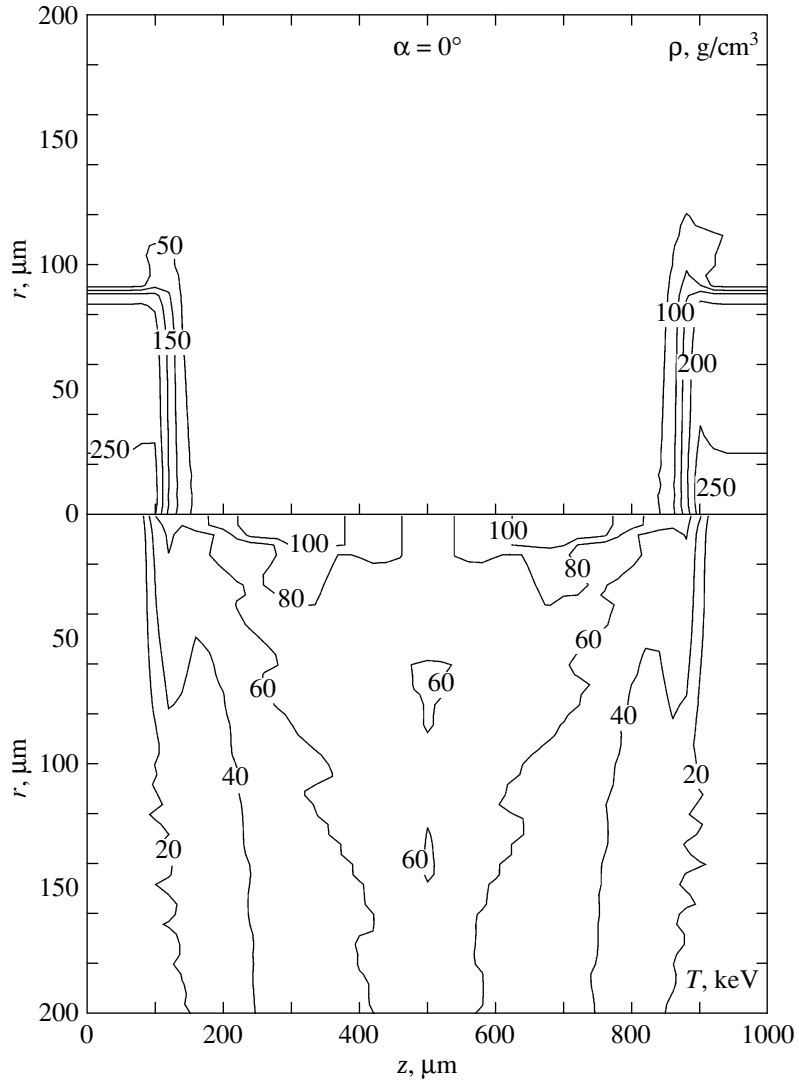

Fig. 12. ρ and T_i contours at t = 92.5 ps for the case of Fig. 11.

correct manner. The discussion of this task is beyond the scope of this theoretical paper.

ACKNOWLEDGMENTS

J.G. Linhart wishes to thank Ferrara Ricerche for support, Dr. A. DaRe for help with the elaboration of the graphs, and Dr. G. Verri for assistance in editing the final version.

APPENDIX 1

A Plane Detonation in Deuterium

An approximate estimate of minimum U_D [see (1)] can be made using (2). In this case, the second term on the r.h.s. is absent because in plane geometry there is no radial loss ($\Omega = \Omega_0$). We obtain for the D–D reaction

$$\frac{s}{6} n \langle \sigma v \rangle_{DD} \frac{Q_{DD}}{b} = q\beta \frac{(kT)^{3/2}}{\sqrt{M_d} l_{\min}}, \qquad \text{(A1.1)}$$

where Q_{DD} = 9.2 MeV. If neutrons contribute to the detonation propagation, then b = 1. If only charged particles power the detonation, then b = 2 [18]. We get for $l_{\min}$

$$l_{\min} \equiv 7 \frac{\beta q b}{s} \phi' \frac{n_s}{n}, \qquad \text{(A1.2)}$$

where $\phi' = 10^{-18} \dfrac{\alpha^{3/2}}{\langle \sigma v \rangle_{DD}}$ and $\alpha = T/10^8$ ($\phi' \simeq 1.1$ for $\alpha = 1$). In plane geometry, the Ω of our slug remains constant and s = 1 (local fusion energy deposition).

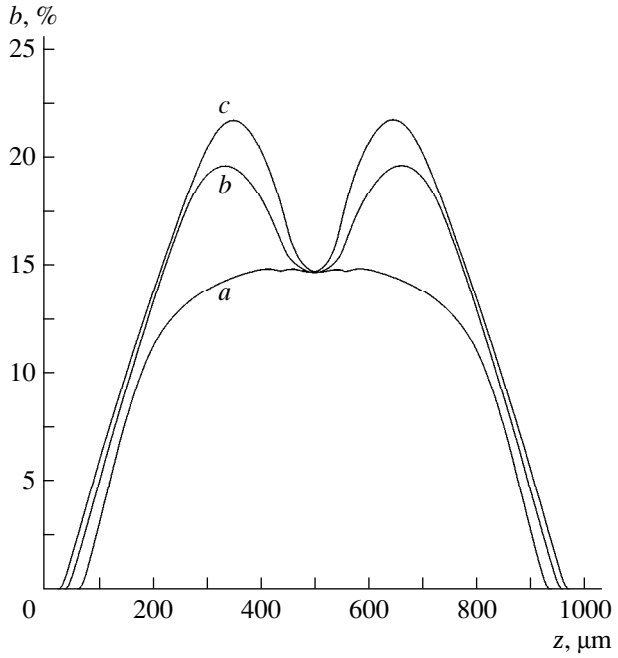

Fig. 13. Burn $b(z)$ at $r = 0$ at the moment the detonation arrives at $z = 500$ μm for $\alpha = (a)\ 0, (b)\ 10°$, and $(c)\ 20°$.

Taking $q = 1.3$ and $\beta = 2$ as before, we get

$$l_{\min} = 21\frac{n_s}{n}\phi' b. \qquad \text{(A1.2a)}$$

The function $\phi'(T)$ has a minimum of 0.6 at $\alpha \simeq 4$; at $\alpha = 10$, we have $\phi' \simeq 0.83$. The energy of the plane slug (per cm^2) is

$$U_D = 3nkTl_{\min}q.$$

Using (A1.2a), we obtain

$$U_D = 5.7\alpha\phi' b\ [\text{GJ/cm}^2] \qquad \text{(A1.3)}$$

independent of the density n. At $\alpha = 10$ and $b = 1.5$, we get $U_D \sim 64.7$ GJ/cm^2.

The effect of nonlocal deposition of the fusion energy and heat and radiation losses will increase the value of U_D; a more precise estimate of U_D requires a reliable numerical simulation.

APPENDIX 2

Fusion Heat-Wave Propagation

Let us assume that a cylindrical plasma is heated by a hot plate (temperature T_1). The heat conduction will propagate a heat wave in the z direction. Let us assume first that during this heat diffusion the plasma remains stationary. The heat skin depth δ after a time t will be

$$\delta = \sqrt{\frac{\langle\chi\rangle t}{(3/2)kn}}, \qquad \text{(A2.1)}$$

where $\langle\chi\rangle$ is the mean heat conductivity and n is the plasma density. Let us assume that $T \geq 10^8$ K; then, the α-heat conductivity $\chi_\alpha > \chi_e$ and we have (see definitions of y and u in Appendix 3)

$$\chi_\alpha = c10^{16}\alpha_i^{y+2-3u} \qquad \text{(A2.2)}$$

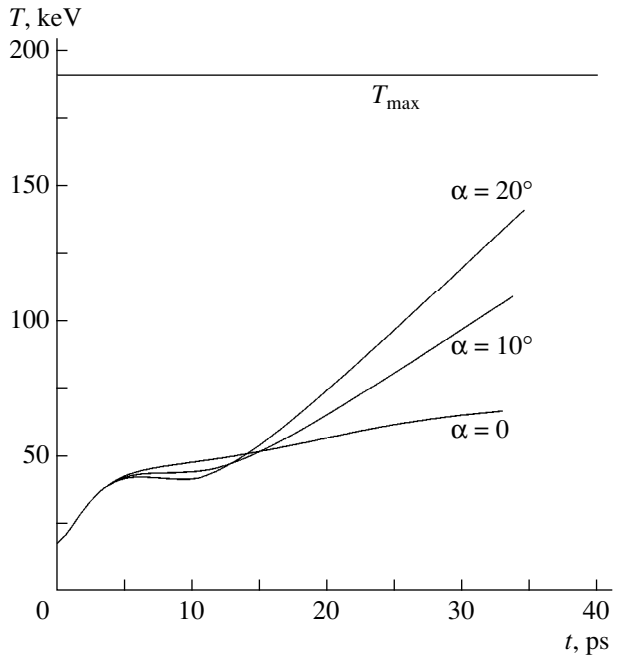

Fig. 14. $T_{\max}(t)$ for $\alpha = 0$, 10°, and 20°.

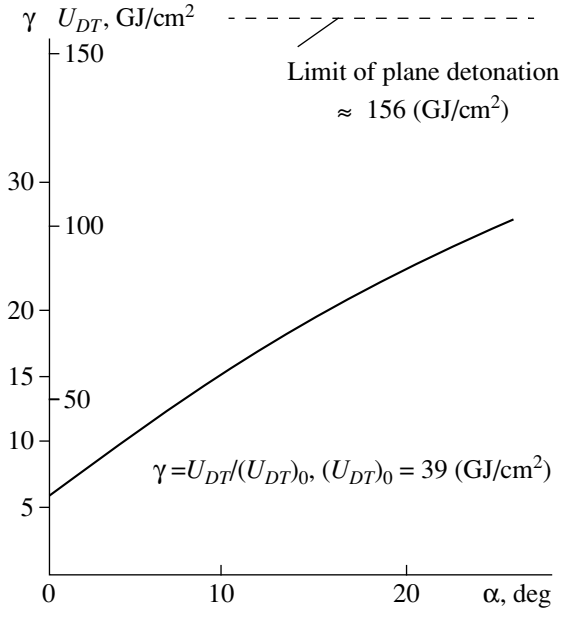

Fig. 15. The U_{DT} multiplication as a function of α.

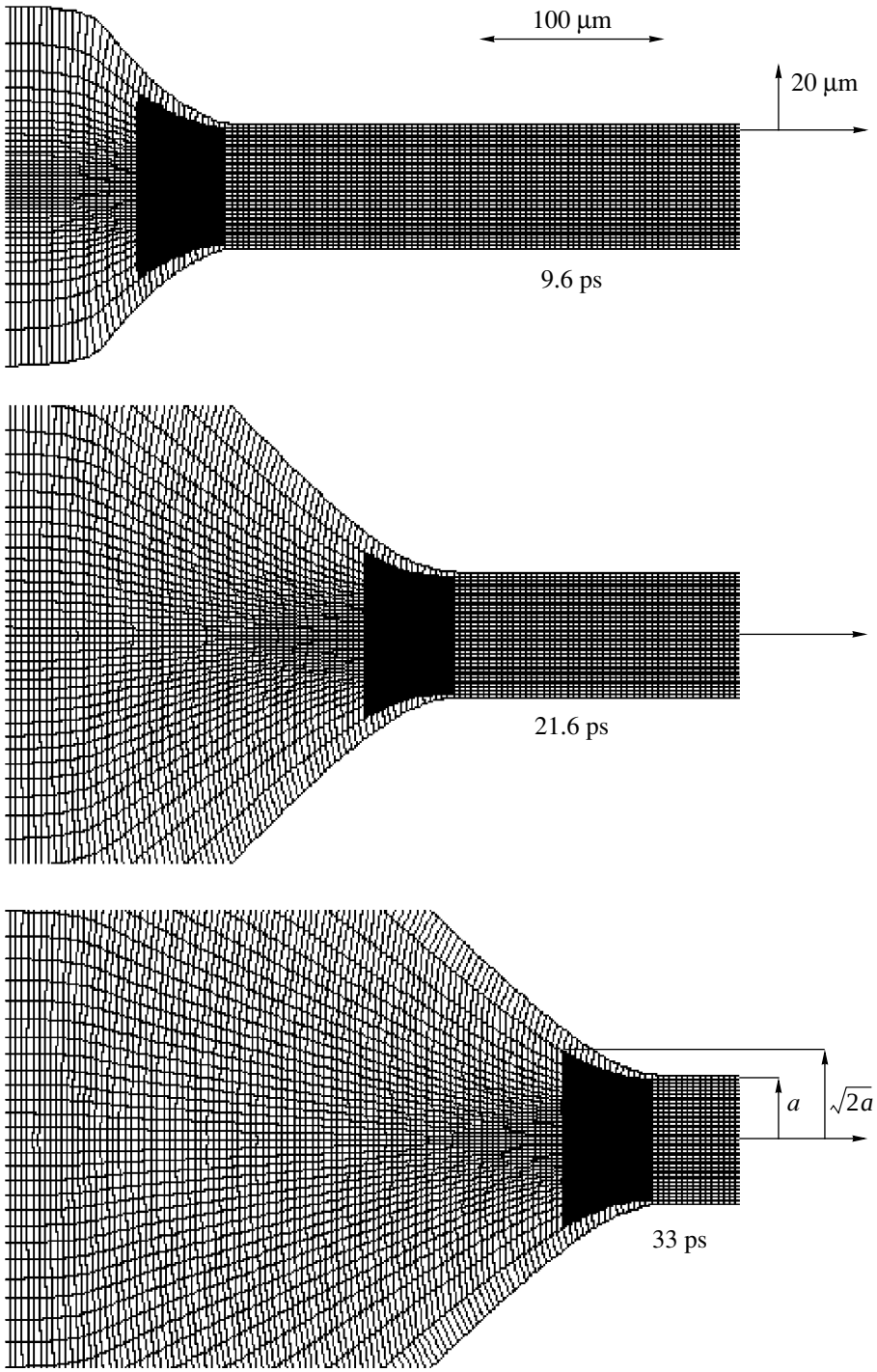

Fig. 16. The Lagrangian grid corresponding to Fig. 4. The slug with $T > 20$ keV remains almost invariant in form and volume.

and

$$\eta = \frac{\chi_\alpha}{\chi_e} = 10c\alpha_i^{y-0.5-0.5u}, \qquad \text{(A2.3)}$$

from which follows (put $c = 0.1$) that $\chi_\alpha > \chi_e$ in the interval from 8 keV to about 148 keV. The $\eta_{max} \simeq 3.6$ at $T = 30$ keV. The total χ is

$$\chi = \chi_\alpha + \chi_e = \chi_\alpha(1 + \eta^{-1}). \qquad \text{(A2.4)}$$

Given the form of χ_α, which is a steep function of T, we shall divide the region of $T(z)$ into two portions: the

first between T_1 and $T_\delta = T_1/e$ with a relatively flat $T(z)$ distribution and the second between T_δ and T' with a rapid fall of $T(z)$. In order to get a detonation wave, we will require that the first portion gets enough energy during a time t to raise the temperature from T_δ to T_1 (the hot plate propagates from $z = 0$ to $z = \delta$).

The time t then follows from

$$3nk(T_1 - T_\delta) < \frac{1}{4}n^2\langle\sigma v\rangle Q_\alpha t,$$

which for $T_1 \gg T_\delta$ gives

$$t \geq 6\times 10^{-9}\frac{n_s}{n}\alpha_1^{1-y}. \qquad \text{(A2.5)}$$

During this time, the $T(z)$ distribution in the second portion creates a new δ. Substituting (A2.5) into (A2.1), we obtain for the speed of the detonation heat wave v_h

$$v_h = \frac{\varepsilon\delta}{t} = \varepsilon\sqrt{\frac{2\chi_\alpha(1+\eta^{-1})}{1.8k\times 10^{-8}n_s\alpha_i^{1-y}}}, \qquad \text{(A2.6)}$$

where $\varepsilon < 1$ is a coefficient that compounds the uncertainties concerning the correct value of $\langle x\rangle$. We have for $c = 0.1$

$$v_h = 1.26\times 10^8\varepsilon\alpha_1^{y+0.5-1.5u}\sqrt{1+\eta^{-1}} \qquad \text{(A2.6a)}$$

For example, if $\alpha_1 = 9$ and $\varepsilon = 0.8$, then $v_h = 10.5 \times 10^8$ cm/s.

APPENDIX 3

α-Heat Conductivity

The use of an α heat conductivity χ_α instead of a more accurate α diffusion method is justified by

(a) the relative simplicity in its use in numerical simulations where nonlocal fusion energy deposition dominates and

(b) the many factors that invalidate the use of the α-diffusion calculation, such as the presence of magnetic fields and the electric α-boundary layer due to sharp density gradients.

The derivation of χ_α can be based on the energy transport by the forward (in the sense of $-dT/dx$) and backward α-stream, which in simple form is written as

$$-\chi_\alpha\frac{dT_i}{dx} = \dot{q}_\alpha - \dot{q}'_\alpha, \qquad \text{(A3.1)}$$

where (for n = const)

$$\dot{q}_\alpha = g\lambda_\alpha\frac{1}{4}n^2\langle\sigma v\rangle Q_\alpha,$$

$$\dot{q}'_\alpha = g\lambda'_\alpha\frac{1}{4}n^2\langle\sigma v\rangle' Q_\alpha.$$

Let us approximate $dT_i/dx \sim \dfrac{\Delta T_i}{\frac{1}{2}\langle\lambda\rangle_\alpha}$ and $\langle\lambda\rangle_\alpha = \varepsilon'\lambda'_{\alpha'}$.

Using the approximation $\langle\sigma v\rangle = 10^{-16}\alpha_i^y$, $y = 3/\sqrt{\alpha_i}$, and $\lambda_\alpha \simeq 10^{12}\dfrac{T_e^{3/2}}{n\Lambda}$, we obtain

$$\chi_\alpha = \frac{0.35\varepsilon'}{\Lambda\Lambda'}10^{18}\left(\frac{T'_e}{T_e}\right)^{3/2}\left(\frac{T_e}{T_i}\right)^3\left(\frac{3}{2}+y\right)\alpha_i^{y+2}.$$

We shall approximate $T_i/T_e = \alpha_i^u$, $u = 0.2\alpha_i^{1/4}$, and $\left(\frac{3}{2}+y\right)\frac{0.35\varepsilon'}{\Lambda'} \sim 0.2$. Consequently,

$$\chi_\alpha \simeq \frac{2\times 10^{17}}{\Lambda}\left(\frac{T'_e}{T_e}\right)^{3/2}\alpha^{y+2-3u}. \qquad \text{(A3.2)}$$

This is a very rough approximation and breaks down when $dT_i/dx \gg \dfrac{\Delta T_i}{\frac{1}{2}\langle\lambda\rangle}$ and also when $v_h > (v_\alpha)_{\max}$ in (A2.6).

The expression (A3.2), used in Appendix 2 in the form of $\chi_\alpha = 10^{15}\alpha_i^{y+2-3u}$, is very nearly the same as that of Sokolov [19], whose article on fusion heat waves in D–T describes them as "weak detonation waves," clearly seen in our numerical simulations.

In a uniform magnetic field B in which the α-particle Larmor radius is small, $\rho_\alpha \ll \lambda_\alpha$, the heat conductivity χ'_α will be cut down by $\left(\dfrac{\rho_\alpha}{\lambda_\alpha}\right)^2$. However, in a nonuniform B, the α-ion will drift with a drift velocity u_α and, therefore, the mean ion displacement between its birth and thermalization will be $\lambda_\alpha\dfrac{u_\alpha}{\langle v_\alpha\rangle}$, where $\langle v_\alpha\rangle \approx 10^9$ cm/s. It follows that

$$\chi'_\alpha = \chi_\alpha\left[1+\left(\frac{\langle v_\alpha\rangle}{u_\alpha}\right)^2\right]^{-1}. \qquad \text{(A3.3)}$$

REFERENCES

1. V. V. Vikhrev and G. A. Rozanova, Fiz. Plazmy **19**, 79 (1993) [Plasma Phys. Rep. **19**, 40 (1993)].
2. J. G. Linhart, in *Proceedings of Workshop on Plasma Physics, Pichl, 1993*, p. 284; J. G. Linhart, in *Proceedings of 3rd D Z-Pinch Conference, London, 1993*, p. 664; J. G. Linhart, Nuovo Cimento D **16D**, 281 (1994).
3. V. V. Neudachin and P. V. Sasorov, Nucl. Fusion **33**, 475 (1993).
4. J. G. Linhart, Nuovo Cimento A **106A**, 1949 (1993).

5. M. D. Churazov and B. Yu. Sharkov, Fusion Engin. Desing **32–33**, 577 (1996).
6. M. M. Basko, Nucl. Fusion **30**, 2443 (1990).
7. G. H. Miley, in *Laser Interaction and Related Plasma Phenomena* (Plenum, New York, 1981), Vol. 5, p. 313.
8. G. H. Miley *et al.*, in *Laser Interaction and Related Plasma Phenomena* (Plenum, New York, 1982), Vol. 6, p. 1049.
9. J. G. Linhart, Nucl. Fusion **10**, 211 (1970).
10. M. Tabak, J. Hammer, M. E. Glinsky, *et al.*, Phys. Plasmas **1**, 1626 (1994).
11. A. Caruso and V. A. Pais, Nucl. Fusion **36**, 745 (1996).
12. S. Atzeni and M. L. Ciampi, Nucl. Fusion **37**, 1665 (1997).
13. T. A. Melhorn, IEEE Trans. Plasma Sci. **25**, 1336 (1997).
14. M. S. Chu, Phys. Fluids **15**, 413 (1972).
15. J. G. Linhart, Plasma (Warsaw) **97**, 11 (1997).
16. J. G. Linhart and L. Bilbao, Nucl. Fusion (in press).
17. E. N. Avrorin, A. A. Bunatyan, A. D. Gadzhiev, *et al.*, Fiz. Plazmy **10**, 514 (1984) [Sov. J. Plasma Phys. **10**, 298 (1984)].
18. S. Y. Guskov and V. Rozanov, *Nuclear Fusion by Inertial Confinement* (CRC, Boca Ratón, Fl, 1993), p. 310.
19. I. V. Sokolov, Zh. Éksp. Teor. Fiz. **100**, 173 (1991) [Sov. Phys. JETP **73**, 95 (1991)].

Plasma Physics Reports, Vol. 26, No. 3, 2000, pp. 219–224. Translated from Fizika Plazmy, Vol. 26, No. 3, 2000, pp. 238–243.

PLASMA DYNAMICS

One-Dimensional Hydrodynamic Model of the Atom and Ion Dynamics in a Stationary Plasma Thruster

A. I. Morozov* and V. V. Savel'ev**

**Nuclear Fusion Institute, Russian Research Centre Kurchatov Institute, pl. Kurchatova 1, Moscow, 123182 Russia*

***Keldysh Institute of Applied Mathematics, Russian Academy of Sciences, Miusskaya pl. 4, Moscow, 125047 Russia*

Received March 4, 1999

Abstract—A one-dimensional hydrodynamic model of the atom, ion, and electron dynamics in the channel of a stationary plasma thruster is developed. The relevant set of integrodifferential equations is derived and investigated both analytically (steady-state solutions) and numerically (dynamic regimes). It is shown that adjusting only one parameter (the channel resistivity) makes it possible to achieve a good agreement between the calculated global parameters and experimental data. The general features of oscillations revealed with the help of the model are also found to agree fairly well with the experiment. © *2000 MAIK "Nauka/Interperiodica".*

1. INTRODUCTION

The rather specific features of the processes occurring in a stationary plasma thruster (SPT)[1] stem from the strong interaction between the plasma electrons and the dielectric walls of the channel. This interaction governs, to a large extent, the electron distribution function (EDF) as well as electron transport along the channel (the conductivity of the wall plasma), and thereby the electric field distribution, and influences the ionization rate and the rate at which the atoms and ions are excited. The electron kinetics, in turn, is governed by the rate coefficients for the secondary electron emission from the walls, the evolution of Debye sheaths and their parameters, and the characteristic features of the main conductivity mechanism—the conductivity of the wall plasma.

The processes in the SPT channel can be described systematically only by using kinetic models for atoms, ions, and electrons. However, such a self-consistent description seems to be too sophisticated at present. That is why, in some papers [4, 5], the ion kinetics was investigated against the prescribed electron background and, in other papers [6, 7], the electron kinetics was treated against the ion background. However, attempts were also made to study the ion and electron dynamics self-consistently, but in the hydrodynamic (or, at most, hybrid) approximation under the assumption that the processes are steady and, in some cases, with allowance for linear waves [1, 8]. To the best of our knowledge, we were the first to formulate a one-dimensional set of hydrodynamic equations aimed at describing the atom and ion dynamics self-consistently and including an integral equation for the discharge circuit [9].

[1] In early papers, such a system was referred to as a closed electron drift accelerator.

Here, the results of a thorough analysis of the model are presented and are compared with the experimental data in the range of working parameters of an SPT. We show, in particular, that the global parameters of the model are weakly sensitive to the presence (or absence) of oscillations. Surprisingly, a number of characteristics derived with our model turned out to agree with the relevant experimental data not only qualitatively but also quantitatively.

2. FORMULATION OF THE PROBLEM IN A ONE-DIMENSIONAL HYDRODYNAMIC APPROXIMATION

2.1. Basic Equations

It is clear that a complete self-consistent model of the processes in an SPT will be extremely involved and complicated. Consequently, it seems expedient to develop a series of comparatively simple models that describe different features of the processes, thereby reconstructing a true overall picture. Since no azimuthally asymmetric oscillations are excited in the course of SPT operation, models for the processes occurring on the characteristic time scales $\tau \geq \tau_0$ (where τ_0 is the ion transit time) are simpler to derive. Hence, we begin with a one-dimensional hydrodynamic model of the dynamics of electrons, atoms, and ions [9]. We restrict ourselves to considering only singly charged ions. However, even in this model, the processes in an SPT exhibit fairly complicated and nontrivial behavior.

We direct the x-axis along the channel so that $x = 0$ is the anode surface and the channel end $x = L$ is the cathode surface. The main parameters in our model are the ion density $n(x, t)$ (the electron density being the same by virtue of plasma quasineutrality), the ion

1063-780X/00/2603-0219$20.00 © 2000 MAIK "Nauka/Interperiodica"

velocity $V(x, t)$, the neutral density $n_a(x, t)$, and the electric current $J(t)$ in the system. The model set of equations consists of the ion continuity equation,

$$\frac{\partial n}{\partial t} + \frac{\partial nV}{\partial x} = \beta n n_a; \quad (1)$$

the equation of ion motion,

$$\frac{\partial nV}{\partial t} + \frac{\partial nV^2}{\partial x} = \frac{en}{M}E + \beta n n_a V_a; \quad (2)$$

Ohm's law (with allowance for the fact that the model is one-dimensional and the discharge current is independent of x),

$$E = \frac{J - enV}{\sigma(x)}; \quad (3)$$

the continuity equation for atoms,

$$\frac{\partial n_a}{\partial t} + V_a\frac{\partial n_a}{\partial x} = -\beta n n_a; \quad (4)$$

and the equation for the electric circuit,

$$L_c\frac{dJ}{dt} + RJ + \int_0^L E dx = U_0. \quad (5)$$

In (5), U_0 is the emf of the power supply; in (4), V_a = const > 0 is the atom velocity; and, in (5), L_c is the inductance of a circuit and R is its resistance.

The right-hand side of (1) describes electron impact ionization with the ionization rate β (we assume that $\beta \equiv$ const). In (3), the model plasma conductivity $\sigma(x)$ depends only on the transverse magnetic field, which is considered a prescribed parameter:[2]

$$\sigma(x) = \sigma_0\left(\frac{H_0}{H(x)}\right)^2, \quad \sigma_0 = \text{const}, \quad H_0 = \text{const}, \quad (6)$$

where H_0 is the magnetic field at the anode surface and $H(x)$ is the profile of the transverse magnetic field.

Equations (1)–(5) are investigated under fairly arbitrary initial conditions and are supplemented with the following time-independent boundary conditions at the anode surface $x = 0$:

$$n(0, t) = n_0, \quad n_a(0, t) = n_{a0}, \quad V(0, t) = V_0 > 0. \quad (7)$$

For convenience of further analysis, we switch to new units of measurement. We introduce the length unit L (the channel length); the density unit n_{a0}; the unit of the electric field $E_0 = U_0/L$; the velocity unit V_0; the time unit $t_0 = L/V_0$; and the unit of the electric current $I_0 = U_0/R_{ch}$, where $R_{ch} = L/\sigma_0$ is the resistance of a channel with a unit cross-sectional area $S = 1$ cm^2. In these units, equations (1)–(5) with the same notation for the main parameters reduce to

$$\frac{\partial n}{\partial t} + \frac{\partial nV}{\partial x} = \nu n n_a,$$

$$\frac{\partial nV}{\partial t} + \frac{\partial nV^2}{\partial x} = \mu n E + \nu n n_a V_a,$$

$$E = h^2(x)(J - \chi n V), \quad (8)$$

$$\frac{\partial n_a}{\partial t} + V_a\frac{\partial n_a}{\partial x} = -\nu n n_a,$$

$$l\frac{dJ}{dt} + rJ + \int_0^1 E dx = 1$$

and the boundary conditions (7) become

$$n(0, t) = n_0, \quad n_a(0, t) = 1, \quad V(0, t) = 1. \quad (9)$$

The main dimensionless parameters are

$$\mu = \frac{eU_0}{MV_0^2}, \quad \nu = \frac{\beta n_{a0} L}{V_0}, \quad \chi = \frac{en_{a0}V_0R_{ch}}{U_0},$$
$$l = \frac{L_cV_0}{LR_{ch}}, \quad r = \frac{R}{R_{ch}} \quad (10)$$

and the magnetic field is taken to be

$$h(x) = h_0 + (1 - h_0)x^2, \quad h_0 = H(0)/H_0. \quad (11)$$

The boundary-value problem for equations (8), which contain a nonlocal term, is highly nonlinear and involves a number of parameters. Presumably, the problem can be investigated more or less completely only by solving equations (8) numerically using computer codes.

2.2. Specifying the Model Parameters

We consider a practically important range of the SPT parameters, such that the mass flow rate is $\dot{m}$ = 2–4 mg/s and the discharge voltage is U_0 = 200–400 V, the working gas being Xe.

Let us estimate the main dimensionless parameters in (10) assuming that $\dot{m}$ = 3 mg/s. For a channel with a cross-sectional area of about 25 cm^2, the atom density at the anode is $n_{a0} \simeq 3 \times 10^{13}$ cm^{-3} and the atom velocity near the anode is $V_a \simeq 2 \times 10^4$ cm/s. We set the ion velocity near the anode $V_0 \simeq 2 \times 10^5$ cm/s, in which case the ion energy is about 3 eV. For a channel as long as $L \simeq 3$ cm, we obtain $t_0 \simeq 15$ μs. For β, we adopt the value $\beta \simeq 5 \times 10^{-8}$ cm^3/s, which is characteristic of Xe at T_e = 15 eV. As a result, we arrive at the following estimates:

$$\mu = \frac{1}{6}U_0, \quad \nu = 20, \quad V_a = 0.1. \quad (12)$$

[2] Here, we use the condition $\omega_e\tau_e \gg 1$, which definitely holds in a real situation.

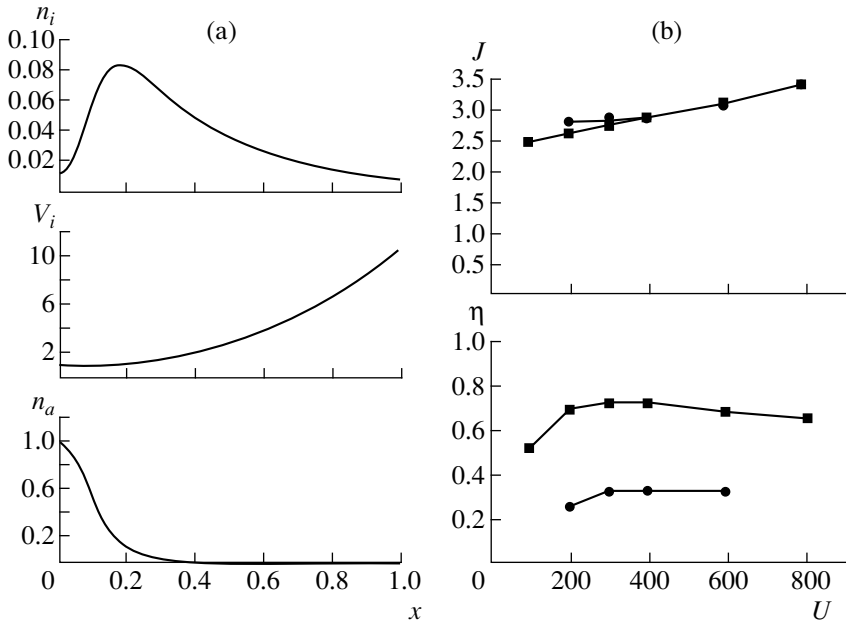

Fig. 1. (a) Spatial profiles of the ion density, ion velocity, and atom density in the steady-state regime and (b) *I–V* characteristic $J(U_p)$ and efficiency $\eta(U)$ for the time-independent (squares) and time-dependent (circles) models.

The channel resistivity R_{ch} and, accordingly, the parameter χ,

$$\chi = 0.9\frac{R_{ch}}{U_0}, \quad [R_{ch}] = \Omega\ \text{cm}^2 \tag{13}$$

(here, R_{ch} is in $\Omega\ \text{cm}^2$), are the most difficult to estimate. The resistivity R_{ch} can be evaluated as follows. We find such a value of R_{ch} for which the time-independent model (see below) gives the net discharge current $J = 3$ A, the discharge voltage being $U_p = 300$ V. Our calculations showed that this requirement is satisfied by $R_{ch} \simeq 8 \times 10^4\ \Omega\ \text{cm}^2$, so that we have

$$\chi = 7 \times 10^4 / U_0. \tag{14}$$

The parameters l, r, and h_0 can be chosen from the experiment,

$$l \simeq 10^{-2}, \quad r \simeq 10^{-3}, \quad h_0 = 0.1. \tag{15}$$

3. RESULTS OF SIMULATIONS WITH A HYDRODYNAMIC MODEL

3.1. Time-Independent Model

First, we set $\partial/\partial t = 0$ in order to analyze solutions to the time-independent equations (8), which now become

$$\frac{dnV}{dx} = \nu n n_a, \quad \frac{dn_aV_a}{dx} = -\nu n n_a, \tag{16a}$$

$$\frac{dnV^2}{dx} = \mu n h^2(x)(J - \chi nV) + \nu n n_a V_a, \tag{16b}$$

$$(r + r_0)J - \chi\int_0^1 h^2(x) nV dx = 1, \quad r_0 = \int_0^1 h^2(x)dx \tag{16c}$$

and adopt the boundary conditions (7). We solve the problem over the interval $0 \le x \le 1$. Equations (16) obviously have the first integral $nV + n_aV_a = n_0V_0 + V_a$, which allows us to eliminate n_a. Since equation (16c) contains a nonlocal term, equations (16) can be treated as an eigenvalue problem. Without going into mathematical detail, we only note that, in the parameter range under consideration, the problem possesses a unique solution.

Simulations carried out in the range 200–400 V gave the following results. The atoms are ionized with the highest rate at $U_0 = 200$ V. The ion velocity at the exit from the channel increases with U_0, and, at $U_0 = 400$ V, it becomes as high as $10V_0$ (2×10^6 cm/s). Figure 1a illustrates representative profiles of n, V, and n_a computed for $U_0 = 400$ V and $\dot{m} = 3$ mg/s.

The efficiency η of the system can be introduced as

$$\eta = \frac{\langle nV^2\rangle_{X=L}^2}{2n_{a0}V_aU_0\langle J\rangle} = \frac{1}{2}\frac{\chi}{\mu V_a}\frac{\langle nV^2\rangle_{X=1}}{\langle J\rangle}, \tag{17}$$

where the angular brackets stand for the time-averaged quantities (obviously, such averaging is not required in solving the time-independent problem). Note that the efficiency η is often evaluated using the voltage $U_p = \int E\,dx$ across the channel instead of U_0; this approach

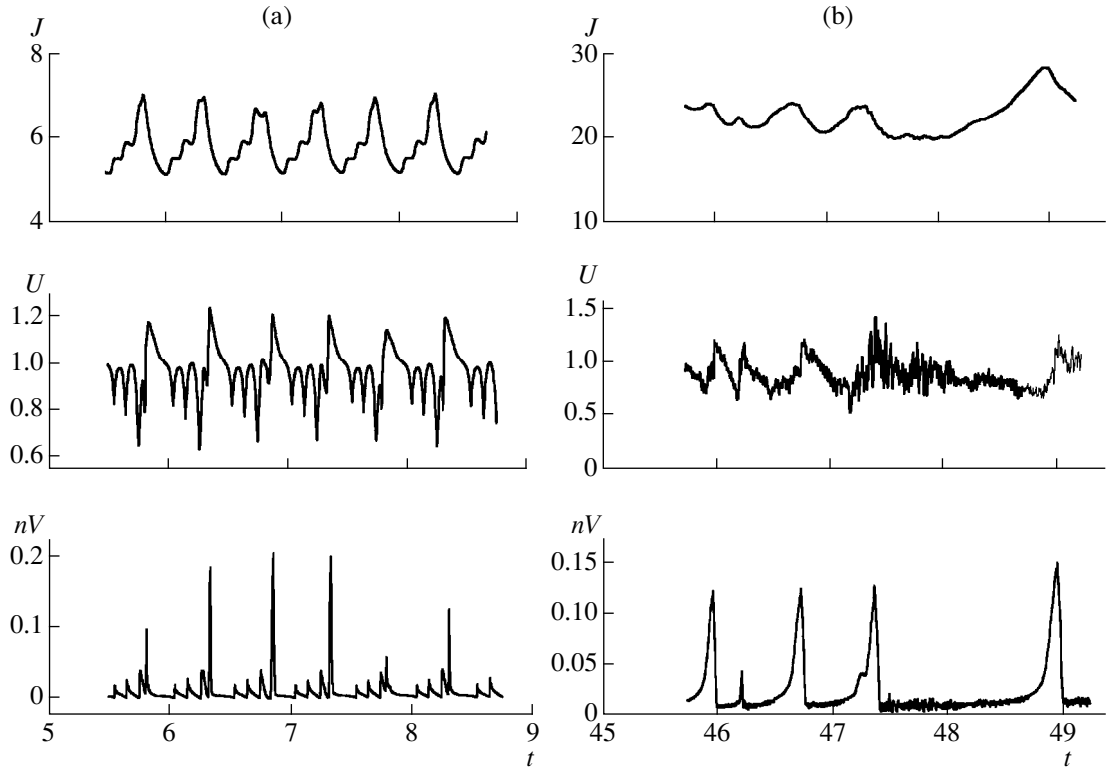

Fig. 2. Time evolutions $J(t)$, $U_p(t)$, and $nV(t, x = 1)$ in (a) the periodic regime and (b) the aperiodic (stochastic) regime for $\dot{m} = 3$ mg/s and $U_0 = 400$ V.

yields a somewhat overestimated efficiency because $U_p \le U_0$.

Figure 1b shows the current–voltage (I–V) characteristic $J(U_0)$ and the efficiency $\eta(U_0)$ calculated from equations (16) in the range $100 < U_0 < 800$ V. The I–V characteristic is seen to be nearly straight. The efficiency reaches its maximum $\eta_{max} = 0.72$ at $U_0 = 350$ V, gradually decreases as U_0 grows, and falls off sharply as the voltage decreases. Such behavior of $\eta(U_0)$ is confirmed by experiments. The maximum efficiency computed with the SPT-ATON model [3] was as high as $\eta_{max} \approx 67\%$.

As an example, we present the simplest analytic solutions to equations (16). For a fully ionized plasma, $\nu = 0$, and a uniform magnetic field, $h(x) \equiv 1$, we have $nV \equiv 1$, in which case it is easy to obtain

$$J = \frac{1+\chi}{1+r}, \quad E = \frac{1-r\chi}{1+r}, \quad V = \sqrt{1 + 2\mu\frac{1-r\chi}{1+r}x}. \quad (18)$$

We can see that the solutions can be divided into three different groups: (i) for $r\chi < 1$, the velocity is monotonically decreasing and the density is decreasing; (ii) for $r\chi = 1$, they are both constant, $V \equiv n \equiv 1$; and (iii) for $r\chi > 1$, the velocity is monotonically decreasing, while the density is increasing. At the point $x^* = (1 + r)/2(r\chi - 1)\mu$, we have $V = 0$ and $n = \infty$. In the range $x^* < 1$, the boundary-value problem has no solutions. In the general case, the situation is qualitatively the same.

3.2. Unsteady Regimes

In order to analyze the stability of the steady solutions derived above, we can regard them as initial conditions for the time-dependent equations (8). Our simulations performed in a fairly broad parameter range revealed the following picture. Varying the channel resistivity and fixing the remaining parameters, we inferred the existence of a steady stable solution in the range of sufficiently low χ values. Increasing the channel resistivity, we found that, at a certain value of χ, this solution became unstable and a periodic solution appeared (Fig. 2a). A further increase in χ resulted in the appearance of solutions describing unsteady aperiodic ("stochastic") regimes (Fig. 2b). Also, our simulations showed that the time evolutions of the plasma parameters are strongly sensitive to small variations of the input parameters. This feature agrees well with the experimentally established fact that even a slight variation of the experimental parameters makes it impossible to reproduce oscillations. We found that, in the parameter range under consideration, which is of much practical interest, all of the steady solutions derived above are unstable. However, this does not mean that the steady solutions are physically meaningless,

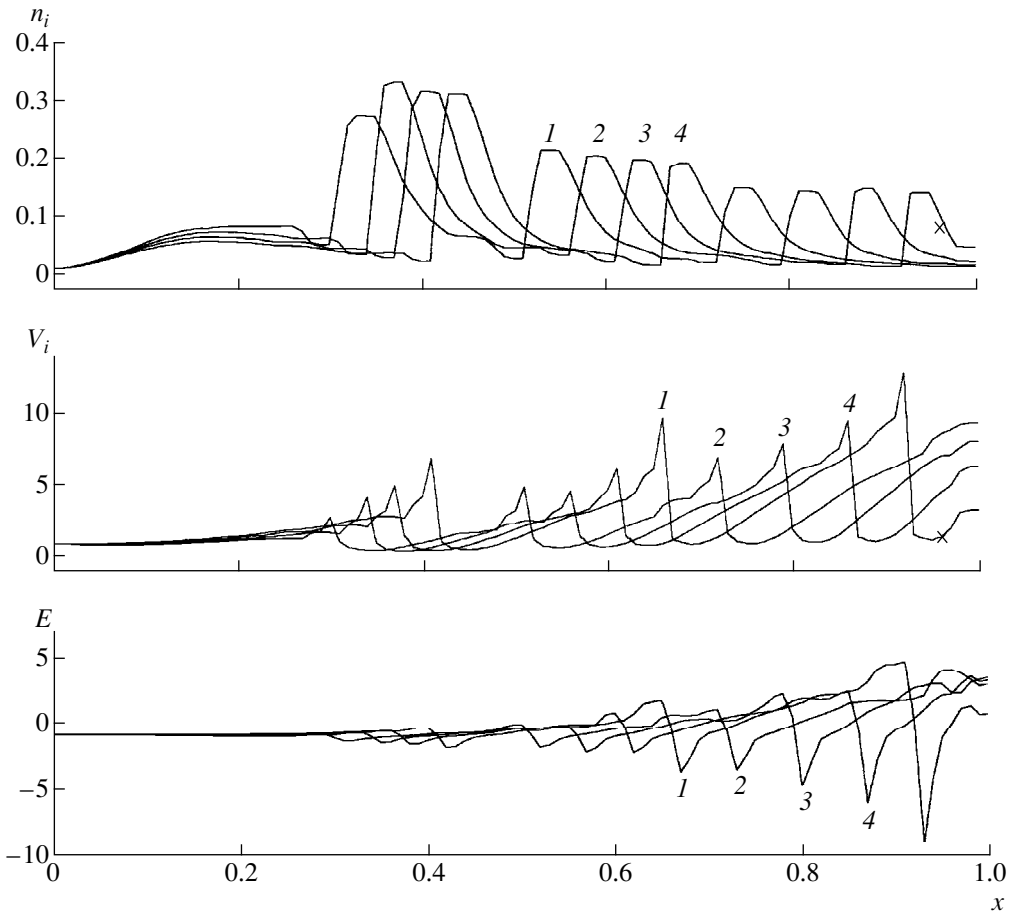

Fig. 3. Spatial profiles of the ion density, ion velocity, and electric field for $\dot{m}$ = 3 mg/s and U_0 = 400 V at different times t = (*1*) 41.4, (*2*) 41.6, (*3*) 41.8, and (*4*) 41.9.

because they may be stable in other parameter ranges. Moreover, our simulations of unsteady regimes showed that the evolution of a number of time-averaged quantities is qualitatively the same as their behavior in steady-state regimes.

Of considerable practical interest is also the case with fixed parameters, except for μ and χ, which only satisfy the requirement $\mu\chi$ = const. Treating this case, we analyze how the discharge voltage U_0 affects the properties of the model solutions. The relevant series of simulations was conducted with equations (8) in the range $200 < U_0 < 600$ V.

Figure 2b shows time evolutions of the discharge current $J(t)$, the voltage $U_p(t)$ across the channel, and the ion density at the exit from the channel (x = 1) for U_0 = 400 V, the unit time interval being t_0 = 15 μs. Simulations carried out for other voltages showed that the main (low-frequency) oscillation period τ_0 increases with U_0: for U_0 = 200 V, we have $\tau_0 \simeq 170$ μs and, for U_0 = 600 V, we have $\tau_0 \simeq 45$ μs. Time evolutions of the voltage across the channel also provide evidence that there are high-frequency oscillations occurring on a characteristic time scale τ_h of about several microseconds (i.e., about the ion transit time). Low-frequency oscillations are presumably associated with ionization oscillations, in which case the modulation depth of the plasma flow parameters amounts to 100%.

It is of interest to compare the *I–V* characteristic and the efficiency calculated with a time-independent model with those evaluated in solving the time-dependent problem. Figure 1b illustrates the time-averaged discharge current $\langle J \rangle$ and efficiency η as functions of U_0. As can be seen, the discharge currents in the dynamics regimes are somewhat higher. The efficiency in the unsteady regime is lower than that in the steady-state regime and exhibits qualitatively the same behavior.

3.3. Oscillation Dynamics

Let us consider in more detail the results of calculating the transit waves (see below) by using a one-dimensional hydrodynamic model. Since the nature of these oscillations remains qualitatively the same in the presence and absence of ionization, we restrict ourselves to

examining the case with realistic parameters and with allowance for ionization ($\dot{m}$ = 3 mg/s, U_0 = 400 V).

Figure 3 shows profiles of the quantities n, V, and E along the channel axis at different times. We can see higher density bunches, the related dips in the velocity, and the related sites where the electric field decelerates the ions. We can see that the high-density bunches propagate along the channel; initially, their shapes are essentially unchanged, but then the maximum bunch density is seen to decrease. The bunches originate mainly near the outer edge of the ionization front (on the side facing the channel end) and grow to their maximum density on a time scale too short for them to propagate over a significant distance. Three bunches are usually observed to propagate in the channel, but situations with one or two bunches are also possible (a solitary bunch may also originate in the middle of the channel).

Using the above parameter values, we can estimate the dimensionless propagation velocity V_b of the bunches: $V_b \sim 0.2$–0.4. On the other hand, the time-averaged velocity (starting from the ionization front) is $\langle V_i \rangle \sim 2$, so that the ion transit time equals $\tau_0 \sim 0.5$. From Fig. 3, we can estimate the distance between the bunches as $l_b \sim 0.2$; consequently, the interval τ_b between the times at which two successive bunches reach the channel end is $\tau_b \sim \tau_0$. This indicates that the term "transit wave" reflects the repetition rate of the bunches rather than the time required for them to traverse the channel. The bunches behave as if they were impenetrable. The velocity of the ions that have just entered the bunches falls off, while the velocity of the ions that have just escaped from the bunches increases. The propagation velocity of the bunches is close to that of the ions forming the bunches.

4. CONCLUSION

In the Introduction, we pointed out the strong impact of the processes occurring near the channel walls on the SPT operation. The results obtained with our simple one-dimensional model, which is phenomenological in essence, show that numerous complicated processes in an SPT can be described in a unified fashion by adjusting only one parameter and that it is possible to achieve not only qualitative but also fairly good quantitative agreement with the experimental data. This result appears to be somewhat surprising, thereby necessitating a detailed theoretical analysis aimed at understanding the reasons for such a good agreement between theory and experiment.

ACKNOWLEDGMENTS

We are grateful to A.I. Bugrova, A.V. Desyatskov, A.S. Lipatov, and V.K. Kharchevnikov for encouraging this work and valuable remarks. This work was supported in part by the Russian Foundation for Basic Research and the SEP Company (France).

REFERENCES

1. A. I. Morozov, in *Plasma Accelerators*, Ed. by L. A. Artsimovich (Mashinostroenie, Moscow, 1973), p. 85.
2. A. I. Bugrova and A. I. Morozov, in *Ion Injectors and Plasma Accelerators*, Ed. by A. I. Morozov and N. N. Semashko (Énergoatomizdat, Moscow, 1990), p. 42.
3. A. I. Bugrova, A. V. Desyatskov, A. I. Morozov, *et al.*, Fiz. Plazmy **23**, 635 (1997) [Plasma Phys. Rep. **23**, 587 (1997)].
4. A. I. Morozov and I. V. Melikov, Zh. Tekh. Fiz. **44**, 544 (1974) [Sov. Phys. Tech. Phys. **19**, 340 (1974)].
5. Yu. A. Ermakov, in *Proceedings of Joint Meeting on Electric Propulsion, Moscow, 1995*, p. 1204.
6. A. I. Morozov, Prikl. Mat. Teor. Fiz. **3**, 19 (1968).
7. A. I. Morozov and V. V. Savel'ev, Fiz. Plazmy **21**, 970 (1995) [Plasma Phys. Rep. **21**, 917 (1995)].
8. S. A. Yakunin, Vestn. Mosk. Univ., Ser. 15: Vychisl. Mat. Kibern. **4**, 20 (1977).
9. A. I. Morozov and V. V. Savel'ev, in *Proceedings of 24th International Conference on Electric Propulsion, Moscow, 1995*, paper IEPS 95-161.

Translated by G. V. Shepekina

Plasma Physics Reports, Vol. 26, No. 3, 2000, pp. 225–230. Translated from Fizika Plazmy, Vol. 26, No. 3, 2000, pp. 244–249.

PLASMA DYNAMICS

Influence of Kinetic Effects on the Structure of an Ion Shock Wave in a Plasma

I. R. Smirnovskiĭ

Research Institute of Radiophysics, St. Petersburg State University, Universitetskaya nab. 7/9, St. Petersburg, 199164 Russia

Received February 12, 1999; in final form, August 5, 1999

Abstract—The structure of a shock wave in an isotropic plasma is studied with allowance for charge separation and a self-consistent electric field. © *2000 MAIK "Nauka/Interperiodica".*

1. INTRODUCTION

At present, a theory of the structure of a shock wave (SW) in a plasma has been developed that is based on the hyperbolic equations describing systems with dissipation. The equations of one-dimensional unsteady motion have the form [1]

$$A(u)\frac{\partial u}{\partial t} + B(u)\frac{\partial u}{\partial x} + C(u) + D(u)\frac{\partial^2 u}{\partial x^2} = 0, \qquad (1)$$

where u is a set of K independent gas-dynamic variables and the matrices A, B, C, and D have the dimensionality $K \times K$ and satisfy the familiar restrictions [2]. In particular, in a homogeneous plasma for which u = const, we have $C(u) = 0$. The set of hyperbolic equations for the k ($k < K$) parameters of a dissipationless flow can be derived from (1) by neglecting terms with second-order derivatives and expressing some of the components of the vector u in terms of the remaining components assuming that $C(u) \equiv 0$ over the entire flow. The parameter k is the number of hyperbolic undamped waves governing the formation of a discontinuity and its evolution. The front structure of an SW is formed by some dissipative, strongly damped waves.

In a two-temperature plasma, dissipative mechanisms can exist that are purely kinetic in nature. The formation of an SW can also be affected by wave dispersion. These effects cannot be taken into account in a model based on equations (1). However, according to [1, 3, 4], an SW in a plasma is similar to a conventional gas-dynamic SW in a gas.

Papers [5–7] provide a radically different understanding of the role played by kinetic effects in the formation of the structure of a strong SW in an isotropic plasma. Ledenev [5, 6] showed that the energy level characteristic of dissipation of the flow of ions reflected from the shock front may be high enough to satisfy the Hugoniot relations. In my recent paper [8], shock-front structures consistent with the analysis of [5, 6] were found for initially equilibrium, highly and weakly ionized collisional plasmas and a nonisothermal collisionless plasma. The results of the calculations carried out for a collisionless plasma [8] agree with the results obtained earlier by Bardakov *et al.* [9].

It is well known that the SW structure in a plasma is described by a larger number of independent variables in comparison with dissipationless flows on both sides of the front [1]. The electric field potential behind the shock front is governed by the front structure and cannot be expressed merely in terms of the SW velocity and the parameters characterizing the initial and final plasma states. According to the numerical estimate of Jaffrin and Probstein [3], the total amount by which the potential increases in a strong SW is $\Delta\Phi \simeq 2$, where $\Phi = e\varphi/T_e$, φ is the electric field potential; e is the electron charge; T is the temperature; and the subscripts e and i refer to electrons and ions, respectively. The potential grows preferentially in the "ion shock wave" on a spatial scale on the order of the ion mean free path l_i.

The ion SW results from the excitation of ion acoustic waves and, in the long-wavelength approximation, is described by the hyperbolic equations of isothermal hydrodynamics [10]. The hyperbolic equations are derived from kinetic equations by neglecting collision integrals and can be used to approximately describe the ion SW structure, because the shock front thickness is on the order of $\sim l_i$. The evolution of such ion acoustic waves is well studied. In the compression regions, the wave front becomes progressively steeper until the front thickness equals the Debye radius r_D. The dispersion associated with charge separation in the plasma prevents further steepening of the wave front and, consequently, wavebreaking; this process can be accompanied by the excitation of multistream flows [10].

Greywall [11] studied the influence of kinetic effects using the Mott–Smith method and neglecting charge separation. Here, we investigate the structure of an ion SW using the particle distribution functions that satisfy collisionless kinetic equations with a self-consistent electric field. As a result of dissipation, the kinetic energy of supersonic ions reflected from the potential barrier is transformed into the internal and

1063-780X/00/2603-0225$20.00

kinetic energies of the plasma and also into the energy of ion acoustic fluctuations.

2. FORMULATION OF THE KINETIC PROBLEM OF THE SW STRUCTURE

The boundary conditions for gas-dynamic variables at $+\infty$ and $-\infty$ reflect the fundamental conservation laws, which are independent of the character of dissipation. For a fully ionized isotropic plasma, we write these conditions (the Hugoniot relations) as [1]

$$N_2 M_2 = M_s,$$

$$N_2(M_2^2 + 1) = M_s^2(1 + M_{s0}^{-2}), \tag{2}$$

$$M_s^2 = (\gamma + 1)^2 M_{s0}^4 [2M_{s0}^2 + \gamma - 1]^{-1} [M_{s0}^2(\gamma - 1) + 2\gamma]^{-1},$$

where $M_{0,2} = v_{0,2}/V_{s2}$ is the Mach number, v is the plasma flow velocity in the wave frame, $M_{s0} = c/V_{s0}$ is the Mach number of an SW, c is the SW speed, $M_s = c/V_{s2}$, $V_s = \sqrt{(T_e + T_i)/m_i}$ is the ion acoustic speed, m is the mass, N is the density normalized to the background density n_0, and $\Delta = (v_{Te}/c)l_e$, $\gamma = \gamma_e = \gamma_i$ is the adiabatic power-law index. Here and below, the subscripts 0 and 2 refer, respectively, to the unperturbed quantities and the parameters characterizing the plasma state far behind the shock front, at distances much longer than the scale on which the electron thermal conductivity varies, $\Delta = (v_{Te}/c)l_e$.

Let us formulate the problem of the structure of a jump in the potential with allowance for the effective dissipation of the energy of the flow of reflected ions [see formulas (3)–(7) below].

From the particle and momentum flux conservation laws, we obtain the following relationships between the unperturbed fields and the first moments of the distribution functions of the incident and reflected ions in the so-called foot of the shock wave:

$$\begin{aligned} (N_f - N_r)M_f &= M_s', \\ (N_f + N_r)(M_f^2 + 1 + \beta/2) &= M_s'^2(1 + M_{s0}^{-2}), \end{aligned} \tag{3}$$

where $M_f = v_f/V_s'$, v_f is the velocity of the incident ions in the wave frame; $M_s' \equiv c/V_s'$, $V_s' = \sqrt{T_{e1}/m_i}$; the subscripts f and r stand for the fields of the flows of the incident ions and ions reflected from the potential barrier, respectively; and $\beta \equiv 2T_{i1}/T_{e1}$ is the parameter characterizing the degree to which the plasma in the vicinity of a potential jump is nonisothermal (here and below, T_{i1} and T_{e1} are the ion and electron temperatures in the vicinity of the jump).

We assume that, first, the dissipation of the energy of the flow of reflected ions acts exclusively to raise the particle temperatures (mainly, the electron temperature) and the electric field energy can be neglected and, second, the flow of reflected ions is decelerated on a sufficiently short time scale τ_p, much shorter than the time τ_{ei} over which the electron and ion temperatures are equalized (the time τ_p will be estimated below). Under these assumptions, the internal plasma energy in the vicinity of a potential jump can be described by the relationship

$$T_{e1} + T_{i1} = T_{e2} + T_{i2}. \tag{4}$$

On the other hand, the ions in the foot remain sufficiently cold to satisfy the conditions $v_{Te} \gg c \gg v_{Ti}$ (where v_T is the thermal velocity).

Poisson's equation for the potential Φ of a self-consistent electric field can be written as [9]

$$\begin{aligned} (d\Phi/d\xi)^2 &= -2U(\Phi), \\ -U(\Phi) &= \exp(\Phi) \\ &+ N_f \left(\int_{\sqrt{2(\Phi - \Phi_f)}}^{\sqrt{2(\Phi_A - \Phi_f)}} F(W)Q(W, \Phi, \Phi_f)\,dW \right. \\ &\left. + \int_{\sqrt{2(\Phi - \Phi_f)}}^{\infty} F(W)Q(W, \Phi, \Phi_f)dW \right) + C, \quad \xi < 0, \\ -U(\Phi) &= \exp(\Phi) \\ &+ N_f \int_{\sqrt{2(\Phi_A - \Phi_f)}}^{\infty} F(W)Q(W, \Phi, \Phi_f)dW + C, \quad \xi \geq 0, \end{aligned} \tag{5}$$

$$F(W) = \exp[-(W - M_f)^2/\beta]/\sqrt{\pi\beta},$$

$$W = \sqrt{(v/V_s')^2 + 2(\Phi - \Phi_f)},$$

$$Q(W, \Phi, \Phi_f) = W\sqrt{W^2 - 2(\Phi - \Phi_f)},$$

$$C = -N_f(M_f^2 + \beta/2) - \exp(\Phi_f) - N_f \int_0^{\sqrt{2(\Phi_A - \Phi_f)}} F(W)W^2 dW,$$

where $\xi = -(r - ct)/r_D$ and v is the particle velocity. The wave frame is oriented so that $\xi < 0$ ahead of the SW front. The peak value of the potential at $\xi = 0$ is denoted by Φ_A.

The functional N_r of the particle distribution functions is defined by [9]

$$N_r = N_f \int_0^{\sqrt{2(\Phi_A - \Phi_f)}} F(W)dW. \tag{6}$$

Since the spatial scale on which the fields in the foot vary is much longer than r_D, the quasineutrality condition

$$N_r + N_f = \exp(\Phi_f) \tag{7}$$

is satisfied. Let us show that jumps in the gas-dynamic variables can be explained in terms of the Hugoniot relations (2) with allowance for an SW formed as a result of dissipation of the energy of reflected ions.

3. APPROXIMATE EXPRESSIONS FOR THE PARAMETERS OF A SUPERSONIC ION SW

The definition of M_s' and relationship (4) yield the following expression for M_s:

$$M_s' = M_s\sqrt{1+\beta/2},$$

in which case β can be represented as

$$\beta = (M_s'/M_{s0})^2\beta_0(T_{i1}/T_{i0})/(1+\beta_0/2).$$

Consequently, if an SW is sufficiently strong ($M_{s0} \gg M_s$) and/or the initial ion-to-electron temperature ratio is small ($\beta_0 \ll 1$), then we can neglect the term with β in (3).

Behind the potential barrier, the fields experience regular oscillations caused by charge separation. We write out the relationships between the flow parameters N_1, M_1, and Φ_1 averaged over the regular oscillations and those characterizing the state in the foot:

$$N_1M_1 = (N_f - N_r)M_f,$$

$$N_1(1+M_1^2) = (N_f+N_r)(M_f^2+1), \tag{8}$$

$$M_1^2/2 + \Phi_1 = M_f^2/2 + \Phi_f,$$

where $N_1 = \exp(\Phi_1)$ by virtue of the quasineutrality condition. Thus, in the context of seeking only discontinuous solutions, we have reduced the exact problem of the front structure, (5) and (6), to approximate relationships (8).

At $\beta = 0$, we find from (3), (7), and (8)

$$N_1M_1 = M_s,$$

$$N_1(1+M_1^2) = M_s^2(1+M_{s0}^{-2}), \tag{9}$$

$$M_1^2 + 2\Phi_1 = M_s^2(1+M_{s0}^{-2})\exp(-\Phi_f) + 2\Phi_f - 1.$$

Using (9) and (2), we obtain the following set of equations for N_1 and M_1:

$$N_1M_1 = N_2M_2,$$
$$N_1(1+M_1^2) = N_2(1+M_2^2). \tag{10}$$

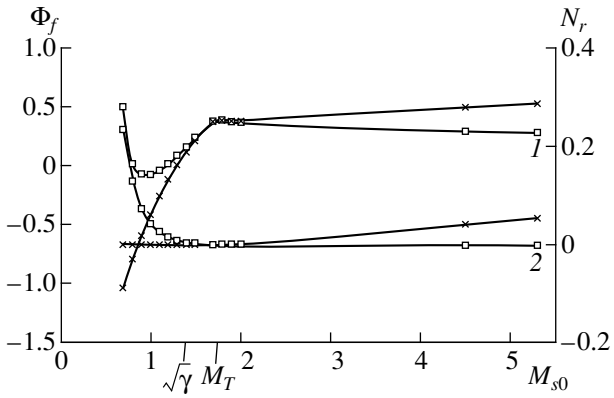

Fig. 1. (*1*) Electric field potential Φ_f and (*2*) density N_r of the reflected ions as functions of the Mach number M_{s0} for two types of ion SWs: (i) $N_r = 0$ (the computed points are marked by squares for $M_{s0} > M_T$ and by crosses for $M_{s0} < M_T$) and (ii) $N_r > 0$ (the computed points are marked by crosses for $M_{s0} > M_T$ and by squares for $M_{s0} < M_T$). The initial ion-to-electron temperature ratio is small ($\beta_0 \ll 1$), the adiabatic power-law index being $\gamma = 5/3$.

Generally, equations (10) have two solutions. The functions $\Phi_f(M_{s0})$ and $N_r(M_{s0})$ can be evaluated from (10), (2), and the last relationship in (9). Figure 1 shows both branches of $\Phi_f(M_{s0})$ and $M_r(M_{s0})$ for low values of M_{s0}.

The SW parameters are uniquely determined by the Mach number M_{s0} and are independent of the initial ion-to-electron temperature ratio. The latter feature is a consequence of neglecting the terms with $\beta \ll 1$.

From (2) and (10), we find the point of intersection of the curves, $M_{s0} = M_T \equiv \sqrt{(3\gamma-1)/(3-\gamma)}$. According to (3), at the intersection point, we have $N_r = 0$, $M_f = 1$, and $N_2 = N_f$, so that $\Phi_A = \Phi_f$. Consequently, at $M_{s0} \longrightarrow M_T$, equations (8) are identically satisfied and the internal discontinuity disappears.

For $M_{s0} > M_T$, we have $N_1 = N_2$, $M_1 = M_2$, and $N_r > 0$ along one branch and $N_r = 0$ along the other, and the boundary conditions (2) fail to hold. This case is very reminiscent of the jumps in the parameters of a weak viscous ion SW that is isothermal for electrons. Indeed, for $T_{e1} = T_{e2}$, equation (4) is approximately satisfied if the jump in the ion temperature is sufficiently small, i.e., if $M_{s0} \simeq M_T$ or if $T_{e2} \gg T_{i2}$ and $T_{e1} \gg T_{i1}$, which refers to the case of an initially nonisothermal plasma and a sufficiently weak SW (in the Appendix, we will show that the plasma behind the shock front remains nonisothermal). We do not consider here the exact boundary conditions for a gas-dynamic ion SW (see p. 75 in [1]).

In the range $\sqrt{\gamma} < M_{s0} < M_T$, the branch along which $N_r = 0$, $N_1 = N_2$, and $M_1 = M_2$ corresponds to a conventional gas-dynamic compression SW, whose front

structure is governed exclusively by electron heat conduction.

In the range $\sqrt{(\gamma-1)/2} < M_{s0} < M_T$, the inequalities $N_1 > N_2$, $M_1 < M_2$, and $N_r > 0$ hold along the other branch, in which case, according to the Hugoniot relations (2), a rarefaction SW forms. Such an SW can exist because the conditions of the Zemplen theorem are not satisfied in the plasma (see below). A rarefaction wave is excited on a spatial scale of about Δ, on which, however, the plasma density is nonmonotonic: in the leading part of the wave (on a scale much shorter than Δ), the plasma is compressed to a density $N_1 > 1 > N_2$ and, in the remaining part, the density decreases gradually to N_2.

A two-temperature plasma is not a conventional gas [2], because each thermodynamic variable depends not only on the remaining two variables but also on the spatial scale on which the process occurs. In fact, the equation of state $p \sim \rho^\gamma$ (where $p = p_e + p_i$ is the pressure and $\rho = \rho_e + \rho_i$ is the density) is valid only for waves with wavelengths longer than Δ. On spatial scales shorter than Δ, it is necessary to take into account two-fluid effects. For $T_e \gg T_i$, the equation of state is $p \sim \rho$ [10].

Ledenev [5, 6] was the first to suggest that an SW in an equilibrium plasma can form via dissipation of the energy of reflected ions, but instead of relationship (4), he used an approximate expression for the energy flux in the foot (the same approach was applied in my earlier paper [8]). Also, he did not justify the applicability of relationships (8) to a collisional plasma [6]. However, equations (8) were derived for a collisionless SW [9, 12] in the absence of regular oscillations behind a "collisionless shock" (an SW with the critical Mach number).

Since, for $M_{s0} > M_T$, the general relationships (2) in the discontinuity fail to hold along the branch where $N_r = 0$, Ledenev [5] concluded that, under conditions corresponding to high electron heat conductivity, there is no viscous jump in the density; i.e., the only possible solution is $N_1 \equiv N_2, M_1 \equiv M_2$, and $N_r > 0$. Velikovich and Liberman [1] rigorously analyzed equation (1) with allowance for adiabatic plasma compression in the heated region. They showed that the jumps in the gasdynamic variables within the internal discontinuity are related by formulas other than (2). In this case, the structure of the internal discontinuity is governed by ion viscosity.

In reality, two types of ion SWs can exist whose fronts are significantly different in structure.

Below, we determine the SW structure that satisfies the boundary conditions corresponding to a branch along which $N_r > 0$ holds (see Fig. 1). Such an SW can form on a short time scale $\tau_p \ll \tau_{ei}$.

4. CONDITION FOR THE FORMATION OF AN SW AND ELECTRON HEATING IN THE FOOT

We estimate the characteristic time τ_p during which the kinetic energy of a reflected ion decreases by a factor of e as a result of its interaction with neighboring particles. We consider a rarefied collisional plasma in which only the long-range Coulomb collisions are important. In this situation, the plasma parameter $g \equiv (nr_D^3)^{-1}$ satisfies the inequality

$$g > 32\pi(m_e/m_i)^{3/2}(M_s')^3. \tag{11}$$

Allowing for short-range Coulomb collisions between neighboring particles can only decrease the estimated time scale τ_p.

A particle loses its energy because of the spontaneous emission of longitudinal and transverse electromagnetic waves [10]. A long-range Coulomb collision event can be regarded as the emission of a plasmon by a plasma particle followed by the absorption of this plasmon by another particle. The change in the energy of a test particle due to such collisions is estimated as [10]

$$\left(\frac{dE}{dt}\right)_{e+i} = -\Lambda\frac{2Z^2e^2\omega_i^2}{2c}\left(\frac{1}{2\sqrt{2\pi}}\sqrt{\frac{m_e}{m_i}}8M_s'^3 + 1\right), \tag{12}$$

where Λ is the Coulomb logarithm, ω_i is the ion plasma frequency, Z is the ion charge number, and the speed of the reflected ion in the rest frame is approximately equal to $2c$. The first term on the right-hand side of (12) describes collisions with plasma electrons and the second term accounts for collisions with plasma ions.

Using (12) and the formula for τ_{ei} in [10],

$$\tau_{ei} = \frac{3\sqrt{\pi}}{2\sqrt{2}}\frac{m_i v_{Te}^3}{\Lambda\omega_e^2e^2} \tag{13}$$

we arrive at the desired estimate:

$$\frac{\tau_p}{\tau_{ei}} = \frac{4\sqrt{2}}{3\sqrt{\pi}}\frac{m_e}{m_i}\frac{M_s'^3}{Z^2} \ll 1. \tag{14}$$

Hence, the temperature distribution required for an SW to form has enough time to be established before the temperature relaxation process (which prevents the excitation of the SW) comes into play.

Formula (12) implies that, because of the scattering of reflected ions, the plasma electrons and ions are heated almost equally. On the other hand, it is well known that SWs preferentially heat the plasma electrons [13, 14].

Moses *et al.* [13] explained an increase in T_e in the foot of an SW near Jupiter as being due to weak electrostatic turbulence. However, as a practical matter, such an instability is a rare event.

The polarization mechanism for energy losses can significantly increase T_e via the interaction of electrons with superthermal electric field fluctuations. In fact, a test particle moving at a speed above the ion acoustic speed causes efficient excitation of ion acoustic waves, in which case the integrand in the initial expression for energy losses should formally contain one more pole. If the ion-to-electron temperature ratio is sufficiently small, $(T_e/T_i)^{3/2}\exp(-T_e/2T_i) < \sqrt{m_e/m_i}$, the contribution of this pole to energy losses is approximately equal to

$$\left(\frac{dE}{dt}\right)_s = -\frac{Z^2e^2\omega_i^2}{8v(1-V_s'^2/v^2)^2}, \quad (15)$$

where v is the velocity of a reflected ion. As v approaches V_s, the energy losses increase resonantly.

That stochastic longitudinal electric fields may be intense in the foot is justified experimentally [13, 14]. The effective temperature T_s of coherent ion acoustic fluctuations is governed by the flow parameters and can be fairly high, $T_s \gg T_e$. It is easy to see that the electron-heating time τ_s, which satisfies the equation $dT_e/dt = (T_s - T_e)/\tau_s$, is about equal to the electron–electron collision time.

In a dense plasma such that the inequality opposite to (11) holds, short-range Coulomb collisions between reflected ions and electrons are responsible for the preferential increase in T_e. Short-range collisions with ions become important in an even denser plasma.

5. SW STRUCTURE FORMED VIA THE DISSIPATION OF THE ENERGY OF REFLECTED IONS

Equations (2)–(7) constitute a closed set, in which equations (2)–(4), (6), and (7) implicitly define the following boundary condition for the first-order ordinary differential equation (5): $\Phi \longrightarrow \Phi_f$ as $\xi \longrightarrow -\infty$. With a prescribed Φ_f, equation (5) behind the SW front ($\xi > 0$) has a single periodic solution satisfying the matching condition at $\xi = 0$.

A similar problem for an initially equilibrium plasma was solved in [8] under the condition $T_{i1} \simeq T_{i0}$. Here, we are investigating N_r and Φ_f as functions of M_{s0} for different values of the parameter β_0 under the condition $T_{e1} \gg T_{i1}$, without assuming that the change in T_i is small.

From (5), we can derive the following transcendental equation for Φ_A:

$$U(\Phi_A) = 0. \quad (16)$$

The results of solving equations (3), (4), (6), and (16) numerically are illustrated in Fig. 2.

The plots of $\Phi_f(M_{s0})$ and $N_r(M_{s0})$ in Fig. 2 are close to the relevant branches in Fig. 1. The higher the parameter β_0, the worse the correlation is between the curves. For $\beta_0 > 10^{-2}$, the branch along which $\Phi_f < 0$ is absent in Fig. 2.

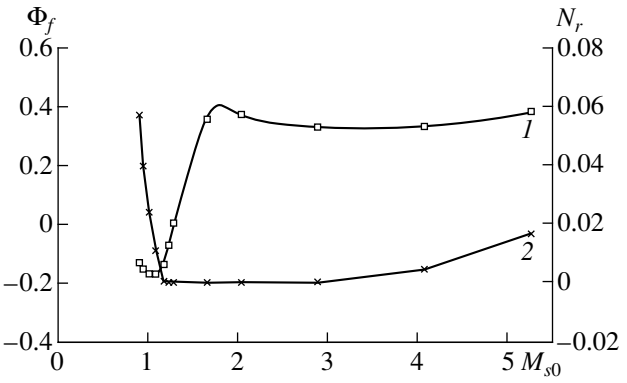

Fig. 2. Functions (*1*) $\Phi_f(M_{s0})$ and (*2*) $N_r(M_{s0})$ at $\beta_0 = 10^{-4}$ obtained by numerically solving the problem of the SW structure with a self-consistent electric field.

6. CONCLUSION

A qualitative agreement between the solutions to the conservation equations for hydrodynamic flows (Fig. 1) and the solutions to the problem of the front structure (Fig. 2) shows that the approach developed in Section 3 is justified. In other words, some of the SW parameters can be estimated neglecting the influence of the ion distribution function and the fine structure of the shock front.

In the limit $M_{s0} \longrightarrow 1$, an SW that forms via the dissipation of the energy of reflected ions cannot convert into a quasi-shock wave [10], which was studied in [9]. The reason is that these waves are different in nature. A collisionless SW is highly nonsteady, since its structure is characterized by a foot that is formed by the reflected ions and moves away from the shock front. This collisionless SW is also a dissipation-free wave, because the energy of reflected ions is not converted back into plasma energy. Consequently, the boundary conditions (2) cannot be satisfied, in particular, by virtue of the fact that the plasma velocity at infinity is nonzero.

In an initially nonisothermal plasma, an SW can form that has a continuous structure and whose energy is dissipated (due to the scattering of the flow of reflected ions) in such a manner that the boundary conditions (2) are satisfied in the range $M_{s0} > \sqrt{(\gamma-1)/2}$.

If the initial ion-to-electron temperature ratio is not too small, $\beta_0 > 10^{-1}$, then an SW that forms in such a plasma should be sufficiently intense, which agrees with the conclusions of [5, 6, 8]. A low-intensity SW can only be a gas-dynamic wave, which forms due to viscosity and heat conduction.

ACKNOWLEDGMENTS

I am grateful to V.A. Pavlov for fruitful discussions and valuable comments.

APPENDIX

It is clear that the state behind the front of an SW that forms in an initially equilibrium plasma is also equilibrium, although conditions (2) are formally satisfied for any β_2 and β_0. Greywall [4] asserted that, in an initially nonisothermal plasma ($T_{e0} \neq T_{i0}$), the plasma behind the shock front approaches an equilibrium state, $T_e \longrightarrow T_i$.

We will show that this assertion is wrong. In the heat balance equations, we must take into account the terms describing the nonisothermal nature of the plasma. From the electron heat balance equation [15], we obtain

$$\begin{aligned} N_e \frac{(T_{e2} - T_{i2})}{\tau_{ei2}} &= q_{e2}, \\ \frac{(T_{e0} - T_{i0})}{\tau_{ei0}} &= q_{e0}, \end{aligned} \tag{17}$$

where q is a source of particle heating. This boundary condition determines how the ion-to-electron temperature ratio changes across the shock front. Hence, the plasma behind the front should remain nonisothermal, $T_{e2} \neq T_{i2}$. Relations (2) should be supplemented with a condition similar to (17), which describes the change in the parameter β.

REFERENCES

1. A. L. Velikovich and M. A. Liberman, *Physics of Shock Waves in Gases and Plasmas* (Nauka, Moscow, 1987).
2. G. G. Chernyĭ, *Gas Dynamics* (Nauka, Moscow, 1988).
3. M. Y. Jaffrin and R. F. Probstein, Phys. Fluids **10**, 1658 (1964).
4. M. S. Greywall, Phys. Fluids **19**, 2046 (1976).
5. V. G. Ledenev, *Structure of Strong Shock Waves in a Plasma* (SIBIZMIR, Irkutsk, 1986), p. 10.
6. V. G. Ledenev, Prikl. Mekh. Tekh. Fiz. **2**, 17 (1990).
7. I. R. Smirnovskiĭ, Izv. Vyssh. Uchebn. Zaved., Radiofiz. **16**, 978 (1998) [Radiophys. Quantum Electron. **41**, 661 (1998)].
8. I. R. Smirnovskiĭ, Prikl. Mekh. Tekh. Fiz. **39** (3), 14 (1998) [J. Appl. Mech. Tech. Phys. **39**, 335 (1998)].
9. V. M. Bardakov, A. G. Morozov, and I. G. Shukhman, Fiz. Plazmy **1**, 955 (1975) [Sov. J. Plasma Phys. **1**, 521 (1975)].
10. *Plasma Electrodynamics*, Ed. by A. I. Akhiezer *et al.* (Pergamon, Oxford, 1975; Nauka, Moscow, 1974).
11. M. S. Greywall, Phys. Fluids **18**, 1439 (1975).
12. D. W. Forslund and J. P. Freidberg, Phys. Rev. Lett. **27**, 1189 (1971).
13. S. I. Moses, F. V. Coroniti, C. F. Kennel, and F. L. Scarf, Geophys. Res. Lett. **12**, 609 (1985).
14. M. A. Balikhin, N. L. Borodkova, O. D. Vaĭsberg, *et al.*, Fiz. Plazmy **14**, 1326 (1988) [Sov. J. Plasma Phys. **14**, 777 (1988)].
15. B. N. Gershman, L. M. Erukhimov, and Yu. Ya. Yashin, *Wave Phenomena in Ionospheric and Space Plasmas* (Nauka, Moscow, 1979), p. 105.

Translated by O. E. Khadin

Plasma Physics Reports, Vol. 26, No. 3, 2000, pp. 231–254. Translated from Fizika Plazmy, Vol. 26, No. 3, 2000, pp. 250–274.

PLASMA OSCILLATIONS AND WAVES

Present Status of the Theory of Relativistic Plasma Microwave Electronics

M. V. Kuzelev* and A. A. Rukhadze**

**Moscow State University of Publishing, ul. Pryanichnikova 2a, Moscow, 127500 Russia*

***Institute of General Physics, Russian Academy of Sciences, ul. Vavilova 38, Moscow, 117942 Russia*

Received August 13, 1998

Abstract—Theoretical research on high-power microwave sources based on stimulated emission from relativistic election beams in plasma waveguides and resonators is reviewed. Both microwave amplifiers and oscillators are investigated. Two mechanisms for stimulated emission—resonant Cherenkov emission from a relativistic electron beam in a plasma and nonresonant Pierce emission arising from the onset of a high-frequency Pierce instability—are studied theoretically. The theory developed here is motivated by recent experiments carried out at the Institute of General Physics of the Russian Academy of Sciences and is aimed at creating high-power pulsed plasma microwave sources [both narrowband ($\Delta\omega/\omega < 0.1$) and broadband (or noisy, $\Delta\omega/\omega \approx 1$)] based on high-current relativistic electron beams. Although the paper is devoted to theoretical problems, all analytic estimates and numerical calculations are made with real experiments in mind and theoretical results are compared with reliable experimental data. Special attention is paid to the opportunity to progress to short (millimeter) and long (decimeter) wavelength ranges. Some factors that influence the formation of the wave spectra excited by relativistic electron beams in plasma sources are discussed. © *2000 MAIK "Nauka/Interperiodica".*

1. INTRODUCTION

Research on relativistic plasma microwave electronics began nearly thirty years ago. This research line originates from nonrelativistic plasma microwave electronics, which dates back to 1949, when A.I. Akhiezer and Ya.B. Fainberg [1] and D. Bohm and E. Gross [2] discovered a beam instability in a plasma. In every review of the advances achieved in research on relativistic plasma electronics that we have published so far in collaboration with other authors in journals, collections of papers, and proceedings of conferences [3–14],[1] we pointed out the important contribution of these pioneering works. Note that, just before the birth of relativistic microwave electronics, Fainberg published review papers [21, 22], where he summarized the successes that have been achieved in research on nonrelativistic plasma electronics and laid the theoretical foundations of plasma microwave electronics.[2] As soon as physicists succeeded in producing relativistic electron beams (REBs) in the early 1970s, the authors of [4, 27, 28], inspired by Fainberg's reviews, suggested that REBs may be used to generate microwaves and formulated the basic principles of relativistic plasma microwave electronics.

The phenomenon of beam instability in a plasma, which was discovered in [1, 2], can be interpreted as stimulated Cherenkov emission of own electromagnetic plasma waves from a straight electron beam. Depending on the beam density, stimulated Cherenkov emission can manifest itself as either a wave–particle effect (single-particle Cherenkov effect or Thomson emission mechanism) or as a wave–wave effect (collective Cherenkov effect or Raman emission mechanism) [9, 11, 25]. In the 1970s and early 1980s, a linear theory of stimulated Cherenkov emission for specific electrodynamic plasma systems was actively developed. The progress achieved in this field by the mid-1980s motivated the construction of a systematic nonlinear theory and the development of analytical and numerical methods that would not only be able to describe the results of current experiments but also suggest promising areas for future research. Among the groundbreaking works on the nonlinear theory of beam–plasma interaction, we should mention papers [29–32], which were published much earlier and were devoted primarily to the interaction of weakly relativistic electron beams with plasma potential oscillations, i.e., to a case that is not of much interest for high-current relativistic plasma microwave electronics. Note, however, that they laid the foundations of a nonlinear theory of the interaction between REBs and plasmas.

The excitation of electromagnetic waves by an electron beam in a plasma and their emission from the plasma were studied not only theoretically but also experimentally. The first experiments conducted with nonrelativistic beams in the 1950s and 1960s showed that the efficiency with which electromagnetic waves were emitted during the beam–plasma interaction was low. This result was attributed to the low phase veloci-

[1] See also monographs [15–20].

[2] See also monographs [23, 24] and reviews [25, 26].

ties of the excited plasma waves ($V_{ph} \approx u \ll c$) and, accordingly, to their highly electrostatic nature. In other words, fairly intense oscillations excited in the plasma were strongly trapped inside the plasma waveguide, so that the extraction of electromagnetic radiation from the waveguide was accompanied by significant losses [26].

The development and fabrication of pulsed sources of high-power REBs in the early 1970s marked a new era of plasma microwave electronics. The very first experiments that were performed jointly by the Lebedev Institute of Physics (Moscow) and the Scientific Research Institute of Radiophysics (Gorki) in 1972 with REBs and a vacuum resonator with a slowing-down structure (a rippled metal waveguide—carcinotron) showed that the emission efficiency was high (a radiation power of 300 MW was achieved at a wavelength of about 3 cm, the efficiency being 13%) [33]. Shortly after that experimental study, similar experiments [34] were carried out in the United States and confirmed the results of [33].

Thus, the true birth of relativistic microwave electronics occurred in 1972, although, at that time, it was purely vacuum electronics. The advances achieved in relativistic vacuum microwave electronics were reviewed in paper [35] and in collection of papers [36].

The first plasma microwave oscillator based on stimulated Cherenkov emission from an REB in a plasma waveguide was created more recently (in 1982) and was actively studied both experimentally and theoretically. In addition to the cited reviews [3–14] and monographs [15–20] (in which one can also find a detailed bibliography), we should mention a number of original papers [37–61], which made important contributions to the development of plasma microwave electronics and demonstrated its advantages over vacuum electronics (the possibility of operating with high-current REBs and the ease of frequency tuning over a range broader than is possible in vacuum devices). The most important advantage of plasma microwave sources over vacuum sources is the possibility of operating with long microwave pulses at high power levels [62] (the possible reasons for the limitation of the pulse duration in vacuum devices are discussed in [36]).

A new direction that has recently appeared in plasma microwave electronics is associated with the phenomenon of nonresonant stimulated emission from an REB (or, in other words, with the radiative Pierce instability of an REB) in a plasma waveguide [63–65]. In contrast to plasma microwave sources based on stimulated Cherenkov emission, the devices based on the radiative Pierce instability are able merely to generate microwaves, without amplifying them.[3]

[3] A vacuum oscillator based on the radiative Pierce instability of a nonrelativistic beam has come to be known as a monotron [66]. Attempts to develop a relativistic theory of monotrons were made in [67, 68], but turned out to be unsuccessful.

Here, we will present a history of and an outlook for relativistic plasma microwave electronics in order to demonstrate the progress achieved in this area of research, beginning with the pioneering papers [1, 2].

2. INITIAL ASSUMPTIONS AND BASIC EQUATIONS

We consider a straight REB propagating along the axis of a cylindrical plasma-filled metal waveguide in a strong longitudinal magnetic field. An REB enters the waveguide along the z-axis by crossing the plane $z = 0$. A collector is placed in the plane $z = L$ and is coupled to the emitter (the outlet horn). In an unperturbed state, the beam and plasma in the waveguide are both assumed to be homogeneous along the z-axis and inhomogeneous in transverse directions. They are also assumed to be cold and completely charge- and current-neutralized. We neglect slow ion motion and consider only pulsed systems operating on short time scales. We assume that the beam density is much lower than the plasma density in order to describe the plasma to the first order in the perturbations. We also assume that the external longitudinal magnetic field is strong enough so that the beam and plasma electrons do not drift radially across the field and their motion can be described in a one-dimensional approximation. The question of the validity of this model was examined in detail in [11, 31, 32, 53, 69] (see also the literature cited therein).

Under the assumptions adopted, it is convenient to represent the electromagnetic field in a plasma waveguide in terms of the polarization potential ψ satisfying the equation [19]

$$\frac{\partial}{\partial t}\left(\Delta_\perp + \frac{\partial^2}{\partial z^2} - \frac{1}{c^2}\frac{\partial^2}{\partial t^2}\right)\psi = -4\pi(j_{bz} + j_{pz}), \qquad (2.1)$$

where $\Delta_\perp$ is the transverse Laplace operator. The perturbed nonzero components of the beam and plasma current densities, j_{bz} and j_{pz}, can be written as

$$j_{pz} = P_p(\mathbf{r}_\perp) j_p, \quad j_{bz} = P_b(\mathbf{r}_\perp) j_b, \qquad (2.2)$$

where $P_p(\mathbf{r}_\perp)$ and $P_b(\mathbf{r}_\perp)$ are the radial profiles of the plasma electron density and beam density, $\mathbf{r}_\perp$ is the transverse coordinate in the waveguide cross section, and j_p satisfies the equation

$$\frac{\partial j_p}{\partial t} = \frac{\omega_p^2}{4\pi} E_z. \qquad (2.3)$$

In deriving this equation, we described the plasma electron motion using the model of independent particles (the cold hydrodynamic model [18]). Here,

$$E_z = \left(\frac{\partial^2}{\partial z^2} - \frac{1}{c^2}\frac{\partial^2}{\partial t^2}\right)\psi \qquad (2.4)$$

is the longitudinal electric-field component and ω_p is the Langmuir frequency of the plasma electrons, which is independent of the transverse coordinate because this dependence is already taken into account in the first relationship in (2.2). The remaining electromagnetic-field components are expressed in terms of ψ as follows (for definiteness, we are working in cylindrical coordinates $\{r, \varphi, z\}$):

$$E_r = \frac{\partial^2\psi}{\partial z\partial r}, \quad E_\varphi = \frac{1}{r}\frac{\partial^2\psi}{\partial z\partial\varphi},$$
$$B_z = 0, \quad B_r = \frac{1}{cr}\frac{\partial^2\psi}{\partial t\partial\varphi}, \quad B_\varphi = -\frac{1}{r}\frac{\partial^2\psi}{\partial t\partial r}. \tag{2.5}$$

Now, we find the perturbed beam current density j_b. Since it cannot be evaluated in the linear approximation, we will trace the behavior of each beam electron. Let the next beam electron be injected into the waveguide through the cross section $z = 0$ at the time t_0 (the electrons are assumed to be injected at the same velocity u). Applying the Liouville theorem of conservation of the phase volume and using a formal solution to the Vlasov equation [19, 51, 70], we can write the beam electron current density in an arbitrary cross section $z > 0$ as [19, 51] (see also [30, 32])

$$j_b = en_b\int v(z, t_0)\delta[t - t(z, t_0)]dt_0, \tag{2.6}$$

where n_b is the unperturbed beam electron density, which is also independent of the transverse coordinate by virtue of the second relationship in (2.2), and $v(z, t_0)$ and $t(z, t_0)$ are solutions to the characteristic set of equations for the Vlasov equation,

$$\frac{dt}{dz} = \frac{1}{v}, \quad v\frac{dv}{dz} = \frac{e}{m}(1 - v^2/c^2)^{3/2}E_z. \tag{2.7}$$

The set of equations (2.7) is solved with the initial conditions $t(z = 0) = t_0$ and $v(z = 0) = u$.

Equations (2.1)–(2.7) are the basic equations in the theory of relativistic microwave electronics. The boundary and initial conditions for the field equation (2.1) will be discussed below in solving particular problems of generating and amplifying electromagnetic radiation. Here, we present only the boundary condition that is imposed on the side metal wall and is physically obvious, because we are interested in a metal waveguide in which the beam interacts with the plasma:

$$\psi|_{\Sigma = 0} = 0. \tag{2.8}$$

3. PLASMA WAVES IN A MAGNETIZED WAVEGUIDE

Before proceeding to the problem of REB–plasma interaction in a waveguide, we need to investigate the frequency spectra and phase velocities of the waves with which the beam can interact. We start by considering the simplest waves, which can be excited in a strongly magnetized plasma waveguide in the absence of an REB. In other words, we solve equations (2.1)–(2.3) with the boundary condition (2.8), neglecting the beam current. Since these equations are linear, we can seek the solution in the form

$$\{j_p, \psi\} = \{\tilde{j}_p(\mathbf{r}_\perp), \tilde{\psi}(\mathbf{r}_\perp)\}\exp(-i\omega t + ik_z z), \tag{3.1}$$

where ω is the frequency, k_z is the longitudinal wavenumber, and the functions $\tilde{j}_p$ and $\tilde{\psi}$ depend only on the transverse coordinate $\mathbf{r}_\perp$. In cylindrical geometry, we have $\mathbf{r}_\perp = \{r, \varphi\}$.

We denote the transverse eigenfunctions of the waveguide by $\varphi_n(\mathbf{r}_\perp)$, where $n = 1, 2, \ldots$ and $k_{\perp n}^2$ are the related eigenvalues,

$$\Delta_\perp\varphi_n = -k_{\perp n}^2\varphi_n. \tag{3.2}$$

For a circular waveguide, we have $\varphi_n = J_l(k_{\perp n}r)$, where J_l is an lth order Bessel function, $k_{\perp n} = \mu_{l,n}/R$, $\mu_{l,n}$ are the roots of the Bessel function, l is the azimuthal wavenumber, and R is the waveguide radius.

We expand $\tilde{\psi}$ in a series of eigenfunctions, find the expansion coefficients from equation (2.1), and substitute them into (2.3). As a result, we obtain the following integral equation for $\tilde{j}_p$:

$$\omega^2\tilde{j}_p(\mathbf{r}_\perp) = \omega_p^2\int_{S_w} K_p(\mathbf{r}_\perp, \mathbf{r}_\perp^*)\tilde{j}_p(\mathbf{r}_\perp^*)d\mathbf{r}_\perp^*,$$
$$K_p(\mathbf{r}_\perp, \mathbf{r}_\perp^*) = \sum_{n=1}^{\infty}\frac{\chi^2}{k_{\perp n}^2 + \chi^2}\frac{P_p(\mathbf{r}_\perp^*)\varphi_n(\mathbf{r}_\perp^*)\varphi_n(\mathbf{r}_\perp)}{\|\varphi_n\|^2}, \tag{3.3}$$

where $\chi^2 = k_z^2 - \omega^2/c^2$, S_w is the cross-sectional area of a waveguide, and $\|\varphi_n\|$ is the norm of an eigenfunction. The most general but implicit dispersion relation for determining the frequency spectra of the plasma waves in a fully magnetized plasma waveguide is simply the solvability condition for equation (3.3).

Adopting the experimental conditions of [7, 12, 37, 38, 55, 58], we consider a particular geometric configuration—a circular waveguide of radius R filled with a thin-walled annular plasma of thickness Δ_p and mean radius $r_p < R$ such that $\Delta_p \ll r_p$. It is convenient to represent the radial plasma profile in the form $P_p = \Delta_p\delta(r - r_p)$, which corresponds to an infinitely thin annular plasma column. The applicability conditions for the validity of the model of such a plasma will be specified below. In this case, the solvability condition for equation (3.3) reduces to the dispersion relation [71]

$$D_p \equiv \omega^2 - \omega_p^2\frac{\chi^2}{k_{\perp p}^2} = 0, \tag{3.4}$$

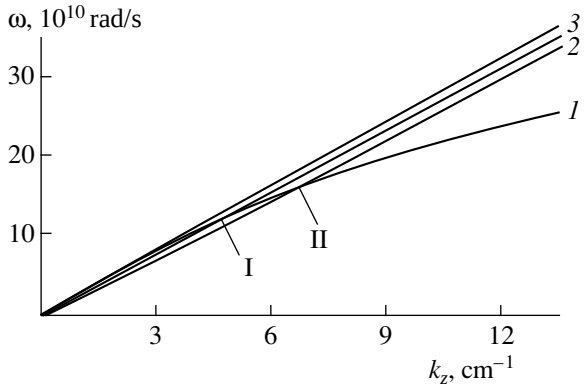

Fig. 1. Wave spectra for a waveguide with a magnetized thin-walled annular plasma and beam with no regard to the beam–plasma interaction: (*1*) plasma wave, (*2*) slow beam wave, (*3*) fast beam wave, (I) point of the single-particle Cherenkov resonance, and (II) point of the collective Cherenkov resonance.

where

$$k_{\perp p}^2 = \left\{ r_p \Delta_p I_l^2(\chi r_p) \left[\frac{K_l(\chi r_p)}{I_l(\chi r_p)} - \frac{K_l(\chi R)}{I_l(\chi R)} \right] \right\}^{-1} \quad (3.5)$$

and I_l and K_l are modified Bessel functions.[4] For $\omega < k_z c$, formulas (3.4) and (3.5) describe the frequency spectra of the surface plasma waves, whose squared transverse wavenumber is described by (3.5).

Let us consider the frequency spectra of the surface plasma waves in different wavelength ranges. In the long wavelength limit $k_z \longrightarrow 0$, we have from (3.4)

$$\omega = \omega_p \frac{k_z c}{\sqrt{k_{\perp p}^2 c^2 + \omega_p^2}}, \quad (3.6)$$

where, according to (3.5), the transverse wavenumber has the form

$$k_{\perp p}^2 = \begin{cases} [r_p \Delta_p \ln(R/r_p)]^{-1}, & l = 0, \\ 2l\{r_p \Delta_p [1 - (r_p/R)^{2l}]\}^{-1}, & l = 1, 2, \ldots. \end{cases} \quad (3.7)$$

For shorter wavelengths (about radius r_p of the annular plasma column), the frequency spectrum is similar to that for waves on the surface of deep water:

$$\omega = \omega_p (k_z \Delta_p / 2)^{1/2}. \quad (3.8)$$

In this wavelength range, the longitudinal electric-field component of the surface wave decreases very sharply (exponentially) outward from the surface of the plasma column to vacuum.

Finally, for wavelengths shorter than $\Delta_p (k_z \Delta_p \geq 1)$, the model of an infinitely thin plasma fails, because it does not take into account the effect of trapping of the fields inside the plasma column. Allowing for the finite thickness of an annular plasma naturally leads to the limiting transition $\omega \longrightarrow \omega_p$ as $k_z \longrightarrow \infty$, in which case, however, the plasma wave is highly electrostatic, so that its excitation by an electron beam due to the Cherenkov effect is uninteresting for relativistic plasma microwave electronics.

In Fig. 1, the dispersion curve $\omega(k_z)$ for the oscillation spectrum of a symmetric ($l = 0$) surface wave in an infinitely thin annular plasma is illustrated by curve *1*, which is plotted for the specific parameter values $R = 1.8$ cm, $r_p = 1$ cm, $\Delta_p = 0.1$ cm, and $\omega_p = 35 \times 10^{10}$ rad/s. The initial, nearly straight portion of the dispersion curve is described by formula (3.6) and refers to the so-called cable plasma wave [10, 19, 40]. The next portion of the dispersion curve is described by the dispersion law (3.8). Closer to the plasma frequency, the dispersion curve ceases to reflect a real situation; in this case, it is necessary to take into account the finite thickness of an annular plasma column.

In Fig. 1, we also plotted the straight line $\omega = k_z u$, which corresponds to the Cherenkov resonance condition (for the beam velocity $u = 2.6 \times 10^{10}$ cm/s), and marked the point of single-particle Cherenkov (wave–particle) resonance—point *I*, at which the straight line $\omega = k_z u$ intersects the curve $\omega(k_z)$. We can see that, as ω_p decreases, the Cherenkov resonance frequency falls off and eventually vanishes at the frequency

$$\omega_p^2 = \omega_{pnop}^2 = k_{\perp p}^2 u^2 \gamma^2, \quad (3.9)$$

where $\gamma = (1 - u^2/c^2)^{-1/2}$. The threshold plasma frequency (3.9) depends on the azimuthal wavenumber *l*. According to (3.7), the threshold plasma frequency for the excitation of the mode with $l = 0$ is the lowest.

For the plasma frequencies below the threshold frequency, single-particle Cherenkov resonance is impossible, which, however, does not imply that there is no stimulated Cherenkov emission and that the beam in the plasma is stable. Below, we will show that, for high-density REBs, the threshold plasma frequency is significantly below (3.9). We will also show that, even in the absence of Cherenkov resonance, microwaves can be emitted nonresonantly via the so-called radiative Pierce instability.

4. STIMULATED CHERENKOV EMISSION FROM AN REB IN A PLASMA WAVEGUIDE: LINEAR THEORY OF A PLASMA MICROWAVE AMPLIFIER

In the linear approximation, it is more convenient to describe an REB using, instead of equations (2.6) and

[4] Formulas (3.4) and (3.5) for an infinitely thin annular plasma column were derived with allowance for the fact that the integrals over radius in (3.3) contain delta functions and, therefore, can be taken exactly.

(2.7), the equations of cold magnetohydrodynamics [18], which give, together with (2.2), the following equation for the function j_b, similar to equation (2.3):

$$\left(\frac{\partial}{\partial t} + u\frac{\partial}{\partial z}\right)^2 j_b = \frac{\omega_b^2\gamma^{-3}}{4\pi}\frac{\partial E_z}{\partial t}, \tag{4.1}$$

where $\omega_b = (4\pi e^2 n_b m^{-1})^{1/2}$ is the Langmuir frequency of the beam electrons. Setting, as in (3.1),

$$j_b = \tilde{j}_b(\mathbf{r}_\perp)\exp(-i\omega t + ik_z z),$$

from the coupled equations (2.1)–(2.4) and (4.1), we obtain the following set of homogeneous integral equations for the functions $\tilde{j}_p$ and $\tilde{j}_b$ [71]:

$$\begin{aligned}
&\omega^2\tilde{j}_p(\mathbf{r}_\perp) - \omega_p^2\int_{S_w} K_p(\mathbf{r}_\perp, \mathbf{r}_\perp^*)\tilde{j}_p(\mathbf{r}_\perp^*)d\mathbf{r}_\perp^* \\
&\quad = \omega_b^2\gamma^{-3}\int_{S_w} K_b(\mathbf{r}_\perp, \mathbf{r}_\perp^*)\tilde{j}_b(\mathbf{r}_\perp^*)d\mathbf{r}_\perp^*, \\
&(\omega - k_z u)^2\tilde{j}_b(\mathbf{r}_\perp) - \omega_b^2\gamma^{-3}\int_{S_w} K_b(\mathbf{r}_\perp, \mathbf{r}_\perp^*)\tilde{j}_b(\mathbf{r}_\perp^*)d\mathbf{r}_\perp^* \\
&\quad = \omega_p^2\int_{S_w} K_p(\mathbf{r}_\perp, \mathbf{r}_\perp^*)\tilde{j}_p(\mathbf{r}_\perp^*)d\mathbf{r}_\perp^*.
\end{aligned} \tag{4.2}$$

The dispersion relation for determining the complex spectra of a linear beam–plasma system is simply the solvability condition for equations (4.2). The quantity K_p in (4.2) is defined by the second expression in (3.3), and the quantity K_b is defined by the same expression but with $P_p(\mathbf{r}_\perp^*)$ in place of $P_b(\mathbf{r}_\perp^*)$.

Before proceeding to an analysis of the general equation, we examine the spectra of beam waves in the absence of a plasma. We set $\omega_p = 0$ in the second equation in (4.2) and consider a thin-walled annular electron beam (like the plasma) with the density profile $P_b = \Delta_b\delta(r - r_b)$, where Δ_b is the beam thickness and r_b is the mean beam radius. Applying the procedure that was used to derive (3.4), we obtain the following dispersion relation for the oscillation spectra in a waveguide with a beam:

$$D_b \equiv (\omega - k_z u)^2 - \omega_b^2\gamma^{-3}\frac{\chi^2}{k_{\perp b}^2} = 0, \tag{4.3}$$

where $k_{\perp b}$ has the same form as $k_{\perp p}$; i.e., it is described by expression (3.5) in which the subscript p should be replaced with b.

Along with the dispersion curves for plasma waves, Fig. 1 shows the dispersion curves for symmetric ($l = 0$) waves of an infinitely thin annular beam at $r_b = 0.65$ cm, $\Delta_b = 0.1$ cm, $I_b = 2$ kA, and $\gamma = 2$, the waveguide radius being, as before, $R = 1.8$ cm (for $\gamma = 2$, the beam velocity is $u = 2.6 \times 10^{10}$ cm/s). A wave with a phase velocity above the injection velocity is called a fast beam wave (curve *3*) and a wave with a phase velocity below u is referred to as a slow beam wave (curve *2*). A slow beam wave has negative energy, thereby giving rise to the instability of a beam in a plasma [25, 72]. Point II, at which dispersion curve *1* of a cable plasma wave intersects dispersion curve *2* of a slow beam wave, is the point of collective Cherenkov (wave–wave) resonance.

If the finite thickness Δ_b of a beam were taken into account, then Fig. 1 would display numerous dispersion curves describing higher radial modes of the internal beam waves and lying closer to the straight line $\omega = k_z u$ than curves *2* and *3*. Although the higher modes are trapped inside the beam, they influence the interaction between a high-density beam and a plasma (see below). Similar internal waves, but that are trapped inside the plasma, appear in an annular plasma column of finite thickness. However, if the plasma column is sufficiently thin, then internal plasma waves do not influence the beam–plasma interaction, because their phase velocities are low. Important effects characteristic of a thick-walled plasma column will be analyzed below.

Now, we turn to the general equations (4.2) and write out the dispersion relation for a beam–plasma system in a waveguide, assuming, as before, that the beam and plasma are infinitely thin:

$$D_p D_b = \theta\omega_p^2\omega_b^2\gamma^{-3}\frac{\chi^4}{k_{\perp p}^2 k_{\perp b}^2}. \tag{4.4}$$

Here, the coefficient θ characterizes the coupling between the beam and plasma waves and is rather lengthy in its general form [71], so we present only asymptotic expressions. For a circular waveguide with an annular beam and annular plasma column such that $r_b \le r_p$ and for symmetric ($l = 0$) waves in the range of low frequencies ($\omega \ll \omega_p$), we have

$$\theta = \ln(R/r_p)/\ln(R/r_b). \tag{4.5}$$

In the range of higher frequencies, instead of (4.5), we obtain

$$\theta = \exp\left(-2\frac{\omega}{u\gamma}|r_p - r_b|\right). \tag{4.6}$$

With the problem of wave amplification in mind, we look for a solution to dispersion relation (4.4) in the form

$$k_z = \frac{\omega}{u}(1 + \delta), \tag{4.7}$$

where δ has the meaning of a dimensionless complex amplification coefficient. Since, in reality, the beam density is always lower than the plasma density, we have $|\delta| \ll 1$. Substituting (4.7) into (4.4) and perform-

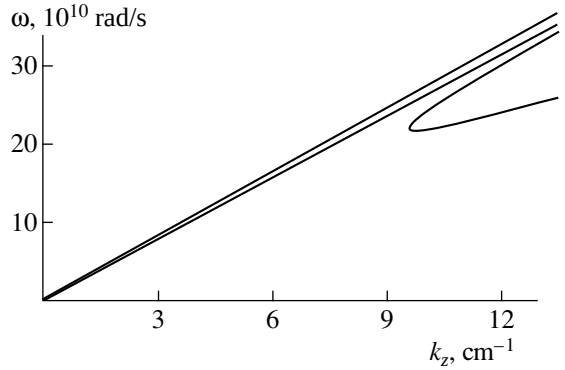

Fig. 2. Dispersion curves for the Thomson amplifier, in which the beam–plasma interaction is strong ($\theta = 1$).

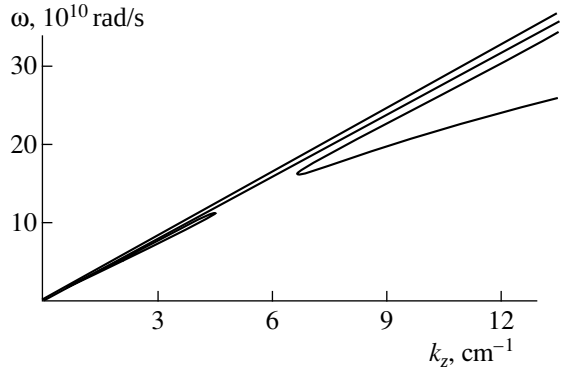

Fig. 3. Dispersion curves for the Raman amplifier, in which the beam–plasma interaction is weak ($\theta = 0.6$).

ing elementary manipulations, we arrive at the following cubic equation, which incorporates the effects associated with both the high beam current and the nonpotential nature of the beam and plasma waves:

$$[1 - \alpha_p(1 + 2\gamma^2\delta)][\delta^2 - \alpha_b(1 + 2\gamma^2\delta)] = \theta\alpha_p\alpha_b(1 + 2\gamma^2\delta)^2, \quad (4.8)$$

where the parameters

$$\alpha_p = \frac{\omega_p^2}{k_{\perp p}^2 u^2 \gamma^2}, \quad \alpha_b = \frac{\omega_b^2 \gamma^{-3}}{k_{\perp b}^2 u^2 \gamma^2} \quad (4.9)$$

characterize the plasma and beam densities. Equation (4.8) was derived for the frequency range $\omega \ll \omega_p$, in which the dispersion of a surface plasma wave is almost linear. However, this equation can be generalized qualitatively to a higher frequency range through the substitution

$$\alpha_p \longrightarrow \alpha_p(1 - \omega^2/\omega_p^2).$$

With this substitution, which is exact for a waveguide entirely filled with a plasma, equation (4.8) can be successfully applied not only to the range of low frequencies but also to frequencies close to the plasma frequency.

In terms of the new variable introduced in (4.7), the zeros of the functions in square brackets on the left-hand side of (4.8) determine the longitudinal wavenumbers of the plasma wave accompanying the beam and fast and slow beam waves. The fast beam wave is uninteresting for further analysis. For a plasma wave, we have

$$\delta_p = \frac{1}{2\gamma^2}\left(\frac{1}{\alpha_p} - 1\right), \quad (4.10)$$

and, for a slow beam wave, we obtain

$$\delta_b^- = \sqrt{\alpha_b + \gamma^4\alpha_b^2} + \gamma^2\alpha_b. \quad (4.11)$$

According to (4.7), the relationship $\delta_p = 0$ is the condition for exact single-particle Cherenkov (wave–particle) resonance. In other words, this is the equation for determining the frequency at which the beam velocity is exactly equal to the phase velocity of the plasma wave. In Fig. 1, this frequency corresponds to point I on the dispersion curve for a plasma wave.

The relationship $\delta_p = \delta_b^-$ is the condition for collective Cherenkov (wave–wave) resonance and serves to determine the frequency at which the phase velocities of a plasma wave and a slow beam wave are exactly equal to one another. In Fig. 1, this frequency corresponds to point II on the relevant dispersion curves. The frequency of the collective resonance is somewhat higher than that of single-particle resonance.

Depending on the parameters of the system, a cable plasma wave may be amplified in different frequency ranges. If the coefficient θ is large, then the waves are amplified in a broad frequency range (from nearly zero to a frequency above the resonant frequency at point II). In the literature, such broadband plasma microwave sources are referred to as Thomson amplifiers. Figure 2 shows the dispersion curves for a Thomson plasma microwave amplifier calculated for $r_b = r_p = 0.65$ cm, $\Delta_b = \Delta_p = 0.1$ cm, $\gamma = 2$, $R = 1.8$ cm, and $\omega_p = 35 \times 10^{10}$ rad/s, the beam current being $I_b = 2$ kA. One can see that microwaves can be amplified in the frequency range from 0 to about $\sim 21 \times 10^{10}$ rad/s. Roughly speaking, taking into account strong coupling ($\theta = 1$) between the beam and the plasma transforms Fig. 1 into Fig. 2.

The situation with a small coupling coefficient $\theta \ll 1$ is radically different. According to Fig. 3, microwaves are amplified in a narrow frequency band. Such narrowband plasma microwave sources are referred to as Raman amplifiers. The dispersion curves in Fig. 3 were calculated for the same parameters as in Fig. 2 but with a mean plasma radius increased to $r_p = 1.1$ cm. As a result, the coefficient θ falls off to 0.6, thereby radically changing the amplification regime: the amplification

band becomes as narrow as (10–17) × 10^{10} rad/s and now contains the wave–wave resonance frequency. Again, we can say that Fig. 1 transforms into Fig. 3 when a weak coupling between the beam and the plasma is taken into account.

For low-current beams, we can readily find simple analytic expressions for the amplification coefficient in the two limiting cases under analysis. For a strong coupling $\theta \approx 1$, we obtain from (4.8)

$$\delta = \frac{1 - i\sqrt{3}}{2}\left(\frac{1}{2\gamma^2}\theta\alpha_b\right)^{1/3}. \qquad (4.12)$$

The dimensionless amplification coefficient is $|\mathrm{Im}\,\delta|$, and the dimensional coefficient can be found from (4.7). The amplification described by coefficient (4.12) is governed by the resonant wave–particle interaction or, in other words, by the stimulated single-particle Cherenkov effect (Thomson amplification regime [9]) and occurs at the frequencies of single-particle and collective Cherenkov resonances. However, these resonant frequencies do not differ from one another, because the resonances overlap when the coupling is strong ($\theta \approx 1$) and the beam current is low.

For a weak coupling ($\theta \ll 1$), we find from (4.8)

$$\delta = \sqrt{\alpha_b} - i\left(\frac{1}{4\gamma^2}\theta\sqrt{\alpha_b}\right)^{1/2}, \qquad (4.13)$$

in which case the amplification is governed by the resonant wave–wave interaction or, in other words, by the stimulated collective Cherenkov effect (Raman amplification regime [9]) and occurs only at frequencies close to the frequency of the collective resonance. Below, we will show that, for $\theta \ll 1$, microwaves cannot, in principle, be amplified at the single-particle resonance frequency.

Note that formulas (4.12) and (4.13) apply exclusively to low-current beams such that

$$\left|2\gamma^2\delta\right| \ll 1. \qquad (4.14)$$

For high-current REBs, analytic solutions to equation (4.8) are very lengthy. However, since the experiments under discussion were carried out with high-current REBs, we consider the results of analyzing equation (4.8) numerically.

Figure 4 shows the most important frequencies characteristic of the beam–plasma interaction versus the plasma frequency ω_p. The region where microwaves can be amplified (the amplification band) is bounded from above by curve *1* and from below, by curve *2*. Curve *3* corresponds to the frequencies at which the dimensional amplification coefficient is maximum. Curves *4* and *5* reflect the collective and single-particle resonance frequencies, respectively. All of the curves were computed for a waveguide with the parameters R = 1.8 cm, r_b = 0.65 cm, $\Delta_b = \Delta_p$ = 0.1 cm, I_b = 2 kA, and γ = 2 and for two plasma radii r_p = 0.8 cm (Fig. 4a) and r_p = 1.1 cm (Fig. 4b).

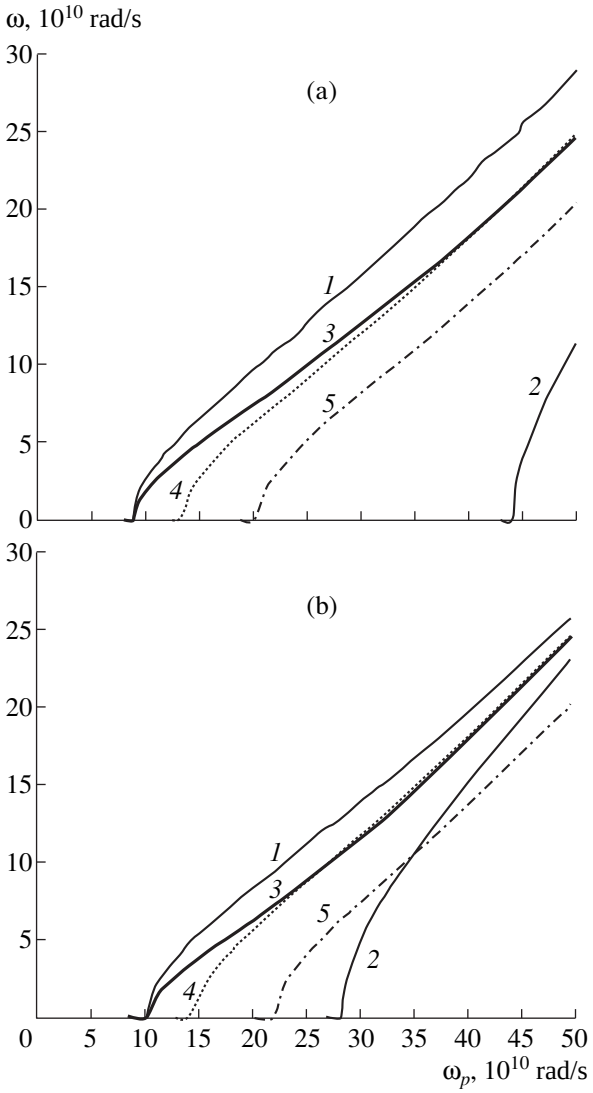

Fig. 4. (a) The most important frequencies for (a) r_p = 0.8 cm and (b) r_p = 1.1 cm: (*1*) and (*2*) upper and lower bounds on the amplification band, (*3*) frequency at which the amplification is maximum, (*4*) frequency of the collective resonance, and (*5*) frequency of the single-particle resonance.

As can be seen in Fig. 4, microwaves can be amplified only when the plasma frequency ω_p is above a certain threshold, which is significantly (by a factor of approximately two) lower than that in (3.9). This can be explained by high beam currents: formula (3.9) shows that, for r_p = 0.8 cm, the threshold plasma frequency is about 20 × 10^{10} rad/s and, for r_p = 1.1 cm, it is about 22 × 10^{10} rad/s. For higher plasma frequencies, there is a range in which the lower boundary frequency of the amplification band is zero. In the range of even higher plasma frequencies, the lower boundary frequency of

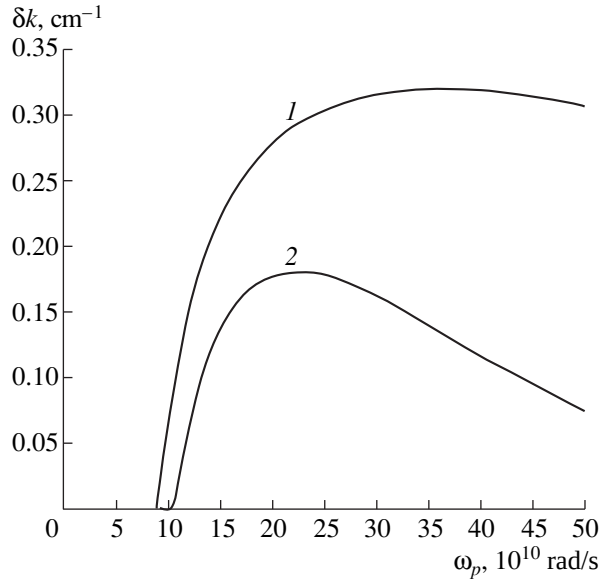

Fig. 5. Maximum amplification coefficient vs. the plasma frequency for r_p = (*1*) 0.8 and (*2*) 1.1 cm.

the amplification band becomes nonzero and the amplification band itself narrows as ω_p grows. A comparison between Figs. 4a and 4b shows that the larger the difference between r_p and r_b, the smaller the coupling coefficient θ and, accordingly, the narrower the amplification band. Clearly, in the range of ω_p under consideration, Fig. 4a generally refers to a broadband Thomson amplifier and Fig. 4b refers to a narrowband Raman amplifier. Figures 4a and 4b also show that, as ω_p increases, the frequency at which the amplification is most efficient (curve *3*) rises and eventually becomes equal to the collective resonance frequency (curve *4*). Consequently, the higher the plasma frequency and the beam current, the clearer the collective nature of the beam–plasma interaction, because the coefficient θ decreases as ω increases. In contrast, as the plasma frequency grows, the single-particle resonance frequency (curve *5*) progressively deviates from the amplification region. Moreover, Fig. 4b demonstrates that amplification at the single-particle resonance frequency ceases above a certain plasma frequency.

The maximum amplification coefficients for microwave sources with the same parameters as in Fig. 4 are shown in Fig. 5 versus ω_p. Note that the maximum amplification coefficients are treated as the quantities $\mathrm{Im}((\omega/u)\delta)$ calculated along curves *3* in Fig. 4. We again see that the amplification has a threshold in terms of ω_p. Above the threshold, the maximum amplification coefficient is seen to fall off as the difference between r_p and r_b grows; this may be attributed to the decrease in the coupling coefficient θ. As can be seen in Fig. 5, the amplification coefficient has an absolute maximum, which is especially pronounced on curve *2*, obtained for r_p = 1.1 cm.

Figures 6 and 7 again illustrate the dimensional amplification coefficients for systems with the same parameters as in the previous three figures, but as functions of the frequency at different ω_p. In Fig. 6, which corresponds to r_p = 0.8 cm, curves *2* and *3* are very similar to the ω-profiles of the amplification coefficients

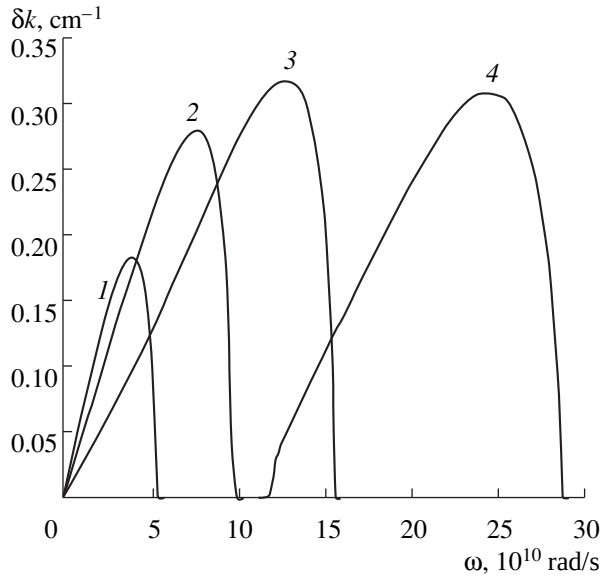

Fig. 6. Frequency profiles of the amplification coefficient for r_p = 0.8 cm and plasma frequencies of (*1*) 13, (*2*) 20, (*3*) 30, and (*4*) 50×10^{10} rad/s.

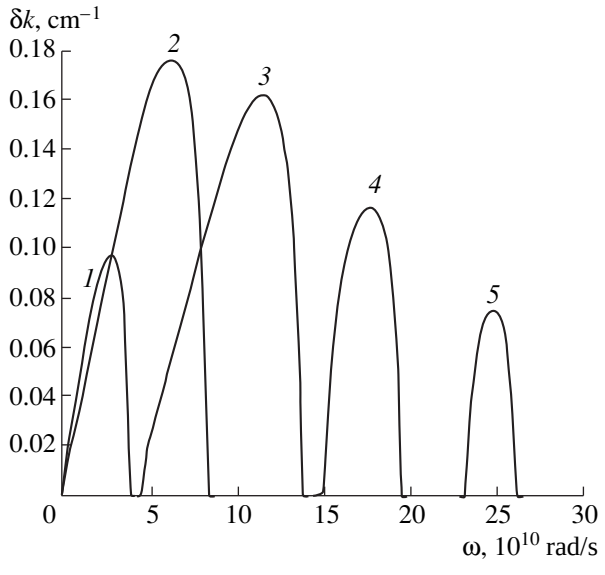

Fig. 7. Frequency profiles of the amplification coefficient for r_p = 1.1 cm and plasma frequencies of (*1*) 13, (*2*) 20, (*3*) 30, (*4*) 40, and (*5*) 50×10^{10} rad/s.

for broadband Thomson amplifiers, whereas curve *4* represents a regime that is intermediate between the Thomson and Raman regimes. In Fig. 7, which corresponds to $r_p = 1.1$ cm, curve *2* is characteristic of a Thomson amplifier and curve *3* applies to an intermediate regime, while curves *4* and *5* are strongly characteristic of the Raman amplification regime.

In Figs. 6 and 7, special attention should be paid to curve *1*, illustrating the amplification coefficients in a near-threshold (at low ω_p) nonresonant regime [39], in which the conditions of both single-particle and collective resonances (Fig. 4) fail to hold. The near-threshold regime may be of considerable interest because of the low working frequencies and fairly high amplification efficiencies (see below and review [14]).

To conclude this section, note that, for systems for which the results illustrated in Figs. 4 and 5 were obtained, the parameter in (4.14) is of order unity. This situation is typical of many recent experiments [12, 14, 55]. For REBs with very high currents ($|2\gamma^2\delta| \gg 1$), equation (4.8) is also easy to solve analytically [73–76] (see also [14, 19]). However, since experiments with such beams have not yet been carried out, we do not examine here the range of very high REB currents.

5. ESTIMATES OF THE EFFICIENCY OF A PLASMA MICROWAVE AMPLIFIER

In constructing the nonlinear theory of a Cherenkov plasma microwave amplifier, we start by estimating the amplification efficiency, which may be defined as

$$E = \langle \Delta\gamma/(\gamma - 1)\rangle \approx \gamma(\gamma + 1)\langle \Delta u/u\rangle, \qquad (5.1)$$

where $\Delta\gamma$ and Δu are the changes in the relativistic factor and velocity of an individual beam electron and the angle brackets denote averaging over all beam electrons.

The maximum amplification efficiency can be estimated by taking Δu to be the amount by which the beam velocity should exceed the wave phase velocity in order for amplification to occur, in which case, according to (4.7), we obtain

$$E \approx 2\gamma^2 \mathrm{Re}(\delta) \approx 2\gamma^2|\delta|, \qquad (5.2)$$

where δ is determined from equation (4.8). For low-current REBs, the quantity δ is defined by (4.12) or (4.13). Note that low-current REBs are the ones that satisfy inequality (4.14), which implies that the amplification efficiency (5.2) is low. The specific value of δ that should be inserted into condition (4.14) is governed by the operating mode of the amplifier. We begin by considering a Thomson amplifier, in which θ is close to unity.

Assuming that $\theta = 1$, we substitute the amplification coefficient (4.12) into $2\gamma^2|\delta|$ to obtain the following parameter, which is very important in the theory of plasma microwave amplifiers [7, 9, 19, 73–76]:

$$\mu_1 = \left(4\frac{\omega_b^2\gamma^{-1}}{k_{\perp b}^2 u^2}\right)^{1/3} \approx \left(4\frac{I_b}{I_0}\right)^{1/3}, \qquad (5.3)$$

where I_0 is the limiting vacuum current of a strongly relativistic electron beam in a waveguide. For a thin-walled annular beam, the limiting current is

$$I_0 = \frac{mc^3}{e}\frac{\gamma}{2\ln R/r_b} \approx 8.5\frac{\gamma}{\ln R/r_b}\ [\mathrm{kA}]. \qquad (5.4)$$

As a result, from (5.2), we find that, in the range $\mu_1 \ll 1$, the efficiency of the Thomson amplifier is $E \approx \mu_1$. The amplification efficiency can also be estimated analytically in the opposite limiting case of high-current REBs [7, 9, 19]:

$$E \approx \begin{cases} \mu_1, & \mu_1 \ll 1 \\ \mu_1^{-3}, & \mu_1 \gg 1. \end{cases} \qquad (5.5)$$

Numerical calculations showed that the amplification efficiency is maximum at $\mu_1 \approx 1$ and may be as high as 30% [19].

Now, we estimate the efficiency of the Raman plasma microwave amplifier, which is based on the collective Cherenkov effect and operates in the regime of weak coupling ($\theta \ll 1$). In this case, according to (4.13), it is convenient to introduce the parameter

$$\mu_2 = \left(4\frac{\omega_b^2\gamma^{-1}}{k_{\perp b}^2 u^2}\right)^{1/2} = \mu_1^{3/2}. \qquad (5.6)$$

However, we must keep in mind that formula (4.13) is valid only when $\mu_2 \ll 1$. The estimate of the amplification efficiency of a Raman microwave amplifier is similar to (5.5) [9, 19],

$$E \approx \begin{cases} \mu_2, & \mu_2 \ll 1 \\ \mu_2^{-1}, & \mu_2 \gg 1. \end{cases} \qquad (5.7)$$

The amplification efficiency is also maximum at $\mu_2 \approx 1$, for which it is somewhat lower than that of the Thomson amplifier. In the Raman regime, the maximum efficiency is lower than that in the Thomson regime. Also, the smaller the coupling coefficient θ, the lower the maximum efficiency. Below, the amplification efficiencies will be calculated in more detail.

Hence, the systems that are optimum in terms of the amplification efficiency are those in which μ_1 (or μ_2) is close to unity or those in which the REB current is close to the limiting vacuum current. Now, we will say a few words about an important aspect of experimental research. Experiments on plasma microwave electronics are still being carried out with magnetically insulated diodes [8, 10, 13, 37, 38, 55, 58], which are capa-

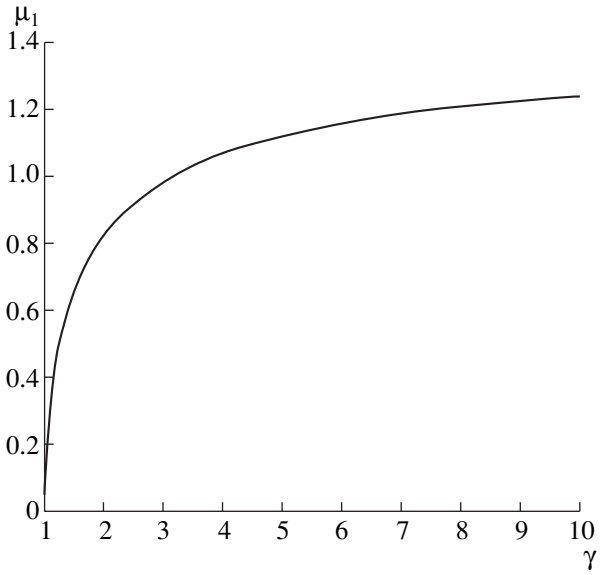

Fig. 8. Parameter μ_1 vs. the relativistic factor γ of a beam.

ble of generating thin-walled annular beams with the currents [77, 78]

$$I_b\ [\mathrm{kA}] = \frac{G}{\ln(R/r_b)}\frac{(\gamma-1)^2}{(\gamma^{2/3}+2)(\gamma^{2/3}-1)^{1/2}} \longrightarrow \frac{G\gamma}{\ln R/r_b}. \quad (5.8)$$

Since the numerical factor G in (5.8) is smaller than the factor 8.5 in (5.4), the current in (5.8) is somewhat lower than the limiting vacuum current. To achieve better agreement with recent experiments [55, 58], we used the value $G \approx 5.5$. Substituting (5.8) into (5.3) yields the dependence $\mu_1(\gamma)$, which is displayed in Fig. 8 [59].

We can see that, when γ increases from 1 to 3, $\mu_1(\gamma)$ grows sharply and approaches $\mu_{1\max} \approx 1.4$ as $\gamma \longrightarrow \infty$. For REBs with $\gamma \approx 2$–3, which are used in experiments, we have $\mu_1 \approx 1$. This value corresponds to the optimum amplification efficiency. Consequently, present-day experiments on plasma microwave electronics are carried out under nearly optimum conditions. It seems strange that the maximum efficiencies attained in experiments are at most 8–10% and, accordingly, the generated microwave powers are lower than those predicted theoretically.

Since the qualitative considerations and estimates given in this section are fairly general in character, they refer to all Cherenkov resonant plasma microwave sources. The results of specific accurate calculations will be presented below.

6. NONLINEAR EQUATIONS FOR A PLASMA AMPLIFIER

We convert the general nonlinear equations (2.1)–(2.7) to a form suitable for solving the problem of microwave amplification. To do this, we must take into account the following circumstances: (a) in a beam–plasma waveguide, the transverse structure of the wave field is not known *a priori* and is established self-consistently with increasing distance from the injection plane along the z-axis; (b) the frequency spectrum of an amplified signal is not necessarily specified *a priori*, so we have to consider the simultaneous amplification of waves with different frequencies, which interact with each other in the nonlinear stage; and (c) the longitudinal wavenumbers of the waves that are efficiently amplified by the beam are close to the wave frequency divided by the unperturbed beam velocity. These considerations enable us to represent the polarization field potential ψ in the form

$$\psi = \frac{1}{2}\sum_{n=1}^{\infty}\left\{\varphi_n(\mathbf{r}_\perp) \times \sum_{s=1}\left[A_{ns}(z)\exp\left(-is\Omega t + is\frac{\Omega}{u}z\right) + \text{c.c.}\right]\right\}. \quad (6.1)$$

Here, Ω is a certain low frequency, which serves to "discretize" the amplified signal and is equal in order of magnitude to $\Omega = 2\pi/T$, where T is the beam pulse duration. Representation (6.1) makes it possible to switch from a Fourier integral over frequencies to a Fourier series.

The next problem is to derive equations for the amplitudes $A_{ns}(z)$ or, more precisely, for some quantities equivalent to them. Note that introducing the amplitudes is justified only when they vary on scales longer than the characteristic scale of the function $\exp[is(\Omega/u)z]$, i.e., when the amplification over a distance equal to the wavelength is insignificant, which is ensured by the inequality $|\delta| \ll 1$ in (4.7).

Using (2.2)–(2.4) and (6.1), we represent the function j_p as

$$j_p = \frac{1}{2}\sum_{s=1}\left[\tilde{j}_{ps}(\mathbf{r}_\perp, z)\exp\left(-is\Omega t + is\frac{\Omega}{u}z\right) + \text{c.c.}\right]. \quad (6.2)$$

We insert (6.1), (6.2), and (2.6) into (2.1), (2.3), and (2.4) and take into account the orthogonality of the

functions $\varphi_n(\mathbf{r}_\perp)$ and $\exp(is(\Omega/u)z)$ to obtain

$$E_z = \frac{1}{2}\sum_{n=1}^{\infty}\left\{\varphi_n(\mathbf{r}_\perp)\right.$$

$$\left.\times\sum_{s=1}\left[\hat{A}_{ns}(z)\exp\left(-is\Omega t + is\frac{\Omega}{u}z\right) + \text{c.c.}\right]\right\}, \quad (6.3a)$$

$$\hat{A}_{ns}(z) = -s^2\frac{\Omega^2}{u^2\gamma^2}\left(1 - i2\gamma^2\frac{u}{s\Omega}\frac{d}{dz}\right)A_{ns}(z),$$

$$-is\Omega\tilde{j}_{ps}(\mathbf{r}_\perp, z) = \frac{\omega_p^2}{4\pi}\sum_{n=1}^{\infty}\varphi_n(\mathbf{r}_\perp)\hat{A}_{ns}(z),$$

$$is\Omega\|\varphi_n\|^2\left[k_{\perp n}^2 + s^2\frac{\Omega^2}{u^2\gamma^2}\left(1 - i2\gamma^2\frac{u}{s\Omega}\frac{d}{dz}\right)\right]A_{ns} \quad (6.3b)$$

$$= -4\pi S_p\varphi_n(\mathbf{r}_p)\tilde{j}_{ps}(\mathbf{r}_p, z) - 4\pi S_b\varphi_n(\mathbf{r}_b)\langle j_b\rangle_s,$$

$$\langle j_b\rangle_s = \frac{\Omega}{\pi}\int_0^{2\pi/\Omega} j_b\exp\left(is\Omega t - is\frac{\Omega}{u}z\right)dt,$$

where j_b is the beam current (2.6). The second relationship in (6.3b) contains the functions $\tilde{j}_{ps}$ taken inside the plasma, i.e., at only one radial position in the waveguide cross section. This circumstance, which is characteristic of a thin-walled annular plasma, substantially simplifies the derivation of the final equations. We introduce the following notation: $j_s \equiv \tilde{j}_{ps}(\mathbf{r}_p)$ and $\langle j_b\rangle_s \equiv en_b u\rho_s$ are the amplitudes of the sth harmonics of the beam and plasma currents, respectively, and ρ_s is the dimensionless amplitude of the sth harmonic of the perturbed beam density. It is convenient to rewrite equations (6.3) in terms of the amplitudes j_s and ρ_s, which depend solely on the coordinate z. We begin by transforming expressions for the amplitudes of the beam current harmonics. First, with allowance for (2.5), we convert from an integration over t to an integration over t_0 in (6.3b). Second, we introduce the new variables

$$y = \Omega[t(z, t_0) - z/u], \quad y_0 = \Omega t_0,$$
$$\eta = \frac{u - v(z, t_0)}{v(z, t_0)}, \quad \xi = \frac{\Omega}{u}z, \quad (6.4)$$

where $t(z, t_0)$ and $v(z, t_0)$ are solutions to the characteristic equations (2.7). In terms of the first three variables in (6.4), we obtain

$$\rho_s = \frac{1}{\pi}\int_0^{2\pi}(1+\eta)^{-1}\exp(isy)dy_0$$
$$\approx \frac{1}{\pi}\int_0^{2\pi}\exp(isy)dy_0. \quad (6.5)$$

The approximate equality in (6.5) is a consequence of the fact that the beam electron velocity changes only slightly, which agrees with the smallness of $|\delta|$ in (4.7).

We extract the amplitudes A_{ns} from the second relationship in (6.3b) and, with allowance for (6.3a), substitute them into equations (2.6) and the first expression in (6.3b). In terms of the dimensionless longitudinal coordinate ξ introduced in (6.4), we finally arrive at the set of equations

$$\frac{dy}{d\xi} = \eta,$$

$$\frac{d\eta}{d\xi} = \frac{i}{2}\left(1 + 2\gamma^2\frac{u^2}{c^2}\eta\right)^{3/2}$$
$$\times\sum_{s=1}[s\exp(-isy)\hat{L}_s(\alpha_{bs}\rho_s + j_s) - \text{c.c.}], \quad (6.6)$$

$$(1 - \alpha_{ps}\hat{L}_s)j_s = \theta_s\alpha_{ps}\alpha_{bs}\hat{L}_s\rho_s,$$

where

$$\hat{L}_s = 1 - 2i\gamma^2\frac{1}{s}\frac{d}{d\xi}, \quad (6.7)$$

and the coefficients α_{ps}, α_{bs}, and θ_s are defined by formulas (4.5), (4.6), and (4.9) (see [71] for details) with the replacement

$$\frac{\omega}{u\gamma} \longrightarrow s\frac{\Omega}{u\gamma}, \quad s = 1, 2, \ldots. \quad (6.8)$$

It is convenient to rewrite the third equation in (6.6) as

$$\frac{dj_s}{d\xi} = \frac{is}{2\gamma^2}\left[\left(\frac{1}{\alpha_{ps}} - 1\right)j_s - \theta_s\alpha_{bs}\hat{L}_s\rho_s\right] \quad (6.9)$$

in order to show that it is this equation that determines the amplitudes and spectra of plasma waves. Equations (6.6) were derived in the low-frequency limit. However, recall that they can be readily generalized to the entire frequency range by the simple change $\alpha_{ps} \longrightarrow \alpha_{ps}(1 - s^2(\Omega^2/\omega_p^2))$. In the linear approximation, equations (6.6) give dispersion relation (4.8).

The first integral of equations (6.6) that reflects the energy flux conservation along a waveguide has the form

$$\langle P\rangle + \frac{q\gamma^2}{4}\sum_{s=1}\theta_s^{-1}\alpha_{bs}^{-1}|j_s|^2 + \frac{q\gamma^2}{4}\sum_{s=1}\alpha_{bs}|\rho_s|^2$$
$$+\frac{q\gamma^2}{4}\sum_{s=1}(j_s\rho_s^* + j_s^*\rho_s) = \text{const}, \quad (6.10)$$

$$\langle P\rangle = \frac{1}{2\pi}\int_0^{2\pi}(1+q\eta)^{-1/2}dy_0,$$

where $\langle P \rangle$ is the mean kinetic energy flux of the beam electrons in units of the kinetic energy flux of an unperturbed beam at the injection plane, the terms proportional to $q\gamma^2/4$ determine the energy fluxes of the interacting plasma and beam waves, and $q = 2\gamma^2(u/c)^2$. The asymmetry of (6.10) with respect to j_s and ρ_s is fictitious: the first integral can be made symmetric with respect to ρ_s and ρ_{ps} through the replacement $j_s \longrightarrow \sqrt{\theta_s \alpha_{bs} \alpha_{ps}}\, \rho_{ps}$.

The amplification efficiency is defined as a relative fraction of the beam kinetic energy that is converted into microwave energy:

$$E = 1 - \langle P \rangle. \tag{6.11}$$

This is the quantity that enters (5.1) and is used in further estimates. Strictly speaking, as can be seen from (6.10), definition (6.11) refers to the fraction of the beam kinetic energy that is transferred into both the beam and plasma waves; however, for real experimental parameters, the fraction of the beam energy that is converted into plasma wave energy plays the dominant role.

Equations (6.6) should be supplemented with the boundary conditions. In the amplification problem, they are specified in the injection plane $z = 0$ and can be written in a fairly general form as follows [14]:

$$j_s|_{\xi = 0} = j_{s0},$$

$$y|_{\xi = 0} = y_0 + \frac{1}{2}\sum_{s=1} [b_s \exp(isy_0 + i\phi_s) + \text{c.c.}], \tag{6.12}$$

$$\eta|_{\xi = 0} = 0,$$

where j_{s0} are the amplitudes of the current harmonics of the plasma oscillations at the entrance to an amplifier, $y_0 \in [0, 2\pi]$ refers to an unperturbed beam, and the second term on the right-hand side of the second condition describes the electron density modulation of a beam (we did not consider the modulation of the beam in velocity, η). For definiteness, we restrict ourselves to treating the case in which there are no plasma oscillations at the entrance to an amplifier; i.e., we assume that all of the amplitudes of the plasma-current harmonics j_{s0} are equal to zero. On the other hand, we assume that the injected beam is weakly modulated: in the simulations, we set $|b_s| = 0.01$–0.05. It is of interest to consider beams with two types of modulation: monochromatically modulated beams, for which only one of the coefficients b_s is nonzero, and noisy beams, for which all of the coefficients b_s are nonzero and the phases ϕ_s in (6.12) are random numbers in the interval $[0, 2\pi]$ (other kinds of modulation were studied in [14]).

7. AMPLIFICATION DYNAMICS IN SPACE AND THE FREQUENCY SPECTRA OF A PLASMA MICROWAVE AMPLIFIER

After formulating the nonlinear problem of a beam–plasma amplifier, we proceed to a discussion of the results obtained in solving this problem. Since the range of plasma frequencies above 35×10^{10} rad/s was not investigated experimentally, we simulated the operation of a broadband noisy amplifier in the frequency range 0–40×10^{10} rad/s with evenly distributed $S_{\max} = 50$ modes. We solved equations (6.6) numerically for each sth mode from the set of $S_{\max}$ modes. The beam was modeled by $10S_{\max}$ particles. The amplifier of a monochromatic signal was simulated using only two modes, with $s = 1$ and $s = 2$. Only the first mode with frequency Ω [see (6.8)], at which the linear amplification coefficient is maximum, was assumed to be applied to the entrance plane into the amplifier. The $s = 2$ mode served to take into account the nonlinear excitation of the second harmonic.

We start by analyzing the Thomson amplifier of monochromatic signals, which is based on the single-particle Cherenkov effect. We choose the same beam parameters and waveguide radius as in Figs. 4–7 and set $r_p = 0.8$ cm. The relevant amplification coefficients are shown in Fig. 6, in which curve *3*, computed for the plasma frequency $\omega_p = 30 \times 10^{10}$ rad/s, is characteristic of the Thomson amplifier and the amplification is maximum at the frequency $\Omega = 12.1 \times 10^{10}$ rad/s. Now, we present the simulation results that were obtained precisely for these two frequencies.

Figure 9 shows the amplitude of the first harmonic of a plasma wave, the electromagnetic energy flux of a plasma wave, and the energy flux of a beam wave (in arbitrary units). The energy flux of a plasma wave is seen to be much more intense than that of a beam wave. The amplitude of the saturated plasma wave varies strongly in a periodic fashion along the waveguide axis. Such variations are a consequence of a well-known effect, namely, beam-electron trapping by the plasma wave [9, 30–32], but for the case of a high-current REB. From Fig. 9, one can also see that the distance over which the amplification saturates is shorter than 15 cm (the saturation length is determined by the z-coordinate, corresponding to the first maximum in the amplitude of the first harmonic). Of course, the saturation length depends on the depth b_1 of the initial beam modulation, but this dependence is weak and, for a beam with a different initial modulation depth b_1', it can be recalculated from the formula

$$L' - L = \frac{1}{\delta k} \ln \left| \frac{b_1'}{b_1} \right|, \tag{7.1}$$

where, for the case at hand, δk is represented by curve *1* in Fig. 5.

Curve *1* in Fig. 10 illustrates the maximum efficiency of the Thomson amplifier of a monochromatic signal as a function of ω_p, and curve *1* in Fig. 11 reflects the optimum amplifier length L over which the maximum efficiency is achieved. These curves were obtained for frequencies Ω corresponding to curve *3* in Fig. 4a. We can see that the efficiency of the Thomson oscillator is fairly high over the entire range of plasma frequencies under consideration and that the oscillator length is not large and is essentially independent of ω_p.

Now, we turn to the Raman amplifier of monochromatic signals, which is based on the collective Cherenkov effect. We set the plasma radius to be $r_p = 1.1$ cm. In Fig. 7, curve *4*, which is characteristic of the Raman amplifier, was computed for the plasma frequency $\omega_p = 40 \times 10^{10}$ rad/s; the relevant amplification coefficient δk is maximum at $\Omega = 17.7 \times 10^{10}$ rad/s. Thus, we present the numerical results that were obtained precisely for these two frequencies.

Figure 12 illustrates the same parameters of the Raman amplifier as those shown in Fig. 9 for the Thomson amplifier. We again see that the electromagnetic energy flux of a beam wave is negligible in comparison with that of a plasma wave. On the other hand, nonlinear variations of the plasma wave amplitude are much weaker, because the nonlinear saturation occurs via a different mechanism: in a Thomson amplifier, the beam electrons are trapped by the charge density wave of the beam rather than by the plasma wave; this effect is known as the self-trapping of the beam electrons [9, 19]. As a result, the beam wave breaks and the beam thermalizes.

Curve *2* in Fig. 10 illustrates the maximum efficiency of the Raman amplifier of a monochromatic signal versus ω_p, and curve *2* in Fig. 11 reflects the optimum amplifier length L over which the maximum efficiency is achieved. These curves were obtained for frequencies Ω corresponding to curve *3* in Fig. 4b. We can see that, in the range of moderate plasma frequencies, the efficiency of the Raman amplifier is also high, but, on the whole, it is lower than the efficiency of the Thomson amplifier. A sharp reduction in the efficiency of the Raman amplifier in the range of high plasma frequencies is attributed to the increase in Ω and the related decrease in the coupling coefficient θ. For the same reason, the higher the plasma frequency ω_p, the longer the optimum length of the Raman amplifier.

Now, we turn to multimode noisy amplifiers. We begin by considering the Thomson amplification regime. For several plasma frequencies, Fig. 13 illustrates the spectral densities of microwave radiation at the exit from an amplifier with an optimum length corresponding to the maximum output power. The spectral density of the input signal was assumed to be uniform over the entire frequency range of Fig. 13. Curves *1–4* were computed for the same parameters for which the relevant curves $\delta k(\omega)$ in Fig. 6 were obtained from linear theory. We can see that the emission spectra are somewhat narrower than those predicted by linear theory, while the maximum spectral density corresponds to the maximum in the linear amplification coefficient $\delta k(\omega)$. Table 1 shows that the width of the emission spectra and their central frequencies depend strongly on the plasma frequency.

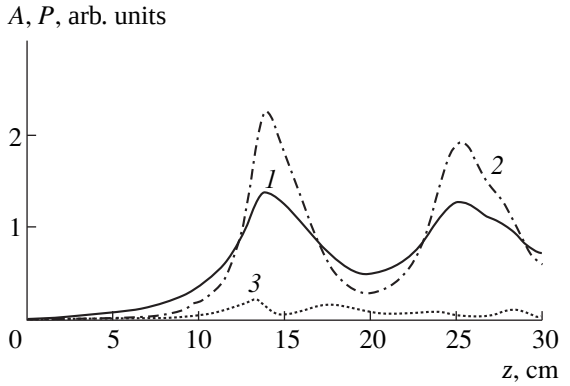

Fig. 9. Spatial profiles of the wave amplitudes in a Thomson amplifier: (*1*) amplitude of the plasma wave, (*2*) energy flux of the plasma wave, and (*3*) energy flux of the beam wave.

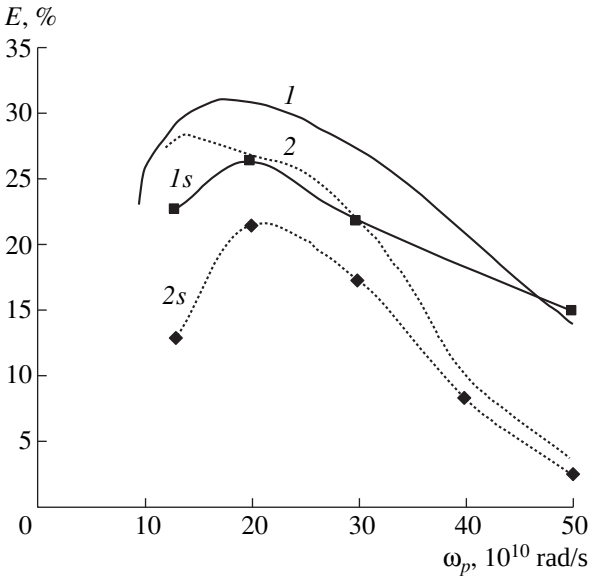

Fig. 10. Amplifier efficiency vs. the plasma frequency for (*1*, *1s*) $r_p = 0.8$ cm and (*2*, *2s*) $r_p = 1.1$ cm for (*1*, *2*) monochromatic and (*1s*, *2s*) noisy signals.

Table 1. Parameters of the Thomson amplifier

Plasma frequency ω_p, rad/s	Central frequency ω, rad/s	Central wavelength λ, cm	Spectral width $\Delta\omega/\omega$
13×10^{10}	4×10^{10}	4.7	0.5
20×10^{10}	8×10^{10}	2.4	0.4
30×10^{10}	12.5×10^{10}	1.5	0.35
50×10^{10}	25×10^{10}	0.75	0.25

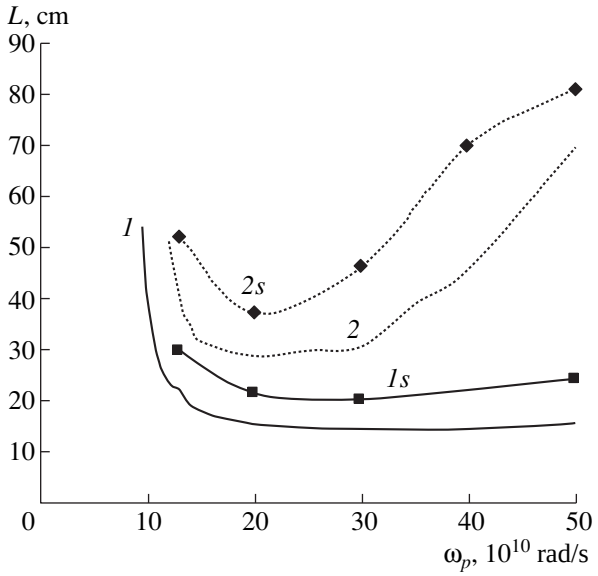

Fig. 11. Optimum amplifier length vs. the plasma frequency for (*1*, *1s*) r_p = 0.8 cm and (*2*, *2s*) r_p = 1.1 cm for (*1*, *2*) monochromatic and (*1s*, *2s*) noisy signals.

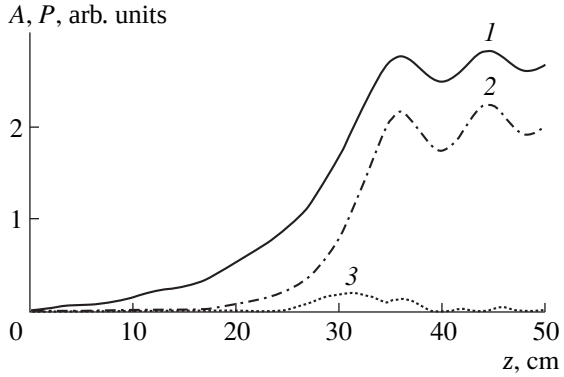

Fig. 12. Spatial profiles of the wave amplitudes in a Raman amplifier: (*1*) amplitude of the plasma wave, (*2*) energy flux of the plasma wave, and (*3*) energy flux of the beam wave.

The efficiency of the Thomson noisy amplifier is illustrated by curve *1s* in Fig. 10 as a function of ω_p and is seen to be somewhat lower than that of the related single-mode amplifier. However, the higher the plasma frequency, the closer the two efficiencies are to one another. This is illustrated by Table 1, which shows that the higher the plasma frequency ω_p, the narrower the spectrum, so that the multimode amplifier will resemble more and more the single-mode one.

Table 2. Parameters of the Raman amplifier

Plasma frequency ω_p, rad/s	Central frequency ω, rad/s	Central wavelength λ, cm	Spectral width $\Delta\omega/\omega$
13×10^{10}	3.5×10^{10}	5.4	0.6
20×10^{10}	7×10^{10}	2.7	0.6
30×10^{10}	12×10^{10}	1.6	0.3
40×10^{10}	17×10^{10}	1	0.12
50×10^{10}	25×10^{10}	0.75	0.08

Now, we consider the results of modeling a Raman noisy amplifier with the same parameters as in the previous example, but for the plasma radius r_p = 1.1 cm. Figure 14 displays the emission spectra for the Raman amplifier, computed for several plasma frequencies. Comparing Fig. 14 with Fig. 7, we can readily see that, as in the case of a Thomson amplifier, the spectral density of emission is peaked at the frequency at which the linear amplification coefficient is maximum. However, in the range of high ω_p, the spectra of the Raman amplifier are significantly narrower than those of the Thomson amplifier. The parameters of the Raman noisy amplifier are presented in Table 2.

Curves *2s* in Figs. 10 and 11 illustrate, respectively, the efficiency of the Raman noisy amplifier and its length.

Note that the terms “Raman amplifier” and “Thomson amplifier” are rather conditional. Microwaves can be amplified in a purely Thomson regime only when $r_b = r_p$. In the range of plasma frequencies under consideration, an amplifier with r_b = 0.65 cm and r_p = 0.8 cm (Figs. 6, 13) operates mainly in the Thomson regime, whereas an amplifier with r_b = 0.65 cm and r_p = 1.1 cm operates mainly in the Raman regime. However, in the range of high plasma frequencies, both of the amplifiers operate in the Raman regime.

Special attention should be paid to amplification at low plasma frequencies close to the thresholds for the onset of a beam–plasma instability (curves *1* in Figs. 6, 7, 13, 14). Figures 4a and 4b show that, in this case, neither wave–wave resonance nor wave–particle resonance is possible. With this in mind, we can say that, in the case of amplification at low plasma frequencies, the terms “Raman regime” and “Thomson regime” have a purely formal meaning. The amplification occurs at very low frequencies with a fairly high efficiency and broad bandwidth. The results presented above show that, by altering only the plasma density and slightly changing the plasma radius, we can vary the emission parameters over a very broad range, keeping the amplification efficiency high. For example, it is possible to amplify microwaves with wavelengths from several centimeters to several millimeters, the relative width of the emission spectra being from several tens of percent to several percent. Moreover, these ranges may be even broader. For example, oscillators with longer waveguides and lower plasma densities are, in fact, capable of amplifying microwaves with λ up to one decimeter or longer, whereas increasing the plasma density makes it possible to progress into millimeter and submillimeter wavelength ranges.

Recall that all of the results presented here were obtained for real systems studied in experiments [55–

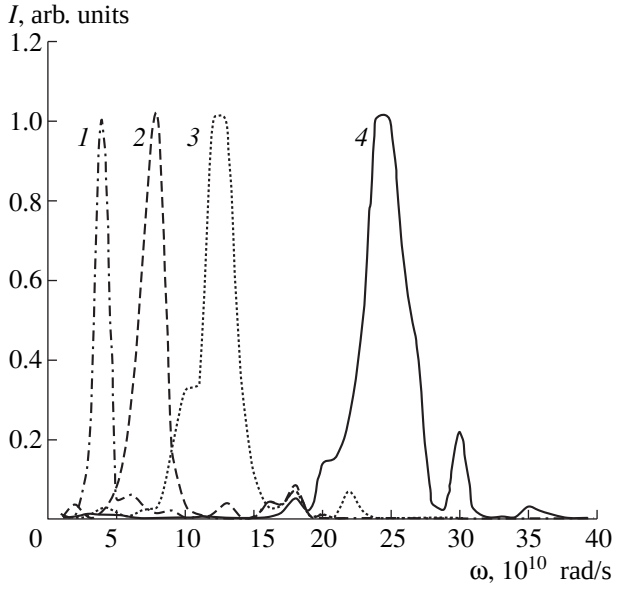

Fig. 13. Spectral density of microwave radiation at the exit from an amplifier for $r_p = 0.8$ cm and plasma frequencies of (*1*) 13, (*2*) 20, (*3*) 30, and (*4*) 50×10^{10} rad/s.

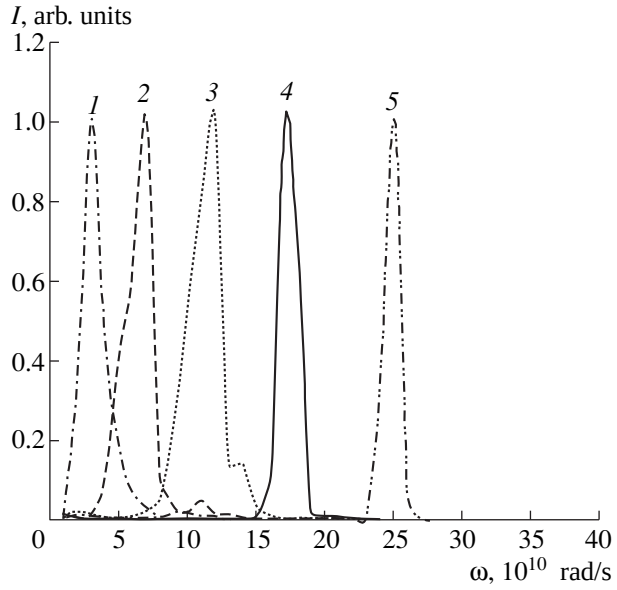

Fig. 14. Spectral density of microwave radiation at the exit from an amplifier for $r_p = 1.1$ cm and plasma frequencies of (*1*) 13, (*2*) 20, (*3*) 30, (*4*) 40, and (*5*) 50×10^{10} rad/s.

58]. On the whole, theoretical predictions for the most important parameters, specifically, the threshold plasma frequency, the start current of a beam (see below), the frequency band of the emitted radiation, and the spectral width of the emission spectrum, are consistent with the experimental data. However, the theoretical and experimental data on the total emission efficiency are contradictory: the efficiency achieved in experiments is two times lower than the predicted one. There are also other respects in which theory and experiments disagree. For example, Kuzelev *et al.* [55] presented the experimental data demonstrating that, in some cases, the emission spectra of plasma microwave sources are much broader than those evaluated theoretically. On the other hand, some measurement results obtained in those experiments agree well with theoretical predictions. For this reason, it is very important to understand why the measured emission spectra are broader than the predicted ones. This is the subject of the next section.

8. FACTORS GOVERNING THE BROADENING OF THE EMISSION SPECTRA OF ELECTROMAGNETIC WAVES IN PLASMA MICROWAVE SOURCES

Up to this point, we applied the term "multimode signal" to numerous amplified waves with different frequencies and studied the formation of the emission spectrum just in that case. However, there are a number of factors (e.g., the presence of numerous modes with different azimuthal and transverse mode numbers and possible background plasma in the waveguide and others) that can also influence the spectral content of the amplified signal. Using linear theory, we will consider the factors that are, in our opinion, most important.

First, we examine the effect of modes with different azimuthal mode numbers. In the previous sections, we considered only an azimuthally symmetric mode with $l = 0$, so the role played by the other modes needs to be established. For low-current beams (more precisely, for beams with negligible currents), we can do that by using relationships (3.9), (3.5), and (3.7). In the range

$$\omega_p^2 < u^2\gamma^2 k_{\perp p}^2 (l = 0)_{\omega \to 0}, \tag{8.1}$$

no modes are amplified; in the range

$$u^2\gamma^2 k_{\perp p}^2 (l = 0)_{\omega \to 0} < \omega_p^2 < u^2\gamma^2 k_{\perp p}^2 (l = 1)_{\omega \to 0}, \tag{8.2}$$

only an azimuthally symmetric mode is amplified; and so on [clearly, the transverse wavenumbers (3.7) enter (8.1) and (8.2)]. The rules formulated in (8.1) and (8.2) for selective amplification of the modes cannot be applied to finite-current (and the more so high-current) beams, because the higher the beam current, the lower the threshold plasma frequency (see above). In the case of high-current REBs, several azimuthal modes are simultaneously amplified under approximately the same conditions. As an example, Fig. 15 illustrates frequency profiles of the amplification coefficients for the first four azimuthal modes, beginning with the zeroth, in a Raman amplifier. The computation parameters are the same as in Fig. 3. The azimuthal mode numbers are given above the corresponding curves. The entire frequency band in which the four azimuthal modes are amplified is seen to be significantly broader than the

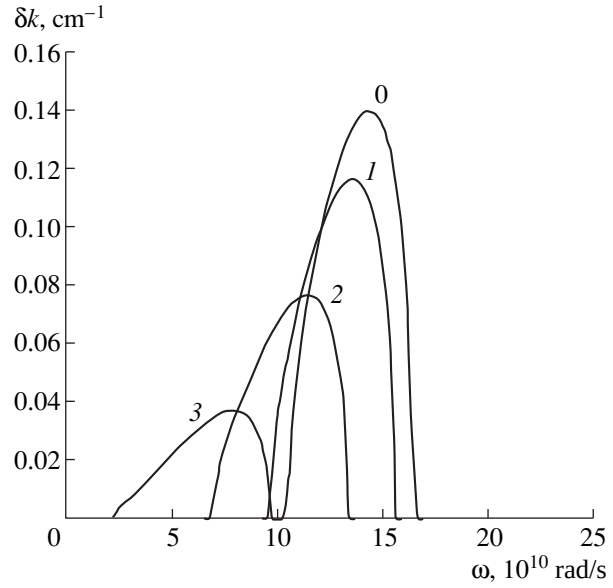

Fig. 15. Frequency profiles of the amplification coefficient for modes with azimuthal mode numbers 0, 1, 2, and 3.

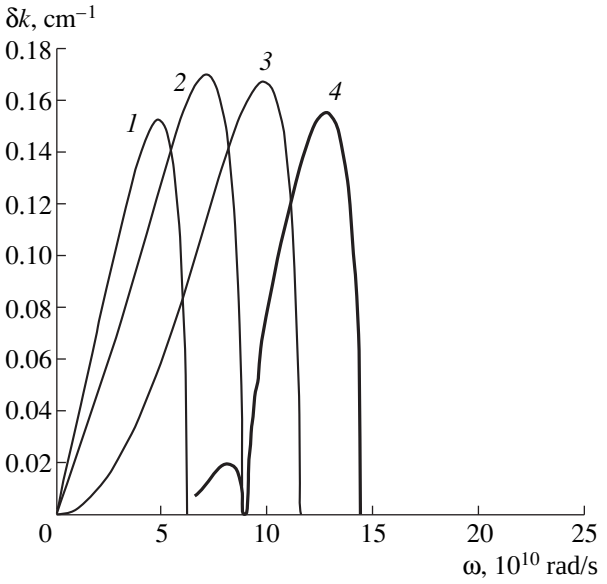

Fig. 16. Amplification coefficients for azimuthally symmetric modes in the model in which the thickness of the beam and plasma is finite.

amplification band obtained for a single azimuthally symmetric mode.

Another reason for broadening of the frequency amplification band is the finite thickness of a high-current REB. In beams of finite thickness, in addition to surface waves, there are internal waves, which give rise to additional resonances and, consequently, lead to a broadening of the amplification band. In a finite-thickness annular plasma column, internal plasma waves are also present, but an REB excites no internal plasma waves, so that no plasma-related resonances appear. In the regime of the collective Cherenkov effect ($\theta \ll 1$), in which the amplification band is narrow, the influence of the finite thickness of an REB can be significant. The impact of the finite beam thickness can be captured only numerically by solving the relevant dispersion relation [14, 79]. As an example, we consider a circular waveguide in which a thin-walled annular beam and plasma have the density profiles

$$P_\alpha(r) = \begin{cases} 0, & r < r_\alpha - \Delta_\alpha/2, \\ 1, & r_\alpha - \Delta_\alpha/2 < r < r_\alpha + \Delta_\alpha/2, \\ 0, & r > r_\alpha + \Delta_\alpha/2, \end{cases} \qquad (8.3)$$

where $\alpha = p$ and b. For $\Delta_\alpha \ll R$, the plasma and beam are thin-walled but they cannot be regarded as being infinitely thin, so that the model profiles $P_\alpha = \Delta_\alpha \delta(r - r_\alpha)$ (see above) fail to describe them. To save space, we omit a very lengthy dispersion relation [79] for the beam–plasma system described by profiles (8.3) and refer the interested reader to, e.g., papers [19, 53], which contain analogous dispersion relations (with detailed derivations).

Numerical solutions to the relevant dispersion relation are displayed in Fig. 16, which shows the imaginary parts of the complex amplification coefficient computed for different plasma frequencies, the remaining parameters being the same as in Fig. 3. An analysis of curves *1*, *2*, and *3*, corresponding to the plasma frequencies 20, 25, and 30×10^{10} rad/s, shows that, in the range of low plasma frequencies where the frequencies at which the emission is amplified are not yet high and the coupling coefficient is not small, the behavior of the amplification coefficient does not deviate from that in the case of the single-particle Cherenkov effect. However, for a plasma frequency of 35×10^{10} rad/s (heavy curve *4*), for which the behavior of the amplification coefficient turns out to be the same as in the case of the collective Cherenkov effect, microwaves are amplified not only in the main frequency band but also in a lower frequency range; this range appears because of the interaction between an internal beam wave and a surface plasma wave, which is weaker than the interaction between a surface beam wave and a surface plasma wave. Using (4.13) and the estimates obtained for the transverse wavenumbers of the internal and surface waves, we can show that the ratio of the corresponding amplification coefficients is on the order of $(\Delta_b/R)^{1/4}$.

One more reason for broadening of the amplification band is associated with the fact that real transverse plasma density profiles may be more complicated than those in (8.3). There is experimental evidence that the transverse plasma profiles are fairly complicated functions of radius r. Thus, the main thin-walled annular plasma is often observed against the background of an almost homogeneous, lower density plasma, which is

created due to ionization of the residual gas. Let us analyze the effects of such a background plasma [60].

We assume that the transverse density profiles of the plasma and beam are

$$N_p(r) = n_{pf} + n_p\Delta_p\delta(r - r_p), \quad N_b(r) = n_b\Delta_b\delta(r - r_b), \tag{8.4}$$

where n_{pf} is the constant background density and n_p and n_b are the densities in terms of which the Langmuir frequencies ω_p and ω_b were introduced. We also introduce the Langmuir frequency of the background plasma, $\omega_{pf} = \sqrt{4\pi e^2 n_{pf}/m}$, and the notation

$$X^2 = \chi^2(\omega_{pf}^2/\omega^2 - 1). \tag{8.5}$$

First, we consider a waveguide with a thin-walled annular plasma against a homogeneous lower density plasma background, assuming that there is no beam. The dispersion relation for this waveguide coincides with equation (3.4) in which $k_{\perp p}^2$ should be replaced by

$$k_{\perp p}^2 = \left[\frac{\pi}{2} r_p\Delta_p J_0^2(Xr_p)\left(\frac{N_0(XR)}{J_0(XR)} - \frac{N_0(Xr_p)}{J_0(Xr_p)}\right)\right]^{-1}. \tag{8.6}$$

In the range $k_z c > \omega > \omega_{pf}$, the quantity in (8.5) is negative and expression (8.6) reduces to

$$k_{\perp p}^2 = \left\{r_p\Delta_p I_0^2(\hat{X}r_p)\left[\frac{K_0(\hat{X}r_p)}{I_0(\hat{X}r_p)} - \frac{K_0(\hat{X}R)}{I_0(\hat{X}R)}\right]\right\}^{-1}, \tag{8.7}$$

where the sign of $\hat{X}^2$ is opposite to that of (8.5). In the absence of a background plasma ($\omega_{pf} = 0$), expression (8.7) passes over to (3.5).

In contrast, in the absence of a thin-walled annular plasma ($\omega_p = 0$), equation (3.4) for a waveguide filled with a homogeneous background plasma gives $k_{\perp p}^2 = 0$, which is valid, by virtue of (8.6), only when $J_0(XR) = 0$. This yields the familiar dispersion relation for the spectra of the internal waves of a homogeneous plasma with the Langmuir frequency ω_{pf} in a waveguide.

Let us consider the spectra for a waveguide with both a thin-walled annular plasma and a background plasma. We again turn to the parameters of a real experimental device [55]: the waveguide radius is R = 1.8 cm, the mean plasma radius is r_p = 1.1 cm, the plasma thickness is Δ_p = 0.1 cm, the Langmuir frequency of the annular plasma is $\omega_p = 35\times10^{10}$ rad/s, and the Langmuir frequency of the background plasma is $\omega_{pf} = 8\times10^{10}$ rad/s. The latter frequency is taken tentatively, because it was not measured directly in the experiments. However, in accordance with the parameter values adopted, we are justified in taking the background density to be lower than the annular plasma density by a factor of 10 to 20. We again describe an REB by the parameters used throughout the paper.

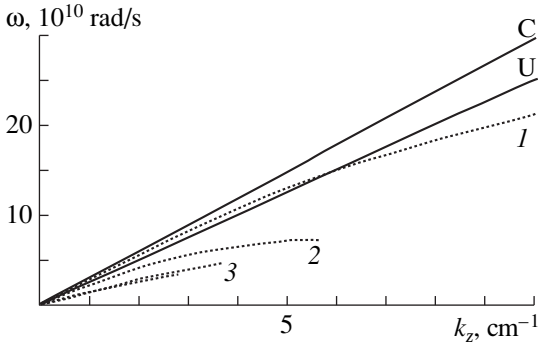

Fig. 17. Dispersion curves for an annular plasma in the presence of the low-density homogeneous plasma background: (*1*) surface wave of the annular plasma, (*2*, *3*) internal waves of the background plasma, (*C*) $\omega = k_z c$ line, and (*U*) $\omega = k_z u$ line.

Figure 17 shows dispersion curves obtained by numerically solving dispersion relation (3.4) with $k_{\perp p}^2$ defined in (8.6) or (8.7) for the above parameters of the annular and background plasmas in a waveguide with no beam. Curve *1* reflects the dispersion of the wave that arises in the waveguide because of the presence of a thin-walled annular plasma. In the frequency range $k_z c > \omega > \omega_{pf}$, this is a conventional surface (cable) plasma wave. However, in the low-frequency range $\omega < \omega_{pf}$, this wave is an internal wave. Curves *2* and *3* in Fig. 17 correspond to conventional internal waves (the fundamental and first radial modes) in a homogeneous background plasma. Of course, the waves of the annular and background plasmas interact with each other (e.g., curve *1* "forces" curve *2* to displace downward). However, we can readily show that this interaction is too weak to play a decisive role. To do this, it is sufficient to solve dispersion relation (3.4) for $\omega_p = 0$ and $\omega_{pf} = 0$, plot the corresponding dispersion curves, and compare them with those shown in Fig. 17. Hence, the major conclusion is that the surface wave of a thin-walled annular plasma and the internal waves in the background plasma have essentially no impact on each other, so that the beam can interact with both of them simultaneously.

To elucidate the relative positions of the dispersion curves in Fig. 17, we plotted the line $\omega = k_z c$ (marked by *c*). Clearly, all of the dispersion curves of interest to us lie below this line. In Fig. 17, we also plotted the resonance line $\omega - k_z u = 0$ corresponding to the single-particle Cherenkov resonance (marked by *u*). We can see that the resonance line intersects dispersion curve *1* of the surface wave in the range of fairly high frequencies and is unlikely to intersect dispersion curve *2* (and the more so curve *3*) of the internal wave. Consequently, the single-particle Cherenkov resonance condition is

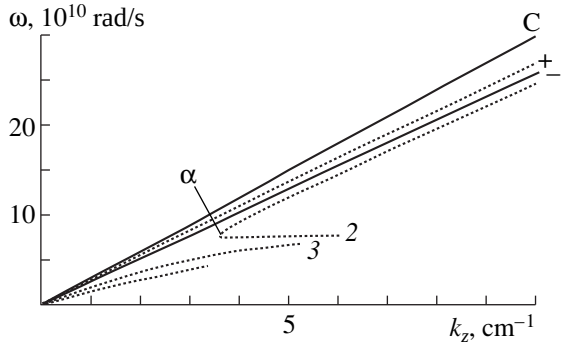

Fig. 18. Interaction of an annular beam with a low-density homogeneous background plasma: (*2*) and (*3*) refer to the internal plasma waves and the plus and minus signs mark the fast and slow waves, respectively.

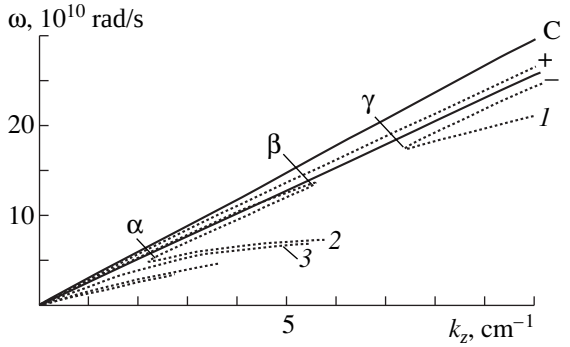

Fig. 19. Interaction of an annular beam with a thin-walled annular plasma and low-density homogeneous background plasma.

definitely satisfied for the surface wave and may be violated for the internal wave. However, in the presence of a dense beam, both of these waves may be amplified simultaneously.

Now, we examine an intermediate case in which a thin-walled annular electron beam propagates through a waveguide filled with a background plasma in the absence of an annular plasma. The relevant dispersion relation obviously coincides with equation (4.3) in which $k_{\perp b}^2$ is defined by (8.6) or (8.7) and the subscript *p* (referring to the plasma) should be replaced by the subscript *b* (referring to the beam).

Figure 18 illustrates the results of solving the above version of dispersion relation (4.3) numerically. Along with curves *2* and *3* (which are plotted in Fig. 17), Fig. 18 displays two new dispersion curves, which are marked by plus and minus signs and correspond to slow and fast waves of the space charge of an electron beam. One can see that the slow wave of the space charge interacts with the internal wave *2*. As a result, the internal plasma wave begins to be amplified over a frequency band lying between zero and the frequency corresponding to the point α on dispersion curve *2* in Fig. 18.

Hence, we have shown that the internal wave in the background plasma is amplified over a wide low-frequency band. Let us estimate the corresponding amplification coefficient $\delta k = |\mathrm{Im}(k_z)|$. Since equation (4.3) is difficult to solve, we assume that the beam acts only to perturb the plasma waveguide. This assumption enables us to transform (4.3) into the following dispersion relation, which is well known in the theory of beam–plasma amplifiers and oscillators [15, 19]:

$$k_\perp^2 + \chi^2\left(1 - \frac{\omega_{pf}^2}{\omega^2}\right) = \chi^2 G \frac{\omega_b^2 \gamma^{-3}}{(\omega - k_z u)^2}, \qquad (8.8)$$

where $G = (2\Delta_b r_b/R^2)[J_0^2(k_\perp r_b)/J_1^2(k_\perp R)]$ is the geometric factor of a thin-walled annular beam, $k_\perp = \mu_{01}/R$ is the transverse wavenumber of the fundamental mode of the internal plasma wave, and $\mu_{01} \approx 2.4$ is the first root of the zero-order Bessel function. Of course, the assumption that the dense beam acts only to perturb the plasma is not quite correct; however, a more thorough analysis shows that it may be used for estimates.

Since we are content merely with estimates, we turn to equation (8.8) and the familiar solution to this equation [15, 19]:

$$\delta k = \frac{\sqrt{3}}{2}\frac{\omega}{u}\left(G\frac{\omega_b^2\gamma^{-7}}{2k_\perp^2 u^2}\right)^{1/3}. \qquad (8.9)$$

Assuming that ω in (8.9) is some mean frequency in the amplification band for the internal wave, we obtain $\delta k \approx 0.1\ \mathrm{cm}^{-1}$. Below, we will compare this value with the amplification coefficient for the surface wave.

Now, we consider the most general case of a waveguide with a beam and with both annular and background plasmas. The general dispersion relation coincides with equation (4.4), but with appropriately corrected quantities $k_{\perp p}^2$ and $k_{\perp b}^2$ and with the coupling coefficient

$$\theta = \frac{J_0(Xr_b)[N_0(Xr_p)J_0(XR) - N_0(XR)J_0(Xr_p)]}{J_0(Xr_p)[N_0(Xr_b)J_0(XR) - N_0(XR)J_0(Xr_b)]}. \qquad (8.10)$$

This formula is written for the case $r_b < r_p$, which was realized in the experiments under discussion.

Figure 19 illustrates the results of solving dispersion relation (4.4) numerically. Along with the curves plotted in Fig. 18, we can see the dispersion curve of the surface wave of an annular plasma. As a result of the interaction between this wave and the slow wave of the space charge of the beam, a new amplification band appears, which lies between the frequencies corresponding to the points β and γ on the dispersion curves.

Additionally, the amplification band between the zero frequency and the frequency corresponding to the point α becomes somewhat narrower in comparison with that in Fig. 18.

Hence, the background plasma causes the entire amplification band to broaden: the amplification occurs in both high- and low-frequency bands. In order to understand to what extent this circumstance is important in a real situation, we must compare the amplification coefficients in different frequency ranges. In the low-frequency band, the amplification coefficient has already been estimated by means of (8.9). To obtain the desired estimate in the high-frequency band, we may assume that the background plasma has only a minor effect on the amplification coefficient. Under this assumption, Fig. 15 immediately gives the numerical estimate $\delta k = 0.14$ cm^{-1}, which is of the same order of magnitude as the amplification coefficient in the low-frequency range. We can therefore conclude that, in the presence of a low-density plasma background in the waveguide, the amplification band extends well into the low-frequency range. A similar effect was observed in some of the experiments described in [55].

Above, we have considered the amplification in the collective Cherenkov regime, in which case the idealized spectrum is narrow and the factors that lead to a broadening of the spectrum should be investigated in detail. The question arises of how the background plasma affects the amplification in the single-particle Cherenkov regime. As $r_p \longrightarrow r_b$, the coefficient θ approaches unity and the collective Cherenkov regime goes over to the single-particle regime. Accordingly, the points β and α in Fig. 19 approach the origin of the coordinates. As a result, the two amplification bands merge into one broad band, which extends between the zero frequency and the frequency corresponding to the point γ, and the internal wave *2* is no longer amplified. Consequently, in the single-particle Cherenkov regime, the role of the low-density background plasma is insignificant.

To conclude the discussion of the impact on amplification of a homogeneous background plasma in a waveguide, we consider the features of an amplifier operating with a thin-walled annular beam against the plasma background in the absence of an annular plasma. The dispersion relation for determining the complex spectra in this system is similar in structure to (4.3), but we rewrite it in a form that is convenient for our purposes [19]:

$$(\omega - k_z u)^2 = \omega_b^2 \gamma^{-3} S_b \sum_{n=1}^{\infty} \frac{\chi^2}{k_{\perp n}^2 + \chi^2 \varepsilon_p} \frac{\varphi_n^2(\mathbf{r}_b)}{||\varphi_n||^2}, \quad (8.11)$$

where $S_b = 2\pi r_b \Delta_b$ is the cross-sectional area of the beam and $\varepsilon_p = (1 - \omega_p^2/\omega^2)$. The poles of the right-hand side of (8.11), i.e., the zeros of the functions

$$k_{\perp n}^2 + \chi^2 \varepsilon_p = 0, \quad n = 1, 2, \ldots, \quad (8.12)$$

determine the spectra (3.3) of internal plasma waves. Since, in equation (8.11), these waves are coupled to each other through the beam even in the linear approximation, the problem of the competition between the modes and the problem of the width of the amplification band are more difficult to solve. We can assume that, if the beam is dense and the inequalities

$$\omega_p^2 > k_{\perp n}^2 u^2 \gamma^2 \quad (8.13)$$

hold for several modes with the mode numbers *n*, then the amplification band will be broad (it will extend from zero to nearly the plasma frequency) and a large number of modes with different azimuthal and radial mode numbers will be amplified regardless of the spectral content of the input signal.

9. MICROWAVE GENERATION IN THE REGIME OF THE STIMULATED CHERENKOV EFFECT

We first considered a Cherenkov plasma microwave amplifier in order not to begin with a complicated problem of the extraction of microwaves from the plasma. Now, we examine the exit boundary $z = L$ of the system, thereby switching from the amplification problem to the problem of microwave generation in a beam–plasma waveguide. We analyze the generation problem qualitatively (more rigorous relationships can be found, e.g., in our book [19]).

A plasma wave amplified by a beam is partially reflected from the exit boundary $z = L$ and returns to the entrance plane $z = 0$. This effect may result in the self-excitation of the amplifier (i.e., in the start-up of microwave generation). Let us determine the conditions under which this happens.

We consider a wave with amplitude A_0 that enters the waveguide through the entrance plane $z = 0$ from the outside. Let the plasma wave amplified by the beam have the amplitude A^+ at the exit plane and let the plasma wave that propagates in the direction opposite to the propagation direction of the beam and provides feedback have the amplitude A^-. We denote the reflection coefficient of the boundary $z = L$ for the amplified wave by κ and the amplification coefficient for the plasma wave, i.e., the absolute value of the imaginary part of (4.7), by δ^+.

At the boundary $z = L$, the amplitude of the amplified wave is equal to $A^+\exp(\delta^+ L)$ and the amplitude of the backward plasma wave is

$$A^- = A^+ \kappa \exp(\delta^+ L). \quad (9.1)$$

Since an oppositely propagating plasma wave does not interact with the beam, its amplitude at the entrance plane $z = 0$ is also determined by (9.1). Additionally, at $z = 0$, the amplitudes of the injected wave, amplified

plasma wave, and backward plasma wave satisfy the balance relation

$$A^+ = A^- + A_0. \quad (9.2)$$

Formulas (9.1) and (9.2) give the amplitude of the amplified plasma wave:

$$A^+ = \frac{A_0}{1 - \kappa \exp(\delta^+ L)}. \quad (9.3)$$

The self-excitation of the Cherenkov plasma microwave amplifier occurs when the amplitude of the amplified plasma wave in (9.3) becomes infinitely large. This allows us to determine the condition for the self-excitation of the amplifier (i.e., for the start-up of microwave generation) [6, 19, 40]:

$$\delta^+ = \frac{1}{L}\ln\frac{1}{|\kappa|} \approx \frac{1}{L}\ln(4\gamma^2). \quad (9.4)$$

In deriving this condition, we used the estimate [40, 55] (see also the refined estimate presented in [57])

$$\kappa = (4\gamma^2)^{-1}. \quad (9.5)$$

Of course, the derivation of both the self-excitation condition and estimate (9.5) is not rigorous. The most difficult task here is to determine the reflection coefficient κ. The experiments carried out in [8, 12, 37, 38, 55] provide evidence that, for a low-frequency cable plasma wave emitted through the coaxial horn, the results obtained are likely to be qualitatively correct. We can readily verify that by comparing them with the relevant experimental data. Setting $\gamma = 2$ and varying the system length L from 10 to 30 cm, we obtain from (9.4) that the start amplification coefficient δ^+ changes from 0.1 to 0.3 cm^{-1}, which is equal in order of magnitude to the coefficients computed from dispersion relation (4.8) and shown in Fig. 5. In our opinion, the experimental conditions in [12] most likely correspond to a plasma microwave amplifier, whereas the conditions in [55] correspond to an oscillator.

In this paper, we intentionally restricted ourselves to the linear theory of a plasma microwave oscillator. The construction of a systematic quantitative nonlinear theory of an oscillator requires a deeper understanding of the processes occurring in the emitter. Unfortunately, we still lack such an understanding (although some progress in constructing the nonlinear theory of a plasma microwave oscillator and in modeling the emitter has been achieved in papers [45, 54, 56–58], in which it was shown that certain parameters of a length-optimized microwave oscillator, namely, the oscillator efficiency, the spectral content of the emitted microwaves, and the maximum output power, are almost the same as those of a plasma microwave amplifier). For this reason, we do not discuss in detail the current status of the nonlinear theory of plasma microwave oscillators. In experiments, the optimum length of the oscillator is chosen individually for each specific unit for extracting microwave radiation. In our opinion, the fact that the efficiency of the oscillators used in the experiments under discussion is lower than that predicted theoretically may be explained by the inappropriate choice of the oscillator length.

10. NONRESONANT PLASMA MICROWAVE OSCILLATOR—PLASMA MONOTRON

Thus, we can conclude that significant progress has been achieved in developing high-power Cherenkov resonant plasma sources of coherent, nearly monochromatic microwave radiation and broadband noisy microwave radiation: the sources operate in the millimeter wavelength range and their efficiency is fairly high. Hopefully, sources capable of operating in a broader wavelength range—from ≈10 cm to fractions of a millimeter—will also be developed in the near future. But it is more difficult to move into the longer-wavelength range, essentially because the sources under consideration are capable of emitting microwaves only when the plasma density is above a certain threshold. Clearly, in order to work with lower frequencies, it is necessary to reduce the threshold plasma density. This, in turn, can be done mainly by increasing the waveguide radius R, in which case, however, the length L of the entire system must be increased accordingly. The calculations show that, in order to achieve microwave generation at the wavelength $\lambda = 30$ cm (for the same beam parameters as those treated above), the radius and length of the waveguide should be enlarged to $R \geq 10$ cm and $L \geq 100$ cm. However, creating a strong magnetic field in such a large source would be too expensive.

Hence, in this section, we consider the possibility of exciting microwave radiation with a relatively long wavelength during the radiative Pierce instability in a plasma waveguide with an annular plasma.[5] Unlike the aperiodic Pierce instability, which occurs at beam currents above the Pierce limiting current [15, 19, 80]

$$I_P = \gamma^2 I_0, \quad (10.1)$$

where I_0 is the vacuum limiting current (5.4), and leads to beam destruction, the radiative Pierce instability can occur at arbitrarily low beam currents. Moreover, the radiative Pierce instability may develop in waveguides with no plasma, i.e., in purely vacuum devices [63]. However, since we are primarily interested here in the

[5] To the best of our knowledge, Bignard *et al.* [66] were the first to observe the radiative Pierce instability of a nonrelativistic beam and to introduce the term "monotron." Since the generation mechanism underlying their operation lacked a theoretical explanation, the efficiency of monotrons was generally considered to be low [67]. Klochkov *et al.* [63–65] established that this mechanism is the radiative Pierce instability. They developed a systematic linear theory of the relativistic radiative Pierce instability and demonstrated the promising outlook for using relativistic monotrons, including those filled with a plasma. Here, we restrict ourselves to considering a plasma monotron capable of exciting a low-frequency (plasma) oscillation branch with the frequency spectrum (3.6).

excitation of a low-frequency cable plasma wave in the course of the radiative Pierce instability, we consider a plasma-filled waveguide. In order to avoid the onset of the resonant Cherenkov instability, we assume that the plasma density is below the threshold.

We emphasize that the radiative Pierce instability can occur only in the presence of positive feedback, as is the case with aperiodic Pierce instability. This circumstance makes it impossible to create amplifiers based on the radiative Pierce instability. Therefore, we will consider only the type of microwave oscillators that are referred to as plasma monotrons based on a cable wave and restrict ourselves to linear theory and the simplest nonlinear estimates.

Let the oscillator length be $L \gg R$. In the region $0 < z < L$, the field is composed of the fields of four waves: two beam waves with amplitudes A_3 and A_4 and two plasma waves with amplitudes A_1 and A_2. The beam waves propagate in the positive direction along the z-axis. One of the plasma waves (e.g., the wave with A_1) propagates in the same direction, while the other wave (with A_2) moves in the opposite direction and provides feedback. At the boundary $z = L$, the waves with A_1, A_3, and A_4 are partially converted into an oppositely propagating wave with A_2 and partially converted into the wave of the emitting horn. Generally, this process can be described by the following boundary condition at $z = L$ [19]:

$$A_2 \exp(ik_{z2}L) = \sum_{\nu = 1, 3, 4} \kappa_\nu A_\nu \exp(ik_{z\nu}L), \quad (10.2)$$

where $\kappa_\nu = \kappa_{1, 3, 4}$ are the complex coefficients for wave conversion. The wavenumbers $k_{z\nu}$ in (10.2) are determined from dispersion relation (4.4). Under the condition

$$\frac{I_b}{I_P} = \frac{\omega_b^2 \gamma^{-3}}{k_{\perp b}^2 u^2} \ll 1, \quad (10.3)$$

which implies that the electron beam current is lower than the Pierce current, we can assume that the conversion (reflection) coefficient κ_1 for a cable wave is equal to that calculated in the absence of a beam (the same approach was taken in the previous section). The coefficients $\kappa_{3, 4}$ are approximately equal to $\kappa_2 = \kappa_4 \equiv \kappa_b$. Below, we will assume that inequality (10.3) is satisfied and we will refine the coefficients $\kappa_1 \equiv \kappa$ and κ_b.

At the boundary $z = 0$, the injected beam remains unperturbed and the wave with A_2 is reflected as if it were reflected from a metal mirror (see [19, 63–65] for details). This allows us to write the boundary conditions at $z = 0$ as

$$A_\nu = \alpha_\nu A_2, \quad \nu = 1, 3, 4. \quad (10.4)$$

The most general expressions for the transformation coefficients α_ν are derived in [19].

The requirement that the solutions to the linearized equations (2.1)–(2.7) with the boundary conditions (2.8), (10.2), and (10.4) be nontrivial yields the equation for determining the complex frequencies at which microwaves are generated. The approach described in this section is the most general and could also be applied in the previous section to study a conventional plasma microwave oscillator (as was done in [19]). However, a conventional oscillator based on the resonant beam–plasma interaction can be analyzed in a simple qualitative way (just as we did above). However, qualitative considerations are insufficient to study plasma monotrons, in which the interaction of the beam with the electrodynamic system is nonresonant and which therefore require a rigorous analysis. We skip over the details of the mathematical procedure (which are given in [63–65]) and present the final equation for determining the complex frequencies for a plasma monotron based on a cable wave:

$$\kappa \exp\left(i\frac{\omega}{u_p}L\right) - \exp\left(-i\frac{\omega}{u_p}L\right) = 2i\kappa_b \frac{\tilde{\omega}_b L}{u}\frac{u^2}{c^2}\gamma^{-1/2}\frac{(1 - c^2/u_p^2)}{(1 - u^2/u_p^2)} \times \sin\left[\frac{\tilde{\omega}_b L}{u}\gamma^{-5/2}\left(1 - \frac{u^2}{u_p^2}\right)^{-1/2}\right] e^{i\frac{\omega}{u}L}, \quad (10.5)$$

where u_p is the phase velocity of a cable wave [see (3.6)], $\tilde{\omega}_b^2 = \omega_b^2/\varepsilon_p$, and ε_p is the longitudinal plasma permittivity. Equation (10.5) was derived for a particular case in which the mean radius and thickness of an annular plasma coincide with those of an annular beam.

In the absence of a beam ($\omega_b = 0$), equation (10.5) describes how the microwave field escapes from the plasma resonator, in which case the solution is

$$\frac{\omega}{u_p} = \frac{\pi n}{L} + \frac{i}{2L}\ln|\kappa|, \quad (10.6)$$

where $n = 1, 2, \ldots$. In the low-frequency range of interest to us, $|\omega| \ll \omega_p$, in which the phase velocity u_p is essentially independent of ω, we obtain from (10.6) the damping rate associated with the escape of the microwave field from the resonator:

$$\delta \equiv \mathrm{Im}\,\omega = -\frac{u_p}{2L}\ln\frac{1}{|\kappa|}. \quad (10.7)$$

An instability that can arise in a resonator in the presence of a beam introduces the following correction

to the frequency ω:

$$\delta\omega = (-1)^n \frac{|\kappa_b|}{\sqrt{|\kappa|}} \frac{\omega_b \omega_p \gamma^{-1/2}}{\sqrt{\omega_p^2 + k_{\perp p}^2 c^2}} \frac{k_{\perp p}^2 u^2}{q^{3/2}} \frac{c}{L} \times \sin\left(\pi n \frac{u_p \omega_b \gamma^{-5/2}}{u q^{1/2}}\right) e^{i\pi n \frac{u_p}{u}}. \quad (10.8)$$

Here, the quantity $q = \gamma^{-2}(\omega^2 + k_{\perp p}^2 u^2\gamma^2 - \omega_p^2) > 0$ is positive, because the plasma frequency is below the threshold. Clearly, for the radiative Pierce instability to occur, the growth rate (10.8) should exceed the damping rate (10.7) in absolute value; i.e., the following condition should hold:

$$\omega_b > \omega_{b,\,\mathrm{st}} \equiv \frac{\sqrt{\gamma} q^{3/2}}{2k_{\perp p}^2 u^2} \sqrt{\frac{|\kappa|}{|\kappa_b|^2}} \ln\frac{1}{|\kappa|}, \quad (10.9)$$

where the start Langmuir frequency of the beam, $\omega_{b,\,\mathrm{st}}$, is related to the start current for exciting a plasma monotron based on a cable wave by

$$I_{\mathrm{st}} = 0.5 u \frac{m}{e} r_b \Delta_b \omega_{b,\,\mathrm{st}}^2 \ [\mathrm{A}]. \quad (10.10)$$

Now, we refine the coefficients κ and κ_b. The minimum absolute value of κ is described by formula (9.5) in the previous section. In the case of an ideal resonator, in which the boundary $z = L$ is a metal surface, we have $|\kappa| = 1$. The actual value of the reflection coefficient κ is between these two limiting values. The conversion coefficient κ_b for beam waves can be evaluated as $|\kappa_b| = u_p/u$, which is smaller than unity if the plasma density is below the threshold.

To complete the picture, note that the condition for the beam electrons to slip out of resonance due to deceleration [mathematically, this means that the argument of the sine in (10.8) changes sign],

$$\frac{\omega L}{u}\frac{(\delta u)}{u} = \arccos\left[\frac{\omega_{b,\,\mathrm{st}}/\omega_b}{\sin(\omega_b L/u\gamma^{5/2})}\right] \equiv \Delta, \quad (10.11)$$

yields the following estimate for the generation efficiency in a plasma resonator:

$$E \le \gamma^2 \frac{c}{\omega L}\Delta. \quad (10.12)$$

To estimate the efficiency with which microwaves are emitted from the resonator, expression (10.12) should be multiplied by $(1 - |\kappa|^2)$. At $\kappa \sim 1$, the emission efficiency is much lower than (10.12); nevertheless, for $\omega \simeq 6 \times 10^9$ rad/s, $|\kappa| \simeq 0.9$, $\gamma \simeq 2$, $\Delta \simeq 1$, and $L \simeq$ 30–50 cm, it may be as high as 10–15%.

11. CONCLUSIONS

Finally, we briefly summarize the most important results.

(i) At present, we have a fairly complete theory of plasma amplifiers based on the stimulated Cherenkov effect, which is adequate for explaining many experimental results. The main shortcoming of this theory is that the methods for calculating the outlet horns for extracting microwave radiation have not been worked out in detail.

(ii) The problem of calculating the outlet horns is especially important in the theory of both resonant (based on stimulated Cherenkov emission) and nonresonant (based on the radiative Pierce instability) plasma microwave oscillators. It is for this reason that a systematic nonlinear theory of plasma microwave oscillators is still not fully developed.

(iii) Resonant plasma microwave oscillators and amplifiers successfully operate in the centimeter wavelength range, in which narrowband ($\Delta\omega/\omega < 0.1$) and broadband ($\Delta\omega/\omega \approx 1$) microwave radiation can be produced by the highly efficient sources that have already been designed.

(iv) In the long-wavelength range (at frequencies $\omega \le 10^9$ rad/s), nonresonant plasma microwave sources (plasma monotrons based on a cable wave) seem to be more promising. However, the theory of monotrons is still far from being fully developed, and they have not been implemented in experiments.

REFERENCES

1. A. I. Akhiezer and Ya. B. Faĭnberg, Dokl. Akad. Nauk SSSR **555**, 65 (1949).
2. D. Bohm and E. Gross, Phys. Rev. **75**, 1851 (1949).
3. L. S. Bogdankevich and A. A. Rukhadze, Usp. Fiz. Nauk **103**, 609 (1971) [Sov. Phys. Usp. **14**, 163 (1971)].
4. M. S. Rabinovich and A. A. Rukhadze, Fiz. Plazmy **2**, 715 (1976) [Sov. J. Plasma Phys. **2**, 397 (1976)].
5. L. S. Bogdankevich, M. S. Rabinovich, and A. A. Rukhadze, Izv. Vyssh. Uchebn. Zaved., Fiz. **10**, 47 (1979).
6. L. S. Bogdankevich, M. V. Kuzelev, and A. A. Rukhadze, Usp. Fiz. Nauk **133**, 3 (1981) [Sov. Phys. Usp. **24**, 1 (1981)].
7. M. V. Kuzelev, A. A. Rukhadze, and D. S. Filippychev, in *Relativistic High-Frequency Electronics* (IPF Akad. Nauk SSSR, Gorki, 1981), p. 170.
8. M. V. Kuzelev, A. A. Rukhadze, P. S. Strelkov, and A. G. Shkvarunets, Usp. Fiz. Nauk **146**, 709 (1985) [Sov. Phys. Usp. **28**, 724 (1985)]; in *Relativistic High-Frequency Electronics* (IPF Akad. Nauk SSSR, Gorki, 1983), p. 160.
9. M. V. Kuzelev and A. A. Rukhadze, Usp. Fiz. Nauk **152**, 285 (1987) [Sov. Phys. Usp. **30**, 507 (1987)].
10. M. V. Kuzelev, A. A. Rukhadze, P. S. Strelkov, and A. G. Shkvarunets, Fiz. Plazmy **13**, 1370 (1987) [Sov. J. Plasma Phys. **13**, 793 (1987)].

11. M. V. Kuzelev and A. A. Rukhadze, in *Relativistic High-Frequency Electronics* (IPF Akad. Nauk SSSR, Gorki, 1988), p. 7; in *Problems of Physics and Astrophysics* (Nauka, Moscow, 1989), p. 70.
12. A. A. Rukhadze, P. S. Strelkov, and A. G. Shkvarunets, Fiz. Plazmy **20**, 682 (1994) [Plasma Phys. Rep. **20**, 613 (1994)].
13. M. Birau, J. M. Buzi, M. V. Kuzelev, *et al.*, in *Proceedings of 11th International Conference on High-Power Particle Beams, Prague, 1996*, Vol. 1, p. 225.
14. M. Birau, M. A. Krasil'nikov, M. V. Kuzelev, and A. A. Rukhadze, Usp. Fiz. Nauk **167**, 1025 (1997) [Phys. Usp. **40**, 975 (1997)].
15. A. A. Rukhadze, L. S. Bogdankevich, S. E. Rosinskiĭ, and V. G. Rukhlin, *Physics of High-Current Electron Beams* (Atomizdat, Moscow, 1980).
16. A. N. Didenko, V. P. Grigor'ev, and Yu. P. Usov, *High-Power Electron Beams and Their Applications* (Atomizdat, Moscow, 1997).
17. E. A. Abramyan, B. A. Al'terkop, and G. D. Kuleshov, *Intense Electron Beams* (Énergoatomizdat, Moscow, 1984).
18. A. F. Alexandrov, L. S. Bogdankevich, and A. A. Rukhadze, *Principles of Plasma Electrodynamics* (Vysshaya Shkola, Moscow, 1988; Springer-Verlag, Berlin, 1984).
19. M. V. Kuzelev and A. A. Rukhadze, *Electrodynamics of Dense Electron Beams in a Plasma* (Nauka, Moscow, 1990).
20. A. F. Aleksandrov, L. S. Bogdankevich, and A. A. Rukhadze, *Oscillations and Waves in Plasma Media* (Mosk. Gos. Univ., Moscow, 1990).
21. Ya. B. Faĭnberg, At. Énerg. **11**, 313 (1961).
22. Ya. B. Faĭnberg, Usp. Fiz. Nauk **93**, 617 (1967) [Sov. Phys. Usp. **10**, 750 (1967)].
23. G. A. Bernashevskiĭ, E. V. Bogdanov, V. A. Kislov, and Z. S. Chernov, *Plasma and Electronic Microwave Amplifiers and Oscillators* (Sov. Radio, Moscow, 1965).
24. M. V. Nezlin, *Beam Dynamics in a Plasma* (Énergoatomizdat, Moscow, 1982).
25. M. V. Nezlin, Usp. Fiz. Nauk **120**, 481 (1976) [Sov. Phys. Usp. **19**, 946 (1976)].
26. D. I. Trubetskov and L. A. Pishchik, Fiz. Plazmy **15**, 342 (1989) [Sov. J. Plasma Phys. **15**, 200 (1989)].
27. A. A. Rukhadze, Vestn. Akad. Nauk SSSR, Ser. Fiz **1**, 19 (1972).
28. L. S. Bogdankevich and A. A. Rukhadze, in *Problems of Plasma Theory* (Naukova Dumka, Kiev, 1972), p. 210.
29. T. O'Neil, Phys. Fluids **8**, 591 (1972).
30. I. N. Onishchenko, A. R. Linetskiĭ, V. D. Shapiro, *et al.*, Pis'ma Zh. Éksp. Teor. Fiz. **12**, 407 (1970) [JETP Lett. **12**, 281 (1970)]; Sov. J. Plasma Phys. **14**, 591 (1972).
31. R. I. Kovtun and A. A. Rukhadze, Zh. Éksp. Teor. Fiz. **58**, 1709 (1970) [Sov. Phys. JETP **31**, 915 (1970)].
32. V. D. Shapiro, in *Problems of Plasma Theory* (Naukova Dumka, Kiev, 1972), p. 257.
33. N. F. Kovalev, M. I. Petelin, M. D. Raĭzer, *et al.*, Pis'ma Zh. Éksp. Teor. Fiz. **18**, 232 (1973) [JETP Lett. **18**, 138 (1973)].
34. J. Carmal, M. Friedman, and M. Raizer, Phys. Rev. Lett. **33**, 1478 (1974).
35. A. V. Gaponov-Grekhov and M. I. Petelin, Vestn. Akad. Nauk SSSR **4**, 11 (1979).
36. *Relativistic High-Frequency Electronics* (IPF Akad. Nauk SSSR, Gorki, 1979–1988), Vols. 1–6; *Free-Electron Generators of Coherent Radiation*, Ed. by S. F. Jacobs *et al.* (Addison-Wesley, Reading, Mass., 1980; Mir, Moscow, 1983).
37. M. V. Kuzelev, F. Kh. Mukhametzyanov, M. S. Rabinovich, *et al.*, Zh. Éksp. Teor. Fiz. **83**, 1358 (1982) [Sov. Phys. JETP **56**, 780 (1982)].
38. M. V. Kuzelev, F. Kh. Mukhametzyanov, M. S. Rabinovich, *et al.*, Dokl. Akad. Nauk SSSR **267**, 829 (1982) [Sov. Phys. Doklady **27**, 1030 (1982)].
39. Yu. P. Bliokh, V. I. Karas', Ya. B. Faĭnberg, *et al.*, Dokl. Akad. Nauk SSSR **275**, 56 (1984) [Sov. Phys. Doklady **29**, 205 (1984)].
40. M. V. Kuzelev, F. Kh. Mukhametzyanov, and A. G. Shkvarunets, Fiz. Plazmy **9**, 1137 (1983) [Sov. J. Plasma Phys. **9**, 655 (1983)].
41. M. V. Kuzelev, V. R. Maĭkov, A. D. Poezd, *et al.*, Dokl. Akad. Nauk SSSR **300**, 1112 (1988) [Sov. Phys. Doklady **33**, 444 (1988)].
42. M. V. Kuzelev, R. V. Romanov, and A. A. Rukhadze, Zh. Éksp. Teor. Fiz. **95**, 1625 (1989) [Sov. Phys. JETP **68**, 939 (1989)].
43. M. V. Kuzelev, V. A. Panin, A. P. Plotnikov, and A. A. Rukhadze, Zh. Éksp. Teor. Fiz. **96**, 865 (1989) [Sov. Phys. JETP **69**, 491 (1989)].
44. M. V. Kuzelev and A. A. Rukhadze, Fiz. Plazmy **15**, 1122 (1989) [Sov. J. Plasma Phys. **15**, 651 (1989)].
45. M. V. Kuzelev, A. A. Rukhadze, A. G. Sveshnikov, *et al.*, Mat. Model. **1**, 16 (1989).
46. M. V. Kuzelev, V. A. Panin, and A. P. Plotnikov, Zh. Tekh. Fiz. **59** (7), 164 (1989) [Sov. Phys. Tech. Phys. **34**, 810 (1989)].
47. M. V. Kuzelev, V. A. Panin, A. P. Plotnikov, and A. A. Rukhadze, Fiz. Plazmy **17**, 969 (1991) [Sov. J. Plasma Phys. **17**, 565 (1991)].
48. M. V. Kuzelev, V. A. Panin, and A. P. Plotnikov, Fiz. Plazmy **17**, 1459 (1991) [Sov. J. Plasma Phys. **17**, 845 (1991)].
49. M. V. Kuzelev, V. A. Panin, A. P. Plotnikov, and A. A. Rukhadze, Zh. Éksp. Teor. Fiz. **101**, 460 (1992) [Sov. Phys. JETP **74**, 242 (1992)].
50. M. V. Kuzelev and V. A. Panin, Fiz. Plazmy **19**, 732 (1993) [Plasma Phys. Rep. **19**, 376 (1993)].
51. M. V. Kuzelev and A. A. Rukhadze, Izv. Vyssh. Uchebn. Zaved., Radiofiz. **36**, 867 (1993).
52. O. T. Loza, P. S. Strelkov, and A. G. Shkvarunets, Tr. Inst. Obshch. Fiz., Ross. Akad. Nauk **45**, 3 (1994).
53. M. V. Kuzelev, R. V. Romanov, I. A. Selivanov, *et al.*, Tr. Inst. Obshch. Fiz., Ross. Akad. Nauk **45**, 17 (1994).
54. M. A. Krasil'nikov, M. V. Kuzelev, and A. A. Rukhadze, Zh. Éksp. Teor. Fiz. **108**, 521 (1995) [JETP **81**, 280 (1995)].

55. M. V. Kuzelev, O. T. Loza, A. V. Ponomarev, *et al.*, Zh. Éksp. Teor. Fiz. **109**, 2048 (1996) [JETP **82**, 1102 (1996)].
56. M. A. Krasil'nikov, M. V. Kuzelev, and A. A. Rukhadze, Zh. Éksp. Teor. Fiz. **112**, 1299 (1997) [JETP **85**, 705 (1997)].
57. M. Birau, M. A. Krasil'nikov, M. V. Kuzelev, and A. A. Rukhadze, Zh. Éksp. Teor. Fiz. **111**, 1258 (1997) [JETP **84**, 694 (1997)].
58. M. Birau, J.-M. Buzzi, Y. Caillez, *et al.*, in *Proceedings of International Conference on Phenomena in Ionized Gazes, Toulouse, 1997*, Vol. 3, p. 46.
59. M. V. Kuzelev and A. A. Rukhadze, Fiz. Plazmy **24**, 530 (1998) [Plasma Phys. Rep. **24**, 486 (1998)].
60. M. V. Kuzelev and A. A. Rukhadze, Fiz. Plazmy **25**, 471 (1999) [Plasma Phys. Rep. **25**, 426 (1999)].
61. Yu. V. Bobylev, M. V. Kuzelev, A. A. Rukhadze, and A. G. Sveshnikov, Fiz. Plazmy **25**, 615 (1999) [Plasma Phys. Rep. **25**, 561 (1999)].
62. O. T. Loza and P. S. Strelkov, Abstracts of Papers, *International Workshop on High-Power Microwaves, Edinburg, 1997*, p. 24.
63. D. N. Klochkov and A. A. Rukhadze, Fiz. Plazmy **23**, 646 (1997) [Plasma Phys. Rep. **23**, 598 (1997)]; D. N. Klochkov and M. Yu. Pekar, Fiz. Plazmy **23**, 650 (1997) [Plasma Phys. Rep. **23**, 602 (1997)].
64. D. N. Klochkov, M. Yu. Pekar, and A. A. Rukhadze, Zh. Éksp. Teor. Fiz. **115**, 2037 (1999) [JETP **88**, 1115 (1999)].
65. D. N. Klochkov, M. Yu. Pekar, and A. A. Rukhadze, Radiotekh. Électron. **44** (3), 379 (1999).
66. F. Bignard, P. Grivet, and A. Septer, IEEE Trans. **IM-17**, 354 (1968).
67. V. K. Yulpatov, Izv. Vyssh. Uchebn. Zaved., Radiofiz. **13**, 1784 (1970); A. V. Sorgonskiĭ, Izv. Vyssh. Uchebn. Zaved., Radiofiz. **16**, 150 (1973).
68. A. A. Rukhadze and V. V. Sever'yanov, Zh. Tekh. Fiz. **62** (12), 99 (1992) [Sov. Phys. Tech. Phys. **37**, 1179 (1992)].
69. V. G. Dorofeenko, V. B. Krasovitskiĭ, and G. V. Fomin, Zh. Éksp. Teor. Fiz. **98**, 419 (1990) [Sov. Phys. JETP **71**, 234 (1990)].
70. R. Libov, *Introduction to the Theory of Kinetic Equations* (Wiley, New York, 1969; Mir, Moscow, 1974).
71. A. F. Aleksandrov, M. V. Kuzelev, and A. N. Khalilov, Zh. Éksp. Teor. Fiz. **93**, 1714 (1987) [Sov. Phys. JETP **66**, 978 (1987)].
72. B. B. Kadomtsev, A. B. Mikhaĭlovskiĭ, and A. V. Timofeev, Zh. Éksp. Teor. Fiz. **47**, 2266 (1964) [Sov. Phys. JETP **20**, 1517 (1964)].
73. T. Tajima, Phys. Fluids **15**, 139 (1972).
74. N. I. Aĭzatskiĭ, Fiz. Plazmy **6**, 597 (1980) [Sov. J. Plasma Phys. **6**, 327 (1980)].
75. M. V. Kuzelev and A. A. Rukhadze, Pis'ma Zh. Tekh. Fiz. **6**, 1388 (1980) [Sov. Tech. Phys. Lett. **6**, 597 (1980)].
76. V. V. Bogdanov, M. V. Kuzelev, and A. A. Rukhadze, Fiz. Plazmy **10**, 548 (1984) [Sov. J. Plasma Phys. **10**, 319 (1984)].
77. A. I. Fedosov, E. A. Litvinov, S. Ya. Belomyttsev, and S. P. Bugaev, Izv. Vyssh. Uchebn. Zaved., Fiz. **10**, 134 (1977).
78. S. Ya. Belomyttsev, E. A. Litvinov, G. A. Mesyats, and A. I. Fedosov, Fiz. Plazmy **7**, 86 (1981) [Sov. J. Plasma Phys. **7**, 48 (1981)].
79. M. Birau, Phys. Rev. E **54**, 5599 (1996).
80. M. V. Kuzelev and A. A. Rukhadze, Fiz. Plazmy **9**, 1002 (1983) [Sov. J. Plasma Phys. **9**, 584 (1983)].

Translated by I. A. Kalabalyk

Plasma Physics Reports, Vol. 26, No. 3, 2000, pp. 255–261. Translated from Fizika Plazmy, Vol. 26, No. 3, 2000, pp. 275–281.

PLASMA OSCILLATIONS AND WAVES

Conversion of the Energy of a High-Current REB into Electromagnetic Wave Energy

V. I. Kurilko† and I. F. Kharchenko†

National Science Center Kharkov Institute of Physics and Technology, ul. Akademicheskaya 1, Kharkov, 310108 Ukraine

Received February 22, 1999

Abstract—Results are presented from a theoretical investigation and quantitative analysis of the physical processes that govern the efficiency of a coaxial device aimed at converting the energy of a relativistic electron beam into the energy of a TEM wave (a wave in a circular cylindrical coaxial waveguide). The key diffractional problem is solved exactly using a simplified theoretical model, which makes it possible to understand the mechanisms for the formation of a TEM wave and determine how the beam parameters and the design parameters of the converter affect the relative fractions of the kinetic energy of a relativistic electron beam and the energy of its own magnetic and electric fields that are transferred into the energy of the TEM wave field. The results obtained are analyzed quantitatively, and prospects for further theoretical and experimental research in this area are outlined. © *2000 MAIK "Nauka/Interperiodica".*

1. INTRODUCTION

It is well known that a primary goal of relativistic (high-current) microwave electronics is to develop techniques and devices capable of ensuring the most efficient conversion of the energy of relativistic electron beams (REBs) into electromagnetic field energy. A distinctive feature of the sources of intense REBs is that the energy stored in the source (energy storage) is partly converted into the kinetic energy of an REB and partly expended on the excitation of natural charge-density waves of the beam. In particular, for a cylindrical beam of radius a propagating in a waveguide with conducting walls of radius b, the ratio of the energy flux P_F of the beam field to the kinetic energy flux P_K of an REB is a linearly increasing function of the beam current I_B,

$$\frac{P_F}{P_K} = \frac{I_B}{I_A(\gamma-1)}\ln\left(\frac{b}{a}\right), \quad (1)$$

where γ is the relativistic factor of the beam and $I_A = mc^3/|e|$ is the Alfvén current.

We can readily see that, for beam currents comparable with the limiting current I_L in a given waveguide (see [1]),

$$I_L = I_A\frac{(\gamma^{2/3}-1)^{3/2}}{1+2\ln\left(\frac{b}{a}\right)}, \quad (2)$$

and for realistic beam energies ($2 \le \gamma \le 4$), the right-hand side of (1) is generally not small in comparison with unity. Physically, this indicates that, under the condition $b - a \sim a$, a significant fraction of the energy of the source of an REB is expended on the excitation of its own fields.

This naturally brings up the following questions. What is the role of the self-fields of high-current REBs in the excitation of TEM waves in a circular cylindrical coaxial waveguide? How is the kinetic energy of an REB converted into the energy of TEM waves? What is the conversion efficiency?

The first question was answered theoretically by Kalmykova and Kurilko [2]. They considered the idealized model of a device in the form of a magnetized plasma waveguide in which a slow space charge wave (SCW) is amplified by a monoenergetic REB and, thereby, is converted into a TEM mode of a semi-infinite circular cylindrical waveguide. They showed that, under the conditions adopted in their studies, the fraction of the energy flux of a slow SCW that is concentrated between the conducting shell and the plasma waveguide serves as the main source of the energy flux of a TEM mode. For convenience of further analysis, we will call this fraction of the energy of the REB source the "beam potential energy." According to [2], the efficiency of this conversion is

$$P_{\mathrm{TEM}} = P_{\mathrm{POT}}\left[1 - O\left(\frac{1}{\sqrt{N_P}}\right)\right], \quad P_{\mathrm{POT}} = P_F, \quad (3)$$

where $N_p \equiv \omega_p^2 a^2/c^2$ is the plasma linear density.

Formula (3) implies that, for the model device treated in [2], the contribution of the kinetic energy flux of an REB to the energy flux of a TEM wave is insignificant. In this case, the main mechanism for forming the TEM wave is transient emission at the open edge of

† Deceased.

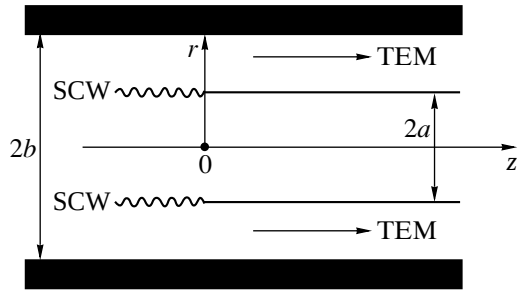

Fig. 1. Schematic of a converter.

a semi-infinite coaxial waveguide from the bunches of an REB formed by the field of the amplified SCW: it is this emission that ensures the conversion of the potential energy of an REB into the energy of a TEM wave.

At first glance, it may appear that these results and the conclusions of the theory developed in [2] contradict the data from recent experiments at the Naval Research Laboratory (NRL, Washington DC, USA) [3–5], in which the kinetic energy of an REB was converted into the energy of TEM waves in both cases with harmonically modulated REBs (at frequencies of 280 MHz and 1.320 GHz) and unmodulated beam-current pulses. In fact, there is no discrepancy between the theoretical [2] and experimental [3–5] results. Below, we will show that this contradiction stems exclusively from the difference between REB configurations and energy converters treated theoretically and those used in experiments. Accordingly, the mechanisms involved in the formation of the fields of TEM waves are essentially different.

The primary aim of our paper is to clarify the physical mechanisms for the formation of TEM waves in a coaxial converter excited directly by a modulated REB and to analyze this process quantitatively. To do this, we will work from an exact analytic solution to the key diffractional problem for an idealized model of a coaxial converter excited by a modulated monoenergetic REB.

2. STATEMENT OF THE PROBLEM AND THE METHOD OF SOLUTION

We consider a semi-infinite ($z > 0$) cylindrical waveguide with an infinitely thin conducting wall of radius a. Let this waveguide serve as a collector for an infinitely thin annular monoenergetic REB with the same radius and let the entire system be surrounded by a conducting shell of radius b (Fig. 1).

The total energy flux $P_{\text{tot}}^{\text{in}}$ entering the converter under consideration consists of the kinetic energy flux P_K of the beam electrons and the energy flux P_{POT} of the self-field of an REB:

$$P_{\text{tot}}^{\text{in}} = P_K + P_{\text{POT}}. \tag{4}$$

At the exit from the converter, the total energy flux from the edge of a coaxial waveguide is a superposition of the energy flux P_{TEM} of electromagnetic waves and the heat flux P_I stemming from the beam energy deposition in the collector material via ionization losses:

$$P_{\text{tot}}^{f} = P_{\text{TEM}} + P_I \approx P_{\text{tot}}^{\text{in}}. \tag{5}$$

We will focus our further analysis on the following questions:

(i) How does the efficiency of the energy conversion under discussion,

$$\eta = P_{\text{TEM}}/P_{\text{tot}}^{\text{in}}, \tag{6}$$

depend on the external parameters of the system (the relativistic factor γ of an REB, the working frequency ω, and the geometric parameters of the converter)?

(ii) What fraction of the beam kinetic energy P_K is converted into the energy P_{TEM} of a TEM wave of a coaxial waveguide and what fraction is expended on heating the collector material (via ionization losses at the edge of the inner cylinder of the waveguide)?

(iii) How should we choose the parameters of an REB and a device in order to ensure the most efficient conversion of the energy stored in the source into the energy of a TEM wave?

In order to find adequate answers to these questions, we develop an analytic theory of a coaxial converter. In the simplest case of exciting an idealized model converter device shown in Fig. 1 by a harmonically modulated current, this can be done using the theory of coupled integral equations and equivalent problems of conjugating analytic functions (see, e.g., [6–8]). The usefulness of this theory in modeling piecewise uniform electrodynamic systems analytically was demonstrated earlier in solving the problems of matching a semi-infinite isotropic plasma waveguide with a semi-infinite coaxial waveguide [9] and a semi-infinite magnetized beam–plasma waveguide with the same coaxial waveguide [2]. Below, we will apply an analogous mathematical apparatus to solve the following diffractional problem.

Let a semi-infinite ($z > 0$) coaxial waveguide ($a \le r \le b$) be excited by a slow axisymmetric SCW of an REB. Assume that the SCW has a frequency ω_m, wavenumber $k_m = \omega_m/V_0$, and current amplitude $\tilde{J}_m$. The current density of the SCW can be represented as

$$j_z(r, z, t)) \equiv \frac{\tilde{J}_m}{2\pi a}\delta(r-a)\exp(ik_m z - i\omega t). \tag{7}$$

At the entrance edge of a coaxial waveguide, the SCW current excites all axisymmetric natural TM waves of the three joined semi-infinite waveguides, specifically, a cylindrical ($z < 0$, $0 \le r \le b$), a coaxial ($z > 0$, $a \le r \le b$), and an inner cylindrical ($z > 0$, $0 \le r \le a$) waveguide. Below, we will assume that the beam modulation fre-

quency ω_m is lower than the first boundary frequency $\omega_1^{(0)}$ of the left cylindrical waveguide,

$$\omega_m^2 < (\omega_1^{(0)})^2 = (c\lambda_1^{(0)}/b)^2, \quad (8)$$

where c is the speed of light in vacuum and $\lambda_1^{(0)}$ is the first root of the zero-order Bessel function $J_0(x)$ ($J_0(\lambda_1^{(0)}) = 0$, $\lambda_1^{(0)} \approx 2.405$).

Under condition (8), the only wave that can travel a large distance from the edge of a coaxial waveguide is a TEM wave; the remaining TM waves are exponentially damped away from the waveguide edge. Let us find the amplitudes of these waves.

From an electrodynamic standpoint, this model assumes the boundary conditions that are uniform at the semiaxes $z < 0$ and $z > 0$ of the cylinder $r = a$. With such boundary conditions, we can solve the above problem exactly using the theory of coupled integral equations and the Rieman–Hilbert boundary-value problem, which was earlier solved in [2, 9] for the cases of semi-infinite plasma and beam–plasma waveguides. Below, we will briefly describe how this approach can be utilized in solving the problem at hand.

3. SOLUTION

3.1. Formulation of the Problem

The physical problem under discussion reduces to solving the homogeneous Helmholtz equation for the field E_z on the outside of a cylinder with the radius $r = a$,

$$\frac{1}{r}\frac{\partial}{\partial r}\left(r\frac{\partial E_z}{\partial r}\right) + \frac{\partial^2 E_z}{\partial z^2} + k_0^2 E_z = 0, \quad k_0 = \omega_m/c, \quad (9)$$

which should be supplemented with the following piecewise uniform boundary conditions at the cylindrical surface:

$$E_z(r = a + 0, z) - E_z(r = a - 0, z) = 0, \quad z < 0, \quad (10a)$$

$$H_\varphi(r = a + 0, z) - H_\varphi(r = a - 0, z) = \frac{2\tilde{J}_m}{ca}\exp(ik_m z), \quad z < 0, \quad (10b)$$

$$E_z(r = a + 0, z) = E_z(r = a - 0, z) = 0, \quad z > 0. \quad (10c)$$

3.2. Choice of the Field Structure

In each of the axially homogeneous regions of the spatially nonuniform system under consideration, the solutions to the Maxwell equations can be searched for as the sum of the SCW fields that are coming from infinity (from the left) and the SCW fields that are moving away from the region where the running TM waves are nonuniform. In other words,

(a) in region 1, defined by $0 < r < a$ and $-\infty < z < +\infty$, we can set

$$\begin{aligned} E_z^{(1)}(r, z) &= E_{\mathrm{SCW}}^{(1)}(r, z) + E_{\mathrm{TM}}^{(1)}(r, z), \\ H_\varphi^{(1)}(r, z) &= H_{\mathrm{SCW}}^{(1)}(r, z) + H_{\mathrm{TM}}^{(1)}(r, z); \end{aligned} \quad (11a)$$

and

(b) in region 2, defined by $a < r < b$ and $-\infty < z < +\infty$, we can set

$$\begin{aligned} E_z^{(2)}(r, z) &= E_{\mathrm{SCW}}^{(2)}(r, z) + E_{\mathrm{TM}}^{(2)}(r, z), \\ H_\varphi^{(2)}(r, z) &= H_{\mathrm{SCW}}^{(2)}(r, z) + H_{\mathrm{TM}}^{(2)}(r, z). \end{aligned} \quad (11b)$$

Here, we introduce the following notation for the SCW fields:

$$E_{\mathrm{SCW}}^{(2)}(r, z) \equiv \frac{A_m \Delta_{00}(\chi_m r)}{\Delta_{00}(\chi_m a)}\Phi(z),$$

$$H_{\mathrm{SCW}}^{(2)}(r, z) \equiv \left(\frac{-ik_0}{\chi_m}\right)\frac{A_m \Delta_{10}(\chi_m r)}{\Delta_{00}(\chi_m a)}\Phi(z),$$

$$E_{\mathrm{SCW}}^{(1)}(r, z) \equiv \frac{A_m I_0(\chi_m r)}{I_0(\chi_m a)}\Phi(z),$$

$$H_{\mathrm{SCW}}^{(1)}(r, z) \equiv \left(-\frac{ik_0}{\chi_m}\right)\frac{A_m I_1(\chi_m r)}{I_0(\chi_m a)}\Phi(z),$$

$$\chi \equiv (k^2 - k_0^2)^{1/2}, \quad \Phi(z) \equiv \exp(ik_m z),$$

$$k_0 \equiv \omega_m/c, \quad \chi_m \equiv \chi(k = k_m),$$

$$\Delta_{00}(\chi r) \equiv I_0(\chi r)K_0(\chi b) - I_0(\chi b)K_0(\chi r),$$

$$\Delta_{10}(\chi r) \equiv I_1(\chi r)K_0(\chi b) + I_0(\chi b)K_1(\chi r),$$

$$A_m \equiv \frac{2i\chi_m^2 \tilde{J}_m}{k_0 c}\frac{\Delta_{00}(\chi_m a) I_0(\chi a)}{I_0(\chi_m b)}.$$

The fields of TM waves can be searched for as a superposition of plane waves,

$$\begin{aligned} E_{\mathrm{TM}}^{(2)}(r, z) &\equiv \int_{-\infty}^{+\infty} C(k)\frac{\Delta_{00}(\chi r)}{\Delta_{00}(\chi a)}e^{ikz}dk, \\ E_{\mathrm{TM}}^{(1)}(r, z) &\equiv \int_{-\infty}^{+\infty} C(k)\frac{I_0(\chi r)}{I_0(\chi a)}e^{ikz}dk, \end{aligned} \quad (12a)$$

$$\begin{aligned} H_{\mathrm{TM}}^{(2)}(r, z) &\equiv -\int_{-\infty}^{+\infty} \frac{ik_0}{\chi}C(k)\frac{\Delta_{10}(\chi r)}{\Delta_{00}(\chi a)}e^{ikz}dk, \\ H_{\mathrm{TM}}^{(1)}(r, z) &\equiv -\int_{-\infty}^{+\infty} \frac{ik_0}{\chi}C(k)\frac{I_1(\chi r)}{I_0(\chi a)}e^{ikz}dk. \end{aligned} \quad (12b)$$

3.3. TM-Wave Amplitudes

Each of the modes in (12) satisfies both equation (9) and the condition for the field E_z to be continuous at the cylindrical surface $r = a$ for $-\infty < z < +\infty$. This condition is a consequence of (10a) and (10c). Conditions (10b) and (10c) yield the following set of two coupled integral equations for the unknown function $C(k)$:

$$\int_{-\infty}^{+\infty} C(k)e^{ikz}dk + A_m e^{ik_m z} = 0, \quad z > 0, \tag{13a}$$

$$\int_{-\infty}^{+\infty} C(k)D(k)e^{ikz}dk = 0, \quad z < 0, \tag{13b}$$

where

$$D(k) \equiv \frac{I_0(\chi b)(-ik_0)}{\chi^2 a I_0(\chi a)\Delta_{00}(\chi a)}.$$

According to Rappoport's lemma [10], these two equations are necessary and sufficient conditions for the integrands to be analytic functions in the upper (+) and lower (–) half-planes of the complex variable k, respectively:

$$C(k) + \frac{A_m}{2\pi i(k-k_m)} = \varphi^{(+)}(k), \tag{14a}$$

$$C(k)D(k) = \varphi^{(-)}(k). \tag{14b}$$

Eliminating the function $C(k)$ from these equations, we finally arrive at the Rieman–Hilbert inhomogeneous boundary-value problem for the functions $\varphi^{(\pm)}(k)$:

$$\varphi^{(+)}(k) = \frac{1}{D(k)}\varphi^{(-)}(k) + \frac{A_m}{2\pi i(k-k_m)}. \tag{15}$$

Using (14), we find the desired representations of the function $C(k)$,

$$C(k) = \varphi^{(+)}(k) - \frac{A_m}{2\pi i(k-k_m)}, \quad C(k) = \frac{\varphi^{(-)}(k)}{D(k)},$$

which are convenient for calculating the fields of TM waves in the regions $z > 0$ and $z < 0$, respectively.

Analytic representations of the functions $\varphi^{(\pm)}(k)$ are given in the Appendix.

3.4. Evaluation of the Amplitudes of TEM and TM Waves

The first representation is convenient for calculating the field amplitude of the TEM wave, which moves away from the edge of a coaxial waveguide along the waveguide axis. The second representation will be used to calculate the fields of TM waves, which are exponentially damped away from the edge of the coaxial waveguide and penetrate into the left waveguide.

The desired TEM-wave amplitude is determined by the residue of the integrand in the formula for $H^{(2)}_{\mathrm{TM}}$ at the point $k = k_0$:

$$T \equiv \operatorname*{Res}_{k=k_0}\left\{\frac{\Delta_{10}(\kappa a)k_0}{\chi\Delta_{00}(\chi a)}\right\}\left[\varphi^{(+)}(k) - \frac{A}{2\pi i(k-k_m)}\right] = \frac{2\tilde{J}_m}{ca}\{1 + O(1/\gamma^2)\}. \tag{16}$$

Corrections on the order of $\gamma^{-2} \ll 1$ on the right-hand side of (16) account for the contribution of diffractive terms proportional to $\varphi^{(+)}(k_0)$:

$$\varphi^{(+)}(k_0) = \frac{A_m}{2\pi i(k_m - k_0)}\left\{\frac{X_0^{(+)}(k_0)}{X_0^{(+)}(k_m)}\sqrt{\frac{2k_0}{k_0 + k_m}} - 1\right\}.$$

Here, the symbol $X_0^{(+)}(k)$ stands for the solution to the homogeneous matching problem corresponding to (15); this solution is bounded at infinity and is analytic in the upper half-plane of the complex variable k (see the Appendix).

In the region $z < 0$, condition (8) implies that the fields of TM waves are exponentially damped away from the edge of the inner cylinder of a coaxial waveguide. The power transferred from the SCW current (7) into these fields is

$$P^{(s)}_{kin} \equiv -\mathrm{Re}\int_{-\infty}^{0} dz \int_0^{2\pi} d\varphi \int_0^b r\,dr E_z^{(s)}(r,z)\tilde{J}_z^* = -\mathrm{Re}\left\{\frac{4\pi\tilde{J}_m^2(\lambda_s^2 a)}{|k_s|b^4(|k_s| - i|k_m|)^2 c}\right\}\left[\frac{J_0\left(\lambda_s\frac{a}{b}\right)}{J_1(\lambda_s)}\right]^2 \times \frac{X_0^{(-)}(-i|k_s|)}{X_0^{(+)}(k_m)}\frac{k_0\eta}{\sqrt{(k_m + k_0)(-k_0 - i|k_s|)}}. \tag{17}$$

Here, we introduce the following notation: λ_s is the sth root of the Bessel function $J_0(x)$ ($\lambda_1 \approx 2.405$), $|k_s|^2 = \lambda_s^2/b^2 - k_0^2$ is the squared absolute value of the sth longitudinal wavenumber of the field, and $\eta \equiv \ln(b/a)$. The symbol $X_0^{(-)}$ stands for the solution to the homogeneous matching problem corresponding to (15); this solution is bounded at infinity and is analytic in the lower half-plane of the complex variable k (see the Appendix).

Generally, the right-hand side of (17) is a complicated function of the external parameters of the converter and the REB. The only exception is the range of sufficiently high energies of an REB ($\gamma^2 \gg 1$) and relatively low beam modulation frequencies for which inequality (8) is satisfied by an ample margin. In this

range, the analytic asymptotic expression for the partial beam power P_s transferred into the field power expended on the excitation of the sth field harmonic is

$$P_s = \frac{\sqrt{2}\pi\tilde{J}_m^2}{\gamma^2 c}\sqrt{\frac{a}{b}}\eta\frac{1}{\lambda_s^{3/2}}\left[\frac{J_0^2\left(\lambda_s\frac{a}{b}\right)}{J_1^2(\lambda_s)}\right]\cos\left[\frac{\pi}{4}+F_0(\gamma)\right], \quad (18)$$

where

$$F_0(\gamma) \equiv \frac{1}{2\pi}\int_0^{+\infty}\frac{dx}{x^2-(1+1/\gamma^2)}\ln(|x^2-1|).$$

From the plot shown in Fig. 2, we can see that, in the range of γ values that are of interest from a practical standpoint, the function $F_0(\gamma)$ depends weakly on the beam energy. As a result, the right-hand side of (18) is a monotonically decreasing function of γ.

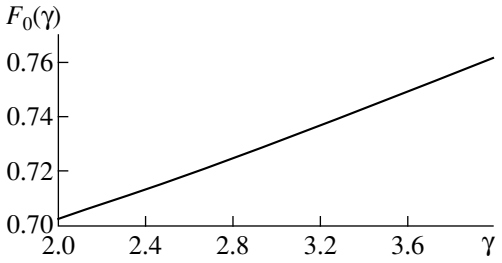

Fig. 2. Function F_0 versus the argument γ.

4. DISCUSSION OF THE RESULTS AND CONCLUSIONS

Formulas (17) and (18) illustrate the main results of the above theoretical analysis of an idealized model coaxial converter. Going over to a discussion of the physical aspects of the results obtained, we must point out the following features of (17) and (18):

(i) their right-hand sides are independent of the modulation frequency of an REB, and,

(ii) the right-hand side of (18) decreases fairly rapidly as both the relativistic factor γ of an REB and the number s of the beam-excited field harmonic increase.

The first feature implies, in particular, that formulas (17) and (18) apply not only to REBs with harmonically modulated currents, which we have analyzed above, but also to unmodulated beam-current pulses whose characteristic durations τ_p satisfy the condition $\tau_p^2 c^2 \gg b^2$.

A sharp decrease in the right-hand side of (18) as s increases indicates that the sum of the fluxes of energy transferred from an REB to the fields of TM waves remains finite. On the other hand, the factor γ^2 in the denominator in (18) implies that, under the conditions adopted here, the total energy flux of the TEM wave, which moves away from the edge of a coaxial waveguide, coincides with the potential energy flux of an REB to within small corrections:

$$\frac{P_{\mathrm{TEM}}}{P_{\mathrm{POT}}} = 1 + O\left(\frac{\sum_s P_s}{P_{\mathrm{POT}}}\right), \quad (19)$$

$$\sum_s \frac{|P_s|}{P_{\mathrm{POT}}} \simeq \sqrt{\frac{a}{b}}\eta\frac{1}{\gamma^2}\sum_s\frac{1}{\lambda_s^{3/2}}\left[J_0\left(\lambda_s\frac{a}{b}\right)/J_1(\lambda_s)\right]^2.$$

Physically, this result can be explained by the fact that, under the above conditions, the field configuration of the SCW, which approaches the edge of a coaxial waveguide, is close to that of the TEM wave, which travels away from this edge [2]. Since inequality (8) implies that the field energy cannot be carried away to the left of the waveguide edge, the SCW energy is converted almost completely into the energy of a TEM wave. This conversion is attributed to an elementary effect—coherent transient emission from beam-driven electron bunches (or, in the case of one current pulse, emission from a single electron bunch) at the egde of the inner cylinder of a coaxial waveguide, where the medium is electrodynamically nonuniform.

Note also that, from an electrodynamic standpoint, the converter under discussion is a kind of semi-infinite open-ended waveguide. In fact, recall that microwave radiation can be emitted from the edge of the inner cylinder of a coaxial waveguide exclusively in the form of a TEM wave, while the SCW, which approaches this edge from the left, excites the waveguide. This physical picture can, in particular, explain why two different types of converters (the one we have considered above and the one used in experiments at the NRL [3–5]) operate in different modes. On the one hand, the converter treated in our model is similar to that used in recent NRL experiments because its coaxial waveguide was designed to have only one open edge and was excited by the SCW of an REB. On the other hand, the assumptions made in our analysis differ from the NRL experimental conditions in terms of the following three points.

First, in the NRL experiments [3–5], a coaxial waveguide was excited with the help of an annular slit in the inner cylinder of the waveguide. Second, an annular beam almost reached the slit. Finally, the slit width D was small in comparison with the wavelength λ, $2\pi D \ll \lambda$. In contrast, our model naturally refers to the opposite limiting case $2\pi D \gg \lambda$. Under the condition $b - a \ll b$, the potential energy of an REB in the NRL experiments [3–5] was relatively low, which made it possible to generate fairly intense beam-current pulses [see (2)]. On the other hand, such a narrow slit ensured a cophased deceleration of an REB by the fields of the so-called "surface" TM waves, which are exponentially damped away from the slit edges.

On the whole, all of the aforementioned features of the converter geometry and REB configuration ensured the governing role of the deceleration of an REB by the fields of the surface TM waves and the conversion of the beam kinetic energy into the energy of a TEM wave in the NRL experiments [3–5].

Because of the lack of experimental data [3–5] on the kinetic energy lost by an REB in the collector, we failed to determine whether the measured converter efficiency η_{exp} agrees with the theoretical estimate (6) and to what extent the measurement results under discussion are close to the optimum ones, which correspond to the most efficient conversion of REB energy into the energy of a TEM wave. To make such a comparison, it is necessary to carry out theoretical modeling of a slit converter (the device used in NRL experiments [3–5]) and experimental measurements of η_{exp} as a function of the external parameters of the converter (including control of the kinetic energy lost by an REB in the collector).

Summing up the above discussion, we conclude that coaxial converters can be optimized in the following two ways: first, by reducing the relative fraction of the potential energy of an REB and by ensuring its efficient deceleration by the fields of TM waves that the beam itself excites (this approach was implemented in the NRL experiments [3–5]), and second, by forming an REB with a relatively low kinetic energy flux (the main fraction of which is lost in the collector) and ensuring that precisely the potential energy of the REB is efficiently converted into the energy of a TEM wave. The first way holds promise for REBs with sufficiently high total currents and energies [see (1)] and the second, for REBs with relatively low total currents and energies. Various aspects of creating an optimized version of the converter (in particular, whether it can compete with the converter that was fabricated and tested at the NRL) should be verified experimentally for REBs with relatively low currents and energies.

ACKNOWLEDGMENTS

We are grateful to A.A. Rukhadze for a fruitful discussion of the results and to E.V. Bulyak and A.P. Tolstoluzhskiĭ for helping with the work.

APPENDIX

Solution to the Boundary-Value Problem (15)

The boundary-value problem (15) can be reduced to the standard form [6–8],

$$\Phi^{(+)}(k) = G_0(k)\Phi^{(-)}(k) + f(k), \qquad (A.1)$$

through the following change of the desired functions $\varphi^{(\pm)}(k)$ and the kernel $G(k) \equiv [D(k)]^{-1}$:

$$\Phi^{(+)}(k) \equiv \frac{\varphi^{(+)}(k)}{\sqrt{k+k_0}}, \quad \Phi^{(-)}(k) \equiv \frac{\varphi^{(-)}(k)\sqrt{k-k_0}}{ik_0},$$

$$G_0(k) \equiv \frac{ik_0}{\chi}G(k), \quad f(k) \equiv \frac{A_m}{2\pi i(k-k_m)\sqrt{k+k_0}},$$

$$\lim_{|k|\to\infty}[G_0(k)] = 1.$$

The symbols $X_0^{(\pm)}(k)$ signify such solutions to the homogeneous problem (A.1) of matching the analytic functions

$$X_0^{(+)}(k) = G_0(k)X_0^{(-)}(k), \qquad (A.2)$$

that are bounded at infinity. We emphasize that the requirement for the functions $X_0^{(\pm)}(k)$ to be bounded at infinity is imposed in order for the solution to the boundary-value problem (A.2) be unique and the total field energy near the edge of a semi-infinite waveguide ($r = a$, $z = 0$) be finite (the latter is a consequence of Mikesner's conditions [11]).

Solutions (A.2) are well known:

$$X_0^{(\pm)}(k) \equiv \text{const} \times \exp\left\{\frac{1}{2\pi i}\int\limits_{C_\pm}\frac{dk'}{k'-k}\ln G_0(k')\right\}. \qquad (A.3)$$

Here, const is an arbitrary constant (which does not enter the final results); the contours $C_\pm$ pass around the point $k' = k$ from below (+) and from above (–), respectively; and the integral in braces on the right-hand side converges at infinity by virtue of the condition $\lim_{|k|\to\infty}[G_0(k)] = 1$.

Knowing explicit expressions for the functions $X_0^{(\pm)}(k)$, we can readily find explicit solutions to the inhomogeneous boundary-value problem (A.1),

$$\Phi^{(\pm)}(k) = \frac{A_m}{2\pi i}X_0^{(\pm)}(k)\int\limits_{C_\pm}\frac{dk'}{(k'-k)(k'-k_m)X_0^{(+)}\sqrt{k'+k_0}}, \qquad (A.4)$$

in order to obtain analytic representations of the functions $\varphi^{(\pm)}(k)$, which enter into formulas (16) and (17) for the desired fields of TM waves:

$$\varphi^{(+)}(k) = \sqrt{k+k_0}\Phi^{(+)}(k),$$

$$\varphi^{(-)}(k) = \frac{ik_0}{\sqrt{k-k_0}}\Phi^{(-)}(k).$$

REFERENCES

1. L. S. Bogdankevich and A. A. Rukhadze, Usp. Fiz. Nauk **103**, 609 (1971) [Sov. Phys. Usp. **14**, 163 (1971)].
2. S. S. Kalmykova and V. N. Kurilko, Prikl. Mat. Mekh. **33**, 637 (1969).
3. M. Friedman and V. Serlin, Rev. Sci. Instrum. **54** (12), 1764 (1983).
4. M. Friedman and V. Serlin, Rev. Sci. Instrum. **58** (1), 58 (1987).
5. V. Serlin and M. Friedman, IEEE Trans. Nucl. Sci. **22**, 692 (1994).
6. R. E. A. C. Paley and N. Wiener, *Fourier Transforms in the Complex Domain* (American Mathematical Society, New York, 1934; Nauka, Moscow, 1964).
7. V. A. Lavrent'ev and B. N. Shabat, *Methods of the Theory of Functions of a Complex Variable* (Nauka, Moscow, 1965).
8. N. N. Muskhelishvili, *Singular Integral Equations* (Nauka, Moscow, 1968).
9. S. S. Kalmykova, Ukr. Fiz. Zh. **9**, 216 (1964).
10. I. M. Rappoport, Dokl. Akad. Nauk SSSR **59**, 1403 (1948).
11. F. M. Morse and H. Feshbach, *Methods of Theoretical Physics* (McGraw-Hill, New York, 1953; Inostrannaya Literatura, Moscow, 1958, 1959), Vols. 1 and 2.

Translated by O. E. Khadin

Plasma Physics Reports, Vol. 26, No. 3, 2000, pp. 262–265. Translated from Fizika Plazmy, Vol. 26, No. 3, 2000, pp. 282–286.

PLASMA DIAGNOSTICS

Determination of the Plasma Density in a Current Sheet from the Profiles of the HeII 6560-Å and H_α Spectral Lines

V. P. Gavrilenko*, N. P. Kyrie, and A. G. Frank****

**Center for Surface and Vacuum Research, Russian State Committee for Standards, Andreevskaya nab. 2, Moscow, 117334 Russia*

***Institute of General Physics, Russian Academy of Sciences, ul. Vavilova 38, Moscow, 177942 Russia*

Received March 18, 1999; in final form, July 7, 1999

Abstract—The electron density in the midplane of a current sheet and far from it is determined from an analysis of the profiles of the HeII 6560-Å and H_α spectral lines. A new approach to calculating the Stark broadening of the HeII 6560-Å line is developed. The results obtained can be used to determine the plasma density in other experimental devices. © *2000 MAIK "Nauka/Interperiodica".*

1. INTRODUCTION

One of the conventional techniques for measuring the electron density in dense low-temperature plasmas is the method based on the analysis of the profiles of the spectral lines of helium ions. The most frequently used lines are the HeII 4686-Å and HeII 3203-Å lines, which belong to the Pashen series (P_α and P_β, respectively) [1, 2]. In the studies involving a dense current-sheet plasma produced under high-pressure filling [3], the evolution of the maximum electron density (i.e., in the midplane of the sheet) was obtained from the broadening of the HeII 4686-Å line [4]. The density increased with time from 4×10^{16} to 9×10^{16} cm^{-3}; accordingly, the full width at half maximum (FWHM) of the HeII 4686-Å line profile varied within the range $\Delta\lambda_{1/2} = 2.5$–4.1 Å. In [4], the HeII 6560-Å line was also recorded; the FWHM of this line was unexpectedly large, $\Delta\lambda_{1/2} \approx$ 47 Å. This line belongs to the Bracket series and corresponds to the transition between the $n = 6$ and $n = 4$ levels, where n is the principal quantum number. Since the typical value of the dipole moment for the $n = 6$ level exceeds those for the $n = 4$ and $n = 5$ levels, the radiative transitions from which form the P_α and P_β spectral lines of the HeII ions, the HeII 6560-Å line should be more sensitive to the action of the electric field than P_α and P_β lines. However, to our knowledge, the Stark broadening of the HeII 6560-Å line has not yet been addressed in the literature. One possible explanation is that the HeII 6560-Å line is overlapped by the intense H_α line of hydrogen atoms. This effect was also observed in our experiments. In this case, as is shown in [4], a rather complicated experimental profile can be represented as a superposition of two profiles with significantly different FWHMs corresponding to the H_α and HeII 6560-Å lines.

In this study, we calculated the Stark broadening of the HeII 6560-Å line in the electric microfields of the plasma electrons and ions. When calculating the effect produced by the electrons, we used the impact approximation, whereas the quasistatic approximation was used for the ions. As a result, the relation between the electron density and the FWHM of the HeII 6560-Å spectral line was obtained for the first time. This relation allowed us to determine the electron density in the current-sheet midplane (from which the spectral lines of helium ions were emitted) using a new technique based on measurements of the broadening of the HeII 6560-Å line. It should be emphasized that the new data agree well with the previous results obtained from the broadening of the HeII 4686-Å line [4]. The electron density inferred from the broadening of the H_α line is nearly 30 times lower than the maximum density in the sheet. This means that the H_α line is emitted from the periphery of the current sheet. This confirms the previous conclusion [4–6] that the lower the excitation energy of the spectral line, the farther from the midplane of the current sheet is the region from which this line is emitted.

2. EXPERIMENTAL DEVICE AND THE TECHNIQUE OF SPECTROSCOPIC MEASUREMENTS

Spectroscopic measurements were carried out in the CS-3D device [3, 7]. A plane current sheet was produced when the electric current was generated in a plasma along the zero line of a two-dimensional magnetic field configuration. In these experiments, the gradient of the quasistatic magnetic filed was 570 G/cm, the half-period of the plasma current pulse was 5 μs, and the maximum current was 40–60 kA. The diameter of the quartz vacuum chamber was 18 cm, and the length of the plasma gap was 60 cm. The current sheet

1063-780X/00/2603-0262$20.00 © 2000 MAIK "Nauka/Interperiodica"

was produced under high-pressure helium filling, the initial pressure being $p_0 \approx 300$ mtorr [3, 4], which was nearly one order of magnitude higher than in previous experiments [7]. The initial electron density corresponding to 100% one-electron ionization was $N_e^0 \approx 10^{16}$ cm^{-3}. The maximum density in the formed sheet was one order of magnitude higher, $N_e^{sh} \approx 10^{17}$ cm^{-3}, and the plasma temperature was $T_e \approx T_i \approx 2$–3 eV [3, 4]. The sheet width was $2\Delta x \approx 15$–18 cm, the thickness was $2\Delta y \approx 1$–2 cm, and the length was $\Delta z \approx 60$ cm.

Spectroscopic measurements were carried out with the use of an optical scheme similar to that described in [4]. Plasma emission in the visible range was collected by a glass achromatic objective producing a strongly reduced image of the central 60-cm-long and 1.2- to 1.5-cm-diameter quasi-cylindrical region of the vacuum chamber (and, correspondingly, the current sheet) on the end of a quartz fiber that was 10 m long and 400 μm in diameter. The plasma emission was transmitted along the fiber into the entrance slit of an MDR-3 monochromator; the focal length of the monochromator entrance lens was 600 mm. In this experiment, we used a 1200-line/mm diffraction grating providing an inverse linear dispersion of 13 Å/mm. The spectral line profiles obtained in the monochromator exit plane were recorded with an MORS-3 multichannel optical recording system [4, 8] and stored in the memory of a personal computer. The MORS-3 consists of an image tube and a multichannel CCD detector. The total inverse linear dispersion of the system was 0.46 Å/channel; the instrumental FWHM was $\lambda_{1/2}^{app} \approx 3$ channels ≈1.4 Å. The spectra were recorded and averaged over time intervals of 0.6–0.7 μs.

3. ANALYSIS OF EXPERIMENTAL DATA

The study of the spectrum of emission from the current sheet plasma in the vicinity of the H_α line revealed that this spectrum changed significantly with time [4]. This is seen from a comparison of Figs. 1 and 2. At the instant $t_1 = 0.5$ μs, after the electric current has been excited in the plasma and the current sheet has started to form, the emission spectrum contains only the H_α line, whose FWHM is equal to 1.8 Å. At $t_2 \approx 3.7$ μs, when the current sheet has already been formed and the plasma has been compressed into a sheet, the emission spectrum is a superposition of two lines: the hydrogen H_α and HeII 6560-Å lines. In this case, the H_α line is shifted by nearly 6.5 cm^{-1} (or by nearly three angstroms in wavelength units) to the red side in comparison with the position of the center of the HeII 6560-Å line.[1]

[1] In this paper, the frequency ω is measured in spectroscopic units, cm^{-1}. The frequency ω expressed in cm^{-1} and the wavelength λ expressed in cm are related by ωλ = 1.

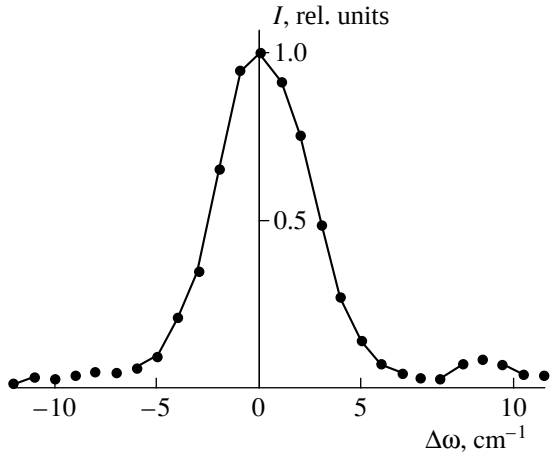

Fig. 1. Experimental profile of the hydrogen H_α spectral line (λ = 6563 Å) recorded at the instant $t = 0.5$ μs. This profile was used to determine the electron density at the periphery of the current sheet, $N_e = 2.5 \times 10^{15}$ cm^{-3}.

Let us analyze the experimental profile of the H_α spectral line shown in Fig. 1. The FWHM of this profile is equal to $\Delta\omega_{1/2}^{exp} \approx 4.9$ cm^{-1}. In this case, the main contribution to the FWHM comes from the instrumental width, which was equal to $\Delta\omega_{1/2}^{app} \approx 3.25$ cm^{-1}. The measurements showed that the spectral line profile associated with the instrumental broadening was a Gaussian. In addition, the Doppler effect (at a temperature of $T \approx 1$ eV) also contributed to the broadening of the H_α line (see [3, 4]), producing a Gaussian profile of the spectral line. As a result, instrumental plus Doppler broadenings lead to a Gaussian profile with the FWHM equal to $\Delta\omega_{1/2}^{G} \approx 3.46$ cm^{-1}. Hence, the experimental profile of the H_α line shown in Fig. 1 is a convolution of a Gaussian profile (resulting from the instrumental plus Doppler broadenings) and a Stark profile due to the ion and electron microfields. For analyzing the Stark broadening of the H_α line, we used the results of [9], in which the data on the calculated FWHMs of a number of hydrogen spectral lines in a plasma are presented. These data take into account both the electron and ion contributions to the broadening of hydrogen spectral lines. To estimate the FWHM of the Stark profile, we assumed this profile to be nearly a Lorentzian. Numerical calculations showed that the best fit to the experimental profile of the FWHM $\Delta\omega_{1/2}^{exp} = 4.9$ cm^{-1} is obtained if the Gaussian profile of the FWHM $\Delta\omega_{1/2}^{G} = 3.46$ cm^{-1} is convoluted with the Lorentzian profile of the FWHM $\Delta\omega_{1/2}^{L} \approx 2.69$ cm^{-1}. Then, based on the data from [9], we obtain the following estimate for the electron density at the periphery of the current sheet: $N_e \approx 2.5 \times 10^{15}$ cm^{-3}, the measurement accuracy being ≈20%.

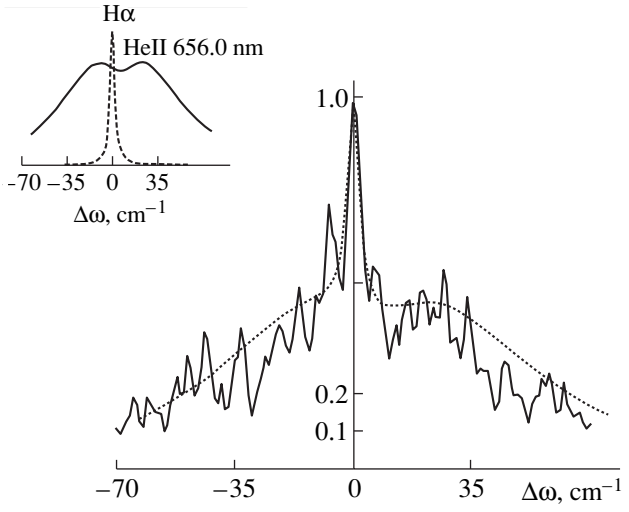

Fig. 2. Emission spectrum of the current-sheet plasma in the red spectral region (on the frequency scale). The spectrum is a superposition of the helium ion HeII 6560-Å and hydrogen H_α spectral lines. The solid line shows the experimental profile recorded at the instant $t = 3.7$ μs, and the dashed line shows the theoretical profile that provides the best fit for the experimental spectrum. The theoretical spectrum is a superposition of the calculated profiles of the HeII 6560-Å and H_α lines. These profiles are shown separately in the insert: the HeII 6560-Å profile is shown by the solid line, and the H_α profile is shown by the dashed line.

It is seen from Fig. 2 that the experimentally measured broadening of the HeII 6560-Å line for $t = 3.7$ μs was 100 ± 10 cm^{-1}, which is more than one order of magnitude larger than the total half-width of the instrumental profile and Doppler broadening for $T_i = 2$ eV [3, 4].

When analyzing the experimental profile of the HeII 6560-Å line shown in Fig. 2, we took into account the Stark broadening of this line due to the combined action of the electric fields produced by the plasma electrons and ions. The contribution from the electrons was calculated by the impact model, whereas that from ions was calculated by the quasistatic model [10, 11]. In the calculations, we assumed that the ion electric microfield F splits the HeII 6560-Å spectral line into a number of spectral components in accordance with the linear Stark effect and the electron impact broadening forms Lorentzian profiles of these spectral components. According to this assumption, for the fixed value F of the ion microfield, the spectral line profile was represented in the form

$$S_F(\Delta\omega) = \sum_k \frac{f_k}{2\pi} \frac{\gamma}{(\Delta\omega - \alpha_k F)^2 + \gamma^2/4}. \qquad (1)$$

Here, the frequency $\Delta\omega$ is counted from the unperturbed position of the HeII 6560-Å line; the quantities f_k are the intensities of the Stark components, whose positions in the emission spectrum are determined by the frequencies $\Delta\omega = \alpha_k F$, where α_k is the constant of the linear Stark effect for the kth components; and γ is the FWHM of the Lorentzian profile formed due to the electron impact mechanism. The quantities f_k and α_k are determined by the quantum numbers corresponding to the upper and lower energy levels of the HeII ion; their analytical formulas are presented, e.g., in [12]. For the impact FWHM γ expressed in cm^{-1}, we used the approximate formula [11]

$$\gamma = \frac{16\hbar^2}{3\pi c \langle v \rangle m_e^2} N_e \left(\ln \frac{R_D}{\rho_0} + 0.215 \right) I(6, 4), \qquad (2)$$

where N_e is the electron density; $\langle v \rangle$ is the mean electron thermal velocity; c is the speed of light; R_D is the Debye radius; and ρ_0 is the Weisskopf radius,

$$\rho_0 = [2I(6, 4)/3]^{1/2} \hbar/(m_e \langle v \rangle).$$

For the factor $I(6, 4)$, we take the value $I(6, 4) = 196$, which can be derived using the results of [13, 14]. The resulting profile of the $I(\Delta\omega)$ line, emitted by the ensemble of the HeII ions, can be obtained by averaging the profile $S_F(\Delta\omega)$ (1) over the distribution function $W(F)$ of ion microfields:

$$I(\Delta\omega) = \int_0^\infty S_F(\Delta\omega) W(F) dF. \qquad (3)$$

For the ion-microfield distribution $W(F)$, we used the function proposed in [15] and based on the model of a uniform neutralizing electron background. We also used the analytical approximation for this function from [16]. As a result, numerical calculations of the profile of the HeII 6560-Å spectral line yield the following approximate relationship for the FWHM $\Delta\lambda_{1/2}$ and the plasma density N_e (provided that $N_e = N_i$):

$$\Delta\lambda_{1/2} \approx 2.7 \times 10^{-10} N_e^{2/3}, \qquad (4)$$

where $\Delta\lambda_{1/2}$ is expressed in Å and N_e is expressed in cm^{-3}. When deriving relationship (4), we assumed the charged-particle temperature to be 2 eV [3, 4]. Relationship (4) can be used in the range $10^{16} \le N_e \le 10^{17}$ cm^{-3}.

The emission spectrum $I^{exp}(\Delta\omega)$ shown in Fig. 2 was approximated by the function $I(\Delta\omega)$, which is a linear combination of the functions $I_1(\Delta\omega)$ and $I_2(\Delta\omega)$:

$$I(\Delta\omega) = I_1(\Delta\omega) + \kappa I_2(\Delta\omega), \qquad (5)$$

where $I_1(\Delta\omega)$ is the profile of the HeII 6560 Å line and $I_2(\Delta\omega)$ is the profile of the hydrogen H_α line. The constant κ in (5) was a variable parameter, which was chosen from the condition of the best approximation of the experimental profile $I^{exp}(\Delta\omega)$ shown in Fig. 2 by the theoretical dependence $I(\Delta\omega)$ (5). Two factors played an important role in approximating the experimental profile $I^{exp}(\Delta\omega)$ by the theoretical profile $I(\Delta\omega)$ (5). First, we took into account that the profile of the H_α line

is much narrower than the profile of the HeII 6560-Å line. Second, there is a dip in the center of the profile of the HeII 6560-Å line, which is a result of the Stark effect for this line in the quasistatic microfields of the plasma ions. It follows from here (in view of the fact that the H_α line lies close to the center of the HeII 6560-Å line) that most of the intensity of the H_α line is localized near the center of the experimental profile $I^{exp}(\Delta\omega)$, whereas most of the intensity of the HeII 6560-Å line is localized in the wings of the experimental profile $I^{exp}(\Delta\omega)$.

The theoretical profile $I(\Delta\omega)$ (5), which provides the best fit for the experimental profile $I^{exp}(\Delta\omega)$, is shown in Fig. 2 by the dashed line. Also shown in Fig. 2 are the profiles $I_1(\Delta\omega)$ and $I_2(\Delta\omega)$, whose linear combination yields the resulting profile $I(\Delta\omega)$. Note that the resulting profile $I(\Delta\omega)$ shown by the dashed line in Fig. 2 corresponds to $\kappa = 1$ in (5). The theoretical profile $I_1(\Delta\omega)$ was calculated using formulas (1)–(3) for the plasma density $N_e = N_i = 7 \times 10^{16}$ cm^{-3}. The accuracy of determining N_e in this case was $\simeq 15\%$ and was primarily related to the measurement accuracy of the broadening of the HeII 6560-Å line. When analyzing the experimental profile $I^{exp}(\Delta\omega)$ shown in Fig. 2, we could not determine exactly the shape of the H_α profile (because this line partially overlaps the HeII 6560-Å line). Because of this, for the sake of simplicity, we assumed the profile $I_2(\Delta\omega)$ to be a Lorentzian. In this case, the best agreement between the approximate profile $I^{exp}(\Delta\omega)$ (5) and the experimental profile $I(\Delta\omega)$ was achieved when the FWHM of the profile $I_2(\Delta\omega)$ was equal to 4.5 cm^{-1}, which coincided to within an accuracy of 10% with the FWHM of this spectral line measured in the previous experiments at $t = 0.5$ μs (see above).

4. CONCLUSION

Based on the analysis of the profiles of the H_α and HeII 6560-Å lines, we have determined the electron density in different regions of the current sheet. It is found that, at the current-sheet periphery (from which the H_α line is emitted), the electron density is equal to $N_e \approx 2.5 \times 10^{15}$ cm^{-3}. Thus, based on the new data, we refined the lower estimate for the electron density in the sheet presented in our previous paper, $N_e \leq 10^{16}$ cm^{-3} [4]. It is found that, in the central region of the current sheet (from which the HeII 6560-Å line is emitted), the density is equal to $N_e \approx 7 \times 10^{16}$ cm^{-3}, which agrees with the value of N_e obtained from the broadening of the HeII 4686-Å line [4] under the same experimental conditions. Another important result is the calculation of the Stark broadening of the HeII 6560-Å line. The results obtained can be used to determine plasma parameters in other devices.

ACKNOWLEDGMENTS

We thank V.S. Markov for assistance in the experiments. This work was supported in part by the Russian Foundation for Basic Research (project no. 97-02-17657) and INTAS (grant no. 96-456).

REFERENCES

1. S. Büscher, S. Glenzer, Th. Wrubel, and H.-J. Kunze, J. Phys. B: At. Mol. Opt. Phys. **29**, 4107 (1996).
2. C. Stehlé, Phys. Scr. T **65**, 183 (1996).
3. S. Yu. Bogdanov, V. B. Burilina, and A. G. Frank, Zh. Éksp. Teor. Fiz. **114**, 1202 (1998) [JETP **87**, 655 (1998)].
4. S. Büscher, N. P. Kyrie, H.-J. Kunze, and A. G. Frank, Fiz. Plazmy **25**, 185 (1999) [Plasma Phys. Rep. **25**, 164 (1999)].
5. S. Yu. Bogdanov, V. S. Markov, A. I. Morozov, and A. G. Frank, Pis'ma Zh. Tekh. Fiz. **21** (24), 5 (1995) [Tech. Phys. Lett. **21**, 995 (1995)].
6. S. Yu. Bogdanov, V. B. Burilina, N. P. Kyrie, *et al.*, Fiz. Plazmy **24**, 467 (1998) [Plasma Phys. Rep. **24**, 427 (1998)].
7. S. Yu. Bogdanov, N. P. Kyrie, and A. G. Frank, Tr. Inst. Obshch. Fiz., Ross. Akad. Nauk **51**, 5 (1996).
8. V. B. Burilina, N. P. Kyrie, É. G. Sil'kis, and A. G. Frank, Abstracts of Papers, *IX Conference on Diagnostics of High-Temperature Plasmas, St. Petersburg, 1997*, p. 58.
9. M. A. Gigosos and V. Cardeñoso, J. Phys. B: At. Mol. Opt. Phys. **29**, 4795 (1996).
10. H. R. Griem, *Spectral Line Broadening by Plasmas* (Academic, New York, 1974; Mir, Moscow, 1978).
11. I. I. Sobelman, L. A. Vainshtein, and E. A. Yukov, *Excitation of Atoms and Broadening of Spectral Lines* (Nauka, Moscow, 1979; Springer-Verlag, Berlin, 1981).
12. H. A. Bethe and E. E. Salpeter, *Quantum Mechanics of One- and Two-Electron Atoms* (Academic, New York, 1957; Fizmatgiz, Moscow, 1960).
13. L. A. Minaeva (Bureeva), Astron. Zh. **45**, 578 (1968) [Sov. Astron. **12**, 459 (1968)].
14. C. Stehlé, Astron. Astrophys. **292**, 699 (1994).
15. C. A. Iglesias and J. L. Lebowitz, Phys. Rev. A **30**, 2001 (1984).
16. I. O. Golosnoĭ, Mat. Model. **5**, 11 (1993).

Translated by N. F. Larionova

Plasma Physics Reports, Vol. 26, No. 3, 2000, pp. 266–271. Translated from Fizika Plazmy, Vol. 26, No. 3, 2000, pp. 287–292.

IONOSPHERIC PLASMA

Plasma Dynamics near an Earth Satellite and Neutralization of Its Electric Charge during Electron Beam Injection into the Ionosphere

V. A. Fedorov

Mints Radiotechnical Institute Joint Stock Company, ul. Vos'mogo marta 10/1, Moscow, 125083 Russia

Received March 4, 1999

Abstract—A study is made of the dynamics of the ionospheric plasma in the vicinity of an earth satellite injecting an electron beam. The time evolution of the electric charge of the satellite is determined. The electric potential of the satellite is found to be well below the beam-cutoff potential. It is shown that, under conditions typical of active experiments in space, the plasma electrons are capable of neutralizing the satellite's charge. © *2000 MAIK "Nauka/Interperiodica".*

1. INTRODUCTION

The most important problem in preparing active experiments [1] on electron beam injection into the Earth's ionosphere is that of determining the electric charge Q that appears on a space vehicle (here, we will speak about earth satellites), because active experiments in space are usually carried out without artificial systems for neutralizing the charge Q and under the condition $|I_b/I_{0\mathrm{H}}| \gg 1$, where I_b is the injection current and $I_{0\mathrm{H}}$ is the current of thermal electrons of the ionospheric plasma to the satellite surface with allowance for the influence of the geomagnetic field $\mathbf{H}_0$ at $I_b = 0$. As a result, the positive charge Q, which starts to grow at the time the electrons begin to be injected, may exceed a critical level at which the beam energy losses become inadmissible or the electron beam is cut off [1, 2]. This point is especially important for time intervals shorter than the time required for ionizing neutral particles and the time of plasma heating by an electron beam ($t < t_{\mathrm{ion}}, t_h$). The reason is that, when the beam is injected at altitudes $h_I > 130$ km, the satellite collects thermal plasma electrons and acquires a negative charge; this is the only mechanism for neutralizing the satellite's positive charge Q [3].

The plasma dynamics in the vicinity of a satellite and the change in its charge Q were studied in [3–5] under the assumptions that the electron injection is isotropic and $\mathbf{H}_0 = 0$. It was shown that the electric charge Q that appears on the satellite because of the injected electrons is such that the electric potential φ_0 of the satellite is well below the beam-cutoff potential and the process of neutralizing the charge Q is oscillatory in nature. Consequently, under the assumptions adopted in those papers, the charge Q was neutralized by plasma electrons. Note that the geomagnetic field $\mathbf{H}_0$, which plays a decisive role in neutralizing the satellite's charge and in forming the structure of the plasma sheath near the satellite surface, can legitimately be ignored only for satellites moving along a geostationary orbit, at which $|\mathbf{H}_0| \approx 0$ [6, 7].

Here, we study the dynamics of a magnetized ionospheric plasma around a satellite injecting an electron beam at altitudes $h_I > 130$ km and neutralization of the satellite's change Q. We also determine the distributions of the fields and charged particles in the perturbed plasma over time intervals $t < t_{\mathrm{ion}}, t_h$.

2. BASIC EQUATIONS

We consider a satellite of radius R_0 that orbits the Earth along the geomagnetic field $\mathbf{H}_0$ in the ionospheric F-layer ($h_I > 130$ km). At $t = 0$, the satellite starts to inject an electron beam in the direction of $\mathbf{H}_0$; the beam current $I_b(t)$ is a known function of time. We can assume that the plasma around the satellite is collisionless, because the inequalities [1, 6, 7]

$$\omega_0 \gg \nu, \quad l_{e,i} \gg R_c \tag{1}$$

hold in the F-layer (this is also confirmed by experimental data). Here, ω_0 is the plasma frequency, ν is the rate at which the electrons collide with other plasma particles, $l_{e,i}$ are the electron and ion mean free paths, and R_c is the characteristic dimension of the perturbed plasma (or the space-charge sheath). We assume that, in the rest frame of the satellite, the following inequalities hold:

$$|v_e| \gg v_{Te}, \quad |v_i| < v_{Ti}, \tag{2}$$

where $v_{e,i}$ are the directed electron and ion velocities and $v_{Te,i}$ are the electron and ion thermal velocities. Conditions (1) and (2) imply that the processes in the vicinity of a satellite should be analyzed over time scales no longer than $t \ll 1/\nu$ and $t \ll R_c/|v_i|$.

1063-780X/00/2603-0266$20.00

Under conditions (1) and (2), the plasma processes can be described by the set of equations of the quasihydrodynamic approximation for a collisionless plasma, written for the electrons [6] (the background ions serve merely to maintain plasma quasineutrality). In Eulerian form, this set can be written as

$$[\nabla \times \mathbf{B}] = \frac{1}{c}\frac{\partial \mathbf{E}}{\partial t} + \frac{4\pi}{c}\mathbf{j}, \tag{3}$$

$$[\nabla \times \mathbf{E}] = -\frac{1}{c}\frac{\partial \mathbf{B}}{\partial t}, \tag{4}$$

$$\frac{\partial n_e}{\partial t} + \nabla(n_e \mathbf{v}_e) = 0, \tag{5}$$

$$\frac{\partial}{\partial t}(n_e \mathbf{v}_e) + \nabla(n_e \mathbf{v}_e \mathbf{v}_e) = \frac{e n_e}{m_e}\left(\mathbf{E} + \frac{1}{c}[\mathbf{v}_e \times \mathbf{B}]\right), \tag{6}$$

where $\mathbf{E}$ and $\mathbf{B}$ are the electric field and magnetic induction, $\mathbf{v}_e$ and n_e are the velocity and density of the plasma electrons, and $\mathbf{j}$ is the electric current density of the beam and plasma electrons.

In equations (3)–(6), we incorporated the displacement current and the convective current, which are usually neglected in magnetohydrodynamics under the conventional simplifying assumptions that the plasma is highly conducting and $\omega \approx \omega_0 \ll \omega_{Hi}$, where ω_{Hi} is the ion cyclotron frequency. However, for the processes around a satellite injecting an electron beam, we have $\omega_0 \gg \omega_{Hi}$ [6, 7], so that these currents should be taken into account. In analyzing equations (3)–(6), we will not distinguish between the vectors $\mathbf{B}$ and $\mathbf{H}$ ($\mathbf{H}$ is the magnetic field strength), because the magnetic permeability in the ionospheric plasma is extremely close to unity [8]. We represent the vectors $\mathbf{E}$ and $\mathbf{H}$ as

$$\mathbf{E} = \mathbf{E}_p + \mathbf{E}_b + \mathbf{E}_S, \quad \mathbf{H} = \mathbf{H}_p + \mathbf{H}_b + \mathbf{H}_0, \tag{7}$$

where $\mathbf{E}_p$ and $\mathbf{H}_p$ are the electric and magnetic fields of the plasma, $\mathbf{E}_b$ and $\mathbf{H}_b$ are those of the beam, and $\mathbf{E}_S$ is the electric field of a satellite that is being charged as a result of electron injection in the absence of a plasma.

Since the inequality $W_b \gg |e\varphi_0|$ (where W_b is the beam-electron energy), which holds in most active experiments on electron beam injection into the ionosphere [1], implies that the beam energy losses are low, the fields and current of a beam can be regarded as given functions. Consequently, the self-fields of a beam enter equation (6) only and the beam current density drops out of equation (3). We neglect the beam front–driven vortex fields [9], because they are carried away from a space-charge sheath of radius R_c during a time interval $t \approx R_c/v_b \le 10^{-7}$ s $< 1/\omega_0$ and are subsequently damped. We also neglect the reverse current I_f [9], because, by virtue of $r_{b0} < \lambda_E = c/\omega_0$, it satisfies the condition $I_f \approx -I_b(\omega_0/c)^2\pi R_0^2 \ll I_n$ [10]. In these relationships, v_b is the beam velocity, I_n is the neutralizing current of the plasma electrons, and r_{b0} is the beam radius at the exit from the injector.

Equation (3) and the results obtained in [3] enable us to estimate the field $\mathbf{H}_p$ produced by the currents of the plasma electrons as $|\mathbf{H}_p| \sim 10^{-3}$ Oe; i.e., we have $|H_p/H_0| \ll 1$. Consequently, the field $\mathbf{H}_p$ and equation (4) can be eliminated from set (3)–(6). Given the above remarks, we can rewrite equations (3)–(6) as

$$\frac{\partial \mathbf{E}_p}{\partial t} + 4\pi e n_e \mathbf{v}_e = 0, \tag{8}$$

$$\frac{\partial n_e}{\partial t} + \nabla(n_e \mathbf{v}_e) = 0, \tag{9}$$

$$\frac{\partial}{\partial t}(n_e \mathbf{v}_e) + \nabla(n_e \mathbf{v}_e \mathbf{v}_e) = \frac{e n_e}{m_e}\left(\mathbf{E}_p + \mathbf{E}_b + \mathbf{E}_S + \frac{1}{c}[\mathbf{v}_e \times (\mathbf{H}_0 + \mathbf{H}_b)]\right). \tag{10}$$

Since the problem is treated in axisymmetric geometry, the projections of equations (8)–(10) onto the axis of the spherical coordinate system, which will be used in further analysis, can be written as

$$\frac{\partial E_{pR}}{\partial t} = -4\pi e n_e v_{eR}, \tag{11}$$

$$\frac{\partial E_{p\theta}}{\partial t} = -4\pi e n_e v_{e\theta}, \tag{12}$$

$$\frac{\partial E_{p\varphi}}{\partial t} = -4\pi e n_e v_{e\varphi}, \tag{13}$$

$$\frac{\partial n_e}{\partial t} = -\frac{1}{R^2}\frac{\partial}{\partial R}(R^2 n_e v_{eR}) - \frac{1}{R\sin\theta}\frac{\partial}{\partial \theta}(\sin\theta\, n_e v_{e\theta}), \tag{14}$$

$$\frac{\partial v_{eR}}{\partial t} = -v_{eR}\frac{\partial v_{eR}}{\partial R} - \frac{v_{e\theta}}{R}\frac{\partial v_{eR}}{\partial \theta} + \frac{e}{m_e}(E_{pR} + E_{bR} + E_{SR}) - \omega_{He} v_{e\varphi}\sin\theta - \omega_{Hb} v_{e\theta}, \tag{15}$$

$$\frac{\partial v_{e\theta}}{\partial t} = -v_{eR}\frac{\partial v_{e\theta}}{\partial R} - \frac{v_{e\theta}}{R}\frac{\partial v_{e\theta}}{\partial \theta} + \frac{e}{m_e}(E_{p\theta} + E_{b\theta}) - \omega_{He} v_{e\varphi}\cos\theta - \omega_{Hb} v_{eR}, \tag{16}$$

$$\frac{\partial v_{e\varphi}}{\partial t} = -v_{eR}\frac{\partial v_{e\varphi}}{\partial R} - \frac{v_{e\theta}}{R}\frac{\partial v_{e\varphi}}{\partial \theta} + \frac{e}{m_e}E_{p\varphi} + \omega_{He}(v_{eR}\sin\theta + v_{e\theta}\cos\theta), \tag{17}$$

where ω_{He} is the electron cyclotron frequency and $\omega_{Hb} = |e|H_{b\varphi}/m_e c$. Note that, for $\theta = 0$ and π, equations (11)–(17) pass over to equations (5) from [3], which describe the dynamics of the plasma electrons near a

satellite under the assumptions that electron injection is isotropic and the geomagnetic field is zero ($\mathbf{H}_0 = 0$).

Since the self-fields of a beam are assumed to be prescribed and the electric field of a satellite that is being charged as a result of electron injection (i.e., without allowance for the satellite charging by a neutralizing current) depends exclusively on the beam current, these fields can be expressed through the beam parameters. Following [11], we assume that the electron beam is cylindrical and obtain

$$W_b \approx \text{const}, \quad v_b = (2W_b/m_e)^{1/2} \approx \text{const}, \tag{18}$$

$$E_{bR} = \frac{I_b(t)}{v_b R}\left(1 - \frac{R_0}{\sqrt{R^2 + R_0^2 - 2RR_0\cos\theta}}\right),$$

$$E_{b\theta} = \frac{I_b(t)}{v_b R\tan\theta} \tag{19}$$

$$\times\left[1 - \frac{1}{\sqrt{R^2 + R_0^2 - 2RR_0\cos\theta}}\left(R_0 - \frac{R}{\cos\theta}\right)\right],$$

$$H_\varphi = \frac{I_b(t)}{cR\sin\theta}\left(1 - \frac{R_0 - R\cos\theta}{\sqrt{R^2 + R_0^2 - 2RR_0\cos\theta}}\right), \tag{20}$$

$$E_{SR} = \frac{1}{R^2}\int_0^{t-(R-R_0)/v_b} I_b(t)dt, \tag{21}$$

where $I_b(t) = I_m f_b(t)$, $I_m = \text{const} < 0$, $0 \le f_b(t) \le 1$, $t' = t - (R - R_0)/v_b$ is the delay time. If the inequality $|\Delta f/f| \ll 1$ holds for the functions in equations (11)–(17) for a time $(R_c - R_0)/v_b$, then we have $t' \approx t$. Below, we will show that the most rapid plasma processes occur on the time scale $t \sim 1/\omega_0$. For parameter values characteristic of active ionospheric experiments [1, 6, 7], a comparison between these time intervals gives $(R_c - R_0)/v_b \ll 2\pi/\omega_0$. Consequently, the time delay in equations (11)–(17) can be ignored. Note also that expressions (19) and (20) are written without allowance for "shadowing" of the regions around a satellite, because, otherwise, they would be too involved.

3. INITIAL AND BOUNDARY CONDITIONS FOR THE BASIC EQUATIONS

Equations (11)–(17) should be supplemented with the initial conditions characteristic of the vicinity of a satellite moving along the geomagnetic field $\mathbf{H}_0$ in the ionosphere. However, these conditions, which were presented in [7], refer to regions with low ion and electron densities $n_{e,i}$ and are too complicated to be used in a hydrodynamic description of the plasma processes. To simplify them, we turn to the inequalities $Q(t > 0) \gg |Q(0)|$ and $\varphi_0(t > 0) \gg kT_e^0/|e|$ (where k is the Boltzmann constant and T_e^0 is the plasma electron temperature), which are satisfied in active experiments with electron beam injection into the ionosphere. Consequently, in contrast to [7], we can impose the following initial conditions at $t = 0$ [3]:

$$\sigma(0) = 0, \quad \mathbf{E}_p(R, \theta, 0) = 0, \quad \mathbf{v}_e(R, \theta, 0) = 0,$$
$$n_e(R, \theta, 0) = n_{e,i}^0 \exp(-\varphi^*), \tag{22}$$

where $\sigma(t)$ is the surface charge density. The function $\varphi^* = e\varphi(0)/kT_e^0$, which was given numerically in [7], can be approximated by $\varphi^* = a\exp[-b(R/R_0 - 1)] - d(R/R_0)^{-2}$ [3] with $a = 0.418$, $b = 0.9301$, and $d = 0.272$.

In order to specify the boundary conditions, we must analyze the properties of the satellite surface and the plasma sheath structure around the satellite. We assume the satellite surface to be perfectly conducting. We also assume the sheath structure to be such that the satellite surface is perfectly absorbing for plasma electrons and neutralizes the plasma ions that hit it. Al'pert *et al.* [7] showed that the plasma sheath around a conducting body is very similar in structure to that around a perfectly reflecting body. Consequently, the reflection coefficient A of plasma particles from the surface of a conducting body should be close to unity:

$$1 - A \ll R_0/l_{e,i},\ D/l_{e,i}, \tag{23}$$

where D is the Debye radius. Thus, we can regard the satellite surface as being almost perfectly conducting, because the electron and ion mean free paths in the ionospheric plasma are sufficiently long ($R_0 \sim 100$ cm, $D \sim 1$ cm, $l_{e,i} \sim 10^4$ cm [6, 7]).

With these considerations, we can specify the boundary conditions as follows [12]:

$$E_{SR}(R_0, t) - E_{pR}(R_0, t) - E_{bR}(R_0) = 4\pi\sigma(t),$$
$$E_{p\theta}(R_0, t) = E_{p\varphi}(R_0, t) = 0, \tag{24}$$

$$\frac{\partial\sigma(t)}{\partial t} = \frac{I_m f_b(t)}{4\pi R_0^2}$$
$$+ \kappa e v_{eR}(R_0 + 0, \theta, t) n_e(R_0 + 0, \theta, t), \tag{25}$$

where

$$\kappa = \begin{cases} 1 & \text{for } \mathbf{v}_e(R_0 + 0, \theta, t)\mathbf{N} < 0, \\ 0 & \text{for } \mathbf{v}_e(R_0 + 0, \theta, t)\mathbf{N} > 0, \end{cases}$$

$\mathbf{N}$ is the normal to the satellite surface, and

$$v_{eR}(R_0, \theta, t) = 0. \tag{26}$$

We assume that the plasma outside a space-charge sheath of radius R_c is unperturbed. Since the satellite surface is regarded as being almost perfectly conduct-

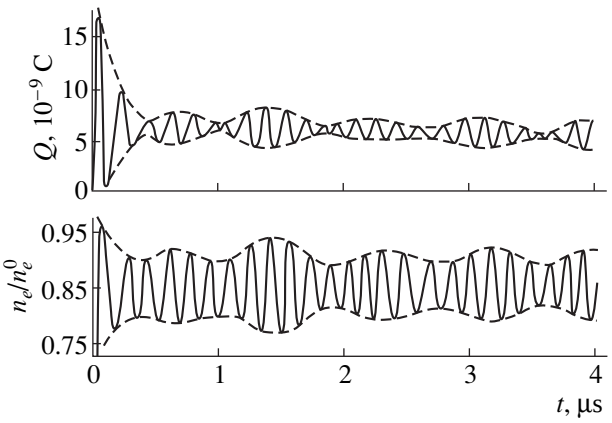

Fig. 1. Time evolution of the satellite's charge and electron plasma density at a distance ΔR from the satellite (in arbitrary units).

ing, the time evolution of the satellite's charge can be described by

$$Q(t) = \int_{S_0} \sigma(t) dS = 4\pi R_0^2 \sigma(t). \quad (27)$$

4. DISCUSSION OF THE RESULTS

Equations (11)–(17) were solved by a finite-difference method [13]. The parameters of the problem were chosen in accordance with the ELECTRON ECHO-1 and ARAKS experiments [1], because they yielded the most rewarding insights into the physical processes accompanying the injection of electron beams from a satellite: I_b = const = –0.5 A, W_b = 10 keV, r_{b0} = 15 cm, R_0 = 50 cm, $n_{e,i}^0 = 5 \times 10^5$ cm^{-3}, and $T_e^0 = 10^3$ K. Some results of solving the problem are illustrated graphically in Figs. 1–5.

Figures 1–3 present time evolutions of the functions Q, n_e, E_R, E_θ, E_φ ($\mathbf{E}_R = \mathbf{E}_{SR} + \mathbf{E}_{pR} + \mathbf{E}_{bR}$, $\mathbf{E}_\theta = \mathbf{E}_{p\theta} + \mathbf{E}_{b\theta}$, $\mathbf{E}_\varphi = \mathbf{E}_{p\varphi}$), v_{eR}, $v_{e\theta}$, and $v_{e\varphi}$. All the time evolutions (except for Q) are plotted at the point $R = R_0 + \Delta R$, $\theta = 60°$, where ΔR is the grid size along the R-coordinate. Figures 1–3 show that neutralization of the satellite's charge is accompanied by unsteady oscillatory processes with a tendency to reach an equilibrium state. The time evolution of the main frequency $\omega_1 \approx \omega_0$, which characterizes the oscillatory character of the processes, is seen to be modulated at the frequency $\omega_2 \approx \omega_{He}$; moreover, we have $\omega_1 < \omega_0$ and $\omega_2 < \omega_{He}$, because dissipation [14] acts to increase the period of the oscillatory processes [15]. The phases of the quantities under consideration are related as follows: the functions Q (and E_R), E_θ, and E_φ are shifted in the phase by $\psi \approx \pi/2$ with respect to v_{eR}, $v_{e\theta}$, and $v_{e\varphi}$, respectively, and the function n_e is shifted by $\psi \approx -\pi$ with respect to Q and E_R because of the plasma inductance due to electron inertia in an alternating electric field [16].

The solutions obtained in the linear approximation are close to the solution of the equation for forced oscillations with friction near the resonance $\omega \approx \omega_0 + \omega_{He}$ [16] under the condition $\lambda \ll \omega_{He} \ll \omega_0$, where $\lambda \sim 10^5$ s^{-1} is the friction coefficient [17]. Over the time interval $t \sim 1/\lambda$, the oscillations have the form $x \approx -B(t)\cos(\omega_0 t + \psi(t))$, where $B(t) = F(t)/2m_e\omega_0\omega_{He}$ is a slowly varying amplitude and $\psi(t)$ is a slowly varying phase. We can see that the amplitude $B(t)$ experiences

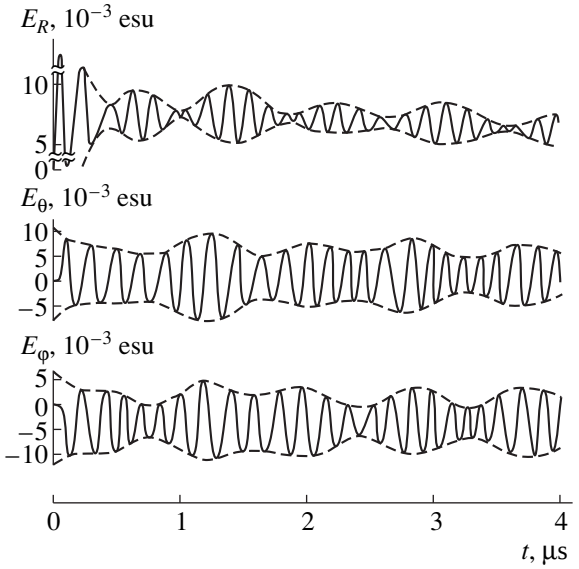

Fig. 2. Time evolution of the electric field components at a distance ΔR from the satellite.

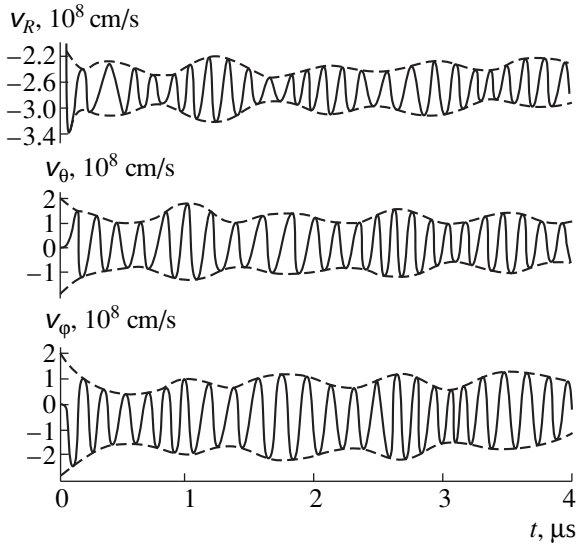

Fig. 3. Time evolution of the components of the plasma electron velocity at a distance ΔR from the satellite.

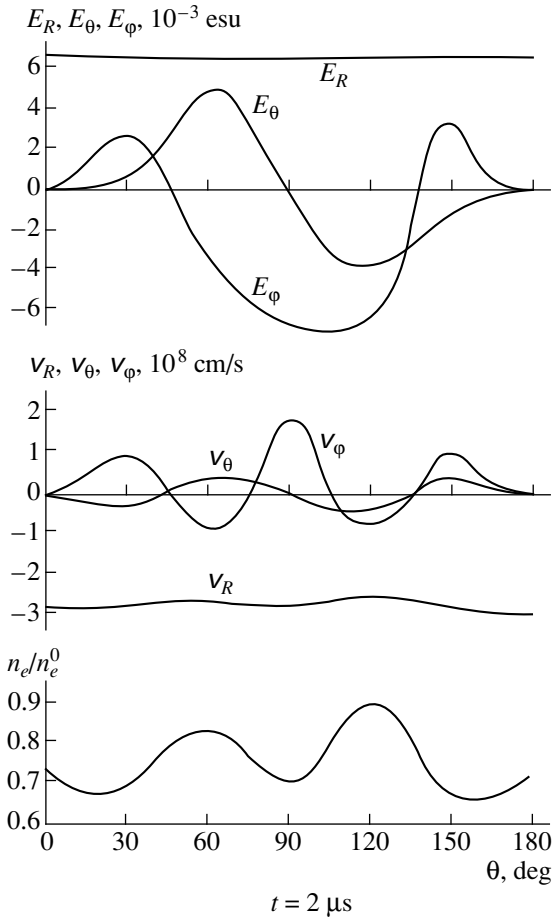

Fig. 4. The electric field components, the components of the plasma electron velocity, and the plasma electron density versus the angle θ at a distance ΔR from the satellite (in arbitrary units).

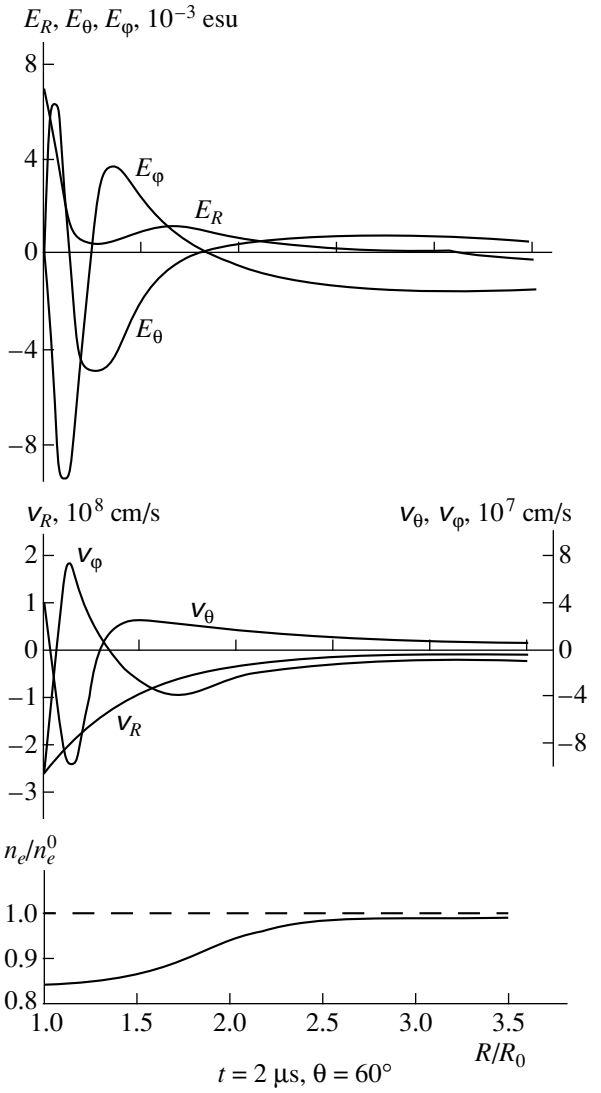

Fig. 5. The electric field components, the components of the plasma electron velocity, and the plasma electron density versus the radius R for θ = 60° (in arbitrary units).

slow periodic variations around its steady-state value, the time required for the oscillations to be established being $t \sim 1/\lambda \ll t_{\text{ion}}, t_h$ [3]. For example, if $F(t) = e\langle\tilde{E}_R\rangle$, $\langle\tilde{E}_R\rangle \approx 7 \times 10^{-4}$ esu ($t \approx 4$ μs), then, for v_{eR}, we obtain $\omega_0 B(t) = e\langle\tilde{E}_R\rangle/2m_e\omega_{He} \approx 2.3 \times 10^7$ cm/s, which agrees well with the parameter values obtained by solving equations (11)–(17) (Fig. 3).

To estimate the potential φ_0, we turn to Fig. 5, which shows that $\langle v_{eR}(R_0 + 0, \theta, t)\rangle \approx -2.6 \times 10^8$ cm/s, so we obtain $\varphi_0 \sim m_e v_{eR}^2/2|e| \approx 19$ V. Consequently, we have $|e|\varphi_0 \ll W_b$; i.e., the beam energy losses are small and the assumption that $W_b \approx$ const is valid. To determine the analytic dependence of the potential φ_0 on the experimental parameters, it is necessary to investigate the structure of the space-charge sheath. This problem will be studied separately in a subsequent paper. When the potential φ_0 is very high, such that $R_0 \gg D$ and $|\varphi_0| \gg (kT_e^0/|e|)(R_c/D)^{4/3}$ [7], we have $\varphi \sim \varphi_0 R_0/R$ near the satellite surface. This circumstance made it possible to simplify the derivation of the desired analytic dependence obtained in [4] for isotropic electron injection under the condition $\mathbf{H}_0 = 0$.

Figures 4 and 5 illustrate the solutions to equations (11)–(17) at $t = 2$ μs versus the angle θ (for $R = R_0 + \Delta R$) and the radius R (for θ = 60°), respectively. Figure 4 shows that all of the functions, except for v_{eR}, depend strongly on the angle θ, primarily because of the large variations in $E_\theta(\theta)$ and $E_\varphi(\theta)$. Since $E_R(\theta) \approx$ const, we have $v_{eR}(\theta) \approx$ const. From Fig. 5, we can see that the solutions change sharply across a sheath of thickness $1 \le R/R_0 \le 1.5$ around the satellite and, at larger distances from the satellite surface, they remain essentially unchanged. Since the sheath thickness is smaller than the electron Larmor radius, the drift approxima-

tion cannot be used to determine the parameters of the perturbed plasma.

The simplifying assumptions made in solving the problem allowed us to employ a quasihydrodynamic description of the processes occurring in the plasma and to neglect ion motion. However, we also assumed that the initial distribution of charged plasma particles differs from the conventional one and the initial radii of the electron beams are larger than those characteristic of actual space experiments (r_{b0} = 1–3 cm [1]). Regarding the effect of these factors on the solutions obtained, we offer the following comments.

According to Figs. 3 and 5, the relationship $|v_e| \gg v_{Te} \sim 10^7$ cm/s holds over an entire sheath of radius R_c [6, 7], which justifies the use of the quasihydrodynamic approximation. Since the problem was solved over the time interval $0 \le t \le 4$ μs, over which the satellite's charge satisfies the relationships $|v_i| \sim eQt/m_{i(O_2^+)}R_0^2 < v_{Ti} \sim 10^5$ cm/s and $t \ll 1/\nu \sim 10^{-4}$ s $\ll R_c/|v_i| = 2.5R_0/|v_i| \sim 10^{-3}$ s [6, 7], we were justified in neglecting ion motion. We used an unconventional initial distribution of charged plasma particles around a satellite, because the hydrodynamic approximation is inapplicable to the region with $n_{e,i}^0 \approx 0$, which forms just behind an orbiting satellite. As initial conditions, we adopted the conditions near a satellite at rest, because the incident plasma flow ahead of a satellite is such that $n_{e,i} \approx 2n_{e,i}^0$ [3, 7]. We also increased the radius of the injected beam so as to avoid the formation of regions with a very low electron density and/or the escape of all of the electrons from the region occupied by the beam under the action of its own electric field $\mathbf{E}_b$.

In conclusion, note that the results obtained in our study may be useful in planning active space experiments with wire arrays [18] and in interpreting the relevant experimental data.

ACKNOWLEDGMENTS

I am grateful to A.A. Rukhadze and K.V. Khodataev for a discussion of the results and useful advice.

REFERENCES

1. *Artificial Particle Beams in Space Plasma Studies*, Ed. by B. Grandal (Plenum, New York, 1982; Mir, Moscow, 1985).
2. L. M. Linson, J. Geophys. Res. **74**, 2367 (1969).
3. V. A. Fedorov, Fiz. Plazmy **9**, 874 (1983) [Sov. J. Plasma Phys. **9**, 510 (1983)].
4. V. A. Fedorov, Kosm. Issled. **22**, 588 (1984).
5. V. A. Fedorov, Geomagn. Aeron. **27**, 69 (1987).
6. V. L. Ginzburg and A. A. Rukhadze, *Waves in Magnetized Plasmas* (Nauka, Moscow, 1970).
7. Ya. L. Al'pert, A. V. Gurevich, and L. P. Pitaevskiĭ, *Artificial Satellites in a Rarefied Plasma* (Nauka, Moscow, 1964).
8. S. I. Syrovatskiĭ, Usp. Fiz. Nauk **62**, 247 (1957).
9. A. A. Rukhadze, L. S. Bogdankevich, S. E. Rosinskiĭ, *et al.*, *Physics of High-Current Relativistic Electron Beams* (Atomizdat, Moscow, 1980).
10. R. N. Sudan, in *Basic Plasma Physics: Supplement to the Second Volume*, Ed. by A. A. Galeev and R. Sudan (Énergoatomizdat, Moscow, 1984).
11. V. A. Fedorov, Kosm. Issled. **26**, 270 (1988).
12. L. I. Sedov, *A Course in Continuum Mechanics* (Nauka, Moscow, 1976; Wolters-Noordhoff, Groningen, 1971), Vols. 1 and 2.
13. D. Potter, *Computational Physics* (Wiley, New York, 1973; Mir, Moscow, 1975).
14. V. A. Fedorov, Geomagn. Aeron. **24**, 205 (1984).
15. L. D. Landau and E. M. Lifshitz, *Mechanics* (Pergamon, Oxford, 1976; Nauka, Moscow, 1973).
16. L. A. Artsimovich and R. Z. Sagdeev, *Plasma Physics for Physicists* (Nauka, Moscow, 1973).
17. N. A. Romanova and V. A. Fedorov, Mat. Model. **2**, 3 (1990).
18. M. Greene, D. Wheelcock, and M. Baginski, J. Spacecr. Rockets, No. 6, 452 (1989).

Translated by I. A. Kalabalyk

Plasma Physics Reports, Vol. 26, No. 3, 2000, pp. 272–277. Translated from Fizika Plazmy, Vol. 26, No. 3, 2000, pp. 293–298.

LOW-TEMPERATURE PLASMAS

Spatial Structure of Emission from an Electrode Microwave Discharge in Hydrogen

Yu. A. Lebedev, M. V. Mokeev, and A. V. Tatarinov

Topchiev Institute of Petrochemical Synthesis, Russian Academy of Sciences, Leninskiĭ pr. 29, Moscow, 117912 Russia

Received April 22, 1999; in final form, June 15, 1999

Abstract—The structure of electrode microwave (2.45 GHz) discharges in hydrogen with electrodes of various shapes and sizes at pressures of 1–8 torr and incident powers of 2–150 W is studied. It is found that the discharges exhibit a common feature that is independent of the antenna-electrode design: near the electrode surface, there is a thin bright sheath surrounded by a less bright, sharply bounded region, which is usually shaped like a sphere. It is suggested that the structure observed arises because the microwave field maintaining the discharge is strongly nonuniform. Near the electrode, there exists a thin dense plasma sheath with a high electron density gradient. A strong dependence of the electron-impact excitation coefficient on the electric field makes the effect even more pronounced. As the electron density decreases due to dissociative recombination, the microwave field gradient decreases and the discharge emission intensity tends to a nearly constant value. Presumably, in the boundary region of the discharge, there exists a surface wave, which increases the emission intensity at the periphery of the discharge. © *2000 MAIK "Nauka/Interperiodica"*.

1. INTRODUCTION

At present, much attention is drawn to stimulated microwave discharges [1–4]. The electrode microwave discharge also belongs to this class of discharges and differs only in that the energy is supplied to the discharge along the initiating antenna. Although such discharges have a number of interesting features and a wide range of potential applications (e.g., in plasmochemistry, for producing diamond coatings [5]), they have remained until now the least understood type of microwave discharges. In [6, 7], these discharges were treated phenomenologically, the spatial structure of the discharge with a cylindrical electrode was described, and results of probe measurements were presented. However, information on the nature of these discharges is lacking and the physical processes giving rise to these discharges are still poorly studied.

The aim of this paper is to study the effect of the shape and size of the electrodes on the properties of the discharge, to determine the structure of an electrode microwave discharge in hydrogen at pressures of 1–8 torr from space-resolved measurements of the integral plasma emission intensity, and to reconstruct the picture of physical processes giving rise to the structure observed.

2. EXPERIMENTAL SETUP

The discharge chamber was a metallic cylinder 8.5 cm in diameter with an antenna inserted through a vacuum-tight connection at its end. The antenna was a component of a coaxial-to-waveguide converter, which was adjusted with the help of a short-circuiting piston (Fig. 1). Antennas of different shapes and sizes were used. The discharge was initiated around the antenna (the exciting electrode), and its size was substantially smaller than the chamber diameter and the distance to the chamber's lower end. The measurements were carried out in the flow system. We used a microwave generator with an output power up to 170 W and a frequency of 2.45 GHz. The discharge emission passed through a window in the wall of the discharge chamber,

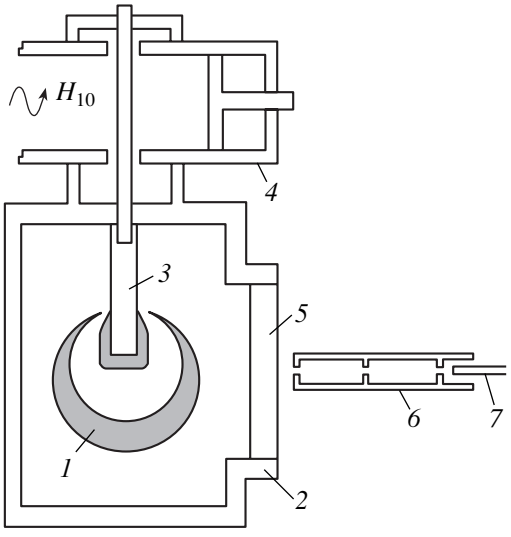

Fig. 1. Schematic of the experimental setup: (*1*) plasma, (*2*) discharge chamber, (*3*) electrode, (*4*) waveguide-to-coaxial converter, (*5*) window, (*6*) collimator, and (*7*) fiber.

1063-780X/00/2603-0272$20.00 © 2000 MAIK "Nauka/Interperiodica"

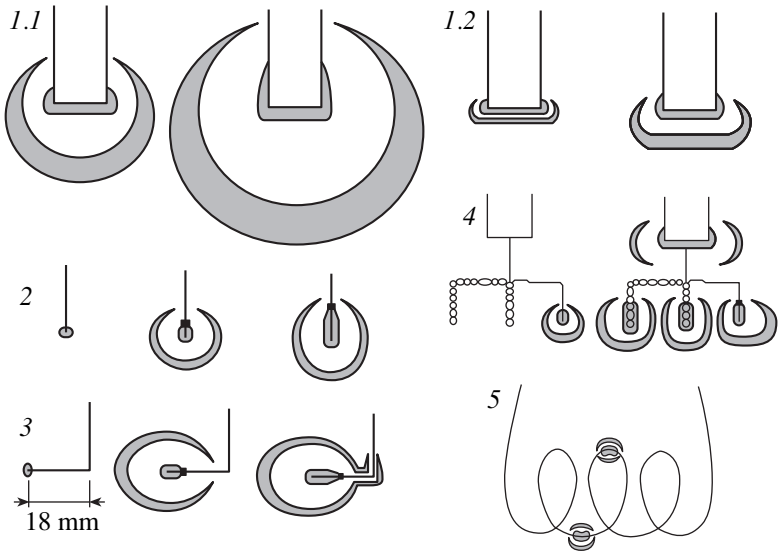

Fig. 2. Structure of discharges with different electrodes: (*1*) cylindrical electrode at (*1.1*) 1–3 and (*1.2*) 4–8-torr pressure, (*2*, *3*) thin wire, (*4*) trident twisted from a wire, and (*5*) wire spiral. Positions *1–4* show the change in the discharge shape with increasing the incident power.

fell into a diaphragm collimator, and was led to a photomultiplier through a fiber. The collimator collected emission from the discharge region ~1.5 mm in diameter. The collimator could be displaced in the plane parallel to the window both in the vertical and horizontal directions; its coordinates were recorded by a two-coordinate recorder. The second recorder input was used to measure signals from an amplifier connected to the photomultiplier. As a result, we obtained the distribution of the integral plasma emission intensity I both along the antenna axis (the axis of symmetry of the discharge) and in the transverse direction.

3. GENERAL FEATURES OF THE DISCHARGE

The dependence of the discharge structure on the shape and size of the initiating electrodes was investigated at a pressure of 1 torr.

3.1. Cylindrical Electrode

3.1.1. Pipes and rods 6 or 4 mm in diameter. The discharge usually consisted of two regions: a bright thin sheath near the electrode and a less bright region surrounding the sheath. The latter was usually spherically shaped and had a sharp boundary (further, this region will be referred to as the "sphere"). The brightness of the discharge in the interior of the sphere (outside of the thin sheath) was less compared to the periphery. The volume and brightness of the sheath and sphere increase with increasing the incident power and decrease with increasing the pressure. At higher pressures and low powers, the sphere is adjacent to the thin sheath or completely disappears. The thin sheath first appeared near the end of the cylindrical electrode; as the incident power increased, the sheath extended along the cylindrical surface toward the microwave generator. When viewed from the electrode end, the sheath was shaped like a ring situated at the periphery of the electrode independently of whether pipe- or rod-electrodes were used. At pressures of 1–3 torr, the sphere had an almost regular shape and its center was situated somewhat lower than the electrode end (the higher the power, the lower the center was situated). The thickness of the sphere was maximum immediately under the electrode and decreased with distance from the electrode end, so that the upper part of the sphere was almost invisible near the electrode. As the pressure increased, the sphere changed shape (Fig. 2). Stainless-steel and copper electrodes were used. The heating traces were observed on the surface of the stainless-steel electrode, which is evidence of substantial heating.

3.1.2. Thin (0.5 mm in diameter) wire. A characteristic feature of a thin-electrode discharge was that the discharge could be ignited at a lower power supply. A weak plasma glow appeared at the end of the wire even at an incident power of $W = 2$ W. At high powers, the sphere elongated and took the shape of an ellipsoid, following the plasma sheath which extended along the electrode as the incident power increased (Fig. 2, position *2*).

3.2. Thin Wire Bent at a Right Angle near Its End

In comparison with Section 3.1, the new feature is that, at high W values, the sphere produced a sprout that surrounded the electrode bend and then went up (Fig. 2, position *3*).

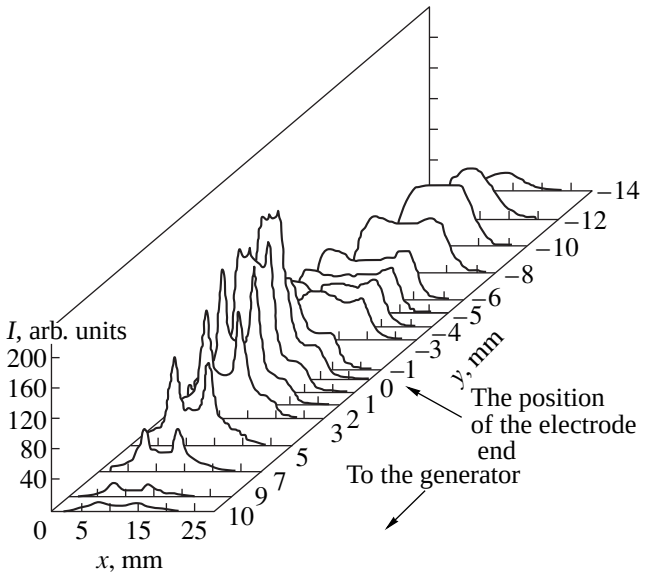

Fig. 3. Spatial distribution of the plasma emission intensity in the case of a cylindrical electrode 6 mm in diameter at a pressure of 1 torr and incident power of 90 W.

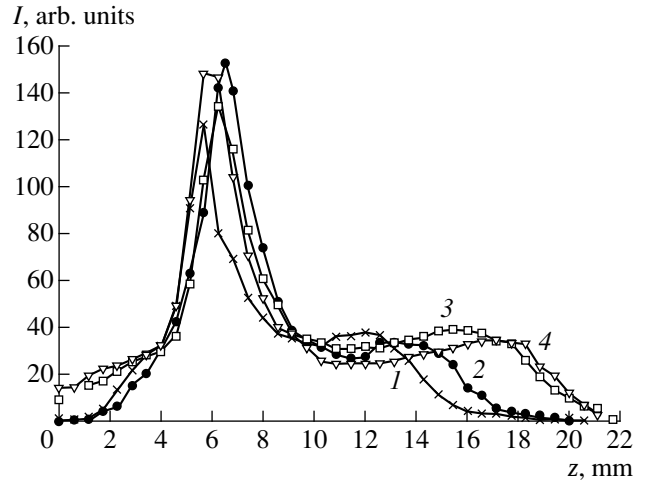

Fig. 4. Distribution of the plasma emission intensity $I(z)$ along the discharge axis at a pressure of 1 torr and different values of the incident power: (*1*) 29, (*2*) 50, (*3*) 70, and (*4*) 92 W.

3.3. A Trident Twisted from a Thin Wire and Inserted into a Pipe Electrode

The discharge first appeared near the sharp edge. As W increased, the discharge arose near the round ends as well and a thin plasma sheath arose along each end of the trident, each sheath being surrounded by its individual sphere following the sheath. Then, the spheres approached each other and became deformed so that there was always a dark gap between them. As W further increased, the discharge arose near the pipe edge as well. In this case, the size and brightness of the discharge at the wire decreased (Fig. 2, position *4*).

3.4. A Wire Wound as a Spiral

Thin plasma sheaths arose simultaneously near several loops of the spiral and then skipped from one loop to another. Spheres were formed around sheaths (Fig. 2, position *5*; experiments were also carried out with spirals of another shape).

In the cases considered in Sections 3.1.2–3.4, when W exceeded a certain threshold value, another discharge arose near the point where the electrode entered the chamber. In this case, either the discharge situated near the end of the electrode quenched or its size and brightness decreased substantially, because most of the input energy was released in the discharge nearest to the generator. As W increased further, the intensity and size of the discharge situated near the electrode end decreased (up to the complete disappearance of the discharge).

Thus, independently of the electrode shape, the discharge always consisted of two regions: a bright thin sheath near the electrode and a less bright (usually spherical) region surrounding the sheath. Hence, the shape of electrodes has little or no effect on the structure of the discharge. Below, we consider in detail the structure of the discharge with a cylindrical electrode. The common feature is that the discharge always occurred at high levels of reflection of microwaves; in the experiments, the standing-wave factor varied from 6 to 11.

Note that spherical structures were observed in dc [8], RF [9, 10], and microwave [3] discharges at pressures of 10^{-2}–100 torr.

4. RESULTS OF EXPERIMENTS WITH CYLINDRICAL ELECTRODES

The basic structure of the discharge glow becomes clear from Fig. 3: there is a bright thin sheath near the electrode, and the emission intensity increases at the periphery of the discharge.

At pressures of 1–8 torr, the distributions of the plasma emission intensity along the electrode, $I(z)$, were measured for various values of the incident power (Fig. 4). The curves are plotted versus the incident power, because in our discharge system, the only possibility to find the absorbed power is to calculate it from the power balance by subtracting the reflected power. The absorbed power calculated in this way is 10–30 W for an incident power of 20–90 W. The absorbed power is a linear function of the incident power. However, the question of which portion of energy is absorbed by the plasma itself remains open. The total intensity of the discharge emission depends linearly on the incident power for any pressures except for pressures close to 1 torr. The latter is likely due to the fact that, at this pressure, the plasma impedance strongly affects the electrodynamic properties of the system.

Figure 5 shows the dependences $I(z)$ for various pressures and the same incident power. The curves $I(z)$

show that there are two luminous regions, which change depending on W and p as described above. It is also seen that the emission intensity decreases from the periphery to the center of the discharge. Figure 6 shows the ratio between the total emission intensities of the sheath and the spherical part of the discharge. This ratio was calculated by integrating the function $I(z)$ over the sheath region and the sphere region. It is seen that the dominant contribution to the discharge emission comes from the bright sheath near the antenna.

5. DISCUSSION OF THE RESULTS

The structure of the discharge emission and the appearance of a bright thin sheath surrounding the antenna can be explained as follows.

The intensity of plasma emission is equal to $I(r) \sim n_e(r)k_{b\Sigma}(r)$, where $n_e(r)$ is the electron density and $k_{b\Sigma}(r) \sim \sum_i \langle \sigma_i v \rangle$ is the total excitation coefficient (here, the angular brackets mean the averaging over the electron energy distribution function and the sum is taken over all radiating states with the excitation cross sections σ_i). Hence, spatial variations in the plasma emission near the antenna may be caused by variations in the radial profiles of n_e and/or $k_{b\Sigma}$. However, the primary cause of these dependences should be a sharp (at a length of 1 mm) change in the amplitude of the microwave field. For further analysis, it is important to keep in mind the experimental fact (see Fig. 6) that the volume-integrated intensity of the sheath emission always exceeds that of the spherical part of the discharge. This allows us to conclude that the energy deposition in the electrode sheath is higher than that in the spherical region. Taking into account the difference between the volumes, we can say that the energy deposition in the electrode sheath is higher by several orders of magnitude.

The aforesaid allows us to obtain the following estimate for the electron density in the plasma sheath assuming that the total power is released in this sheath: $W_{sp} = \bar{\varepsilon}\,\delta_{eff}\nu_{eff}n_e$ (where $\bar{\varepsilon}$ is the average electron energy, δ_{eff} is the mean fraction of the energy lost by an electron in one collision with a heavy particle, and ν_{eff} is the effective frequency of collisions between electrons and heavy particles. The calculation for a hydrogen microwave plasma by the Boltzmann equation (the numerical scheme is described in [11]) for a pressure of 1 torr and a microwave-field amplitude of 100 V/cm shows that $\delta_{eff} \sim 10^{-2}$, $\bar{\varepsilon} \sim 4$ eV, and $\nu_{eff} \sim 10^9$ s^{-1}. Taking this into account, we obtain that $n_e \sim 10^{13}$ cm^{-3}. Note that, at such densities, the electron heat conduction should equalize possible variations of the average electron energy across the sheath.

We can distinguish two regions in the sheath. The first region is adjacent to the electrode, and the electron density here varies from zero (on the antenna surface) to the maximum value. The second region spans from this point up to the periphery of the discharge. In the first region, because of the closeness to the electrode surface, the loss of charged particles occurs primarily through their diffusion to the electrode ($\tau_d \sim \Lambda^2/D_a \sim 10^{-7}$ s). It is of interest to consider the second region.

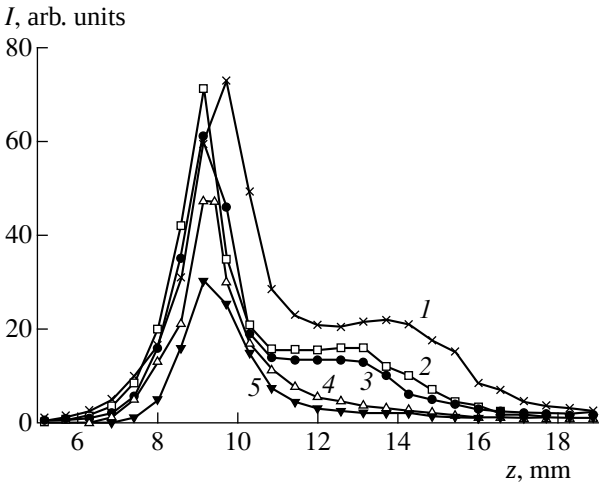

Fig. 5. Distribution of the plasma emission intensity $I(z)$ along the discharge axis at W = 20 W and different pressures: (*1*) 2, (*2*) 3, (*3*) 4, (*4*) 6, and (*5*) 8 torr.

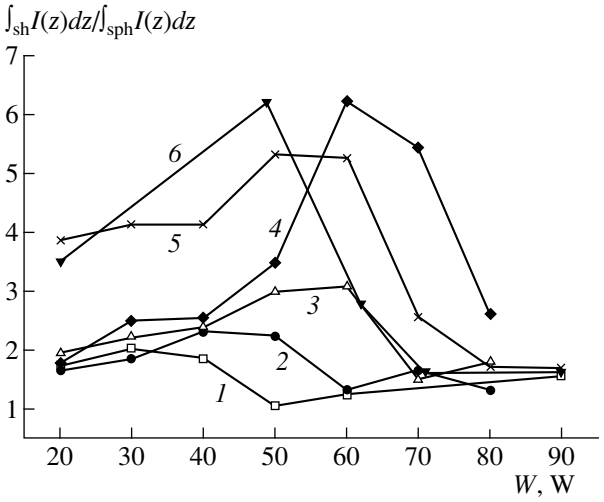

Fig. 6. Ratio between the total emission intensities of the sheath and spherical part of the discharge at (*1*) 1, (*2*) 2, (*3*) 3, (*4*) 4, and (*5*) 6, and (*6*) 8 torr.

The spatial electron density distribution is governed by the balance equation for charged particles and depends on both the spatial distribution of the ionization rate and the ratio of the loss of charge particles through diffusion to the loss through recombination. Outside the sheath, the characteristic diffusion time is determined by the discharge dimensions and is equal to $\tau_d \sim \Lambda^2/D_a$ ($D_a \approx \mu^+$), where (D_e/μ_e) is the ambipolar diffusion coefficient; μ^+, μ_e are the ion and electron

mobilities, respectively; and D_e is the coefficient of free electron diffusion. The mobility of H_3^+ ions (which are the most abundant ions [11]) in hydrogen at a pressure of 1 torr is equal to $\mu^+ \sim 8000$ cm^2/V s; thus, we obtain $D_a \sim 2 \times 10^4$ cm^2/s and $\tau_d \sim 10^{-5}$ s.

The characteristic dissociative electron–ion recombination time is $\tau_r \sim 1/n_e\gamma_r \sim 10^{-6}$ s for an electron density of $n_e \sim 10^{13}$ cm^{-3} (for $\gamma_r \sim (2–3) \times 10^{-6}$ [12]). Consequently, the spatial variations in the charge-particle density profile outside the bright plasma sheath are governed by the volume recombination and the electron density profile must be similar to the field profile. This means that the intensity of the discharge emission decreases with distance from the sheath.

The variations in the radial profile of the electric field can be caused by several effects. One cause is the skinning of the field at the length $\Delta_{sk} = -(\omega/c)\mathrm{Im}[\varepsilon(n_e)]^{1/2}$, where $\varepsilon(n_e)$ is the plasma permittivity. We can estimate n_e assuming that the skin depth is equal to the sheath thickness Δ. Then, we obtain the value $n_e \sim 10^{13}$ cm^{-3}, which coincides with the above estimate for the electron density in the sheath.

Another mechanism for the field variations is described in [13, 14], in which self- consistent steady-state electron-density and field distributions are considered. These distributions are established as a result of the balance of ionization, diffusion, and attachment processes in an RF discharge with dimensions less than the wavelength. In those papers, variations in the electric-field component that is normal to the electrode surface and parallel to the electron-density gradient were studied. In particular, the discharge in a radially symmetric field produced by a single electrode was considered. It was shown that, in this case, the plasma-layer thickness is equal to $\Delta \sim L_a = (D_a/\nu_a)^{1/2}$, where ν_a is the attachment frequency. In our case, the main process leading to the volume loss of charged particles is the dissociative electron–ion recombination. An analysis of the basic equations shows that the method used in those studies can be formally applied to our case if we replace the attachment rate ν_a with the recombination rate $\nu_r = n_e\gamma_r$. Estimates show that the plasma layer with thickness $\Delta \sim 1$ mm is formed when $n_e \sim 10^{13}$ cm^{-3}. This coincides with the above estimate based on the assumption that the plasma-sheath thickness is equal to the skin depth and means that additional data are needed to clarify the role of each of the considered mechanisms in the formation of a plasma sheath near the electrode.

Now, we consider whether the average electron energy can vary at a length equal to the sheath thickness. The characteristic electron-energy relaxation length is equal to $\lambda_\varepsilon \sim v_{av}/\delta_{eff}^{1/2}\nu_{eff}$, where $v_{av} \sim 10^8$ cm/s is the average electron energy. Estimates show that $\lambda_\varepsilon \sim 1$ cm. Hence, variations in the average electron energy cannot be large.

Nevertheless, these variations must be taken into consideration because even small variations in the average electron energy lead to significant variations in the rate coefficients of the processes initiated by electron impact, and these variations increase as the ratio $\varepsilon/\bar{\varepsilon}$ increases. For example, the numerical solution of the Boltzmann equation for a hydrogen microwave plasma at a pressure of 1 torr shows that, if the amplitude of the microwave field decreases by a factor of 1.5 (from 150 to 100 V/cm), then $\bar{\varepsilon}$ decreases by 20% and the direct-ionization coefficient decreases by a factor of 10. This leads to more pronounced variations in the discharge emission intensity in the radial direction.

Under certain conditions, the presence of plasma resonance can affect the field structure. This mechanism can become significant at low pressures. However, the described structure of the discharge was observed even at pressures as high as several tens of torr [3, 6, 7], when the electron collision frequency substantially exceeds the field frequency and this mechanism cannot play a decisive role.

Hence, the spatial structure of the discharge can be explained as follows.

In a nonuniform microwave field produced by an antenna in a large chamber, a narrow plasma region with a high field gradient is created near the antenna surface. This region is characterized by high values of the specific energy deposition, electron density, and emission intensity. Because of volume recombination, the electron density rapidly decreases with the radius, whereas both the excitation rate coefficients for radiating states of heavy particles and the emission intensity decrease with the radius. The decrease in the electron density leads to a more uniform distribution of the microwave-field amplitude and plasma emission in the spherical region. Based on the probe measurements, the conclusion was made in [7] that a surface wave propagates along the spherical boundary of the discharge and this wave is concentrated in the surface layer. The increase in the emission intensity at the edge of the spherical region can be explained by the effect of the surface wave.

The described mechanism of the formation of the discharge structure allows a consistent explanation of the existence of this structure over a wide pressure range in which the discharge was observed.

6. CONCLUSION

An electrode microwave discharge in hydrogen with electrodes of various shapes and sizes has been studied experimentally. It is found that the discharges in such systems exhibit a common feature that is independent of the design of the antenna electrode: near the electrode surface, there is a thin bright sheath surrounded by a less bright, sharply bounded region, which is usually shaped like a sphere. It is suggested that the structure observed arises because the microwave field main-

taining the discharge is strongly nonuniform. Near the electrode, there exists a thin plasma sheath with a high electron-density gradient. A strong dependence of the electron-impact excitation coefficient on the electric field makes the effect even more pronounced. As the electron density decreases due to dissociative recombination, the microwave-field gradient decreases and the discharge emission intensity tends to a nearly constant value. Presumably, in the boundary region of the discharge, there exists a surface wave, which increases the emission intensity at the periphery of the discharge.

ACKNOWLEDGMENTS

We are grateful to V. B. Gil'denburg for interest in this work and critical remarks useful for a more complete understanding of the plasma processes. This work was supported in part by the Netherland Organization for Scientific Research (NWO), grant no. 047.011.000.01.

REFERENCES

1. Yu. A. Lebedev, J. Phys. IV (Paris) **8**, 369 (1998).
2. G. M. Batanov, N. K. Berezhetskaya, E. F. Bol'shakov, *et al.*, Plasma Sources Sci. Technol. **2**, 164 (1993).
3. V. G. Brovkin, Yu. F. Kolesnichenko, and D. V. Khmara, in *Ball Lightning under Laboratory Conditions* (Khimiya, Moscow, 1994), p. 119.
4. V. G. Brovkin, Yu. F. Kolesnichenko, and D. Khmara, Prikl. Fiz., No. 4, 5 (1994).
5. L. Bardos, H. Barankova, Yu. A. Lebedev, *et al.*, Diamond Relat. Mater. **6**, 224 (1997).
6. L. Bardosh and Yu. A. Lebedev, Fiz. Plazmy **24**, 956 (1998) [Plasma Phys. Rep. **24**, 891 (1998)].
7. L. Bardosh and Yu. A. Lebedev, Zh. Tekh. Fiz. **68** (12), 29 (1998) [Tech. Phys. **43**, 1428 (1998)].
8. O. A. Nerushev, S. A. Novopashin, V. V. Radchenko, *et al.*, Preprint No. 285-97 (Inst. of Thermophysics, Siberian Division, Russian Academy of Sciences, 1997).
9. S. T. Ivanov, R. W. Thomae, H. Klein, *et al.*, Bulgar. J. Phys. **25**, 49 (1998).
10. V. B. Gil'denburg and G. A. Markov, Pis'ma Zh. Tekh. Fiz. **8** (20), 1245 (1982) [Sov. Tech. Phys. Lett. **8**, 535 (1982)].
11. Yu. A. Lebedev and I. L. Epstein, J. Moscow Phys. Soc. **5**, 103 (1995).
12. L. S. Polak, A. A. Ovsyannikov, D. I. Slovetskiĭ, *et al.*, *Theoretical and Applied Plasmochemistry* (Nauka, Moscow, 1975).
13. V. B. Gil'denburg, V. L. Gol'tsman, and V. E. Semenov, Radiofizika **17** (11), 1718 (1974).
14. V. B. Gil'denburg and V. E. Semenov, Fiz. Plazmy **6**, 445 (1980) [Sov. J. Plasma Phys. **6**, 244 (1980)].

Translated by N. F. Larionova

Plasma Physics Reports, Vol. 26, No. 3, 2000, pp. 278–282. Translated from Fizika Plazmy, Vol. 26, No. 3, 2000, pp. 299–304.

LOW-TEMPERATURE PLASMAS

Breakdown of Highly Excited Oxygen in a DC Electric Field

N. P. Vagin*, A. A. Deryugin, A. A. Ionin*, Yu. M. Klimachev*, I. V. Kochetov**, A. P. Napartovich**, D. V. Sinitsin*, and N. N. Yuryshev***

**Lebedev Institute of Physics, Russian Academy of Sciences, Leninskiĭ pr. 53, Moscow, 117924 Russia*

***Troitsk Innovation and Fusion Research Institute, Russian State Science Center, Troitsk, Moscow oblast, 142092 Russia*

Received April 21, 1999; in final form, June 8, 1999

Abstract—The breakdown of oxygen in a dc electric field is studied. A high concentration of oxygen molecules in the $a^1\Delta_g$ excited state is obtained in a purely chemical reactor. A decrease in the breakdown voltage at degrees of excitation exceeding 50% is observed. The theoretical decrement in the breakdown voltage obtained by solving the Boltzmann equation is in good agreement with the experimental data. *© 2000 MAIK "Nauka/Interperiodica".*

1. INTRODUCTION

Electron-excited molecules can play an important role in plasma kinetics, especially if we consider long-lived states. One of the most long-lived electron states is the $a^1\Delta_g$ oxygen state with an energy of 0.98 eV. For brevity, oxygen in this state will be further referred to as singlet oxygen. It is well known that, when a singlet-oxygen molecule collides with O^- and O_2^- negative ions, it causes their disintegration. However, the interaction of singlet-oxygen molecules with electrons is still poorly investigated.

Excitation of the discharge in an oxygen jet flowing out of a chemical reactor based on the bubbling of chlorine through a solution of H_2O_2 and KOH allows investigation of a plasma in a wide range of degrees of oxygen excitation (up to 100% of singlet oxygen). Such discharges can provide new information on electron scattering by singlet-oxygen molecules.

An oxygen–iodine chemical laser based on the conversion of singlet-oxygen energy [1] shows promise for industrial applications as one of the few powerful lasers generating in the near-infrared region ($\lambda = 1.315$ μm). However, the use of a highly efficient chemical reaction for singlet-oxygen production has some disadvantages limiting the area of laser application, because the chemicals used are highly aggressive and toxic. This is of particular importance in connection with the problem of environment pollution control. Therefore, it seems reasonable to replace a chemical singlet-oxygen generator (SOG) with an electric-discharge generator. This allows us to get rid of liquid chemical components and holds promise for achieving higher pressures at the generator output [2].

On the other hand, the gas discharge in an oxygen–iodine chemical laser can also be used to generate iodine atoms in gas by dissociating iodine-containing compounds that do not quench singlet oxygen [3]. In this case, it is possible to gain a high peak power of the iodine laser that can hardly be achieved with other methods.

All this has motivated studies of the characteristics of a discharge in oxygen with a high concentration of singlet oxygen.

In this paper, we study the breakdown characteristics of a low-pressure discharge in oxygen with 50% singlet oxygen and compare them with the breakdown characteristics of unexcited oxygen. A high concentration of singlet oxygen is obtained in a bubbling chemical generator with a discharge unit attached to the generator output.

2. EXPERIMENT

In order to obtain oxygen fluxes with a high concentration of excited $O_2(a^1\Delta_g)$ molecules, we used the reaction of chlorinating the alkaline solution of hydrogen peroxide. This reaction is the most efficient source of singlet oxygen [1]. The reaction proceeded in a simple and reliable bubbling SOG consisting of a quartz cylinder 150 mm in diameter and 270 mm in height, which was filled with a working solution (a mixture of 750 ml of 50% H_2O_2 and 400 ml of 50% KOH aqueous solutions). Chlorine was supplied through the punched bottom. Singlet oxygen was produced as a result of the reaction of chlorine with the surface film of the solution. For the 100 l/s fixed pumping rate, the SOG provided an oxygen flux with a pressure up to 3 torr and a singlet-oxygen content up to 50% with respect to the total oxygen pressure. Since the generator used the hydrogen peroxide and alkaline aqueous solutions, the gas flux at the generator output contained water vapor. The water-vapor content depends on the solution temperature. Since the reaction of the singlet-oxygen production is exothermic, the temperature does not stay

1063-780X/00/2603-0278$20.00 © 2000 MAIK "Nauka/Interperiodica"

constant in the course of experiment; consequently, the water content also changes.

The breakdown voltage as a function of the composition, temperature, and pressure of the gas mixture was measured in the discharge chamber connected to the gas channel at a 25-cm distance from the SOG. The electric field was directed perpendicularly to the gas flow (Fig. 1). The sphere–plane electrode system made of stainless steel consisted of a plane electrode 54.8 mm in diameter and 10 mm thick, with rounded edges (curvature radius 5 mm) and a sphere 20.2 mm in diameter. The gap d between the electrodes was 6.6 mm. The dc voltage (which can be smoothly varied in the range 100–2500 V) was applied to the discharge chamber by a VMS-2500 stabilized source through a 100 kΩ limiting resistor. The spherical electrode was at the negative potential.

The voltage U at the discharge-chamber electrodes was monitored by a highly resistive ($R > 10$ MΩ) B7-22 digital voltmeter. The breakdown instant was determined by a sharp decrease in the voltage at the discharge chamber as the output voltage of the source was smoothly increased. The accuracy of determining the breakdown voltage was ~0.5%. To decrease the experimental error, each measurement was carried out four times in approximately one minute; during this time, the basic parameters of the gas mixture flowing through the discharge chamber remained almost unchanged.

Before the working solution was poured into the SOG, we measured the breakdown voltage as a function of the dry-oxygen pressure. The results were used to test the method and determine the extent to which the water pressure affects the measurements. With the same purpose, we carried out measurements at different temperatures of the working gas. The measurements showed that, as the temperature of the solution increases (which is equivalent to an increase in the water-vapor pressure), the breakdown voltage increases, which is opposite to the effect produced by singlet oxygen. Since the water-vapor pressure in the singlet-oxygen generation regime can exceed the water-vapor pressure in the unexcited-oxygen bubbling regime, the observed difference in the values of the measured breakdown voltage can be attributed to the presence of singlet-oxygen molecules in the gas flow. In the first five columns of the table, we present experimental data for different pressures of the mixture and different water-vapor contents. The value of the electric field is defined as U/d. The last column presents the calculated (for the given E/N) values of αd, where α is the first Townsend coefficient. We studied both the mixtures that do not contain singlet oxygen and those with 50% singlet oxygen.

3. PROCESSING THE EXPERIMENTAL DATA

The data from the table are plotted in Fig. 2 in the form of the dependence of the breakdown voltage on the parameter Nd (the so-called Paschen curve for the breakdown of a uniform gap [4]). The same figure presents the Thomas–Bets and Davies [5] data for pure oxygen taken from [6]. Our data for dry oxygen and those cited are connected by polygonal lines. It is seen that the behavior of the breakdown voltage with increasing Nd is similar in both cases. The difference in the values of the breakdown voltage measured in [5] and in our experiments may be ascribed to the difference in the cathode substance (steel in our experiments, gold and platinum in [5]).

The experimental points related to humid oxygen and the mixture containing singlet oxygen are not connected by curves, because at first glance the scatter in these points is on the same order as the distance

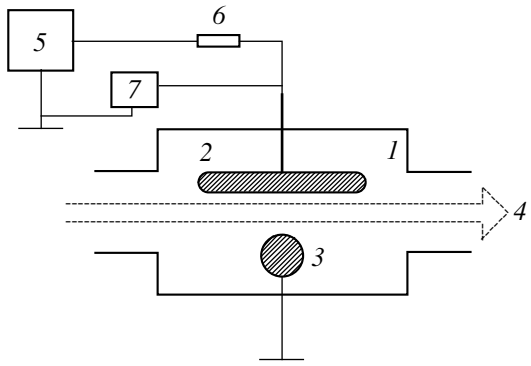

Fig. 1. Schematic of experiments on the measurement of the breakdown voltage for a glow discharge: (*1*) discharge chamber, (*2*) plane electrode, (*3*) spherical electrode, (*4*) gas-mixture flow, (*5*) VMS-2500 dc high-voltage source, (*6*) limiting ballast resistor, and (*7*) digital voltmeter.

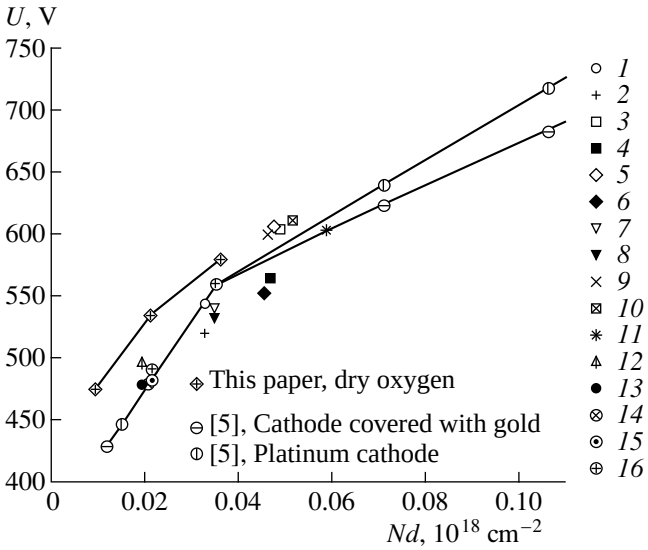

Fig. 2. Breakdown voltage as a function of Nd. Closed symbols and symbols with numbers *2*, *11*, *14*, *15*, and *16* relate to the mixture containing 50% singlet oxygen. The symbol numbers correspond to the row numbers in the table.

Table

no.	$O_2 + O_2(^1\Delta)$, torr	$O_2(^1\Delta)$	H_2O, torr	U, V	Nd, 10^{18} cm^{-2}	E/N, 10^{-16} V cm^2	αd
1	1.4	–	0.1	543	0.0327	166.2	11.31
2	1.4	+	0.1	520	0.0327	159.2	11.32
3	2.1	–	0.15	604	0.0490	123.3	13.86
4	2.0	+	0.15	565	0.0468	120.7	13.52
5	2.1	–	0.09	606	0.0477	127.1	13.82
6	2.0	+	0.09	552	0.0455	121.3	13.22
7	1.4	–	0.2	541	0.0348	155.2	11.56
8	1.4	+	0.2	533	0.0348	152.9	11.83
9	2.1	–	0.03	600	0.0464	129.3	13.62
10	2.1	–	0.27	611	0.0516	118.4	14.12
11	2.0	+	0.7	603	0.0588	102.5	14.66
12	0.88	–	0.01	495.6	0.0194	255.7	8.23
13	0.9	+	0.01	478	0.0198	241.2	8.37
14	0.9	+	0.03	479	0.0203	236.5	8.46
15	0.9	+	0.06	482	0.0209	230.5	8.59
16	0.9	+	0.07	490	0.0211	231.9	8.68
17	0.97	–	–	535.8	0.0211	253.6	12.27
18	1.66	–	–	579.6	0.0362	160.3	8.96

between the sets of points. Note that the breakdown voltage for dry oxygen substantially exceeds that for humid oxygen. To understand the reason for this difference, we calculated the first Townsend coefficient α for the oxygen–water vapor mixtures and the mixtures of a gas containing singlet oxygen with water vapor at the constant total gas density. This coefficient for the typical value of the reduced field $E/N = 120 \times 10^{-16}$ V cm^2 is presented in Fig. 3.

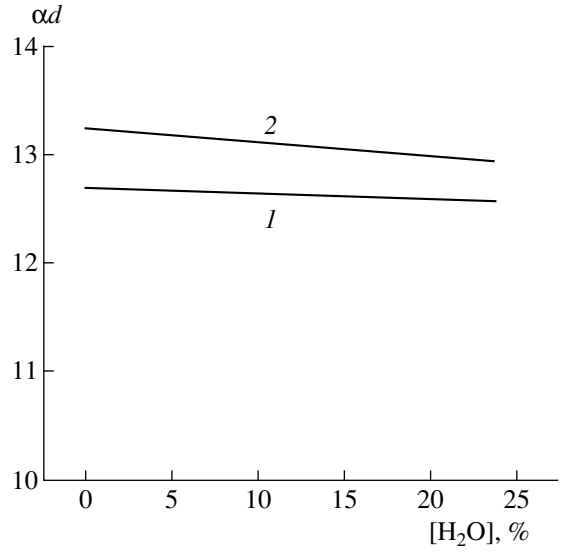

Fig. 3. Parameter αd as a function of the water-vapor concentration at $P = 2.1$ torr and $E/N = 120 \times 10^{-16}$ V cm^2 for (*1*) unexcited oxygen and (*2*) mixture containing 50% singlet oxygen.

In calculating the Townsend coefficient, we solved the Boltzmann equation for the electron energy distribution function (EEDF) taking into account certain processes of electron excitation of oxygen molecules, ionization, and attachment. We used the two-term approximation and found the EEDF under nonsteady Townsend conditions. Such a formulation of the problem does not completely correspond to the experiment, but is rather close to it if the influence of the ionization on the EEDF is included correctly. The most of the necessary cross sections are taken from [6]. Because of the high values of E/N (see table), the calculated quantity αd is almost insensitive to uncertainties in the cross-section data. The ionization cross sections appear to be of the most importance (for example, the dissociative attachment rate for singlet oxygen and oxygen in the ground state is two orders of magnitude less than the ionization rate). The direct data on the ionization cross sections for singlet oxygen are absent. However, the position of the molecular terms for $O_2(a^1\Delta_g)$ and $O_2(X^3\Sigma_g)$ states allows us to say that a simple downward shift along the energy axis gives satisfactory ionization cross section for singlet oxygen. The cross section for the collisions of the second kind was found from the principle of detailed balance. It was verified that, for typical values of E/N, collisions of the second kind have little or no effect on the EEDF shape. The other cross sections for inelastic collisions with singlet-

oxygen molecules were also taken to be equal to the corresponding cross sections for the ground state with a 0.98-eV shift. The transport cross section for singlet oxygen was assumed to be the same as that for the ground state of oxygen. The set of cross sections for scattering by water molecules was chosen according to [7]. For mixtures containing singlet oxygen, the dimensionless quantity αd characterizing the amplification in the electron avalanche is somewhat more sensitive to the water-vapor content. However, on the whole, the water vapor insignificantly influences the ionization rate; estimates show that this influence can be neglected. Estimates also show that, for values of E/N typical of the breakdown, the attachment processes can be neglected. Thus, the observed difference in the breakdown voltage for dry and humid oxygen can only be explained by the change in the secondary-emission properties of the cathode surface in the presence of water vapor. Further, we will neglect the possible dependence of the effective secondary-emission coefficient on the water-vapor concentration at a constant gas density. The reason for ignoring both this dependence and the role of singlet oxygen in the secondary-emission processes is seen in Fig. 4, in which the quantity αd calculated for the experimental values of the breakdown voltage (see also the last column of the table) is plotted as a function of Nd. It is seen that almost all of the points lie on the same smooth curve. The dry-oxygen data are somewhat apart (points 17 and 18), which can be explained by the difference in the effective secondary-emission coefficients, as was mentioned above. Note that, according to the elementary breakdown theory, the almost twofold change in αd corresponds to the change in the secondary-emission coefficient γ from $10^{-6.5}$ to $10^{-3.5}$. The exact reason for such a change in γ is not clear. However, it is noted in [8] that, in the general case, the quantity αd varies within the range $9 < \alpha d < 18$. The possible reasons for the change in the breakdown value of αd are also discussed in [8].

Thus, if we assume that αd is independent of the concentration of singlet oxygen and water vapor (Fig. 3), which is confirmed by the set of points in Fig. 4, we can calculate the breakdown voltage and compare it with the experimental values. The calculation procedure is clarified in Fig. 5. The first two items in the table are obtained for humid oxygen and the mixture containing singlet oxygen at the same gas density. In this case, by calculating αd for humid air for the experimentally determined value of E/N corresponding to the breakdown and equating this value to αd for the mixture containing singlet oxygen, we find E/N for the breakdown in the mixture containing singlet oxygen. In the particular case corresponding to Fig. 5, the calculated values of E/N and U in the mixture containing 50% singlet oxygen are in good agreement with the experiment. The remaining points do not contain data referring to the constant value of Nd; consequently, the direct calculation of the difference between the breakdown voltages is impossible. Therefore, we use the following procedure.

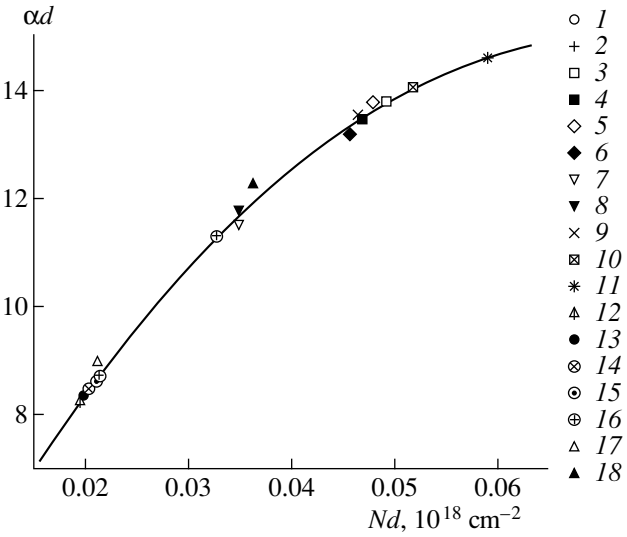

Fig. 4. Parameter αd as a function of Nd. The curve is plotted using the data from the table. The symbol numbers correspond to the row numbers in the table. The solid curve is the polynomial interpolation.

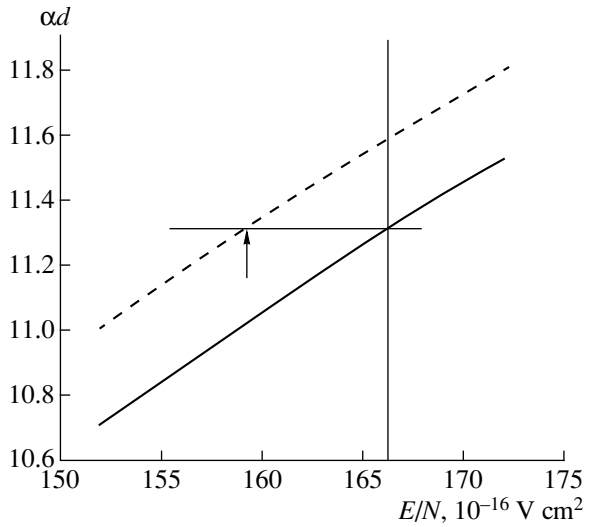

Fig. 5. Explanation for the calculation of the breakdown fields. The dashed and solid lines correspond to humid oxygen (1.4 torr O_2 + 0.1 torr H_2O) and the mixture containing singlet oxygen. The arrow shows the experimental value of E/N.

The dependence of N/E on Nd was approximated by the second-power polynomial and drawn through the experimental points for the humid-air breakdown (solid line in Fig. 6). Note that the points on the solid and dashed curves at the same value of E/N correspond to the same calculated values of αd. Assuming that αd is independent of the concentrations of water and singlet oxygen, we derived the dependence of N/E on Nd for

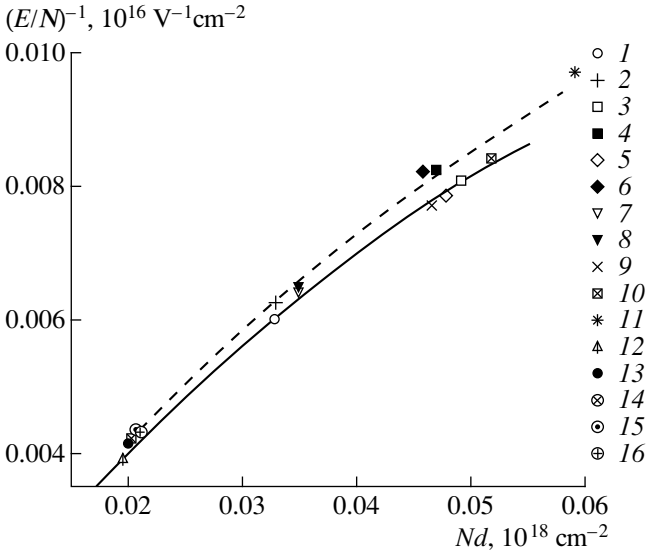

Fig. 6. Comparison of the calculated breakdown values of E/N with the experimental data. The solid line is the polynomial interpolation of the experimental data for unexcited oxygen, and the dashed line is calculated for the mixtures containing singlet oxygen. The symbol numbers correspond to the row numbers in the table.

the 50% singlet-oxygen mixture (dashed curve in Fig. 6). As is seen, the theoretical curve agrees well with the experimental data. The size of the markers in the figure is approximately equal to the experimental error. The use of a large number of the experimental points allows us to conclude that the threshold breakdown voltage decreases when oxygen is excited on the singlet level. Good agreement between the theoretical and experimental data also justifies the procedure of calculating the singlet-oxygen ionization cross section that is based on the assumption that this cross section is equal to the oxygen ionization cross section in the ground state shifted 0.98 eV toward the lower energies.

4. CONCLUSION

We have experimentally observed a decrease in the breakdown voltage in the presence of 50% $O_2(a^1\Delta_g)$ in a mixture of oxygen with water vapor as compared to an unexcited gas. This effect is explained by the increase in the ionization rate due to a lower ionization potential for the $a^1\Delta_g$ state compared to the ground state. The results of calculations agree well with the experimental data.

ACKNOWLEDGMENTS

This work was supported by the Russian Foundation for Basic Research (project no. 98-02-16235) and the Ministry of Science and Technology of the Russian Federation (under Program 09).

REFERENCES

1. W. E. McDermott, N. R. Pchelkin, *et al.*, Appl. Phys. Lett. **32**, 469 (1978).
2. A. Hill, Proc. SPIE **3343**, 1069 (1998)
3. N. P. Vagin, V. S. Pazyuk, and N. N. Yuryshev, Kvantovaya Élektron. (Moscow) **22**, 776 (1995).
4. Yu. P. Raizer, *Gas Discharge Physics* (Nauka, Moscow, 1987; Springer-Verlag, Berlin, 1991).
5. A. Thomas-Betts, and D. E. Davies, Br. J. Appl. Phys., Ser. 2 **2**, 213 (1969).
6. B. Eliasson and U. Kogelschatz, Report No. CH-5405 (Brown Boveri Forschungszentrum, Baden, 1986).
7. M. Yousfi, N. Azzi, I. Gallimberti, and S. Stangherlin, *Electron-Molecule Collision Cross Section and Electron Swarm Parameters in Some Atmospheric Gases (N_2, O_2, CO_2 and H_2O), Data Base Collection* (Toulouse–Padova, 1968).
8. L. B. Loeb, *Electrical Coronas* (University of California Press, Berkeley, 1965), p. 29.

Translated by A. D. Smirnova